Arístides Morillo

Design and Development of a Folded-Sheet Reactor Concept for Hydrogen Production by Steam Reforming of Methanol

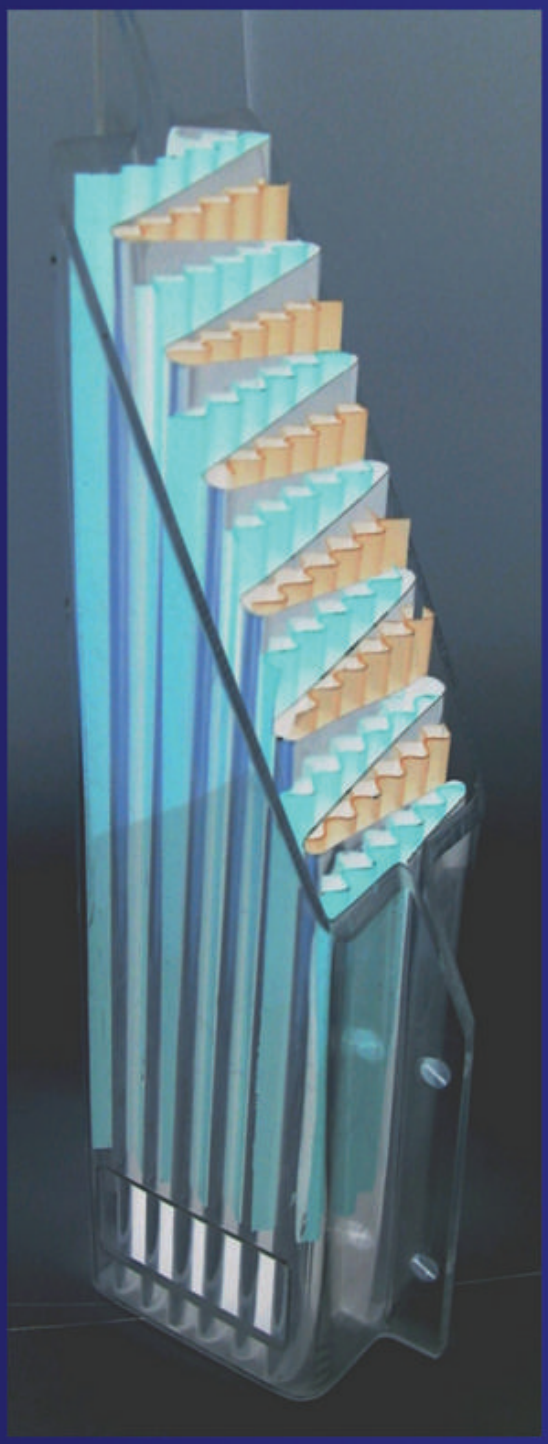

Cuvillier Verlag Göttingen

Design and Development of a Folded-Sheet Reactor Concept for Hydrogen Production by Steam Reforming of Methanol

Von der Fakultät Maschinenbau
der Universität Stuttgart zur Erlangung der Würde
eines Doktors der Ingenieurwissenschaften (Dr.-Ing.)
genehmigte Abhandlung

vorgelegt von
Arístides Morillo
geboren in Valencia, Venezuela

Hauptberichter	:	Prof. Dr.-Ing. habil. Clemens Merten
1. Mitberichter	:	Prof. Dr.-Ing. Gerhart Eigenberger
2. Mitberichter	:	Prof. Dr.-Ing. Rainer Reimert

Tag der mündlichen Prüfung: 18.01.2008

Institut für Chemische Verfahrenstechnik
der Universität Stuttgart
2008

Bibliografische Information der Deutschen Nationalbibliothek
Die Deutsche Nationalbibliothek verzeichnet diese Publikation in der Deutschen Nationalbibliografie; detaillierte bibliografische Daten sind im Internet über http://dnb.ddb.de abrufbar.
1. Aufl. - Göttingen : Cuvillier, 2008
Zugl.: Stuttgart, Univ., Diss., 2008

978-3-86727-782-2

© CUVILLIER VERLAG, Göttingen 2008
Nonnenstieg 8, 37075 Göttingen
Telefon: 0551-54724-0
Telefax: 0551-54724-21
www.cuvillier.de

Alle Rechte vorbehalten. Ohne ausdrückliche Genehmigung des Verlages ist es nicht gestattet, das Buch oder Teile daraus auf fotomechanischem Weg (Fotokopie, Mikrokopie) zu vervielfältigen.
1. Auflage, 2008
Gedruckt auf säurefreiem Papier

978-3-86727-782-2

Preface

The present thesis was accomplished during my Ph.D. research work at the Institute for Chemical Process Engineering (ICVT) of the University of Stuttgart. This was partly supported by the Fundación Gran Mariscal de Ayacucho (Fundayacucho, Venezuela) as a part of a cooperation project with the company Adam Opel AG (Germany). The work deals with the design and development of the so called "Folded-Sheet Reactor Concept" using as an example the autothermal coupling of the hydrogen generation reaction via endothermic steam reforming with a combustion reaction.

First and foremost I wish to express my gratitude to Prof. Clemens Merten for the intensive support and cooperation in the research project. As my "Doktorvater", the German name for the Ph.D.-Tutor, he gave me not only important technical advices but also an admirable and very important familiar treatment. Thanks for the given confidence and for always showing me the right path.

My special gratitudes are towards Prof. Gerhart Eigenberger for the motivation and the technical tutoring of my research work. His brilliant ideas and wise critics defined to a large extent the success of this work. In addition I am deeply gratefully to Prof. Rainer Reimert for the commitment to my work and for the important contribution at the end phase of my thesis.

The construction department and the scientific workshop of the ICVT were the most important contributors in this work, the real artists in the development of the Folded-Sheet Reactor Concept. Mr. Friedrich, as the architect of the concept, and Mr. Lorenz, Mr. Schumacher, Mr. Hildinger and the rest of the crew, as the prefect task-force, made possible that this history could be written.

Moreover I like to thank Gregorios Kolios, Carsten Becker, Achim Gritsch and Bernd Glöckler for the technical input and the inconditional support. Specially I'll remember my dear colleagues and friends Frank Meier, Wolfgang Lengerer, Andreas Gorbach, Oliver Borchers, Axel Salden, Matthias Stegmaier, Andreas Weller, Frank Opferkuch and Eduardo López for the fascinating moments and the great working climate provided during the ICVT phase, making possible to have fun even in the hard working days.

Last but not least I would like to thank my family for the support despite of the distance, my wonderful woman and son for the motivation and the impulse in my life, and God for always being there.

Ludwigshafen am Rhein, January 2008 Arístides Morillo

to Sandra Karina

Contents

PREFACE **I**

NOTATION **IX**

ABSTRACT **XV**

ZUSAMMENFASSUNG **XXI**

1 INTRODUCTION **1**

1.1 The Way to the Fuel Cells 1

1.2 Fuel Cell Process Optimization 2

1.3 Hydrogen Production for Fuel Cells 3

1.4 Objectives and Thesis Structuring 8

2 LITERATURE REVIEW **9**

2.1 Fundamentals on the PEMFC 9

2.1.1 Fuel Cell Characteristic Curve 10

2.2 Determination of the FC Hydrogen Requirement 11

2.3 Thermal Power Output 13

2.4 Fuel Cell Systems - Process Integration 13

2.5 On-board Hydrogen Generation for Fuel Cells 15

2.5.1 Fuel Requirements for Fuel Cells 15

2.5.2 Fuel Processing Technology Review 16

2.5.3 Selection of the Primary Fuel 19

2.6 Steam Reforming of Methanol (SRM) 23

2.6.1 The Water-Gas Shift Reaction (WGS) 25

2.6.2 Steam Reforming and WGS Catalysts 25
2.6.3 Kinetic Model 26

3 PARALLEL-PLATE REACTOR CONCEPTS 29

3.1 Parallel-Plate Devices 29
3.2 Manufacturing Alternatives 33
3.3 The Folded-Sheet Reactor 33

4 KINETIC STUDIES ON SRM 39

4.1 The Catalytic Plug Flow Reactor 39
4.1.1 Description of the Experimental Setup 39
4.2 Experimental Evaluation 48
4.2.1 Influence of the Operating Temperature 48
4.2.2 Influence of the Steam-to-Methanol Ratio 53
4.3 Kinetic Parameter Evaluation 56
4.3.1 Modeling of the Fixed-bed Reactor for SRM 56
4.3.2 Results and Discussion 57

5 REACTOR MODELING 65

5.1 Simplified Reaction System for the SRM 65
5.2 Model Assumptions 65
5.3 Reactor Model 66
5.4 Model Equations 68
5.5 Material Balances 70
5.5.1 Reforming Gas 70
5.5.2 Fuel Gas 71
5.6 Energy Balances 73
5.6.1 Metallic Sheet 73
5.6.2 Reforming Gas 73
5.6.3 Fuel Gas 74
5.6.4 Reforming Catalyst 75

5.6.5 Combustion Catalyst 75
5.7 Ideal Gas Law 76
5.8 Methanol Conversion and CO Selectivity 76
5.9 Numerical Solution Methods 77

6 PRELIMINARY DESIGN AND DEVELOPMENT 79

6.1 SRM in the 1-kW Folded-Sheet Reactor 79
6.1.1 Initial Considerations 79
6.1.2 Reaction Engineering Simulations 80
6.1.3 Experimental Proof of Concept 94
6.2 Evaporation Studies 104
6.2.1 Description of the Evaporation Unit 104
6.2.2 Description of the Experimental Setup 104
6.2.3 Description of the Data Acquisition Method 105
6.2.4 Experimental Evaluation 106

7 THE 10-KW SRM REACTOR 115

7.1 Up-Scaling Strategies 115
7.2 Reaction Engineering Simulations 118
7.2.1 Determination of the 10-kW Operating Conditions 118
7.2.2 Dynamic Simulations on the Cold Reactor Warm-Up 119
7.2.3 Dynamic Simulations on the Start-up of Reforming 122
7.3 Reactor Configuration and Distribution of Feed 124
7.3.1 Operating Principle 124
7.3.2 Optimization of the Combustion Side Feed 125
7.3.3 Optimization of the Fuel Gas Feed 128
7.4 Reformer Construction and Experimental Testing 131
7.4.1 Monitoring of the Reaction Behavior 132
7.4.2 Experiments on the Reformer Start-up 134
7.4.3 Load Changes During Reformer Operation 138

A GENERAL DERIVATION OF THE BALANCE EQUATIONS 143

A.1 Mass Balance 143

A.2 Energy Balance 145

B PARAMETERS AND REACTOR GEOMETRY 149

B.1 Reactor Geometry 149

B.1.1 Spacer Geometry and Reactor Total Volume 150

B.1.2 Phase Volumetric Fraction 154

B.1.3 Specific Transfer Area 156

B.2 Transport Parameters and Material Properties 158

B.2.1 Specific Heat Capacity 158

B.2.2 Solid Density 158

B.2.3 Effective Axial Dispersion 159

B.2.4 Effective Axial Thermal Conductivity 159

B.2.5 Convective Heat and Mass Transfer Coefficients 160

B.2.6 Calculation of the Chemical Equilibrium Constant 161

B.2.7 Pool on Chemical Data 163

B.2.8 *Peppley's* Kinetic Data 164

C OVERALL BALANCES FOR THE 10-KW REFORMER 165

C.1 Overall balances of the 10-kW reformer 165

C.2 Mass and heat flow diagram 169

D COMPLEMENTARY EXPERIMENTAL EVALUATION 171

D.1 Fixed Hydrogen Combustion - Variable Electrical Heating 171

E TECHNICAL DRAWINGS 173

F PHOTOGRAPHS 185

BIBLIOGRAPHY 195

Notation

Latin Symbols

a; A	$[m^2]$	area; surface
c_p	$[\frac{kJ}{kg\ K}]$	specific heat capacity
C_p	$[\frac{kJ}{mol\ K}]$	specific heat capacity
D_{ax}	$[\frac{kg}{m\ s}]$	axial dispersion coefficient
Δg	$[\frac{kJ}{kmol}]$	Gibb's free energy
Δh	$[\frac{kJ}{mol}]$	formation enthalpy
ΔH	$[\frac{kJ}{mol}]$	reaction enthalpy
ΔS	$[\frac{J}{mol\ K}]$	reaction entropy
E	$[\frac{bar\ m^3}{kmol}]$	activation energy
F	$[\frac{A\ s}{mol}]$	*Faraday* constant
h	$[mm]$	height
i	$[\frac{A}{cm^2}]$	current density
J	$[\frac{mol}{m^2\ s}]$	molar flux density
k_1	$[\frac{m^2}{s\ mol}]$	reaction rate constant: steam reforming of methanol
k_2	$[\frac{m^2}{s\ mol}]$	reaction rate constant: methanol decomposition
k_3^*	$[\frac{m^2}{s\ mol}]$	reaction rate constant: water-gas shift reaction
k_4^0	$[\frac{m^2}{s\ mol}]$	reaction rate constant: hydrogen oxidation reaction
K	$[-]$	equilibrium constant; absorption constant
L	$[m]$	length
M	$[\frac{kg}{kmol}]$	molar weight
$\dot{m}$	$[\frac{kg}{m^2\ s}]$	specific mass flux
$\dot{N}$	$[\frac{mol}{s}]$	molar flow

n	$[-]$	number of; *Faraday's* number of equivalent electrons transferred
P	$[W]$; $[\frac{W}{cm^2}]$	power; power density
p	$[bar]$	pressure (1 bar = 10^5 Pa)
$\dot{Q}$	$[W]$	heat flux
r	$[mm]$; $[\frac{mol}{m^2\ s}]$	radius; reaction rate
$r_{m,i}$	$[\frac{mol}{g_{cat}\ s}]$	reaction rate per unit of mass of catalyst
R	$[\Omega]$	resistance
$\mathbb{R}$	$[\frac{bar\ m^3}{kmol\ K}]$	universal gas constant
T	$[K]$; [°C]	temperature
U	$[V]$; $[\frac{kW}{m^2\ K}]$	voltage; heat transfer coefficient
V	$[V]$	voltage
$\dot{V}$	$[\frac{m^3}{s}]$; $[slm]$	volumetric flow rate; standard volumetric flow rate
vol		volume
w	$[\frac{kg}{kg_{total}}]$	mass fraction
wt.		weight
X	$[mm]$; $[-]$	characteristic reactor side dimension; conversion
y	$[-]$	molar/volumetric fraction
z	$[m]$	reactor axial coordinate

Greek Symbols

α	$[\frac{W}{m^2\ K}]$	convective heat transfer coefficient
β	$[\frac{m}{s}]$	mass transfer coefficient
ε	$[\frac{m^3}{m^3_{total}}]$	volumetric fraction
ε^{gas}	$[\frac{m^3_{gas}}{m^3_{total}}]$	gas content
λ	$[\frac{W}{m\ K}]$	heat conduction; molar stoichiometric excess [-]; fictive coordinate $[m]$
η	$[Pa\ s]$	dynamic viscosity
ν	$[\frac{m^2}{s}]$	kinematic viscosity; stoichiometric coefficient
ϱ	$[\frac{kg}{m^3}]$	density
ξ	$[\frac{mol}{h}]$	reaction extent

Indexes

air	air
ch	channel
$conv$	convective
$diff$	diffusive
eff	effective
el	electric
$evap$	evaporation
$endo$	endotherm
exo	exotherm
fg	fuel gas; combustion side
g; G	gas
i	reaction index
iso	isotherm; iso-wall
j	specie index
$jack$	casing
liq	liquid
$overh$	overheating
ref	reforming, reforming side
s	solid; catalyst
$side$	side
sp	spacer
$stack$	fuel cell stack
$steam$	steam
th	thermal
tot	total
$tube$	tubular
v; V	volumetric
w	wall
z	reactor axial coordinate

Acronyms, Abbreviations and Chemical Names

AFC	alcaline fuel cell
ATR	autothermal reforming
DMM	digital multimeter
FC	fuel cell
GHSV	gas hourly space velocity
HTS	high temperature shift
LFC	liquid flow controller
LHV	Lower Heating Value
LPG	liquefied petroleum gas
LTS	low temperature shift
MCFC	molten carbonate fuel cell
MCP	heat capacity flux ratio: fuel gas / reforming gas
MeOH	methanol
MFC	mass flow controller
MFM	mass flow meter
NECAR	New Electric Car
PAFC	phosphoric acid fuel cell
PDE	partial differential equation
PEM	polymer electrolyte membrane
PI	process intensification
POX	partial oxidation
ppm	parts per million (1/10000 wt%)
PrOx	preferential oxidation
PSA	pressure swing adsorption
S/M	steam-to-methanol molar ratio
SOFC	solid oxide fuel cell
SR	steam reforming

SRM	steam reforming of methanol
RDS	rate-determining step
WGS	water-gas shift
Al_2O_3	aluminum oxide (alumina)
CH_3OH	methanol
CH_4	methane
CO	carbon monoxide
CO_2	carbon dioxide
CuO	copper oxide
H_2	hydrogen
H_2O	water
H_2S	hydrogen sulfide
N_2	nitrogen
O_2	oxygen
S	sulfur
ZnO	zinc oxide

Abstract

Due to the growing demand of fossil energy observed in the last years and their foreseeable scarcity, fuel cells are considered to be one of the alternatives for partially replacing conventional energy producing systems. One of the sectors most affected by this problematic would be the automotive sector. Here, because of their advantages regarding operating conditions, power density and flexibility, the Proton Exchange Membrane (PEM) fuel cell has been intensively investigated and successfully tested in automotive vehicles, as for example in the Daimler Chrysler NECAR prototypes [1].

Ideally, hydrogen for fuel cell powered vehicles should be directly stored in pressure or cryogenic tanks and used by the fuel cell to generate motion. Because hydrogen storage still addresses some questions regarding safety and stability, on-board hydrogen production technologies are considered as transitional solution. The method of choice is steam reforming of liquid hydrocarbons or alcohols, an essentially endothermic process. Typical on-board hydrogen processors consist of multi-tubular fixed-bed reactors, heated by an external medium. This kind of reactors features inefficient heat transport, resulting in poor reaction conversion/selectivity, inefficient catalyst utilization, and low thermal performance [2].

The aim of this work is to contribute to the design and development of the folded-sheet reactor concept for hydrogen production for fuel cell applications. Based on a previous parallel plate reformer prototype [3], modification and further optimization steps are proposed and evaluated. Additionally, the folded-sheet reactor concept is tested for reforming related applications, like liquid evaporation. In the folded-sheet reformer, the endothermic reforming reaction takes place in the even channels and the exothermic combustion reaction (counter currently) in the odd ones of this parallel channel array. The combustion reaction is represented by the catalytic oxidation of hydrogen, e.g. using the off-gas stream coming from the anode side of the fuel cell. Here, air flows counter currently to the reformate and hydrogen is side fed over well-positioned catalyst layers in order to provide a locally distributed heat production.

For this work, hydrogen will be produced in the hydrogen processor via steam reforming of methanol (SRM). This endothermic reaction is typically catalyzed by $CuO/ZnO/Al_2O_3$-based catalysts in pellet form. In the first part of this work, the low-temperature water-gas shift (WGS) catalyst BASF K3-110 [4] in pellet form is employed for kinetic studies. Furthermore an equivalent catalyst formulation provided by the project partner is used for the evaluation of the folded-sheet reactor. This time the catalyst is coated over thin, corrugated metal sheets, which are inserted into the reactor channels.

In this work a sequence of development steps has been performed. It starts with a kinetic study of the employed catalyst, providing the kinetics for a first simulation study of the counter-current coupling of methanol steam reforming with hydrogen combustion. The simulation results were the base for the design and experimental evaluation of two versions of a counter-current steam reformer for a hydrogen production, equivalent to 1 kW thermal power. In parallel, the catalytically heated evaporation of water and methanol in a folded-sheet evaporator was also experimentally validated. These results were the fundaments for the manufacturing and experimental testing of an integrated folded-sheet reformer prototype for a hydrogen production corresponding to 10 kW_{LHV}, which includes feed evaporation, steam reforming and CO cleaning up steps in one single apparatus.

For the kinetic studies of the steam reforming reaction on the BASF K3-110 catalyst, an isothermal (electrically heated) fixed-bed reactor, endowed with lateral gas sampling ports for determining the gas composition at five axial positions was employed. This study shows that higher wall temperatures allow for larger methanol conversions. But high reaction temperatures also contribute to elevated CO concentrations in reformate, while lower temperatures favor the CO consumption via WGS reaction. Higher temperature levels should then be provided at the reactor entrance to achieve maximum methanol conversion (with an associated undesired production of CO), and a decreasing temperature profile in the second half of the reactor should favor the conversion of the generated CO by WGS. Steam should be fed in some excess to methanol to guarantee total reaction conversion. On the other hand, larger amounts of excess-steam must be avoided because it results in an inefficient thermal performance (due to the high evaporation energy associated). A steam-to-methanol molar ratio of 1.3 is recommended. Based on the experimental results, a parameter adjustment on *Peppley's* kinetic model [5] was carried out. The results show that methanol steam reforming (to H_2 and CO_2) is the main reaction while methanol decomposition (to H_2 and CO) is a minor side reaction, in particular at low temperatures. At high temperatures part of the H_2 formed may back react to water by the reverse WGS reaction. The WGS reaction therefore has a strong influence on CO selectivity.

A detailed simulation model was developed to evaluate the behavior of the folded-sheet reformer, working for a maximum capacity of 1 kW_{th}. This model allows to study the influence of the reactor dimensions and structuring, as well as to optimize the operating conditions. First simulation results support the conclusions of the fixed-bed kinetic study: most of the heat generated by the hydrogen combustion has to be transferred to the reforming side near the reactor entrance to achieve a maximum methanol conversion, whilst the rest of the reactor must serve as heat exchanger to cool down the reformate and reduce the CO concentration in reformate via WGS. The combustion catalyst can be split in two sections and both have to be carefully installed for a more controlled CO formation: a first zone in the proximity of the reactor entrance and a second near the reactor center. The second zone should support the first one in achieving a maximum methanol conversion, maintaining a moderate operating temperature (thus the CO concentration remains low). A decreasing temperature profile in the second half of the reactor let the WGS reaction consume the produced CO, reducing its concentration to required levels. The feed-air flow rate must be adjusted so that the reactor does not cool down too much, since this negatively influences the conversion of the reforming reaction.

Based on these approaches, a first folded-sheet reformer prototype was manufactured and experimentally tested. The first part of the reforming channel was filled with reforming catalyst and the second one with water-gas shift catalyst. A sample port was installed between both zones to quantify the effect of the WGS section. Results show that the folded-sheet reformer concept works as expected: methanol/steam reforming reaction is heated by the hydrogen combustion reaction in counter current, achieving not only relatively high methanol conversions but also higher CO concentrations in reformate. The performance of the reforming reaction can be finely controlled by adjusting the side-fed hydrogen. The WGS catalytic zone installed in the second reactor half helps to reduce the CO produced in the first section of the reformer to about one half.

Further evaluations on the folded-sheet concept, this time functioning as catalytically heated evaporator for the liquid feed, were carried out. Results indicate that the evaporation process can well be performed in such a configuration. Problems regarding output pulsation were only recognized either when exceeding a critical liquid load in the feed or when the liquid feed system (pump) does not work properly. In general, liquid evaporation showed a very stable behavior in long-time experiments. When starting-up and shutting-down the evaporator unit, it becomes necessary to finely adjust the heat input. Unstable behavior in this short time is expected: initially, pre-evaporation is observed before the liquid enters the preheated evaporator; and inversely, when liquid-pump is shut down, the heat front migrates to the liquid entrance causing pulsations in the output.

Taking as a reference the results from the 1 kW folded-sheet reformer and from the folded-sheet evaporator, process integration and scale-up strategies were implemented in order to achieve a compact hydrogen processor for fuel cell applications that incorporates (methanol/water) liquid evaporation, steam reforming of methanol and water-gas shift reaction in a single device, for an increased output capacity of 10 kW. For the scale-up, the main criterion was the transfer of the specific mass flow rate of the methanol/water mixture successfully tested with the 1 kW reformer to the new prototype. Additionally, to obtain better reactor compactness and higher mechanical stability, a quadratic cross section layout was preset. This resulted in an array of 16 reforming and 17 combustion channels with a channel depth of 130 mm.

The cold start of the 10 kW reformer results in a critical step in the system operation. The hydrogen combustion reaction must provide the necessary heat first to warm the massive reformer unit and afterwards to power the steam reforming reaction. Dynamic simulations on the 10 kW reformer show that it takes about 25 minutes to reach a stationary initial temperature, suitable for starting the reforming reaction. This value should be further reduced in order to start a fuel cell vehicle in short times. Once the reactor has achieved the desired reaction temperature, methanol/water mixture is fed to the reactor. Dynamic simulations demonstrate that methanol and water immediately react to produce hydrogen, although it takes about 160 minutes to achieve a stationary operation of the reformer. Except for the large time required to preheat the reformer, a relatively fast response of the reformer can be predicted for start conditions.

With this information a 10 kW folded-sheet reformer was designed, built-up and experimentally tested. In the construction phase, it was necessary to solve many manufacturing prob-

lems: feed-air stream entering the combustion side with an elevated velocity, was needed to be equally distributed not only along all the parallel combustion channels but also in each's channel depth; side feed hydrogen was required to be uniformly distributed not only in each combustion channel but also in the depth of each channel; front casing plates were needed to be fixed to the folded sheet leakage-free; reformer casing must support mechanical and thermal stresses due to the reactions, as well as possible overpressure.

Experimental results on the 10 kW folded-sheet reformer reveal a cold-start time of about 100 minutes. This time was necessary to preheat the reformer up to operating (reforming) temperature. Reaction conditions for preheating were conservatively adjusted to avoid thermal shocks and damages of the metallic reactor structure. Dynamics of changes of the reactor power output were evaluated at both increasing and decreasing power demand. On the combustion side, hydrogen injection was sensitively adjusted to achieve higher methanol conversions on the reforming side. Additionally, because axial temperature measurements were not implemented for this bench-scale reformer, only the external wall temperatures were monitored so that the overall temperature did not exceed the predefined limit level. Again, the results demonstrate a direct relationship between the methanol conversion and the CO production. As expected, higher methanol conversions lead to higher CO outlet concentrations. Maximum methanol conversion was about 90 $\%$ at 10 kW_{LHV} hydrogen production, but elevated CO concentrations (4.3 $\%$) were observed. This fact can be attributed to a reforming catalyst with lower activity, so that higher temperatures are necessary to achieve maximum methanol conversion. As a result, CO production is highly favored. Adequate catalyst activity and fine control of reaction selectivity are crucial for satisfactory performance. In general, the scaled-up folded-sheet reformer demonstrated a rapid output response to changes in the feed load.

The operating temperature can be easily adjusted by hydrogen side feed on the combustion side, demonstrating that the overall heat transfer is no longer the limiting step. This was also the case for liquid evaporation and overheating (even at unsteady operating conditions), thereby achieving a useful integrated reactor design for hydrogen generation.

To advance in the development of the folded-sheet reactor concept, following points are suggested for future works:

- Because of the large start-up times observed for the 10 kW reformer, a further miniaturization of the reactor concept should be considered.
- Due to certain instabilities observed at the folded-sheet evaporator, it is recommended to provide sufficient cooling to the liquid feed, e.g. by a cooled pump, in order to prevent any pre-evaporation before entering the evaporation channels. Such a provision has been beneficial for the electrically heated evaporators.
- Further investigations should be focused on the development and implementation of catalysts with higher activities and selectivities to guarantee maximum methanol conversions at minimum CO production rates.
- An additional CO conditioning stage such as preferential oxidation (PrOx) should be

incorporated to reach the CO concentration levels ($<$10 ppm) required by PEM fuel-cell systems.

- In order to adapt the operating conditions of the steam reforming reaction to possible process steps installed after the reformer unit which require higher operating pressures (i.e. pressure-swing-adsorption), pressure supporting construction alternatives should be evaluated. A first approach could be stated by suggesting a reactor circular cross section (e.g. a spiral reactor [6, 7]).

Zusammenfassung

Aufgrund der in den letzten Jahren vorhandenen, wachsenden Nachfrage nach fossilen Energieträgern sowie ihrer absehbaren Knappheit, werden Brennstoffzellen als Alternative für den teilweisen Ersatz der konventionellen energieproduzierenden Systeme gesehen. Einer der hiervon am stärksten betroffenen Bereiche wird die Automobilindustrie sein. Die Protonenaustauschmembran-Brennstoffzelle (Proton Exchange Membrane Fuel Cell PEMFC) wurde aufgrund ihrer Vorteile hinsichtlich Betriebsbedingungen, Energiedichte und Flexibilität bereits intensiv erforscht und erfolgreich in Fahrzeugen erprobt, beispielsweise in den NECAR Prototypen von Daimler Chrysler [1].

Idealerweise ist der in Brennstoffzellenfahrzeugen benötigte Wasserstoff direkt in Druck- oder Kryotanks zu speichern, um von dort die Brennstoffzelle zu versorgen. Da die Wasserstoffspeicherung nach wie vor einige Mängel bezüglich Sicherheit und Zuverlässigkeit aufweist, wird die on-board-Wasserstoffherstellung als zeitliche Übergangslösung betrachtet. Das Verfahren der Wahl ist hierbei die Dampfreformierung von flüssigen Kohlenwasserstoffen oder Alkoholen, welche einen im Wesentlichen endothermen Prozess darstellt. Typische on-board-Wasserstoffanlagen bestehen aus Rohrbündel-Rohrreaktoren, die durch externe Wärmeträger beheizt werden. Diese Art von Reaktoren ist durch einen ineffizienten Wärmeübergang gekennzeichnet, was zu geringem Reaktionsumsatz und -selektivität, ineffizienter Katalysatornutzung sowie niedriger thermischer Leistung führt [2].

Das Ziel dieser Arbeit ist, einen Beitrag zum Entwurf und zur Entwicklung des Faltblechreaktor-Konzepts für die Wasserstofferzeugung für Brennstoffzellenanwendungen zu leisten. Aufbauend auf einem bestehenden Parallelplattenreformer-Prototyp [3], wird der Faltblechreaktor modifiziert, optimiert und untersucht, ebenso für weitere Anwendungen, wie die Flüssigkeitsverdampfung, erprobt. Im Faltblechreaktor finden die endotherme Reformierungsreaktion in den geradzahligen Kanälen und die exotherme Verbrennungsreaktion (im Gegenstrom) in den ungeradzahligen Kanälen einer Parallelkanalanordnung statt. Die Verbrennungsreaktion wird durch die katalytische Oxidation von Wasserstoff dargestellt, z. B. aus dem anodenseitigen Abgasstromes der Brennstoffzelle. Hierbei strömt Luft im Gegenstrom zum Reformiergas, der Wasserstoff wird seitlich zugeführt - genau über den zur lokalen Wärmeerzeugung platzierten Katalysatorschichten.

Im Rahmen dieser Arbeit wird der Wasserstoff in einem Wasserstoffprozessor durch Dampfreformierung von Methanol (SRM) erzeugt. Diese endotherme Reaktion findet üblicherweise an $CuO/ZnO/Al_2O_3$-basierten Katalysatoren in Pelletform statt. Im ersten Teil dieser Arbeit wird für die Kinetik-Untersuchungen der Wassergas-Niedertemperatur-

Shift-Katalysator BASF K3-110 in Pelletform verwendet [4]. Weiterhin wird für die Untersuchung des Faltblechreaktors ein vom Projektpartner gelieferter, vergleichbarer Katalysator eingesetzt. Mit diesem Katalysator wurden Feinmetall-Wellstrukturen beschichtet, die in die Reaktorkanäle eingefügt werden.

Die Entwicklung erfolgte in mehreren Schritten. Sie beginnt mit der kinetischen Untersuchung des verwendeten Katalysators, welche die Kinetik für eine erste Simulationsstudie zur Kopplung der Methanol-Dampfreformierung und der Wasserstoffverbrennung im Gegenstrom liefert. Die Simulationsergebnisse sind die Grundlage für den Entwurf und die experimentelle Untersuchung von zwei Gegenstrom-Dampfreformern, ausgelegt für die Wasserstofferzeugung mit einem Äquivalent von 1 kW thermischer Leistung. Gleichzeitig wurde die katalytische Verdampfung von Wasser und Methanol in einem Faltblech-Verdampfer erprobt. Auf Grundlage der erzielten Ergebnisse wurden die Herstellung und experimentelle Erprobung eines Faltblechreformer-Prototypen mit einer äquivalenten thermischen Leistung von 10 kW realisiert, welcher Verdampfung des Zulaufs, Dampfreformierung und CO-Feinreinigung in einem einzigen Apparat integriert.

Für die Kinetik-Untersuchung des Dampfreformierungssystems mit dem BASF K3-110 Katalysator wird ein isothermer (elektrisch beheizter) Integralreaktor verwendet, der in axialer Richtung mit Gas-Seitenabzügen versehen ist, um an fünf verschiedenen Stellen des Reaktors Proben zur Bestimmung der Gaszusammensetzung entnehmen zu können. Die Ergebnisse zeigen, dass höhere Wandtemperaturen einen höheren Methanolumsatz begünstigen. Die höheren Temperaturen führen jedoch auch zu einer erhöhten CO-Konzentration im Reformat, während niedrige Temperaturen den CO-Verbrauch in der WGS-Reaktion fördern. Am Reaktoreintritt sollten aus diesem Grund höhere Temperaturen herrschen, um einen maximalen Methanolumsatz zu erreichen. Dabei wird in größeren Mengen CO produziert. Gleichzeitig ist im zweiten Abschnitt des Reaktors ein abfallendes Temperaturprofil erforderlich, um die Umwandlung des entstandenen CO mittels WGS zu begünstigen. Zusätzlich muss Dampf im Überschuss zugeführt werden, um einen Methanol-Vollumsatz sicherzustellen. Andererseits sind größere Dampfmengen zu vermeiden, da dies aufgrund der zu erbringenden hohen Verdampfungsleistung in einem ineffizienten thermischen Wirkungsgrad resultiert. Ein Dampf-zu-Methanol-Verhältnis von 1,3 wird empfohlen. Auf Basis der experimentellen Ergebnisse wird eine Parameteranpassung des kinetischen Modells nach *Peppley* durchgeführt [5]. Die Ergebnisse zeigen, dass die Dampfreformierung von Methanol (zu H_2 und CO_2) die Hauptreaktion darstellt, während der Methanolzerfall (zu H_2 und CO) vor allem bei niedrigen Temperaturen eine Nebenreaktion ist. Bei höheren Temperaturen reagiert ein Teil des erzeugten Wasserstoffs über die umgekehrte WGS-Reaktion wieder zurück zu Wasser. Deshalb hat die WGS-Reaktion einen starken Einfluss auf die CO-Selektivität.

Ein detailliertes Simulationsmodell wurde erstellt, um das Verhalten des 1-kW-Faltblechreformers zu beschreiben. Dieses Modell ermöglicht die Untersuchung des Einflusses der Reaktorgröße und -strukturierung, sowie die Optimierung der Betriebsbedingungen. Erste Simulationsergebnisse bestätigen die Ergebnisse der Kinetik-Untersuchungen im Integralreaktor: der Großteil der Wärme, die bei der Wasserstoff-Verbrennung entsteht, muss zur Reformierseite in die Nähe des Reaktoreintritts übertragen werden, um einen maximalen Methanolumsatz erreichen zu können. Die verbleibende Reaktorlänge ist als Wärmetauscher

zu nutzen, um das Reformat zu kühlen und die CO-Konzentration mittels der WGS-Reaktion zu senken. Der Verbrennungskatalysator kann in zwei Segmente aufgeteilt werden und ist dabei gezielt anzuordnen, um eine kontrollierte CO-Bildung zu erreichen: das erste Segment in Nähe des Reaktoreintritts und das zweite Segment in der Reaktormitte. Das zweite Segment soll das erste unterstützen, um einen maximalen Methanolumsatz bei einer gemäßigten Betriebstemperatur zu erreichen - dadurch wird die CO-Konzentration niedrig gehalten. Um die angestrebten niedrigen CO-Konzentrationen zu erreichen, wird in der zweiten Reaktorhälfte ein abfallendes Temperaturprofil eingestellt, so dass mittels WGS-Reaktion das gebildete CO verbraucht wird. Der Zulauf-Luftstrom muss dabei so angepasst werden, dass der Reaktor nicht zu stark abgekühlt wird, was sich negativ auf den Gesamtumsatz der Reformierung auswirkt.

Aufbauend auf diesen Erkenntnissen wurde ein erster Faltblechreaktor-Prototyp gebaut und experimentell untersucht. Der erste Abschnitt des Reformierungskanals wurde mit Reformierungskatalysator, der zweite Abschnitt mit Wassergas-Shift-Katalysator gefüllt. Mit Hilfe von zwischen den beiden Katalysatorzonen angeordneten Probenahmestellen konnte der Einfluss der WGS-Reaktionszone quantifiziert werden. Die Ergebnisse zeigen, dass der Faltblechreformer den Erwartungen entsprechend arbeitet: Die Methanol-Dampfreformierung läuft katalytisch in den parallelen Kanälen ab, die Wärmebereitstellung erfolgt durch die Wasserstoffverbrennung im Gegenstrom. Im Reformat werden nicht nur ein hoher Methanolumsatz und sonder auch eine hohe CO-Konzentrationen beobachtet. Der Verlauf der Reformierungsreaktion kann durch die Anpassung des auf der Brenngasseite nachgespeisten Wasserstoffs beeinflusst werden. Die katalytische WGS-Zone in der zweiten Reaktorhälfte trägt dazu bei, die im Abschnitt der Reformierung erreichte CO-Konzentration um 50 $\%$ zu reduzieren.

Des Weiteren wurden Untersuchungen des Faltblech-Apparatekonzepts zur Verdampfung eines Flüssigkeits-Zulaufs durchgeführt. Die Ergebnisse zeigen, dass der Verdampfungsprozess mit diesem Apparatekonzept erfolgreich durchgeführt werden kann. Probleme wie Pulsationen am Austritt des Verdampfers werden nur dann festgestellt, wenn entweder eine kritische Flüssigkeitsbeladung im Zulauf überschritten wird oder wenn die Flüssigkeitsförderung (Pumpe) nicht ordnungsgemäß läuft. Generell zeigt die Flüssigkeitsverdampfung ein sehr stabiles Verhalten im Dauerbetrieb. Beim Ein- und Ausschalten der Verdampfungseinheit ist ein genaues Einregeln des Wärmeeintrags erforderlich. Während dieser Phase ist instabiles Verhalten zu erwarten: einerseits findet zu Beginn eine Vorverdampfung der Flüssigkeit in der Zuleitung des vorgeheizten Verdampfers statt; andererseits, beim Abschalten der Flüssigkeitspumpe, wandert die Verdampfungsfront zum Flüssigkeitseintritt, was ebenfalls zu Pulsationen am Ausgang führt.

Ausgehend von den Ergebnissen des 1 kW-Faltblechreformers und des -verdampfers wurden Schritte zur Prozessintegration und die Maßstabvergrößerung durchgeführt, um einen kompakten Wasserstoffprozessor für Brennstoffzellenanwendungen zu entwickeln, der Methanol-Wasser-Verdampfung, Dampfreformierung und Wassergas-Shift-Reaktion in einem Apparat integriert, sowie eine erhöhte Leistung von 10 kW_{th} aufweist. Für die Maßstabvergrößerung wurde der flächenspezifische Massendurchfluss der Methanol-Wasser-Mischung aus dem 1-kW-Reformer als Hauptkennzahl auf den neuen Prototypen übertragen. Zusätzlich wurde, um eine bessere Kompaktheit und die mechanische Stabilität

des Reaktors zu verbessern, ein quadratischer Apparatequerschnitt gewählt. Daraus resultiert eine Anordnung von 16 Reformier- und 17 Verbrennungskanälen mit einer Kanallänge von jeweils 130 mm.

Der Kaltstart des 10 kW-Reformers stellt einen der kritischsten Betriebszustände dar. Die Wasserstoffverbrennung muss die nötige Wärme bereitstellen, um zunächst die massive Reformereinheit aufzuwärmen, und anschließend die Dampfreformierungsreaktion zu betreiben. Dynamische Simulationen zeigen, dass etwa 25 Minuten benötigt werden, um eine stationäre Reaktoranfangstemperatur zu erreichen - die geeignet ist, um die Reformierungsreaktion zu starten. Diese Zeit muss künftig verkürzt werden, um die Anforderungen an einen instationären Betrieb zu erfüllen. Sobald der Reaktor die gewünschte Starttemperatur erreicht hat, wird ihm das Methanol-Wasser-Gemisch zugeführt. Dynamische Simulationen zeigen auch, dass Methanol und Wasser sofort miteinander reagieren und ein wasserstoffreiches Reformat bilden. Allerdings sind etwa 160 Minuten bis zum Erreichen von stationären Bedingungen im Reformer erforderlich. Trotz der langen Aufwärmzeit des Reformers kann ein relativ schnelles Ansprechverhalten nach Erreichen der Startbedingungen nachgewiesen werden.

Mit diesen Erkenntnissen wurde ein 10 kW-Faltblechreformer entworfen, aufgebaut und experimentell getestet. In der Konstruktionsphase mussten einige Gestaltungs- sowie Herstellungsprobleme gelöst werden: Der auf der Verbrennungsseite mit hoher Geschwindigkeit eintretende Luftstrom muss nicht nur gleichmäßig auf alle Verbrennungskanäle, sondern auch in deren Tiefe verteilt werden. Der über eine Seiteneinspeisung zugeführte Wasserstoff muss nicht nur gleichmäßig auf alle Verbrennungskanäle, sondern ebenso in deren Länge aufgeteilt werden. Die stirnseitigen Endplatten müssen an das Faltblech leckagefrei angebracht werden. Das Reformergehäuse muss die aufgrund der ablaufenden Reaktionen entstehenden mechanischen und thermischen Spannungen aufnehmen können.

Die experimentellen Ergebnisse am 10 kW-Faltblechreformer ergeben Kaltstartzeiten von etwa 100 Minuten. Diese Zeit wird zum Vorheizen des Reformers auf Betriebstemperatur benötigt. Die Reaktionsbedingungen des Vorheizens wurden konservativ eingestellt, um Thermoschocks und Schäden in der metallischen Reaktorstruktur zu vermeiden. Dynamische Änderungen der Reaktorleistung wurden sowohl für ansteigende als auch abfallende Leistung evaluiert. Auf der Verbrennungsseite wurde die Wasserstoffzufuhr angepasst, um einen höheren Methanolumsatz auf der Reformierseite zu erreichen. Zusätzlich werden, da bei diesen Apparateabmessungen keine axialen Temperaturmessstellen integriert sind, die Außenwandtemperaturen überwacht, damit die Gesamttemperatur nicht den vordefinierten Grenzwert übersteigt. Die Versuche bestätigen den direkten Zusammenhang zwischen Methanolumsatz und CO-Bildung. Höhere Methanolumsatzraten sind erwartungsgemäß mit höheren CO-Abgaskonzentrationen verbunden. Bei der Leistung von 10 kW betrug der maximal erreichte Methanolumsatz etwa 90 %, gleichzeitig wurde eine erhöhte CO-Konzentration von 4,3 % beobachtet. Diese Tatsache ist auf den Einsatz eines Katalysators mit niedriger Aktivität zurückzuführen, so dass höhere Temperaturen erforderlich sind, um einen maximalen Methanolumsatz zu erreichen. Als Folge wird die CO-Bildung deutlich gefördert. Für eine befriedigende Leistung sind eine angemessene Katalysatoraktivität und eine genaue Kontrolle der Reaktionsselektivität wesentlich. Generell zeigt der maßstabvergrößerte Faltblechreformer ein schnelles Antwortverhalten am Ausgang bei Änderungen im Zulauf.

Die Betriebstemperatur kann mittels der Wasserstoff-Zufuhr auf der Verbrennungsseite leicht eingestellt werden, was zeigt, dass der Gesamtwärmeübergang nicht mehr der limitierende Faktor ist. Dieser Vorteil konnte erfolgreich auf die Flüssigkeitsverdampfung und -überhitzung (auch unter instationären Bedingungen) übertragen und implementiert werden, wodurch ein brauchbares integriertes Reaktordesign für die Wasserstoffherstellung erreicht wird.

Für die weitere Entwicklung des Faltblechreaktorkonzepts werden folgende Punkte für zukünftige Arbeiten vorgeschlagen:

- Wegen der für den 10 kW-Reformer festgestellten langen Aufheizzeiten ist das Potential einer weiteren Verkleinerung des Reaktorkonzeptes zu erörtern.
- Aufgrund verschiedener Instabilitäten, die am Faltblechverdampfer beobachtet wurden, wird empfohlen, für den Feed eine ausreichende Kühlung z. B. durch eine gekühlte Pumpe vorzusehen, um eine Vorverdampfung zu verhindern. Eine derartige Maßnahme war bei den elektrisch beheizten Verdampfern von Nutzen.
- Weitergehende Untersuchungen müssen sich auf die Entwicklung und Einführung von Katalysatoren mit höherer Aktivität und Selektivität konzentrieren, um eine maximale Methanolumsetzung und minimale CO-Bildung zu gewährleisten.
- Eine weitere CO-Feinreinigungsstufe, wie z. B. durch selektive katalytische Oxidation von CO (PrOx: preferential oxidation), sollte einbezogen werden, um die Anforderungen hinsichtlich der CO-Konzentration für eine PEMFC ($<$10 ppm) zu erfüllen.
- Um die Betriebsbedingungen der Dampfreformierungsreaktion denen nachgeschalteter Prozessschritte, die höhere Betriebsdrücke benötigen (wie z. B. Druckwechseladsorption), anpassen zu können, sind druckbeständige Bauteilausführungen zu untersuchen. Ein erster Ansatz hierzu kann in der Verwendung eines kreisförmigen Reaktorquerschnitts bestehen (z.B. als Spiral-Reaktor [6, 7]).

Chapter 1

Introduction

1.1 The Way to the Fuel Cells

Over the past years, the constant demographic growth has caused an accelerated increase of the general demand of energy, specially but not only in the automotive sector.

In addition, the constant increase of the prices of the primary sources of energy, as a result of a predictable scarcity of the crude-oil and its derivatives, has motivated the intensive search for alternative sources of clean energy, to guarantee an optimal balance between efficient generation of energy, environmental protection and low costs. Several primary energy sources like solar, eolic, chemical, and electrochemical are in competition for producing energy with low- or non-pollutant emissions and high system efficiency.

The use of the so-called Proton Exchange Membrane Fuel Cells (PEMFC), also known as Polymer Electrolyte Membrane Fuel Cell, has been introduced and well accepted for mobile applications, because of their important benefits, in particular:

- high efficiency: fuel cells can theoretically convert up to 90 $\%$ of the energy contained in its fuel into usable electric power and heat. Fuel cell efficiency is not limited by the Carnot limit, because they convert directly chemical energy into electrical energy,
- high power density: depending of the nature of the electrolyte used, fuel cells can operate in a wide power density range, and - contrary to internal combustion engines - can operate at low load with high efficiency,
- fuel cells are friendly to the environment: substitution of conventional internal combustion engines by fuel cells should improve air quality, reduce green-house emissions, and even for power-plants could also reduce cooling water consumption and waste water discharge,
- fuel cells contain no moving parts and eliminate several of the sources of noise associated with conventional transportation systems,
- fuel cells have their highest theoretical efficiency at low temperatures, favoring PEM fuel cells,

- flexible size: depending of the application, fuel cells can be assembled for example in centimeter to meter ranges.

Today it is assumed that fuel cell technology may play a pivotal role in a new technological renaissance - just as the internal combustion engine revolutionized life at the beginning of the 20th century [8]. Such an innovation could have a global environmental and economic impact. Therefore major automobile manufacturers in the world are developing fuel cell vehicles and almost every energy supplying company is thinking seriously about the future application of fuel cells.

1.2 Fuel Cell Process Optimization

In recent decades there has been a significant increase in the energy efficiency of the process industry by optimization of unit operations. To maintain the trend of increasing energy efficiency, it will be necessary to concentrate some physical steps and chemical reactions into a single process step to achieve the desired product with the desired specifications at high efficiency. This combination of unit operations is called ***Process Intensification*** - Figure 1.1.

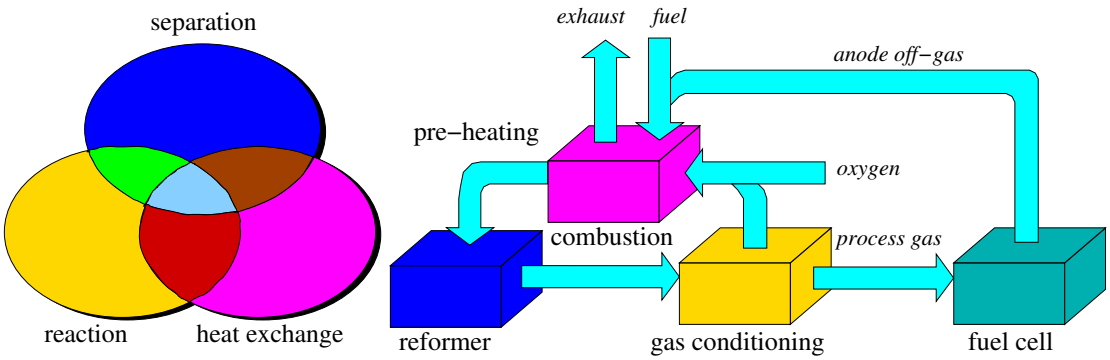

Figure 1.1: Examples for process intensification (*left*) and process integration (*right*)

Process intensification involves making fundamental changes to processing technologies aiming at the development of new compact devices and techniques that lead to substantial improvements in the production processes, reductions in the size of production equipment, lower investment costs, lower energy use and waste production, and finally to more sustainable technologies. In particular, process intensification aims at new and compact designs in which two or more classical unit operations are combined into one hybrid unit.

The process intensification concept is highly related to ***Process Integration*** . Process integration is an established technology for continuous processes in the chemical industry. It involves, for example, the use of heat exchanger networks to optimize heat energy by linking hot and cold process streams in the most thermodynamically advantageous way. While process integration provides valuable incremental improvements, process intensification offers the potential of substantial savings. Both techniques also offer opportunities for higher product quality and yields.

More specifically, fuel cell process optimization requires provision of a suitable fuel, in general hydrogen which at the present will be predominantly generated by reforming of a fossil or renewable organic feedstock. Since reforming requires energy at elevated temperatures the energy integration, using all available energy sources of the process and recovering heat from all hot process streams, is of prime importance. This is shown in Figure 1.1-right, where fuel is fed to a reforming reaction in order to produce a hydrogen rich gas and after, impurities are removed in a conditioning step and mixed with the anode off-gas coming from the fuel cell. This ”fuel cell off-gas” is catalytically burned with oxygen (from air) and the heat released is used to preheat the initial fuel feed up to reforming temperature.

1.3 Hydrogen Production for Fuel Cells

For long time multitubular catalytic fixed-bed reactors filled with catalyst pellets and heated by flame burners from the top or the side walls (see Figure 1.2) were the state of the art for hydrogen generation via endothermic steam reforming of fossil fuels [9, 10, 11, 12].

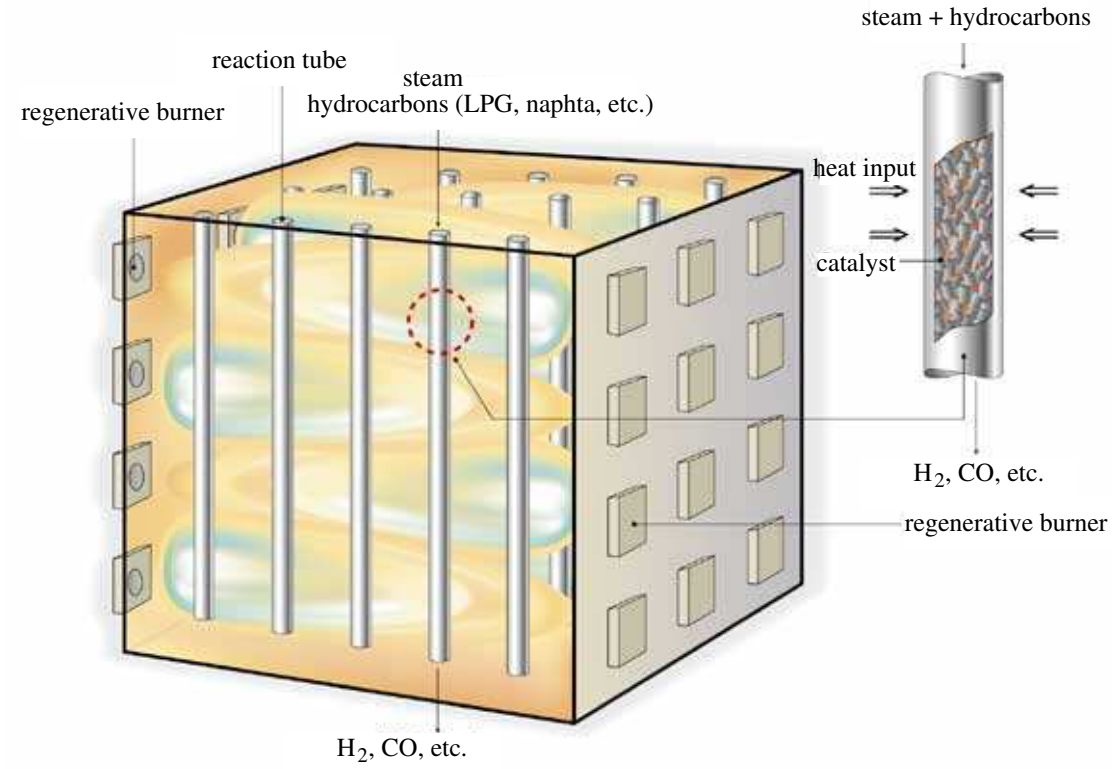

Figure 1.2: Conventional large scale steam reformer [13].

Here, the major problem was faced when attempting to implement this principle for decentralized small scale or mobile on-board production processes. Large scale reformer systems

feature severe limitations regarding heat integration [2]. The heat transfer from the heat carrier (e.g., flame burner, thermo oil, electrical heating, etc.) to the catalyst bulk is hampered by the low thermal conductivities within the catalyst bed (around 1 $\frac{W}{m \cdot K}$), resulting in inefficient catalyst utilization. Substantially improved heat transfer and an efficient heat recovery are therefore crucial for an enhanced process performance.

A way to achieve these goals is to replace the multitubular arrangement by a parallel-plate reactor design where the catalyst of the reforming reaction is coated at one side of a plate and the required heat of reaction is supplied by a catalytic combustion which takes place at the catalyst deposited at the other side of the wall. Then a sequence of parallel reforming and combustion channels are combined into one parallel-plate reactor.

In the past, microchannel devices in form of monolith honeycomb reactors were widely used to help reducing the heat transfer limitations [14, 15, 16, 17]. Ceramic monolith substrates can carry a bigger amount of coating than metallic supports, which gives ceramics the advantage in applications where catalyst deactivators are present or where very high levels of precious metal are needed to reach the desired performance. However, problems with respect to the hermetic seal of the ceramic monolith ends, and in general to the reactor handling (e.g. catalyst interchangeability) were a strong drawback for this class of devices.

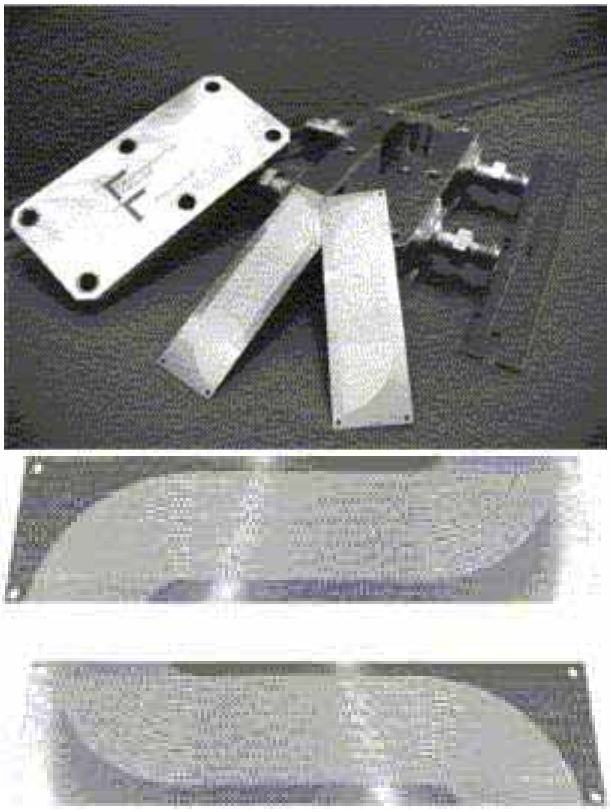

Figure 1.3: Two-passage microstructured reactor with 2500 micro-channels arranged on 25 plates. The channels are 40 mm long, 100 μm deep, and 200 μm large. *Top:* Housing of the reactor; *bottom:* Microstructured plates. (Research Center of Karlsruhe) [18].

Parallel-plate devices were considered as alternative to the monolith reactors. Parallel-plate based apparatuses with an associate large volume-related exchange area have been widely studied and implemented as an alternative for overcoming problems regarding efficient heat transfer. Hydrogen production for fuel cell applications was one of the main targets for this reactor concept. For small scales, some research facilities worked intensively in order to overcome typical construction difficulties. The *IHI* institute proposed a plate-based reformer for hydrogen generation which involves the autothermal heat integration between the endothermic reforming reaction and the exothermic combustion of a fuel gas [19]. A further version of this autothermal parallel-plate reformer was developed by *BG/Advantica* for steam reforming of methane coupled with total combustion of a fuel gas [20]. Here, production equivalents up to 40 $\frac{kW_e}{l}$ have been demonstrated at 650 °C under laboratory conditions. A first microchannel natural gas reformer was achieved by *A. Dicks* in the University of Queensland (Australia) in 2001 [21, 22, 23]. *X. Zhang et al.* studied several catalyst formulations for steam reforming of methanol in microchannel reactors [24]. *Zanfir et al.* performed detailed calculations on plate reformers for hydrogen production by methane steam reforming, pointing out the benefits of the reactor principle regarding heat transfer [25, 26]. A series of very compact microchannel reactors has been successfully constructed by *The Pacific Northwest National Laboratories* and proven for hydrogen production [27]. Hereby important efforts have been carry out by *Reuse et al.* in developing microstructured apparatuses for hydrogen production by methanol steam reforming and partial oxidation [18]. The reactor (Figure 1.3-top) consists of stacked plates (Figure 1.3-bottom) in which steam reforming and partial oxidation can be performed separately. For steam-reforming, the microstructured channels are coated with a suspension of a commercial copper based catalyst (G-66MR, Südchemie). Recently *Whyatt et al.* reported further progress in the steam reforming of natural gas in microchannel hydrogen processors for fuel cell applications (Figure 1.4) [28]. Finally the benefits of plate-based devices have been also proven in the practice in other application fields, like photocatalytical processes [29, 30], reactive etching [31] and classical heat-exchange.

All around the world, companies are working on the development of on-board hydrogen processors for fuel cell applications. Some prototypes have been experimentally validated and put into operation under realistic conditions. In Table 1.1 a list with the most popular companies that are actually working in hydrogen production for mobile applications is given. It can be seen that the majority of the developers are working on processors that are based on gasoline fuels. This responds mainly to the fact that gasoline infrastructure is already available. Methanol and natural gas are even alternative fuels that have been also strongly considered.

Developer	Size unit (kW)	Focus fuel	Reformer technology	Focus stack type
Argonne National Laboratory	3	Gasoline	POX	PEM
Ballard	75	Gasoline		PEM
Daimler Chrysler	75	Gasoline	POX	PEM
General Motors	30	Methanol	SR	PEM
Honda	60	Methanol	ATR	PEM
Hydrogen Burner Technology	50-150	Gasoline	UOB^{TM} (Under-oxidized Burner)	PEM
Innovatek		Methanol	Micro reactors	
Johnson Matthey	6, 20	Methanol	ATR	PEM
McDermott Technology Inc.	50	Gasoline	ATR	PEM
Mitsubishi Electric	10	Methanol	SR - plate	PEM
Nuvera H-POX	0.1-0.5	Natural gas/ propane/methanol	POX	
Nuvera	10, 50	Gasoline	POX	PEM
Plug Power/Epyx	50	Gasoline/methanol	POX	PEM
Toshiba	5	Gasoline/methanol	SR	PEM
Toyota	25	Methanol	SR	PEM
UTC Fuel Cells	100	Gasoline	ATR	PEM

Table 1.1: Main actors in fuel processing for fuel cells for transportation [32]

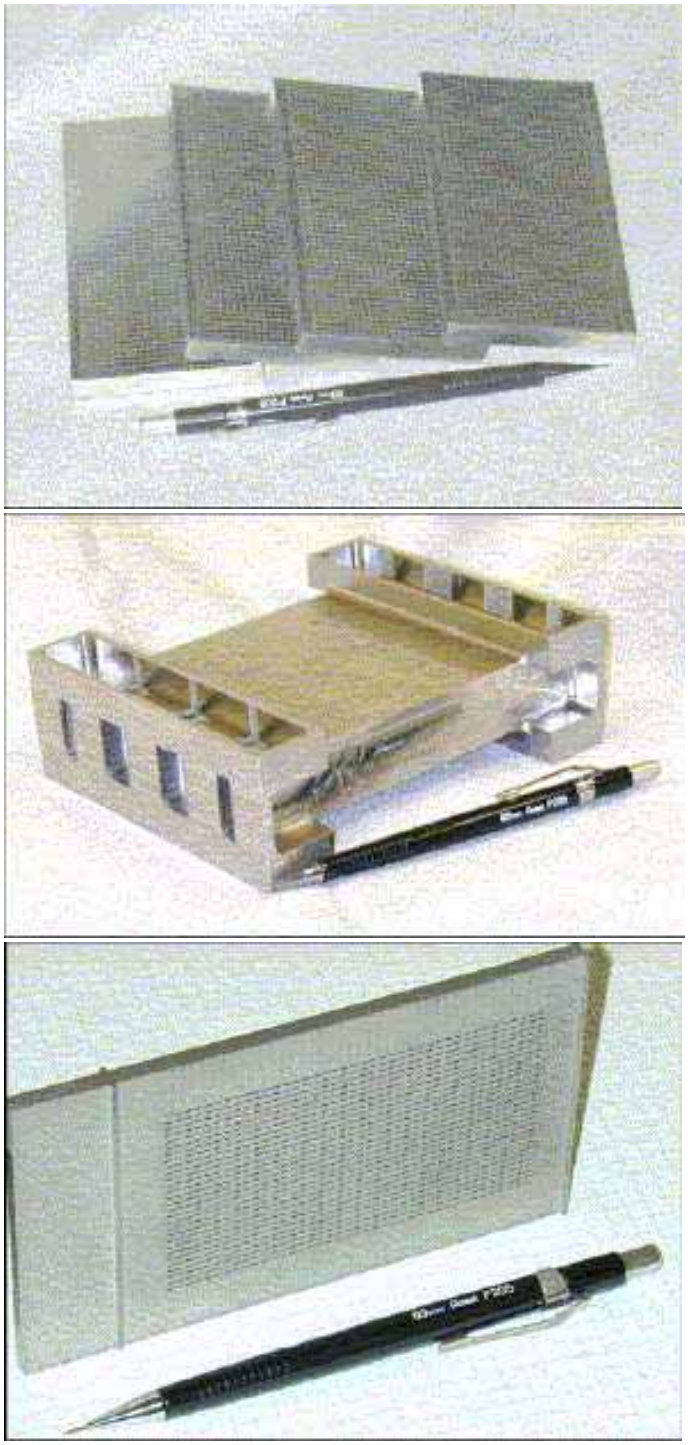

Figure 1.4: PNNL Micro-channel devices. *Top:* 1.8 kW Steam Reforming Micro-Channel Reactor Panels for a 5 kg/day System; *middle:* Air Recuperator for a 5 kg/day System; *bottom:* Micro-Channel Water Vaporizer for 5 kg/day System [28].

1.4 Objectives and Thesis Structuring

The present work focuses on the design, development and implementation of a novel reactor concept for hydrogen generation via steam reforming of methanol: the so-called *Folded-Sheet Reactor Concept*. This reactor should be applicable for feeding fuel cell powered vehicles or to provide hydrogen for small stationary stand-alone applications. All development stages, from the conception to the construction of a reformer unit capable of producing 10-kW thermal equivalent of hydrogen are described.

A main focus of this reactor development is the integration of all steps involved in a single device: feed evaporation of the reactant mixture, steam reforming and subsequent process-gas purification, aiming at the development of an efficient and compact fuel processor.

Development steps comprise the separated study of evaporation, reforming and cleaning-up stages, the integration of all evaluated process stages in a single hydrogen production unit, and the scaling-up to a final prototype, capable of adequately producing the hydrogen amount required for a determined application. The development is based on detailed simulation and oriented experiments.

The content of this work will be presented as follows:

Chapter 2 gives an overview about the fundamentals of fuel cells, hydrogen production, and steam reforming of methanol. General properties and facts on the folded-sheet reactor concept are summarized in **Chapter 3**. A preliminary experimental and simulation study on the kinetics of the methanol-steam-reforming reaction system in an integral fixed-bed kinetic reactor, given in **Chapter 4**, provides the understanding and start considerations for the studies performed in the latter part of this work. The mathematical background on the modeling of the reaction system in a folded-sheet reactor, as well as the numerical simulation strategies are developed in **Chapter 5**. In **Chapter 6** the design and development of the first reactor and evaporator prototypes are discussed, supported by simulation studies and experimental verification. **Chapter 7** presents the steps and development activities as well as experimental tests of the final integrated, up-scaled hydrogen processor. At the end of each section, individual conclusions and further recommendations are given.

Chapter 2

Literature Review

2.1 Fundamentals on the PEMFC

Polymer Electrolyte Membrane Fuel Cells (PEMFC) are electrochemical devices that allow for the combination of hydrogen as fuel and oxygen as oxidant agent to produce water steam and electricity. The reactants hydrogen and oxygen are continuously fed to both electrodes (anode and cathode). Hydrogen diffuses through the porous anode to the three-phase layer catalyst/electrolyte/hydrogen, in which it is split into protons and electrons, as:

$$H_2 \longrightarrow 2H^+ + 2e^- \tag{2.1}$$

The protons (H^+) migrate to the cathode through the polymer electrolyte membrane which requires a great proton conductivity. Simultaneously, the electrons flow over an external current circuit to the cathode. In the other three-phase layer between the cathode and the electrolyte, the protons and electrons from the external circuit react with the oxygen which already has diffused through the porous cathode forming water:

$$2H^+ + \tfrac{1}{2}O_2 + 2e^- \longrightarrow H_2O \tag{2.2}$$

The formed water is removed from the system with the fed excess air on the cathode side. Both electrode reactions sum up to the well-known detonating-reaction:

$$H_2 + \tfrac{1}{2}\,O_2 \longrightarrow H_2O \qquad\qquad \Delta h_R^0 = -241.83\ kJ/mol \tag{2.3}$$

Thus, only oxygen and hydrogen are required to operate a PEMFC (see Figure 2.1). Oxygen is normally taken directly from the air, in spite of dilution effects of the nitrogen present leading to a reduction in the fuel cell efficiency [33].

For automotive applications, hydrogen supply becomes a critical issue, since its on-board storage still addresses important technological limitations. In consequence, on-board hydro-

gen generation from liquid hydrogen carriers has been studied by most car manufacturers and developers.

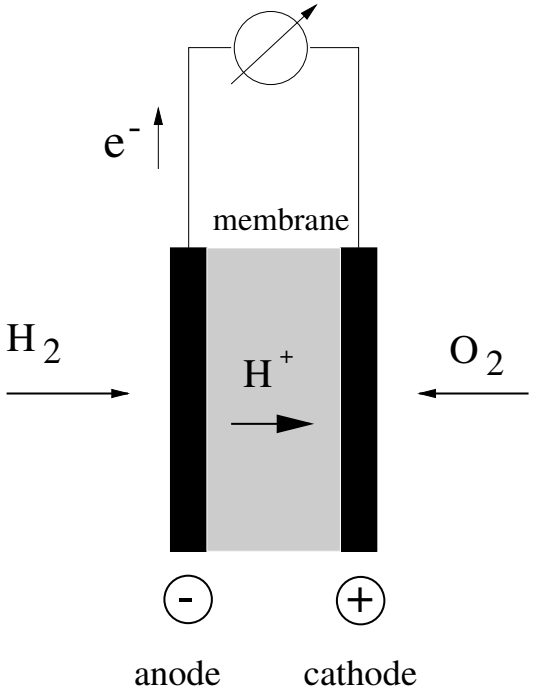

Figure 2.1: Functioning principle of a PEMFC

On-board hydrogen production involves several stages, e.g. storage of hydrogen carrier, gas production and gas conditioning. Several reasons make the low-temperature steam reforming of methanol (SRM) one of the most suitable alternatives for this purpose. Nevertheless, hydrogen generation via SRM also implies the direct formation of carbon dioxide and carbon monoxide. CO_2 is an inert for the rest of the system, but the catalyst of the PEMFC does not tolerate carbon monoxide (CO) concentrations above 50 ppm. Therefore high purity hydrogen is required. This is one of the major challenges in the gas-conditioning stage.

2.1.1 Fuel Cell Characteristic Curve

The power capacity of fuel cells is normally represented by the so-called "*polarization curve*" (or characteristic curve). Cell potential in volts is plotted against the cell current density in amperes per square centimeters. The current density basically represents how fast the reaction 2.3 is taking place[1]. The power capacity of a fuel cell is given as the product of the cell voltage and the current density at the actual operating point in the characteristic curve. Figure 2.2 shows a typical fuel cell characteristic curve and the respective resulting power capacity.

Fuel cell power generation and therefore fuel cell hydrogen consumption are directly dependent on the system power demand. To determine the hydrogen generation requirements,

[1] Number of electrons per second, divided by the surface area of the fuel cell electrolyte face

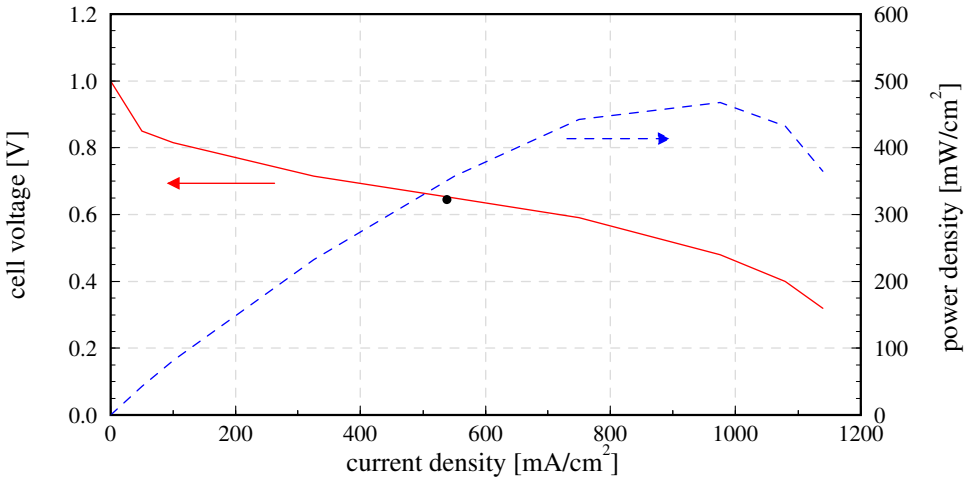

Figure 2.2: Example polarization curve of a fuel cell. Low platinum loading Type B cathodes prepared from 40 w/o Pt catalyst supported on Vulcan XC72C. Low platinum loading Type B anodes; Nafion 117 membrane; 75 °C; H_2/air at 3/3 atm; 1.5/2.0 stoichiometry with a 2/10 pass flow field and internal humidification [34].

operating conditions have to be defined. These are described in detail in the following sections.

2.2 Determination of the FC Hydrogen Requirement

The hydrogen demand of a fuel cell depends on the operation dynamics of the system. As an example of fuel cell demand under dynamic operation, the demand curve for a supercapacitor-assisted fuel cell prototype [35] is presented in Figure 2.3.

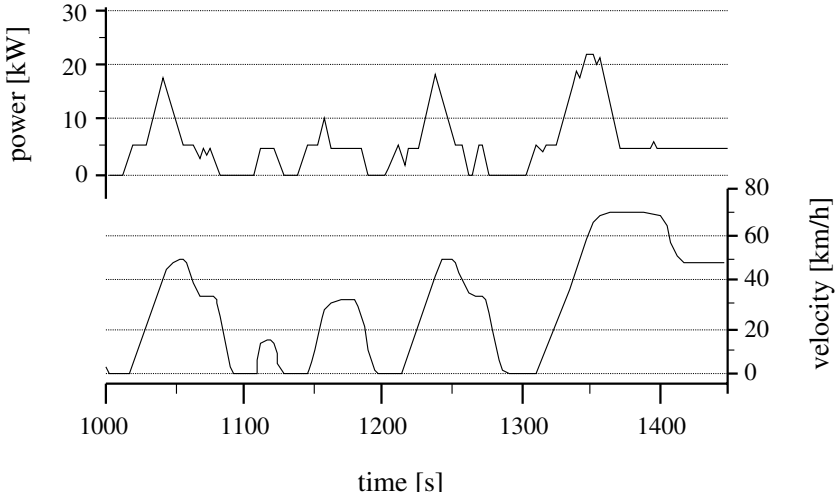

Figure 2.3: Power demand of a fuel cell prototype under dynamical operation [35].

To illustrate the hydrogen requirement of a fuel cell system, an example referred to a specific fuel cell stack [34] is presented.

For a fuel cell stack, composed of 400 single cells of the type referred in figure 2.2 (side dimension: 20 cm), the required hydrogen can be calculated as follows.

The cross section of a single cell is:

$$a_{cell} = 20\ cm\ \cdot\ 20\ cm\ =\ 400\ cm^2. \tag{2.4}$$

Assuming that the fuel cell is operating at a determined point of the polarization curve, e.g., i = 0.52 $\frac{A}{cm^2}$ (at V_{cell} = 0.65 V), the resulting cell current density is:

$$i_{cell} = 0.52\frac{A}{cm^2}\ \cdot\ 400\ cm^2 = 208\ A \tag{2.5}$$

and the correspondent cell and stack *electrical*' power output would be:

$$P_{cell} \ = \ 208\ A\ \cdot\ 0.65\ V\ =\ 135.20\ W_{el} \tag{2.6}$$

$$P_{stack} \ = \ 135.20\ W\ \cdot\ 400\ cells =\ 54080\ W_{el} \quad (54.08\ kW_{el}). \tag{2.7}$$

By using *Faraday's* law [36], which correlates the number of equivalent electrons transferred through the cell (for H_2, n = 2), the *Faraday* Constant (F = 96485 A·s/mol) and the actual electric current, the hydrogen required for this operating point can be obtained by:

$$\begin{aligned} \dot{N}_{H_2} &= \frac{P_{stack}}{n \cdot F \cdot V_{cell}} \\ &= \frac{54080\ W}{2 \cdot 96485\ \frac{A \cdot s}{mol} \cdot 0.65V} \\ &= 0.431155\ \frac{mol}{s}\ \left(1552.16\ \frac{mol}{h}\right). \end{aligned} \tag{2.8}$$

This means that approximately 0.43 $\frac{mol}{s}$ or $1.9{\cdot}10^{-2}$ *nlm* of H_2 are required for the exemplified fuel cell stack working at the selected operating point to produce an equivalent of ca. 54 kW_{el} of electrical energy. It should be mentioned that the considered fuel cell operates at conditions, at which oxygen is fed at a stoichiometric excess of about λ_{O_2} = 1.5 which improves the overall performance of the cell [33].

2.3 Thermal Power Output

In the above example a relationship between the hydrogen required by the fuel cell working at certain conditions and the respective fuel cell *electrical* power output was developed. In order to relate the electrical power output to the energy input of the hydrogen fuel it is common to characterize the fuel with its Lower Heating Value LHV, $\frac{J_{th}}{s}$ or simply W_{th}, the equivalent reaction heat released by the (hypothetical) total oxidation of the produced hydrogen.

Hence, $\dot{n}_{H_2}$ moles per hour of hydrogen consumed represent an equivalent *thermal input* of:

$$thermal\ power\ input\ =\ \dot{n}_{H_2} \cdot \left(-\Delta h^0_{H_2O}\right) \quad [kW_{th}], \tag{2.9}$$

where $\Delta h^0_{H_2O}$ is the standard reaction enthalpy of the hydrogen combustion reaction in $\left[\frac{kJ}{mol}\right]$ (see Eq. 2.3). Considering the example of section 2.2 the thermal energy of hydrogen fed to a fuel cell delivering 54.08 kW_{el} of electrical energy is:

$$thermal\ power\ input\ _{example}\ =\ 0.431155\ \frac{mol\ H_2}{s} \cdot \left(241.83\ \frac{kJ}{mol}\right) = 104.27\ kW_{th} \tag{2.10}$$

In summary 104.3 kW_{th} of energy contained in the hydrogen feed provides 54 kW of electrical energy, resulting in an efficiency of the fuel cell stack of

$$\eta = \tfrac{54}{104.3} \cdot 100\ \% = 51.7\ \%.$$

2.4 Process Integration of Hydrogen Production for Fuel Cell Systems

Figure 2.4 shows a generic fuel cell system, which consists mainly of a hydrogen conditioning (anode side), an oxygen supply (cathode side) and an off-gas reutilization section. An optimal energetic integration between all parts is crucial in order to diminish the energy losses and to enhance the dynamical operation of the complete system.

- Oxygen, either pure or as air, is used in practically all fuel cells as the oxidant. It is obvious that the use of air adds a considerably amount of nitrogen to the system, diminishing the global efficiency because of its diluent-effect. Despite of this fact, pure air is the most economic alternative, since at typical operation conditions it can be taken directly from the surroundings and has not to be stored.
- Given that the direct storage of hydrogen still encounters technical limitations regarding safety and handling, on-board hydrogen production and conditioning stages

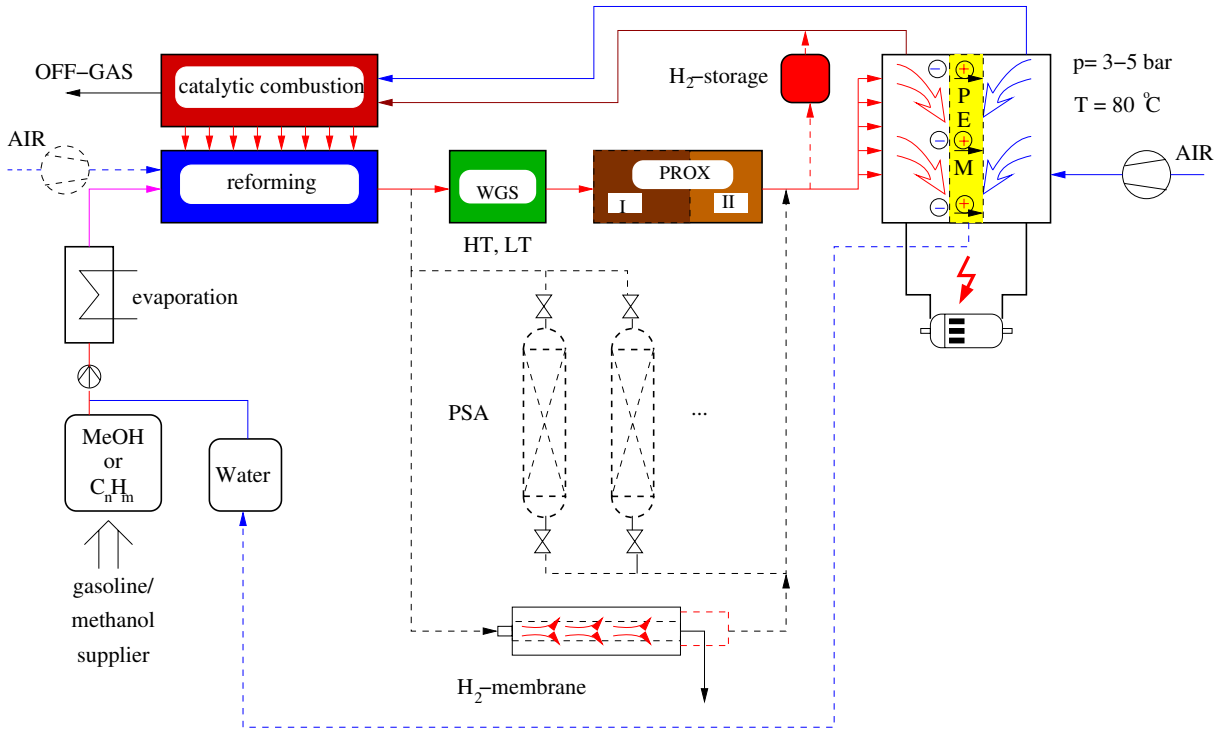

Figure 2.4: Scheme of a fuel cell system with on-board hydrogen production for mobile applications

become relevant. The first factor taken into account considering a hydrogen production system refers to the use of an adequate primary fuel. When using a liquid as primary fuel, an evaporation stage must be added. Depending on the technology employed for hydrogen production, water as steam and/or air are also fed to the system. The fuel/steam/oxygen mixture is directly conducted to the entrance of the hydrogen processor. In this processor unit, a hydrogen-rich gas accompanied with considerable amounts of carbon dioxide (CO_2), carbon monoxide (CO) and eventually traces of methane (CH_4), is chemically produced. The impurities, in special carbon monoxide (poison for the platinum-based fuel-cell anode catalyst), must be removed from the process stream, because they tend to block Pt catalyst sites, preventing H_2 oxidation. For this purpose, as a first clean up unit a water-gas shift reactor is installed. If necessary, a two-level water-gas shift reactor (HT: high-temperature and LT: low-temperature) can be employed. In order to remove the rest of the CO coming from the WGS reactor down to ppm levels, a fine clean-up process is included, e.g. a preferential-oxidation reactor. Preferential-Oxidation reaction (PrOx) means the catalytic conversion of CO with oxygen to CO_2. Because the hydrogen present in the stream also reacts competitively with CO in presence of oxygen, a two stages unit with intensive temperature and oxygen-feed control needs to de incorporated.

- Alternative to the reactive ways of purifying the reforming-gas, physical-chemical processes can be implemented as well, among them pressure swing adsorption (PSA), selective diffusions membrane devices (membrane reactors/separators) and/or the inclusion of CO-, CO_2-sequestrating solids (chemisorption). The feasibility of this tech-

nologies has been already proven, but they must be improved before being implemented in a fuel cell system for mobile applications.

- Off-gas streams contain in the most cases certain amounts of energy which can be recovered by energy integration. A good example of this is given by the off-gas stream, which comes from the anode side. This stream leaves the fuel cell at a temperature of about 70-90 °C and contains considerable amounts of hydrogen. This anode off-gas stream can be fed in a catalytic burner together with the excess air from the cathode side, and the produced heat can be used to evaporate the liquid feed, pre-heat cold currents up to desired temperatures, and/or to cover the energy requirements of the hydrogen processor. This energetic integration represents an important focus point in the development of this work.

2.5 On-board Hydrogen Generation for Fuel Cells

Several different technologies for hydrogen production have been suggested depending on the application field. At industrial scale well-developed processes are available. For application in the transportation sector, several approaches are still under investigation and in development phase. Important criteria, as e.g. start-up time, dynamical behavior, operating conditions and quality of the products, represent the main target of research. The selection of an adequate technology for hydrogen production depends directly on the choice of the fuel cell type, and the selection of an appropriate primary fuel. Different alternatives for producing hydrogen for mobile applications, as well as different primary fuels are presented and discussed in the following sections.

2.5.1 Fuel Requirements for Fuel Cells

The conversion process is dictated not only by the chemical composition of the fuel, but also by the technical requirements of the particular type of fuel cell used. Table 2.1 gives the major fuel cell types together with what is known about their response to various gases present in the feeds.

Whilst all major fuel cell types effectively use hydrogen as a fuel; methane and other hydrocarbons are only usable by the high temperature fuel cell types by internal reforming. Low temperature fuel cells require conversion of hydrocarbons and oxygenates to hydrogen. The most promising type of fuel cell for mobile applications is the low temperature proton exchange membrane (PEM) fuel cell. However, at the operating temperature of PEM fuel cells, the electrocatalyst at the anode is extremely susceptibility to poisoning by carbon monoxide. The high temperature fuel cell types are quite immune and actually able to utilize CO as a fuel but H_2S is generally regarded as a poison. The above facts show that sulfur removal and CO removal are key parts of the fuel processing exercise. In the case of AFC, there is the additional problem of sensitivity to CO_2, which is generally formed in bulk quantities during fuel processing.

gas	PEMFC	AFC	PAFC	MCFC	SOFC
H_2	fuel	fuel	fuel	fuel	fuel
CO	poison ($>$ 10 ppm [a])	poison ($>$ 50 ppm [d])	poison ($>$ 0.5-1 %)	fuel [b]	fuel [b]
CH_4	diluent	diluent	diluent	diluent/fuel [c]	diluent/fuel [c]
CO_2	diluent	poison ($>$ 50 ppm)	diluent	diluent	diluent
S as H_2S	poison	unknown	poison ($>$ 50 ppm)	poison ($>$ 0.5 ppm)	poison ($>$ 1 ppm)

Table 2.1: Fuel requirements for different fuel cell stacks. $(^a)$ Up to 100 ppm can be acceptable if small quantities of air (2 %) are bled into the fuel stream due to oxidation of adsorbed CO. $(^b)$ Most CO utilization is via water gas shift reaction on the anode or internal reforming catalyst. $(^c)$ CH_4 utilization is generally by internal reforming. $(^d)$ Tolerance increases with operating temperature.

2.5.2 Fuel Processing Technology Review

Among the technologies to produce hydrogen on-board for fuel cell applications, partial oxidation (POx), steam reforming (SR) and autothermal reforming (ATR) are the most investigated and developed. A brief overview is given below.

2.5.2.1 Partial Oxidation

As represented by the general reaction path for hydrogen generation via catalytic partial oxidation (Eq. 2.11), the initial fuel reacts exothermally with a sub-stoichiometric amount of oxygen in presence of a catalyst to produce around 60-65 $vol\%$ of hydrogen and additional carbon monoxide and/or dioxide. Equilibrium amounts of these products depend strongly on temperature, less strongly on pressure. The main reaction results in a heat generation and requires elevated temperatures.

$$C_nH_m + (\tfrac{n}{2})\, O_2 \longrightarrow nCO + (\tfrac{m}{2})\, H_2 \qquad \Delta h_R^0 \; < \; 0. \tag{2.11}$$

The partial oxidation of gasoline, diesel or aviation jet fuel (as primary fuel) can be formulated as:

$$C_nH_{2n} + (\tfrac{n}{2})\, O_2 \;\longrightarrow\; nCO + nH_2 \qquad \Delta h_R^0 \; > \; 0. \tag{2.12}$$

$$and \;\; C_nH_{2n} + nO_2 \;\longrightarrow\; nCO_2 + nH_2 \tag{2.13}$$

Although the reaction does not need an external supply of heat, the global efficiency is

affected if the heat produced in the reaction is not recovered from the hot effluents. Partial oxidation of alcohols also runs according to Eqs. 2.14 and 2.15.

$$C_nH_mO_p + \left(\tfrac{n-p}{2}\right) O_2 \longrightarrow nCO + \tfrac{m}{2}\ H_2 \qquad \Delta h_R^0 \ < \ 0. \tag{2.14}$$

$$C_nH_mO_p + \left(n-\tfrac{p}{2}\right) O_2 \longrightarrow nCO_2 + \tfrac{m}{2}\ H_2 \qquad \Delta h_R^0 \ < \ 0. \tag{2.15}$$

CO_2 is usually considered as a product of the water-gas shift reaction, which is the main side-reaction:

$$CO + H_2O \Longleftrightarrow CO_2 + H_2 \qquad \Delta h_R^0 \ < \ 0. \tag{2.16}$$

The use of air as oxygen source introduces nitrogen (inert) in the product stream, leading to outlet hydrogen concentrations of about 40 $vol\%$. Considering the fuel cell operation, this value represents a relatively low hydrogen concentration which can also influence the performance of the cell by reducing its Nernst potential.

In practice, the partial oxidation can be performed in both catalytic and non-catalytic manner [37]. When driven under catalytic conditions the risk of catalyst deactivation exists and in a non-catalytic way there is a risk of carbon precipitation. The product yield from a partial oxidation process can be enhanced by adding an appropriate amount of steam to the product stream in order to steam-reform the remaining (or added) hydrocarbons and clean-up the product gas by means of the water-gas shift reaction.

However, in partial oxidizers for vehicles running with air, the inert nitrogen leads to high flow rates and thus the downstream conditioning units like the water-gas shift and the PrOx must be larger, while the concentration of hydrogen in the reformate remains notable lower.

2.5.2.2 Steam Reforming

Steam reforming (SR) is the most common method for producing hydrogen in the chemical process industry [38]. Even for mobile applications, SR has gained in importance over the last years. The hydrogen generation by steam reforming of a fossil fuel is generally described by the following reaction path:

$$C_nH_m + nH_2O \longrightarrow nCO + \left(n + \tfrac{m}{2}\right) H_2 \qquad \Delta h_R^0 \ > \ 0, \tag{2.17}$$

and in case of steam reforming of gasoline, diesel or aviation jet fuel (as primary fuel):

$$C_nH_{2n} + nH_2O \longrightarrow nCO_2 + 2nH_2 \qquad \Delta h_R^0 \ > \ 0. \tag{2.18}$$

For the steam reforming of alcohols, the following formula applies:

$$C_nH_mO + \left(2n-1\right) H_2O \longrightarrow nCO_2 + \left(2n-1 + \tfrac{m}{2}\right) H_2 \qquad \Delta h_R^0 \ > \ 0, \tag{2.19}$$

The steam reforming reaction is endothermic and depending on the initial fuel and reaction temperature,. It delivers a product stream that contains elevated amounts of hydrogen (about 70-75 $vol\%$ on dry basis). The ratio CO to CO_2 is given by the equilibrium of the water-gas shift reaction. The higher the operating temperature, the greater the amount of CO in the product. Commercial copper-based catalysts have been accepted as good candidates for methanol steam reforming, where relatively low temperatures of 250-300 °C are usually required for a good product selectivity with low CO production. As pointed out, the SR reaction is considerably endothermic and typically limited by heat transfer rather than by reaction kinetics. These constrain represent an important disadvantage when considering the dynamic behavior of the overall system. Consequently, the reformer design is mainly focused on the optimization of the heat-exchange.

A steam reforming system is highly efficient because waste heat from the following process steps can be recycled as input into the endothermic steam reforming process.

2.5.2.3 Autothermal Reforming

Autothermal reforming (ATR) combines the benefits of both partial oxidation and steam reforming in a single process unit. The general scheme for this autothermal reaction is given by:

$$C_nH_mO_p + rO_2 + (2n-2r-p)H_2O \longrightarrow nCO_2 + (2n-2r-p+\tfrac{m}{2})H_2 \qquad \Delta h_R^0 \approx 0. \quad (2.20)$$

This reaction occurs in presence of a catalyst and is, in theory, totally heat balanced (autotherm). The fuel is fed together with a mixture of air and steam. The steam is responsible for the endothermic reforming reaction while the oxygen from the air allows for the exothermic oxidation of part of the fuel. A certain excess of oxygen is fed to compensate the heat losses and to achieve a rapid reformer response, so that the reaction's net result is slightly exothermic. This condition is set by adjusting the parameter "r", better known as the oxygen-to-fuel molar ratio.

The employed catalyst determines the maximum product selectivity and reaction extent. Alumina or oxide-ion-conductor based catalysts combined with transition metals or metallic oxides are commonly employed. In case of employing gasoline as fuel, hydrogen concentrations in the product stream of about 50-60 $vol\%$ can be achieved. Additionally, ATR requires to include severe CO-reducing strategies if it is to be implemented for mobile applications [39].

Closing Remark

Several criteria must be considered for choosing the most appropriate fuel processing technology. Of the three reforming pathways, the steam reforming process yields the highest hydrogen concentration in the product. However, for practical applications, the partial oxidation and autothermal reforming processes have been considered more attractive because no indirect heat transfer from a combustion reaction is required [40]. The low hydrogen concentrations resulting from ATR and partial oxidation however present a strong drawback for both technologies. In addition waste heat from other process steps (e.g. combustion of anode

off-gas) can be efficiently used only in the steam reforming option. Therefore, based upon its important potentials [41, 42], the endothermic steam reforming has been elected in this study for the design, development and implementation of the processor unit for hydrogen generation aiming at mobile and stationary/decentralized applications.

2.5.3 Selection of the Primary Fuel

Several hydrocarbon fuels can be reformed in practice to produce hydrogen for the PEM fuel cell. In this section, standard characteristics and properties of several hydrocarbon fuels are considered in order to select the most promising one to be employed in a hydrogen generation stage to feed a PEM fuel cell. A list of the most popular reforming fuels for steam reforming and their main characteristics is presented in Tables 2.2 and 2.3.

In the considered reaction system, as in general in the chemical reaction engineering, high reaction conversions and product selectivities are the principal criteria for developing a process. These two factors depend not only on the nature of the primary fuel involved but also on the properties of the catalyst used.

Natural Gas
Natural gas is likely to remain the fuel of choice for the many stationary fuel cells for many years. Natural gas comprises a mixture of hydrocarbons of low boiling point. Methane is the component usually present in the greatest concentration, with smaller amounts of ethane, propane etc. In addition to hydrocarbons, natural gas generally contains various quantities of nitrogen, carbon dioxide and traces of other gases such as helium. Sulfur is also present to a greater or lesser extent, mostly in the form of hydrogen sulfide.

Liquefied Petroleum Gas
LPG is a general term that covers propane; butane or some mix of these alkanes and as such is of variable composition. Its boiling point is such that it can be stored easily as a liquid under moderate pressure and vaporizes readily. There is an established supply infrastructure for portable usage and a growing infrastructure for the supply of LPG as a vehicle fuel. As such it is a clear candidate fuel for fuel cells and many developers of fuel processors include it as a focus fuel.

Gasoline
Gasoline is derived from crude petroleum and contains over 500 hydrocarbons, most of which contain between 4 and 12 carbon atoms. Starting from dissolved gases, such as propane and butane (in small amounts) up to heavy sulfur containing components like mercaptanes, gasoline contains a spectrum of organic substances. Paraffins, iso-paraffins, olefins, naphtenes and aromatics are commonly present. Basic compounds are those in range of heptanes and octanes. In the research, gasoline is often modeled as n-octane and/or iso-octane [43, 44]. Gasoline can be reformed but developing an on-board fuel processor represents quite a challenge, and has been compared with installing a mini-oil refinery on-board a vehicle. Key issues for fuel processing systems are cost, size, weight, response time, efficiency and durability. The strongest argument in favor of gasoline-type fuels is the existence of a global infrastructure for their distribution and supply.

Fuel	H/C (molar)	Advantages	Disadvantages
gasoline	1.75-2.00	+ supply infrastructure available	- critical reaction conditions
		+ available manufacturing infrastructure	- coke formation
		+ highest volume-related energy density (31800 kJ/l liquid)	- elevated CO-selectivity
methanol	4.00	+ elevated hydrogen yield (high H/C ratio)	- toxic
		+ mild reaction conditions	- infrastructure not available
		+ less by-products	
		+ high volume-related energy density (15900 kJ/l liquid)	
		+ low storage risks (water-soluble)	
ethanol	3.00	+ easy to use and handle	- low chemical production capacity
		+ environment-friendly production (bio)	- low biological production development
		+ aligned with Flexible Fuel Vehicle Program	- infrastructure not available
		+ reduces petroleum consumption	- high exhaust emissions
natural gas	2.60	+ clean burning, lower exhaust emission	- low vehicle range
		+ availability, transportation	- maintenance
		+ cost	- low volume related energy density
methane	4.00	+ high availability (production)	- high operating temperature
		+ distribution infrastructure available	- gaseous

Table 2.2: Comparison between primary fuels for hydrogen generation

steam reforming of	H_2 *(vol%)*	CO_2 *(vol%)*	H_2O *(vol%)*	N_2 *(vol%)*
methane	64.10	16.30	17.80	1.80
methanol	61.80	21.10	14.10	3.00
ethanol	62.60	21.40	12.50	3.50
gasoline, diesel fuel	58.20	19.70	20.60	1.50

Table 2.3: Typical off-gas compositions by steam reforming of diverse start fuels. All processes except methanol reforming have WGS and preferential oxidation reactors at the end of the process to lower CO to trace amounts.

Diesel
Like gasoline, diesel is represented by a large quantity of hydrocarbon compounds, mainly heavy ones. Diesel fuels are widely distributed and have a high energy density. Diesel fuel processing leads to a better performance when using ATR. Major technical challenges in reforming diesel fuel include preventing coking while maintaining high reforming efficiencies and extending the catalyst lifetime/durability. A diesel oil reformer system requires more components (because of CO and coke formation) and is therefore likely to have slower response dynamics. The hydrogen-to-carbon ratio is also unfavorable for diesel fuels (about 1). Moreover the vaporization of diesel requires special techniques, slowing down start-up and dynamical response times. The sulfur content of these fuels is a further issue.

Ethanol
Ethanol is becoming more and more interesting for hydrogen production because it can be either produced by chemical synthesis from fossil feed stocks via ethylene or by biofermentation of plant components. Particularly, ethanol from corn (grain sorghum) is gaining more attention.

Steam reforming of ethanol runs catalytically at temperatures above 400 °C (up to 700 °C). Severe problems regarding coke deposition present the major challenge in ethanol reforming. The use of high-temperature ethanol steam reformer (at ca. 600 °C) in fuel cells is not practical because the thermal cracking reaction of ethanol is significant. A pre-converter unit at mild temperature of 400 °C is recommended. The pre-converter will change the ethanol molecule to hydrogen rich gas or methane-rich gas. These intermediate gases will create less coke deposition in the high-temperature reformer. More advanced, temperature-stable catalysts have to be developed before ethanol reforming can be technically implemented as alternative for hydrogen production for fuel cell mobile applications.

Closing Remark

For a given H/C ratio, oxygenated fuels (e.g. alcohols) can be reformed at higher efficiencies [40]. The advantage of liquid fuels is principally that they have high energy densities (as a function of volume) and can be easier distributed. Methanol has a number of attractive features that makes it a plausible initial fuel for fuel cell powered vehicles. Like gasoline,

methanol is a liquid fuel that can be easily distributed and stored. Methanol is much easier to be reformed than gasoline in terms of severity in operating conditions. Unlike the gasoline fuel processor, methanol fuel processor technology has already been demonstrated in working vehicles (e.g. Daimler-Chrysler NECAR 3 and 5 [1]). Nevertheless, additional efforts regarding fuel distribution and supply infrastructure are still necessary, in order to make *methanol* the best commercially available liquid fuel to produce hydrogen.

2.6 Steam Reforming of Methanol (SRM)

It is possible to produce hydrogen at relative low temperatures (200-300 °C) by Steam Reforming of Methanol (SRM). Here carbon dioxide is the main by-product. Carbon monoxide is produced in low percent range depending on the operating temperature and the steam-to-methanol ratio. In the literature the steam reforming of methanol has been strongly proposed for supplying hydrogen for fuel cell devices.

At large scales, the SRM is carried out in fixed-bed reactors heated externally. Here methanol and water react at temperatures between 250 and 300 °C and pressures up to 20 bar on CuO/ZnO-based catalysts.

The overall endothermic reaction system is described by the following stoichiometric equations:

(1) Methanol-steam reforming:

$$CH_3OH \ + \ H_2O \Longleftrightarrow CO_2 \ + \ 3H_2, \quad \Delta h_R^0 = +49.53 \, \frac{kJ}{mol} \tag{2.21}$$

(2) Methanol decomposition:

$$CH_3OH \Longleftrightarrow CO \ + \ 2H_2, \quad \Delta h_R^0 = +90.69 \, \frac{kJ}{mol} \tag{2.22}$$

(3) Water-gas shift reaction:

$$CO \ + \ H_2O \Longleftrightarrow CO_2 \ + \ H_2, \quad \Delta h_R^0 = -41.16 \, \frac{kJ}{mol} \tag{2.23}$$

For equilibrium calculations only two of the above three reactions are linearly independent.

Hydrogen production is favored by increasing temperatures, according to equilibrium reactions 2.21 and 2.22. Because higher temperatures also lead to increasing reaction rate, this effect is doubly helpfully. On the other hand undesired CO (a poison for the platinum-based fuel-cell anode catalyst) is formed at higher temperatures by methanol decomposition (Eq. 2.22) and the exothermic equilibrium-limited reverse water-gas shift (RWGS) reaction (Eq. 2.23).

In the design of steam reformers, flame burner or heating liquids (e.g. thermo-oil) are responsible for bringing the necessary heat to the methanol/steam reforming reaction. Hereby large temperature gradients and local temperature peaks, which also favor CO formation by reaction 2.22, should be avoided. CO-formation is commonly controlled by operating in excess of steam in order to favor the steam reforming reaction (Eq. 2.21) and shift the equilibrium of the WGS reaction (Eq. 2.23) towards the right side. Decreasing temperature profile is generally helpful because it restricts equilibrium formation of CO.

Therefore, the reaction system requires a control of the operating temperature profile for optimum performance [45].

Under typical operating conditions the steam reforming reaction (Eq. 2.21) is not equilibrium controlled. This can be seen on the basis of the thermodynamic equilibrium calculations. Figure 2.5 shows the equilibrium gas composition over temperature. It can be noted that above T = 100 °C and along the entire operating window methanol is almost completely converted and the other components vary in their composition according to the equilibrium-limited WGS reaction.

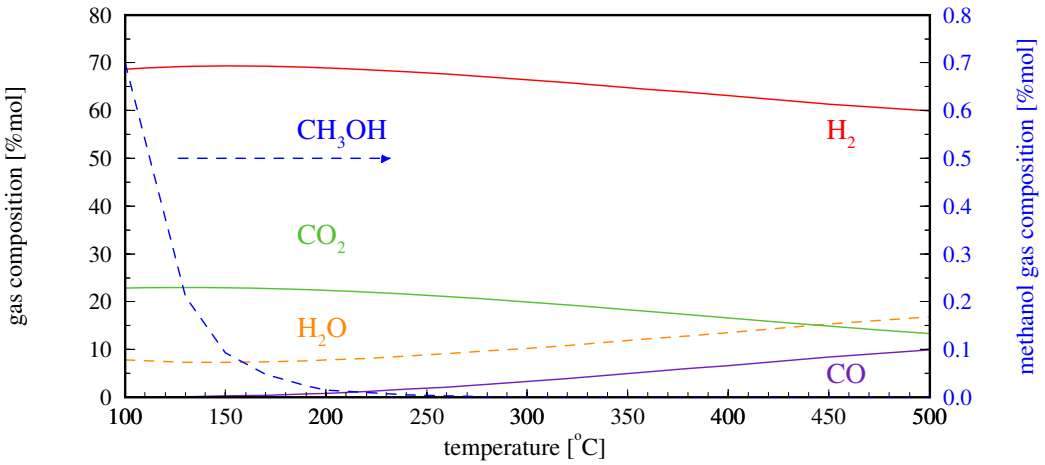

Figure 2.5: Equilibrium compositions for all participant compounds in the SRM reaction system (Eqs. 2.21-2.23). $p = 1.5\ bar$. Initial compositions: $y_{MeOH} = 0.435$; $y_{H_2O} = 0.565$.

Reactants are drawn with dashed lines, products with solid lines. Once methanol is consumed, the concentration of water (initially fed in excess to the reactor) increases due to the reverse water-gas shift reaction, which is endothermic.

Possible side reactions comprise the methane formation from carbon monoxide and carbon dioxide, as well as the formation of carbon black (Boudouard reaction):

$$CO + 3H_2 \iff CH_4 + H_2O \quad \Delta h_R^0 = -214.10\,\frac{kJ}{mol} \tag{2.24}$$

$$CO_2 + 4H_2 \iff CH_4 + 2H_2O \quad \Delta h_R^0 = -147.70\,\frac{kJ}{mol} \tag{2.25}$$

$$2CO \iff C + CO_2 \quad \Delta h_R^0 = -214.10\,\frac{kJ}{mol} \tag{2.26}$$

These side reactions must be suppressed principally by selecting appropriate catalysts.

2.6.1 The Water-Gas Shift Reaction (WGS)

One of the most important reactions in SRM is the Water-Gas Shift Reaction (WGS). WGS occurs in parallel to gasification and steam-reforming reactions and plays a relevant role to convert CO and steam into hydrogen and carbon dioxide (Eq. 2.23) when the raw gases cool down.

At higher temperatures and typical reforming catalysts WGS is in thermal equilibrium. At medium (about 400 °C) and low temperatures (about ≈ 250 °C) specific catalysts are required and the reaction becomes kinetically controlled [46].

2.6.2 Steam Reforming and WGS Catalysts

There are several catalyst systems that serve to catalyze the steam reforming reaction. Most of them are based on copper, iron and chromium oxide, supported on alumina. The use of suitable catalysts improves the hydrogen yield of reforming reactions by reducing CO formation.

In this work the BASF K3-110 catalyst has been used. This is a bulk (unsupported) catalyst that consists of 40 wt. % CuO, 40 wt. % ZnO and 20 wt. % Al_2O_3. It is commercially available in pellet form (5 mm diameter, 5 mm height).

BASF K3-100 is basically a WGS catalyst (according to Eq. 2.23). But it does not only catalyze the water-gas shift reaction but also the steam reforming of methanol. In consequence it is widely used in research facilities for methanol-steam reforming studies [45, 5].

Contrary to the high-temperature-shift (HTS) catalysts, which are based on iron and chromium oxide, the low-temperature-shift (LTS) catalysts contain copper as active compound. Too low operating temperatures can favor water condensation and high temperatures sintering of the catalyst solid. Both effects lead to rapid loss of the catalytic activity.

The active copper is present in delivering conditions as copper oxide. In consequence the catalyst species must be “reduced” (activated) before use. Hydrogen or carbon monoxide is typically used diluted in a carrier gas (normally nitrogen) for reducing the bulk catalyst. The possible pre-conditioning reactions are given as follows:

$$CuO + H_2 \iff Cu + H_2O \quad \Delta h = -87.0\ \frac{kJ}{mol} \tag{2.27}$$

$$CuO + CO \iff Cu + CO_2 \quad \Delta h = -128.1\ \frac{kJ}{mol} \tag{2.28}$$

After pre-conditioning the catalyst must be kept in absence of oxygen to avoid a re-oxidation of the (Cu) active centers. Sulfur and sulfuric compounds are typical poisons and should be also kept out of the system.

The catalyst reducing procedure used in this thesis was taken from the work of *Düsterwald*

[10]. Here the catalyst is heated from room temperature up to 130 °C at 50 °C/h. As reductant gas, a mixture of hydrogen/nitrogen starting from 2 *vol %* of H_2 is employed. When the outlet H_2 concentration equals the inlet concentration, the temperature has to be elevated in 10-20 °C steps until reaching 250 °C. From this level on the feed hydrogen concentration is gradually increased to 100 *vol %* of H_2. GHSV is 300 h^{-1}, p = 1.3 bar.

2.6.3 Kinetic Model

In this work the comprehensive[2] kinetic model of *Peppley et al.* [5] has been used. It considers the methanol-steam reaction, the methanol decomposition reaction, and the water-gas shift reaction, according to Eqs. 2.21−2.23. The reaction rate equations take the respective chemical equilibrium into account. They are formulated for conditions where water vapor is in considerable excess. Of particular importance is the equilibrium of the WGS reaction (Eq. 2.23), which strongly depends on the operating conditions [47]. Equations describing the reaction rates, r_i^{sfc} (in $\frac{mol}{m^2 s}$), in terms of the overall surface area are given below:

Methanol-steam reforming reaction

$$r_1^{sfc} = \frac{k_1 K^*_{CH_3O^{(1)}} \left(\frac{p_{CH_3OH}}{\sqrt{p_{H_2}}}\right) \left(1 - \frac{p^3_{H_2}\, p_{CO_2}}{p_{CH_3OH}\, p_{H_2O}\, K_1^{eq}}\right) C^T_{S_1} C^T_{S_{1a}}}{\left[1 + K^*_{CH_3O^{(1)}} \left(\frac{p_{CH_3OH}}{\sqrt{p_{H_2}}}\right) + K^*_{HCOO^{(1)}} p_{CO_2} \sqrt{p_{H_2}} + K^*_{OH^{(1)}} \left(\frac{p_{H_2O}}{\sqrt{p_{H_2}}}\right)\right] \left(1 + \sqrt{K_{H^{(1a)}} p_{H_2}}\right)} \tag{2.29}$$

Methanol-decomposition reaction

$$r_2^{sfc} = \frac{k_2 K^*_{CH_3O^{(2)}} \left(\frac{p_{CH_3OH}}{\sqrt{p_{H_2}}}\right) \left(1 - \frac{p^2_{H_2}\, p_{CO}}{p_{CH_3OH}\, K_2^{eq}}\right) C^T_{S_2} C^T_{S_{2a}}}{\left[1 + K^*_{CH_3O^{(2)}} \left(\frac{p_{CH_3OH}}{\sqrt{p_{H_2}}}\right) + K^*_{OH^{(2)}} \left(\frac{p_{H_2O}}{\sqrt{p_{H_2}}}\right)\right] \left(1 + \sqrt{K_{H^{(2a)}} p_{H_2}}\right)} \tag{2.30}$$

Water-gas shift reaction

$$r_3^{sfc} = \frac{k_3^* K^*_{OH^{(1)}} \left(\frac{p_{CO}\, p_{H_2O}}{\sqrt{p_{H_2}}}\right) \left(1 - \frac{p_{H_2}\, p_{CO_2}}{p_{CO}\, p_{H_2O}\, K_3^{eq}}\right) C^{T^2}_{S_1}}{\left[1 + K^*_{CH_3O^{(1)}} \left(\frac{p_{CH_3OH}}{\sqrt{p_{H_2}}}\right) + K^*_{HCOO^{(1)}} p_{CO_2} \sqrt{p_{H_2}} + K^*_{OH^{(1)}} \left(\frac{p_{H_2O}}{\sqrt{p_{H_2}}}\right)\right]^2}. \tag{2.31}$$

Here p_j represents the partial pressure of the species j, k_i is the rate constant of reaction i, K_i^{eq} is the equilibrium constant of the reaction i, and K^* is the equilibrium constant of the intermediate reaction steps. $C^T_{S_i}$ denotes the total surface concentration of site i.

To obtain the catalyst mass specific rate r_i^{cat} in $\left[\frac{mol}{kg_{cat}\, sec}\right]$, Eqs. 2.29 to 2.31 have to be multiplied by the BET-surface:

$$r_i^{cat} \;=\; a^{BET} \cdot r_i^{Sfc} \tag{2.32}$$

[2] It simultaneously takes into account all three reversible overall reactions.

This model contains a multiplicity of constants and expressions for adsorbed intermediate species which are explained in [5]. The model is based on the following assumptions:

- The rate-determining step (RDS) of both methanol-steam reforming and decomposition consists of the dehydrogenation of adsorbed methoxy groups. The water-gas shift reaction shall proceed by formation of an intermediate formate species (associative mechanism).
- There are two different types of active sites on the surface of the catalyst. Sites of the type 1 are assumed to be active for methanol-steam reforming and water-gas shift reaction, and sites of type 2 for methanol decomposition. Therefore a mechanism is proposed for methanol decomposition that is independent of the mechanism for the other two reactions. Furthermore it was observed that hydrogen does not compete for the same sites that adsorb the oxygen or carbon-containing species. Active sites exclusively for hydrogen adsorption where therefore incorporated into the mechanism to account for these observations. Hydrogen adsorbing sites associated with the reforming and the water-gas shift reaction are designated as type $1a$ sites, and those associated with the decomposition reaction as type $2a$ sites. Total site concentrations ($C^T_{S_j}$) are kept *separate and explicit* in the rate expressions and are *not* combined with the rate constants. The numerical values for the type 1 and 2 sites are set to $7.5 \cdot 10^{-6}\ \frac{mol}{m^2}$ and $1.5 \cdot 10^{-5}\ \frac{mol}{m^2}$ for the types $1a$ and $2a$. It was the intention of the author to explain the long-time behavior of the catalytic activity and variation in CO-selectivity by finding reasonable functional correlations between the number of active sites and the real catalytic behavior.
- The rate equations cover a wide range of system pressure up to $33\ bar$.

A more detailed description of the kinetic parameters is reported in the literature [5] and in Appendix B, Section B.2.8.

Chapter 3

Parallel-Plate Reactor Concepts

In this chapter, an overview about parallel-plate reactor concepts is given and the folded-sheet reactor concept is introduced. Its more important benefits, relevant properties and possibilities for manufacturing are presented. The folded-sheet concept forms the basis for the design of a final reactor prototype capable of producing hydrogen with 10-kW LHV (as defined in Section 2.3).

3.1 Parallel-Plate Devices

A parallel-plate reactor for endothermic high temperature reactions, using as example the coupling of the endothermic steam reforming of methane with the combustion of methane as heat source has been presented by *Frauhammer* [3]. This reactor concept establishes the basis for the following studies.

In the parallel-plate reactor concept, channels for the reforming reaction are separated from those for the catalytic combustion reaction (which supplies the heat for the reforming reaction) by means of thin metal sheets.

In addition, a countercurrent heat exchange between the cold reforming feed and the hot combustion gas at one end, and of the cold combustion feed with the hot reformate at the other end of the parallel-plate reactor is also present. A sketch of flow configuration is given in Figure 3.1.

In this Figure can be noticed that the separating wall is impregnated with reforming and combustion catalysts at the respective side. When the combustion feed meets the combustion catalyst the generated heat is transported through the thin metal plate to the reforming side. At this reforming side, the reforming catalyst receives the heat and uses it for the endothermic reforming reaction. In such a design it is usual to find a configuration in which each reforming channel is embedded by two combustion channels.

Compared with conventional multitubular reactors, parallel-plate reactors allow for a much larger volume specific heat exchange area ($a^v \ \frac{m^2}{m^3}$). In the following, a parametric comparison between both arrays is sated.

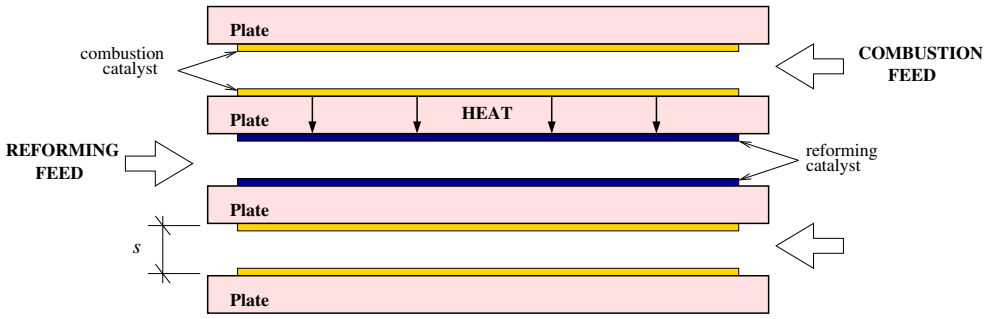

Figure 3.1: Scheme for calculating the volume-specific exchange-area of plate arrays.

In order to compare both reactor concepts (multitubular and parallel-plate assembly), having the same ratio of cross-sectional area on the combustion and the reforming side, following geometric proportions are defined (Figures 3.2 and 3.3):

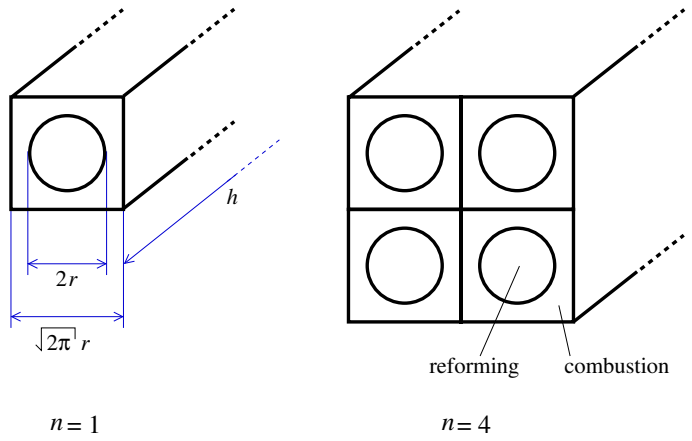

Figure 3.2: Volume-specific exchange-area of multitubular arrays.

The volume specific exchange area for a multitubular reactor array is inversely proportional to the tube radius and independent on the number of reactor units, for example for a n = 1 tubular-reactor configuration:

$$a^v_{tube} = \frac{1\,(2\,\pi\,r\,h)}{\left[1\,\left(\sqrt{2\,\pi}\,r\right)\right]^2\,h} = \frac{1}{r}, \tag{3.1}$$

and for a n = 4 tubular-reactor configuration:

$$a^v_{tube} = \frac{4\,(2\,\pi\,r\,h)}{\left[2\,\left(\sqrt{2\,\pi}\,r\right)\right]^2\,h} = \frac{1}{r}. \tag{3.2}$$

Considering a reactor with a nominal radius of r = 2 mm, the volume-specific exchange area results 500 $\frac{m^2}{m^3}$; whereas with a radius of r = 5 mm (technically more feasible), a^v_{tube} decreases to 200 $\frac{m^2}{m^3}$.

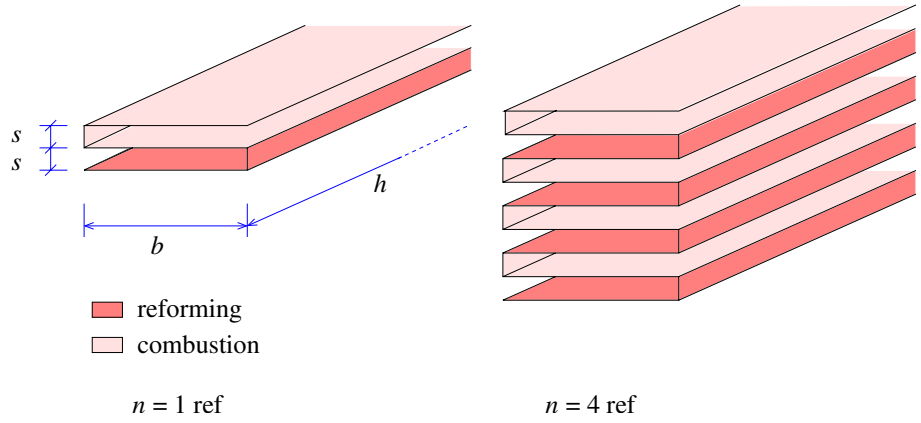

Figure 3.3: Change of the volume specific heat exchange area for a sequence of n reforming and n combustion channels of gap distance s.

Otherwise the volume-related area of a parallel-plate configuration increases with the inverse of the gap distance s between plates. Assuming equal plate separation s = 1 mm for the reforming and combustion channels, the specific exchange area for a 1 channel design (i.e., n = 1 reforming channel and 1 combustion channel: Figure 3.3-*left*) is:

$$a^v = \frac{b\,h}{2\,s\,b\,h}, \tag{3.3}$$

leading to

$$a^v = \frac{1}{2\,s} = \frac{1}{2 \cdot 10^{-3}} = 500\,\frac{m^2}{m^3}. \tag{3.4}$$

For a 4 channel design (i.e., n = 4 reforming channels and 4 combustion channels: Figure 3.3-*right*):

$$a^v = \frac{7\,b\,h}{8\,s\,b\,h}, \tag{3.5}$$

leading to

$$a^v = \frac{7}{8\,s} = \frac{7}{8 \cdot 10^{-3}} = 875\,\frac{m^2}{m^3}, \tag{3.6}$$

and for a n channel design:

$$a^v = \frac{(2n-1)\,b\,h}{(2n)\,s\,b\,h}, \tag{3.7}$$

leading to

$$a^v = \frac{1}{s} = \frac{1}{10^{-3}} = 1000\,\frac{m^2}{m^3} \tag{3.8}$$

when $n \to \infty$.

This comparison reveals directly the advantages of using parallel-plate arrays, when it is important to improve the heat transfer and when the heat exchange equipment has to be up-scaled.

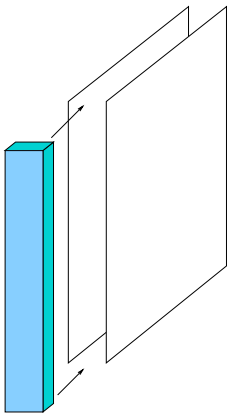

a) Inserting metallic strip between 2 plates

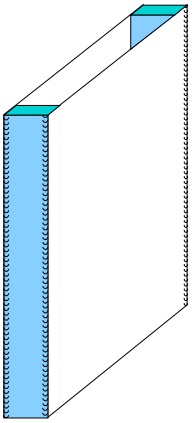

b) Welded lateral bars

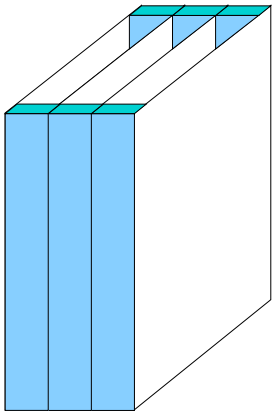

c) Fine-welded chamber array

Figure 3.4: Construction of the parallel-plate units by welding side bars to the metallic plates.

3.2 Manufacturing Alternatives

Alternative 1
Plate based arrays are commonly manufactured by side-welding of metallic plates, as shown in Figure 3.4. Each chamber is closed attached to the neighbor chambers by fine welding seams. Small metallic strips serve as spacers and define the channel width.

Using this method, several difficulties are commonly encountered since each plate has to be welded several times. Most common are deformations due to thermal stress, while imperfect welding seams lead to leakage.

Alternative 2
A second alternative results when metallic "U"-form profiles are used as basic structures to assemble the apparatus body (Figure 3.5). This procedure reduces the manufacturing steps described in the prior section to one half. Not only the time of manufacturing of the core piece but also the risk of damaging the metallic plate during the welding are reduced.

Employing this construction variant, a new benefit is introduced to the concept: the possibility of make each chamber accessible not only from the reactor ends but also from the sides. In fact, this is one of the most important advantages of the concept, because it allows the introduction of side gas injections/extractions to/from the channels at different reactor positions. The reactor concept increases its versatility and compactness due to the possibility of integrating several process steps along the apparatus length. The metallic foil needs to be relatively thick because of the necessity of welding.

Alternative 3
Based on the concept of Alternative 2, the subsequent folding of a metallic foil was implemented so that parallel chambers are automatically formed (see Figure 3.6).

Folding a long metal sheet subsequently creates parallel separated chambers. This concept not only encloses the advantage of having independence between the process channels and accessibility from the sides, but also permits to employ thinner metallic foils, resulting in very small channel widths. In addition, front and rear chambers could have different channel width. The folded-sheet concept will therefore be the basis for the design of a heat-integrated SRM-reactor.

With this approach a parallel-plate reactor concept becomes a folded-sheet reactor (see Figure F.4 in Appendix F).

3.3 The Folded-Sheet Reactor

As indicated, heat transport limitations inherent of classical, multitubular fixed-bed reactors have motivated the development of the "folded-sheet reactor concept". It combines the main features of parallel-plate units regarding heat integration, with compactness and operational feasibility.

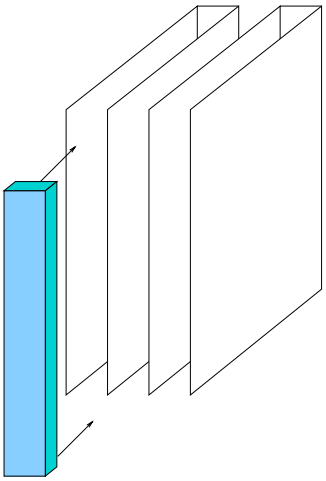

a) Array of two “U”-bent metallic profiles linked by a single metallic strip

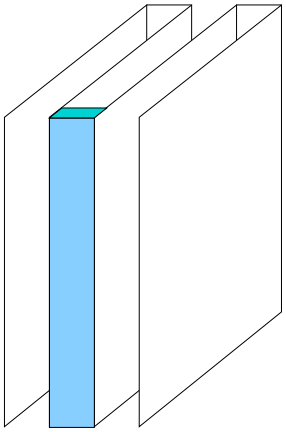

b) Side-welded lateral bar

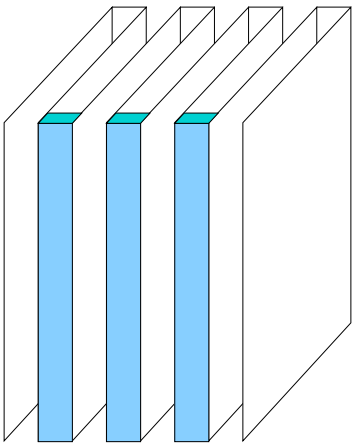

c) Assembled parallel construction units

Figure 3.5: Construction of the plate apparatus by using pre-formed “U”-like metallic profiles. Note the side accessibility of both resulting process chambers.

For the particular case of hydrogen generation by SRM the direct coupling of the endothermic hydrogen production stage (on the reforming side) with a heat release (on the combustion side) is required, leading to an autothermal operation with low temperature feed streams and effluents (see Figure F.1 in Appendix F).

At the reforming side, the following process steps have to be included:

- evaporation of liquid water and methanol, and heating-up of the resulting vapor to the reforming temperature,
- steam reforming,
- water-gas shift reaction (CO clean-up).

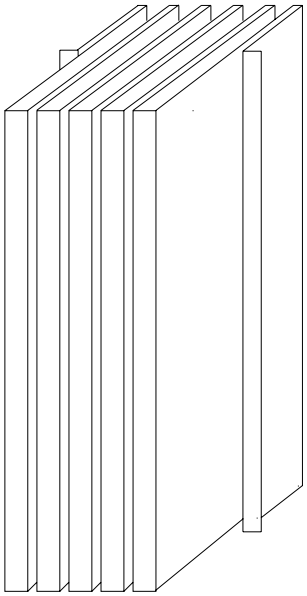

Figure 3.6: Resulting separating wall. Basis structure for the folded-sheet concept.

At the combustion side the requirements are:

- flow counter-current to the reforming side for an optimal heat recovery from the process streams, so that the process heat is retained in the reformer center and the process streams enter and leave the unit at low temperature,
- the heat required by the endothermic steps should be supplied by the catalytic oxidation of hydrogen from anode off-gas, according to:
  $H_2 + \frac{1}{2}\, O_2 \longrightarrow H_2O \qquad \Delta h_R^0 = -241.83\ kJ/mol,$
- while the air for combustion enters the apparatus counter-currently from the reactor top, the hydrogen containing fuel gas (fuel cell anode off-gas) should be fed to the main-air stream at several axial positions so that the combustion heat can be locally generated, only where it is needed.

Once the metallic foil is folded forming two independent sets of chambers (see Figure 3.7-a), each chamber can be filled with inert or catalyst coated structures (Figure 3.8), depending on the process requirements. Both ends of the folded-sheet are sealed by welding or high temperature brazing techniques. The leak-proof sealing of the heads is one of the manufacturing challenges of this design. The technique applied is shown in Figure 3.7-b. Profiled metallic segments are placed tight into the folds. After high temperature brazing a solid head is formed onto which the reactor housing can be attached by welding. The housing is formed by two metallic shells, which are laterally fixed, covering the entire folded-sheet structure as a reactor case (Figure 3.7-c). The shells contain the reactor in- and outlet connectors (previously attached), as well as the gas side injection manifolds.

The reactor in- and outflows are completely separated from each other and can thus be individually controlled and analyzed. Entrance sections of the channels for the air feed on the

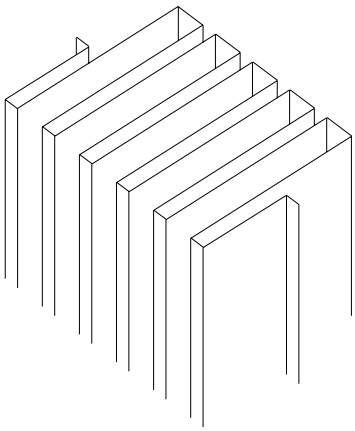

a) Folded separating wall

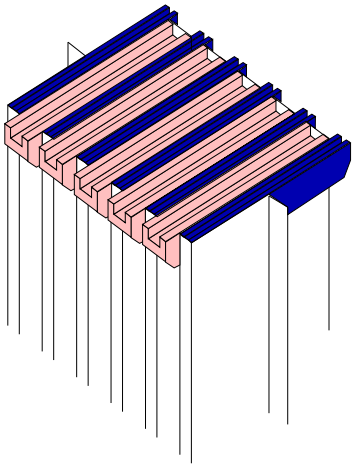

b) Sealed reactor ends

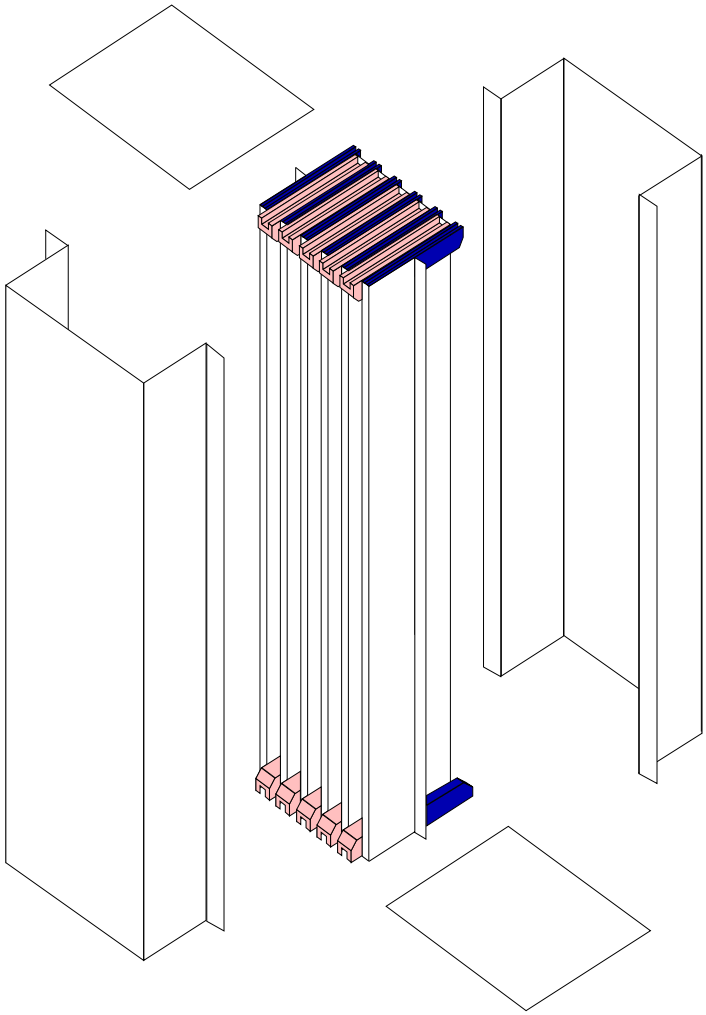

c) The folded-sheet reactor with its casing parts

Figure 3.7: Basic sequence for the construction of the folded-sheet reactor.

combustion side and the methanol/water feed mixture on the reforming side, are equipped with static mixers and flow distributors to ensure that all channels are equally and uniformly fed (see Section 7.3.2). In one channel, a thermocouple can be moved through a capillary (thermal well) to measure the gas temperature profile.

One of the big advantages of the folded-sheet concept is that the accordion-form core-structure is obtained from folding a single metallic sheet. This reduces the complexity of manufacturing and allows for use of thin metallic foils. The resulting multiple-channel geometry offers a large specific surface area for heat transfer (see Figure 3.7).

The use of corrugated structures (spacers) is a further important advantage of this concept. The spacers are metallic slices which are inserted into the reaction channels, orienting their "fishbone" pattern-lines in flow direction (see Figure 3.8). The spacers are either impregnated with catalyst or simply uncoated, which means that they act both as catalyst carrier and also as heat exchange fins between the reactor walls. Compared to micro-channel reactors with catalyst coated walls, the folded sheet design allows easily modifying the channel structure between sections with spacers, catalyst coated spacers and static mixers.

Finally one of the most relevant advantages of the folded-sheet reactor concept lies in the fact that the casing plates can be easily removed and later attached and sealed again. This allows for a simple replacement or modification of the spacer structures.This is a very crucial factor at an early testing stage because several reasons may require the replacement of the catalyst slices, e.g. catalyst aging and/or poor reactor performance (low catalyst activity). The specific details of the design and manufacturing of a folded-sheet methanol steam reformer with hydrogen production of 10-kW LHV will be discussed in Chapter 7.

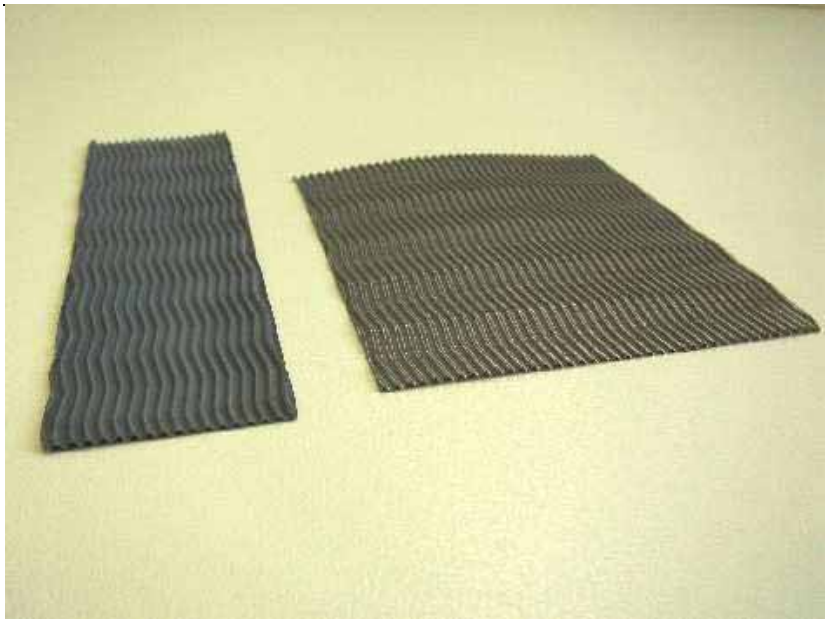

Figure 3.8: Wave-like corrugated metallic structures serving as catalyst carrier (*left*) and uncoated spacer (*right*).

Chapter 4

Kinetic Studies on SRM

In this chapter, preliminary experiments on the catalytic activity of a commercial catalyst for steam reforming of methanol are presented and discussed. These experiments were carried out in a kinetic plug flow reactor (fixed-bed) in order to provide a better understanding of the reaction system under basic operating conditions. A description of the experimental setup (section 4.1) and the experiment results (section 4.2) together with the procedure and the results of kinetic parameter optimization (section 4.3) are given in the following. The results reported in this chapter have been obtained in close cooperation with *C. Becker* and represent an extension of the results presented in Chapter 9 of his thesis [48].

4.1 The Catalytic Plug Flow Reactor

In a first step, the catalytic activity of the commercial catalyst BASF K3-110 [4] for steam reforming of methanol has been evaluated as reference basis for the development of the folded-sheet reactor. The BASF K3-110 is a typical catalyst for low-temperature water-gas shift reaction which has demonstrated a good activity and applicability for the methanol steam reforming reaction [45]. Several kinetic models for the BASF K3-110 published in the literature has been used to validate the experimental results obtained [45, 5, 49, 50]. This study aims at the adjustment of kinetic parameters and the understanding of the considered reaction system. The laboratory setup and experiments carried out are presented and discussed in the following sub-sections.

4.1.1 Description of the Experimental Setup

Experiments were carried out in the experimental setup depicted in Figure 4.1 (see also Figure F.8 in Appendix F), which is dimensioned for steam reforming of methanol for a maximal hydrogen output capacity of 1 kW LHV[1] (see section 2.3). The experimental setup consists of five main sections:

[1] As a measure of the theoretically complete combustion of hydrogen, equivalent to 0.33 $\mathcal{N}\mathrm{m}^3\mathrm{H}_2$/h

- feed section,
- reaction section,
- off-gas after treatment unit,
- analysis of the reaction products, and
- control and data acquisition.

The Feed Section

This section describes the gas supply for either conditioning (reducing) the catalyst bed or for feeding the steam reforming reaction.

In the first case, hydrogen, diluted with nitrogen at defined compositions[2], is fed directly to the reactor entrance through mass flow controllers (MKS, Type 1179). The mass flow controllers (MFC) are remotely operated by an 8-channels controlling unit (MKS, type 647B). Several on/off solenoid valves (NORGREN, Type 2/2, 12 V-DC, normally closed) are placed next to the mass flow controllers for emergency shut-off. High purity hydrogen (99.9990 $vol\%$) and nitrogen (99.9990 $vol\%$) are directly taken from the central gas lines of the laboratory facilities.

In the second case, the reactants methanol and water are stored in two vertical cylindrical tanks (stainless steel, V = 5.75 l, p_{max} = 7 $bar\ abs$, T_{max} = 50 °C, pressurized at 4 $bar\ abs$ with helium) and dosed by means of two independent liquid flow controllers (Bronkhorst HI-TEC, Type LiquidFlo, 300 ml/h of methanol and 400 ml/h of water respectively) connected in parallel. Safety relief valves are placed on the top of each tank to avoid over-pressures. The liquid flow controllers are set by independent digital control units (Bronkhorst HI-TEC, type E700). Before the tanks are pressurized, both liquids are degassed by means of a vacuum pump to avoid malfunctions of the mass flow controllers by gas bubbles. Helium has been used as pressurized gas due to its low solubility in methanol/water. Both vacuum degassing and helium pressurization proved to be necessary and sufficient for a reliable liquid feed control.

Both methanol and water are conducted through two independent electrically heated evaporators [51], which allow for a pulsation-free vaporization of small amounts of liquid by adjustable electrical heating. The heating cartridges of the evaporators (250 Watt) can be temperature controlled by means of the main heating controller device (HORST, HT-60). Both evaporators are complete insulated and its outlet streams are conducted to the reactor entrance by using an insulated and electrically heated flexible-tube (HORST, 400 Watt).

Check valves are also placed at each reactor inlet for emergency shut-off and to avoid back flow. More detailed information about the peripherical controlling configuration is described in the following sections (controlling and data acquisition, page 45).

[2] Following the conditioning procedure suggested by Düsterwald et al. [10] - See Section 2.6.2

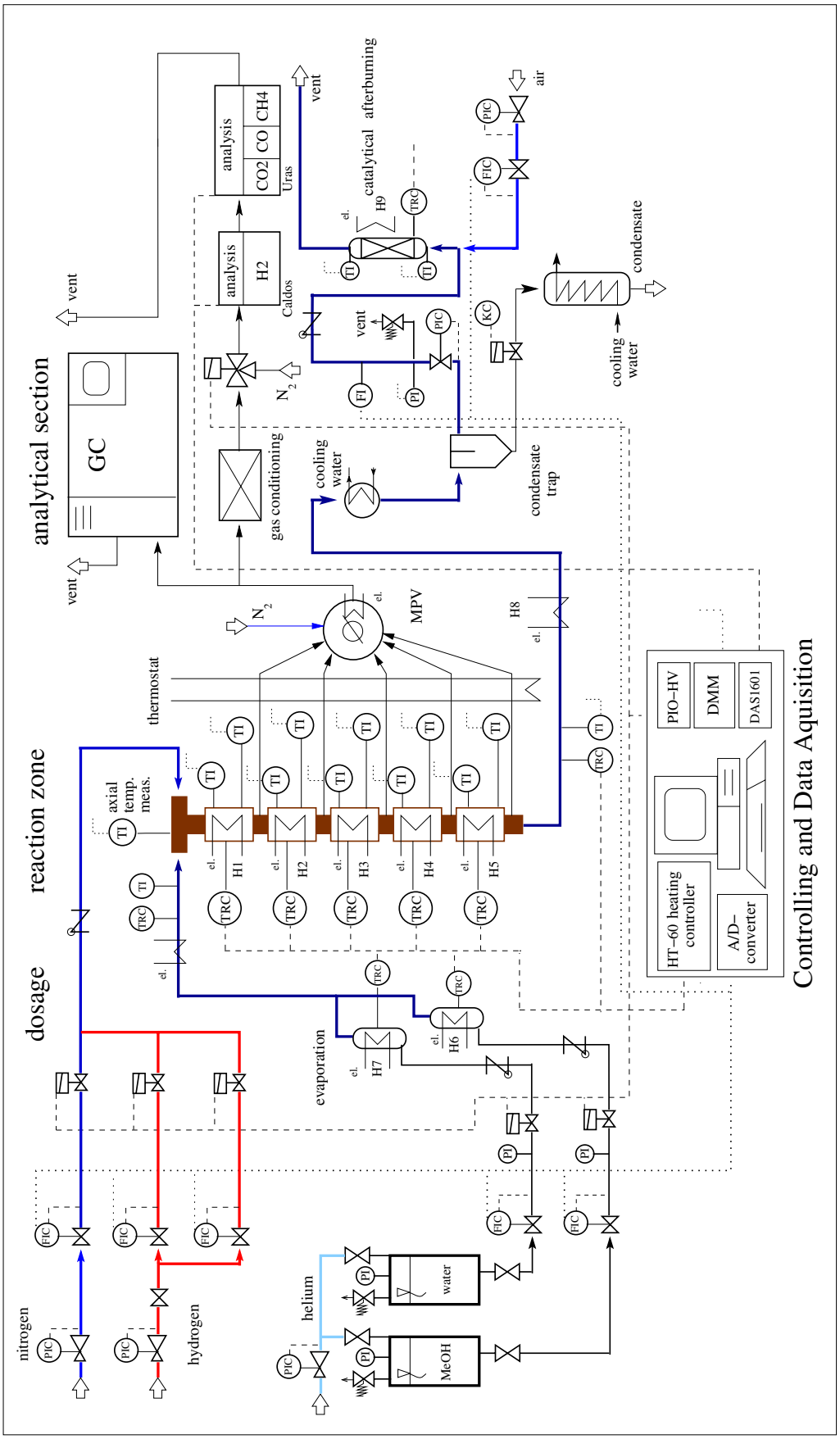

Figure 4.1: Experimental setup - Catalytic plug flow reactor.

The Reaction Section

The reaction section consists of a single tube catalytic fixed-bed reactor (see Appendix E, Figure E.1) with lateral ports for taking small samples of reacting gas. The most important dimensions of the reactor are listed in Table 4.1.

dimension	**value**
material	stainless steel - 1.4571
length	1030 mm
external diameter	14 mm
wall thickness	1.5 mm
max. pressure	5 $bar\ abs$

Table 4.1: Basic dimensions of the fixed-bed reactor.

The axial structuring of the reactor is presented in Figure 4.2. The reactor stands vertically and the flow direction is from the top downwards. The reactor sections are heated by five copper shells (Cu1...Cu5) each supplied with electrical heating cords (HORST, 550 Watt). The external shell temperature is measured with 10 thermocouples, placed along the reactor height (T1...T10). The entire reactor is insulated with a 20 mm-thick glass-fiber coat.

In the centre of the tube a capillary is inserted, in which a movable thermocouple type "K" can be shifted (e.g. each 50 mm) for measuring the axial gas/bed temperature. The first 20 cm of the reactor height are filled with inert material (glass spheres, d = 3 mm) and the following 80 cm with crushed catalyst pellets (1 mm mean diameter). At the bottom of the reactor tube a small ceramic monolith slice (height = 11 mm) is placed to retain the catalyst pellets.

Samples of reacting gas can be taken at five axially distributed withdrawal ports, placed 200 mm apart. By means of a multi-position valve (6 ports) reacting gas samples from the five different reactor segments are extracted and conduced to the analytic section. The sixth port of the multi-position valve serves for passing purge gas (N_2) through the line to wash out traces of previous samples.

The product stream flows from the reactor exit to the after treatment section. A tempered line, for avoiding an intermediate condensation of both unreacted methanol and excess water, conducts the gas mixture to the heat exchanger (p_{max} = 1.5 bar, water-cooled) to condense the methanol and water present. The condensate is separated by a liquid trap (Mader, type L056.2045) and flows to a liquid collector which is emptied each 2 min by activating a time-controlled solenoid valve.

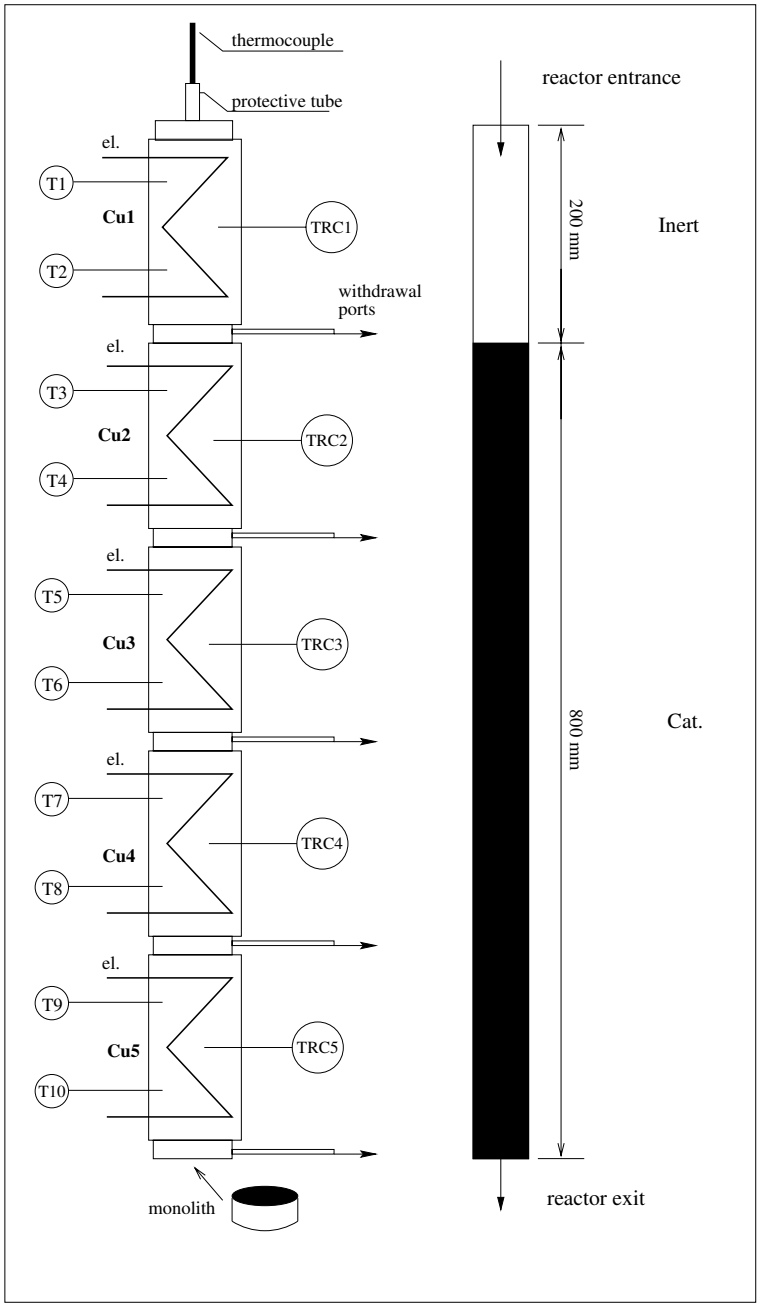

Figure 4.2: Reactor sketch. *Left:* axial distribution of external reactor heatings and lateral gas-sampling ports; *right:* axial structuring of the reactor bulk.

Offgas-Afterburning Unit

The exit gases from the reformer are burned catalytically with air at the offgas-afterburning unit, which contains a ceramic monolith coated with a noble metal based catalyst. The following reactions take place:

$$CO + \tfrac{1}{2}\, O_2 \Longleftrightarrow CO_2 \qquad \Delta h_R = -282.99\, kJ/mol \tag{4.1}$$

$$H_2 + \tfrac{1}{2}\, O_2 \Longleftrightarrow H_2O \qquad \Delta h_R = -241.75\, kJ/mol \tag{4.2}$$

$$CH_4 + 2O_2 \Longleftrightarrow CO_2 + 2H_2O \quad \Delta h_R = -803.07\, kJ/mol. \tag{4.3}$$

For the total combustion of the product gases (hydrogen, carbon dioxide, carbon monoxide and methane), air is supplied in excess to the monolith reactor in order to keep the hydrogen concentrations below the explosion limit (6-8 $vol\%$). Since the ignition temperature for this oxidation reaction is approximately 50 °C, the monolith reactor is electrically preheated to ensure that the reaction starts up immediately as soon as combustible gas is present. Due to the air excess the adiabatic temperature rise of the combustion of the off-gases is about 550-600 °C. This temperature also corresponds to the maximum permissible operating temperature of the catalyst burner. Because of the necessity to prevent any combustible gases leaving the afterburning unit and since the maximum combustion catalyst temperature is limited, the aftertreatment unit represents one of the safety relevant sections of the plant and has to be carefully monitored.

The Analytical Section

A small amount of gas can be taken off either from the product gas stream (at the bottom of the reactor) or from one of the withdrawal ports at the reactor side. By manually switching the multi-position valve (VALCO INSTRUMENTS), any port can be selected at a time and the sample is sent to the analytical section. The sample line is heated by an oil thermostat to avoid condensation of the gases. This line first leads to a conditioning unit which consists of an electrically heated ceramic filter (Hartmann & Braun, mod. R9142T2, 5μ maximum particle size) and a cooling/splitting device for separating traces of water/methanol present (AlphaLaval, type MAK-6 mini). The dry gas is passed through two analytical modules (Hartmann & Braun) to perform analysis of composition of hydrogen, carbon monoxide, carbon dioxide and methane. Hydrogen is analyzed by a thermal conductivity detector (TCD, *Caldos 17* device), and interferences due to hydrocarbon compounds are directly compensated by means of an electronic module. The composition of the rest components (CO, CO_2 and CH_4) is measured by the non-dispersive infrared analyzer (NDIR, *Uras 14* device). Hereby, the gas to be analyzed passes through 2 cuvettes. The first cuvette detects carbon dioxide in values among 0...30 $vol\%$ as well as carbon monoxide and methane in a range of 0...3 $vol\%$. In the second cuvette methane concentrations between 0 and 200 ppm are measured. Zero reference values are manually set by passing an inert (nitrogen) stream through the devices.

The devices are regularly calibrated for intermediate concentrations by using test-gases of fixed composition.

Reaction samples can also be taken from the liquid trap, near the reactor exit, to determine the composition of unreacted methanol in water in the condensate. This determination serves to verify the integral mass balance for methanol. The liquid sample is injected in a gas chromatograph (Perkin-Elmer) equipped with a flame ionization detector (FID), previously calibrated with different standard methanol/water mixtures.

The Control and Data Acquisition Section

In the following a detailed description of the electric and electronic plant-elements, responsible for monitoring and adjusting the most important process variables, like gas and liquid flow rates, system pressure and temperature as well as the communication to the laboratory computer (PC) will be given.

The signals coming from the electric/electronic devices enter the computer through several interface cards. The signals are digitized and evaluated at-place.

The computer program used to control the plant devices was the commercial software package TEST-POINT by Keithley Instruments Inc. [52], which allows to build complete and customized graphic application interfaces to interpret external signals and deliver control commands.

The communication flow between the plant devices and the controlling computer is schematized in Figure 4.3 and described as follows:

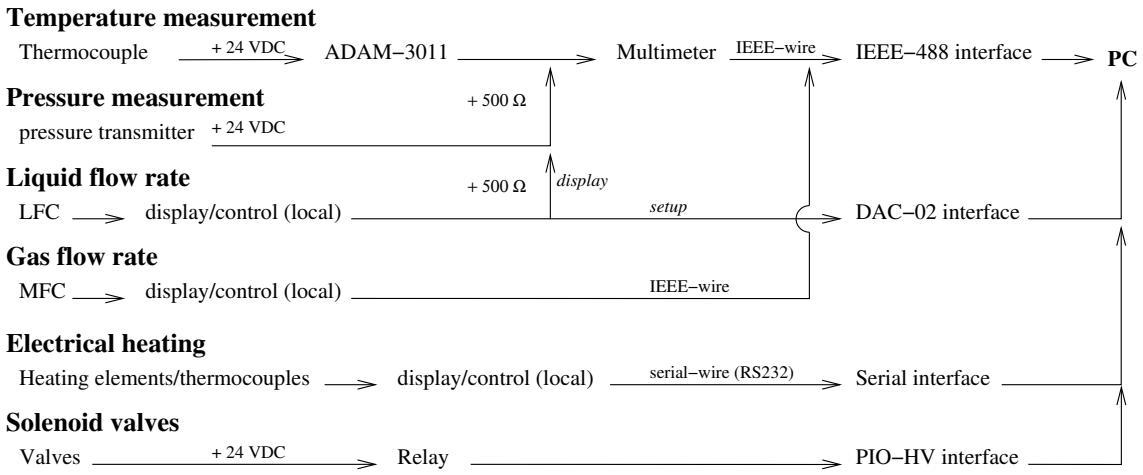

Figure 4.3: Resumed scheme of the devices communication signal flow.

- The *Temperature* is measured by means of thermocouples type "K" (Thermocoax GmbH, -184...1260 °C), which deliver a non-linear voltage signal of 0...40 mVDC. The analog signal is linearized and amplified to 0...10 VDC by compact, 24-VDC field modules (Spectra, type ADAM-3011), so that 10 mVDC correspond to 1 °C. Multiple temperature signals are scanned and digitized by a 20-channels Digital Multimeter (Keithley, type 2000-20). The digital multimeter (DMM) is directly connected to

the computer at the IEEE-interface by means of an IEEE-card (Keithley, GPIB-488). Following this communication path, up to 20 analog signals can be simultaneously scanned and processed.

- The *System Operating Pressure* is measured by using a pressure transductor (Haenni, type 505/414-221/A25) in a range from 0.0 to 5 bar. The delivered current signal (4...20 mA) is converted with the help of a precise resistor (R_L = 500 Ω) into a voltage signal and scanned together with the temperature signals at the DMM. To translate the input signal into pressure values, the following conversion formula, which assumes a linear relationship between the measured voltage (U_B) and the correspondent absolute pressure (p_{abs}), is used:

$$p_{abs}[bar] = \frac{1\ [bar]}{16\ [VDC]} \cdot U_B\ [VDC] - \frac{1}{8}\ [bar]. \tag{4.4}$$

- *Liquid Flow Rate* of methanol and water is adjusted and monitored by Liquid Flow Controllers (LFC). LFC can be locally operated by a remote electronic control unit. To adjust the flow set-point, a current signal of 4 to 20 mA is sent from the PC through an analog interface card (Keithley, type DAC-02). On the other hand, to display the actual flow rate, the delivered analog signal of 4...20 mA is converted into volts by a precision resistance (R_L = 500 Ω), scanned by the DMM, and finally processed at the PC together with the temperature and the pressure signals.

- *Gas Flow Rates* of hydrogen, nitrogen and air are locally adjusted by means of the central controlling unit (MKS, type 647B). Set-points for each mass flow controller MFC (MKS, type 1179/2179) can be simultaneously and independently adjusted at the controlling unit by sending a voltage signal (0...5 VDC) from the PC, via IEEE interface. The actual flow rates can also be read from the controlling unit (IEEE, 0...5 VDC). A PIC control algorithm is applied. The product-gas flow rate is measured by the Mass Flow Meter MFM (MKS, type 258C). Flow rates measured by the MFM were carefully calibrated using model gas with a known composition according to the references at reforming conditions ($y_{H_2} \approx 74\ vol\%,\ y_{CO_2} \approx 24\ vol\%,\ y_{CO} \approx\ 2\ vol\%$).

- *Temperature Control of the Electrical Heating* of the reactor shell, evaporators and other tempered fluid lines is realized by employing a multi-channel micro-processor controlling device (HORST, type HT-60), which uses the Direct-Digital-Control principle [53]. This controller, equipped with PID loop control protocol, features a special programmable start structure capable of linearize the heating-up ramp for avoiding abrupt heating. The set point and the temperature of each channel are independently displayed at the front panel. The temperature value is measured by thermocouples type "K" and a VAC signal is sent to the heating elements (heating cartridges and cords). The heating controller can be connected to the PC using standard serial interface (RS-232). Interface communication protocol can be found in the respective technical leaflet [54].

- *Solenoid Valves* are installed at the most important stream lines for emergency shut-off. This means that the plant goes into the intrinsically safe state if the central power is switched off (emergency shut-off) or fails. The valves are of the on/off-type and remain normally-closed. They can be opened by sending a voltage signal of 24 VDC from a power supply device (Siemens, type SITOP POWER 4). The solenoid valves are managed from PC by means of a digital interface card (Keithley, type PIO-HV) which allows the switching of interconnected 24-VDC relays.

4.2 Experimental Evaluation

In order to characterize the SRM reaction system, several experiments were carried out using the fixed-bed reactor described in section 4.1.1. Variations in the overall operating temperature, the feed loading and the steam-to-methanol ratio (S/M), as well as the influence of the water-gas shift reaction were evaluated. Experimental results and discussion are subsequently presented.

4.2.1 Influence of the Operating Temperature

The reaction temperature has been demonstrated to be the most sensitive and important operating variable for the steam reforming of methanol [10]. Both methanol conversion and product selectivity depends strongly on the local temperature. In order to determine the effect of the temperature on the reaction behavior, experiments at both constant and spacially variable wall temperature were carried out. Additional setting parameters like feed flow rate, S/M ratio and system pressure were set constant, as shown in Table 4.2.

operating parameter	**value**
feed flow rate	170.00 $\frac{g}{h}$
	$\approx$ 7.00 $\frac{mol}{h}$
specific mass flow rate	0.50 $\frac{kg}{m^2 s}$
S/M molar ratio	1.30 $\frac{mol}{mol}$
abs. system pressure	1.5 $bar\ abs$

Table 4.2: General reaction conditions for SRM experiments on the influence of the operating temperature

After adjusting the temperature of each independent heating block along the reactor length either to a constant value (isothermal wall temperature) or to a stepped profile (non-isothermal), both the gas temperature axial profile and the gas concentrations were registered and evaluated.

Constant Wall Temperature:

The temperatures of the five reactor-heating blocks (see Figure 4.2) are subsequently adjusted to the following constant values: 225, 245, 250, 265 and 285 °C. For each wall temperature, the feed gas temperature was set to 100 °C. In each experiment, the axial gas temperature and concentration profile were measured. Typical stationary axial profiles of the gas temperature are shown in Figure 4.4.

Along the inert zone (0...200 mm), the feed is heated up from T = 100 °C to the adjusted heating temperature T_w. After this preheating section, the gas enters the catalytic zone. A considerable temperature depression of about 50°C (*cold spot*), caused by the onset of

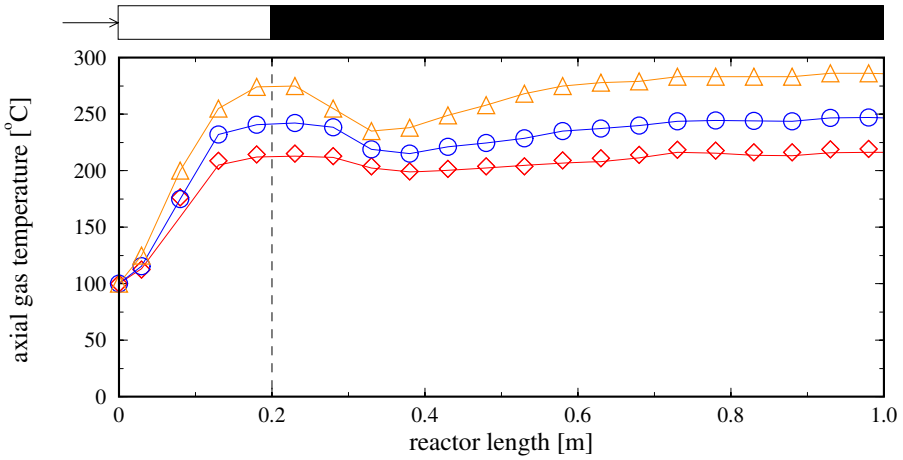

Figure 4.4: Typical thermal behavior for the SRM in a catalytic fixed-bed reactor under isothermal adjusted heating temperature: $T_W = 220\ (\diamond),\ 245\ (\circ)$ and $285\ ^\circ C\ (\triangle)$

the endothermic reforming reaction, is observed. In this zone, the major consumption of methanol takes place. Afterwards, along the second half of the reactor, the reacting mixture is heated up again, by the isotherm wall. Here, the exothermic WGS reaction begins to play a role.

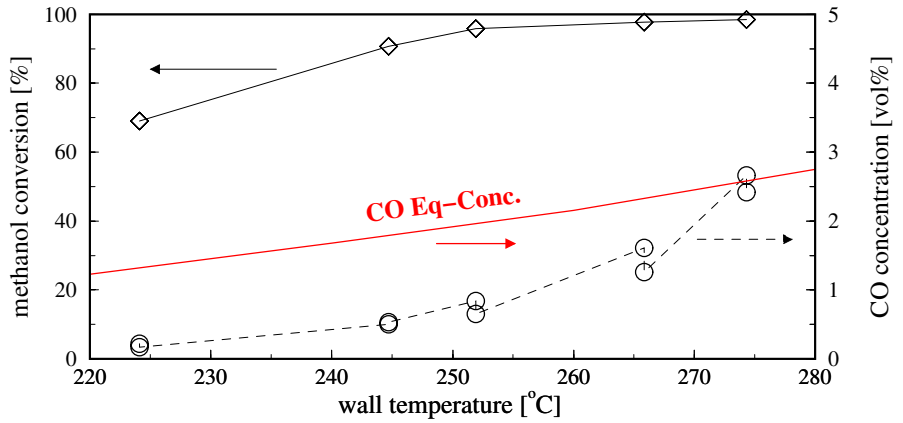

Figure 4.5: Dependence of the methanol conversion and CO concentration on the adjusted heating temperature T_w. Symbols represent experimental measurements, lines trend curves. *CO Eq.-Conc.* line represents calculated values of this variable.

As shown in Figure 4.5, at increasing wall temperatures an increasing methanol conversion is observed, due to the contribution of both endothermic reactions (steam reforming and decomposition) reaching total conversion at temperatures above 250 °C [55]. A major CO formation is also observed at elevated temperatures because of the decomposition of the remaining methanol and the reverse water-gas shift reaction.

Stepwise Wall Temperature Profile:

This experiment was carried out under operating conditions similar to those of the previous section. Here, the adjusted wall temperature is set constant to 285 °C in the first three heating blocks, and reduced to 185 °C afterwards. This step changing wall temperature profile (case B) is compared with the isothermal reference case A (see Table 4.3).

CASE	T_{block1}	T_{block2}	T_{block3}	T_{block4}	T_{block5}
A	285	285	285	285	285
B	285	285	285	185	185

Table 4.3: Adjusted wall temperature. Description of heating zones according to Figure 4.6.

In Figure 4.6, the temperature profiles resulting from the constant and the stepped wall temperature setting (A and B respectively) are plotted. Both cases display almost identical profiles of temperature in blocks 1 to 3. Immediately after block 3 the gas temperature in case B descends to levels in which the reforming reaction should not take place [45].

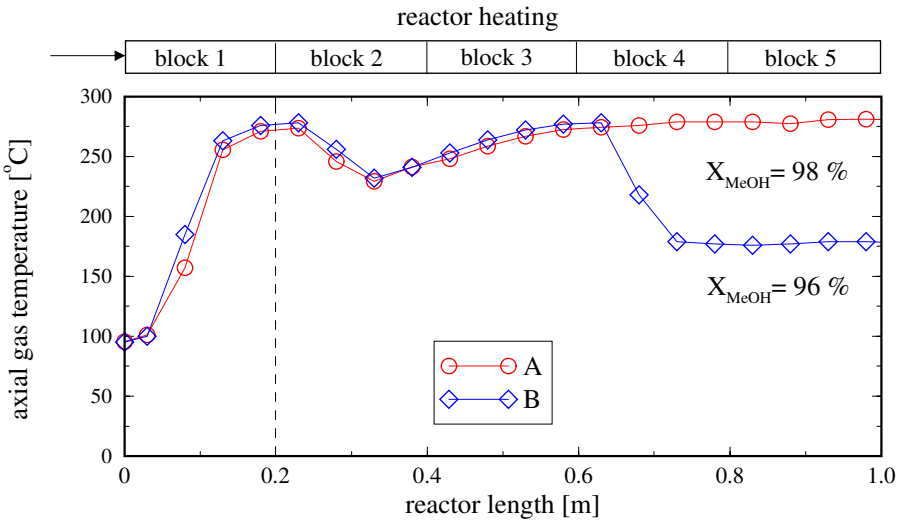

Figure 4.6: Comparison between constant and stepped heating temperature.

It can be noticed that in both cases, similarly high methanol conversions (96 and 98 %) are obtained, revealing that the reactants methanol and water have already reacted, once the half of the catalyst bed is reached. The reforming reactor seems to be over-dimensioned for the throughput considered.

Figure 4.7 adds important information about the influence of the overall temperature level on the product selectivity. Since CO is the most critical product from the reaction system, only its concentration along the reaction zone is discussed.

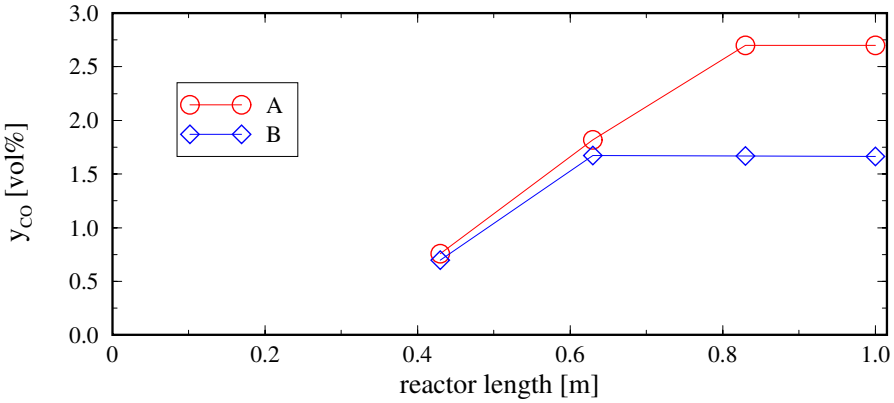

Figure 4.7: Development of the CO production over the reactor length for isotherm (A) and stepped heating temperature.

In both cases, A and B, the CO concentration profiles remain similar as long as the heating temperature is set constant to 285 °C. As soon as in case B, the wall temperature is lowered to 185 °C no more CO is formed. If the wall temperature still remains high (case A), CO is progressively produced. Although the methanol conversion reaches similar high values, the CO concentration seems to be strongly dependent on the local temperature.

The results can be explained as follows:

As shown in Figure 4.5 methanol conversion below 200-220 °C is low, which is in accord with previous studies [56]. At low temperatures methanol steam reforming (Eq. 2.21) seems to be the dominating reaction so that the CO formed by methanol decomposition (Eq. 2.22) is below the water-gas shift equilibrium. With increasing temperatures more CO is formed by methanol decomposition and hence CO concentration will exceed the WGS equilibrium value.

In order to gain more information about the influence of the local operating temperature, and to procure an isothermal reaction behavior, further stepped wall temperature schemes were considered (Table 4.4: D, E and F). The aim was to avoid the formation of a cold-spot. This critical zone corresponds to the heating blocks 2 and 3. As reference case, the experiment C which has a constant heating temperature of T_w = 250 °C is considered.

CASE	$\mathbf{T}_{block1}$	$\mathbf{T}_{block2}$	$\mathbf{T}_{block3}$	$\mathbf{T}_{block4}$	$\mathbf{T}_{block5}$
C	250	250	250	250	250
D	250	265	265	250	250
E	250	265	260	250	250
F	250	270	260	250	250

Table 4.4: Adjusted wall temperature for a stepped reactor heating.

This time, the wall temperature is varied over the heating blocks 2 and 3, keeping constant

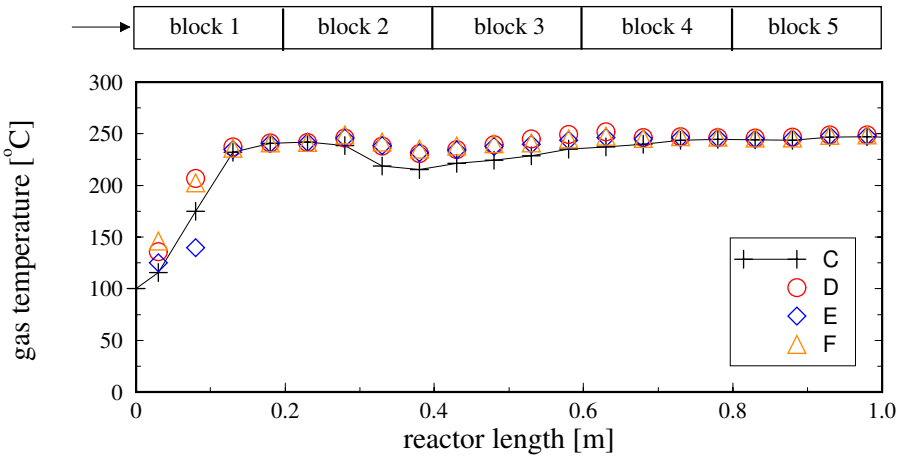

Figure 4.8: Adjusted temperature profile for non-isothermal reaction setting.

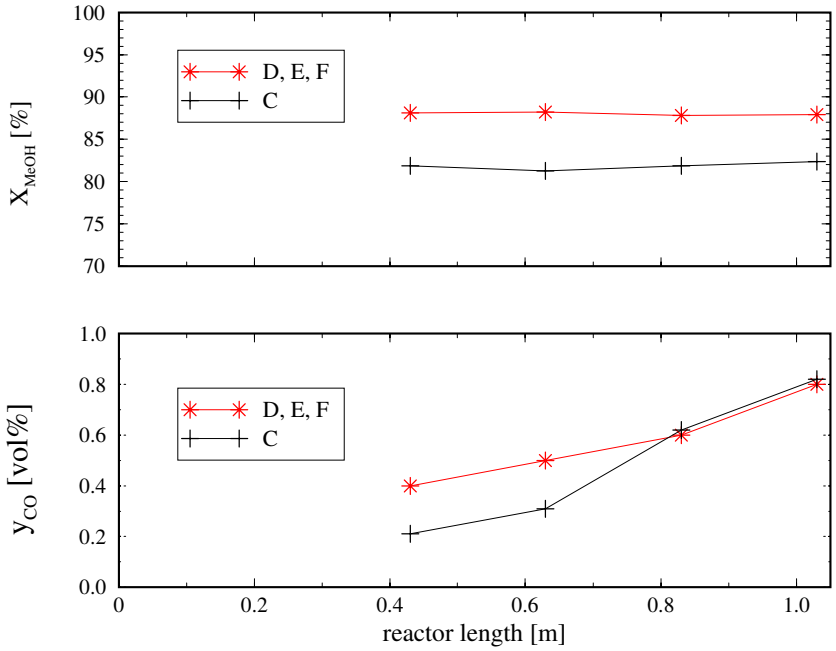

Figure 4.9: Methanol conversion (*top*) and CO concentration (*bottom*) at stepwise wall temperature.

the adjusted temperature over the last two blocks (see Table 4.4 and Figure 4.8). The pre-heating temperature (block 1) is kept constant for all cases.

The resulting CO concentration profile, shown in Figure 4.9, illustrates this behavior. In case of a typical temperature drop (case C), CO is formed slower than in the zones with an almost constant gas temperature (cases D, E, F). Methanol conversion is also affected. Lower axial gas temperatures lead to lower methanol conversion values. The cold-spot observed in the first half of the reactor when adjusting a constant wall temperature leads not only to lower local CO concentration but also to lower methanol conversion values.

Surprisingly, the final methanol conversion in all examples is already reached after 400 mm whereas at the rest of the reactor length only the CO concentration is increased. No higher operating temperatures were evaluated, aiming at 100 $\%$ methanol conversion because this clear tends to a higher formation of CO and could lead to catalyst damages [4].

Closing Remark

The results from the experiments with an adjusted stepwise wall temperature suggest that a high entrance temperature with a fast temperature decrease towards the reactor end leads to high methanol conversion with moderate CO formation whereas high temperatures towards the reactor end only enhance CO formation but no methanol conversion.

4.2.2 Influence of the Steam-to-Methanol Ratio

Besides temperature, the second important variable for steam reforming reaction is the molar ratio of steam-to-methanol in the feed (S/M). The SRM consumes 1 mole of water per mole of methanol reacted (the stoichiometric S/M-ratio is 1). A steam excess is favorable for ensuring a total methanol conversion. The WGS reaction shifts the state of equilibrium to the side of the hydrogen-production/CO-consumption. Nevertheless, the more water is fed the higher are the energetic costs, because of the high evaporation enthalpy of water.

Several authors recommend operating the SRM at S/M relationships between 1.0 and 2.0. *Peppley et al.* suggest S/M ratios higher than 1.3 [5].

The present section is focused on the evaluation of the influence of the steam-to-methanol feed ratio on the overall reaction conversion and the product selectivity. In order to quantify this effect, systematic experiments were carried out, at which feed flow rate, operating temperature and system pressure remain constant. General operating conditions are listed in Table 4.5.

operating parameter	**value**
feed flow rate	170 $\frac{g}{h}$
specific mass flow rate	0.5 $\frac{kg}{m^2 s}$
wall temperature	250; 265 °C
system pressure	1.5 $bar\ abs$

Table 4.5: General operating conditions for experiments on the variation of the S/M ratio

The S/M molar ratio was varied in intervals of 0.2 from 0.8 to 2.0. For a better understanding of the reaction behavior, two operating temperatures T_W were chosen. Experimental results are presented in the following.

As extracted from Figure 4.10, the CO formation depends on the steam-to-methanol molar ratio. Not only higher operating temperatures (as described in section 4.2.1) but also lower

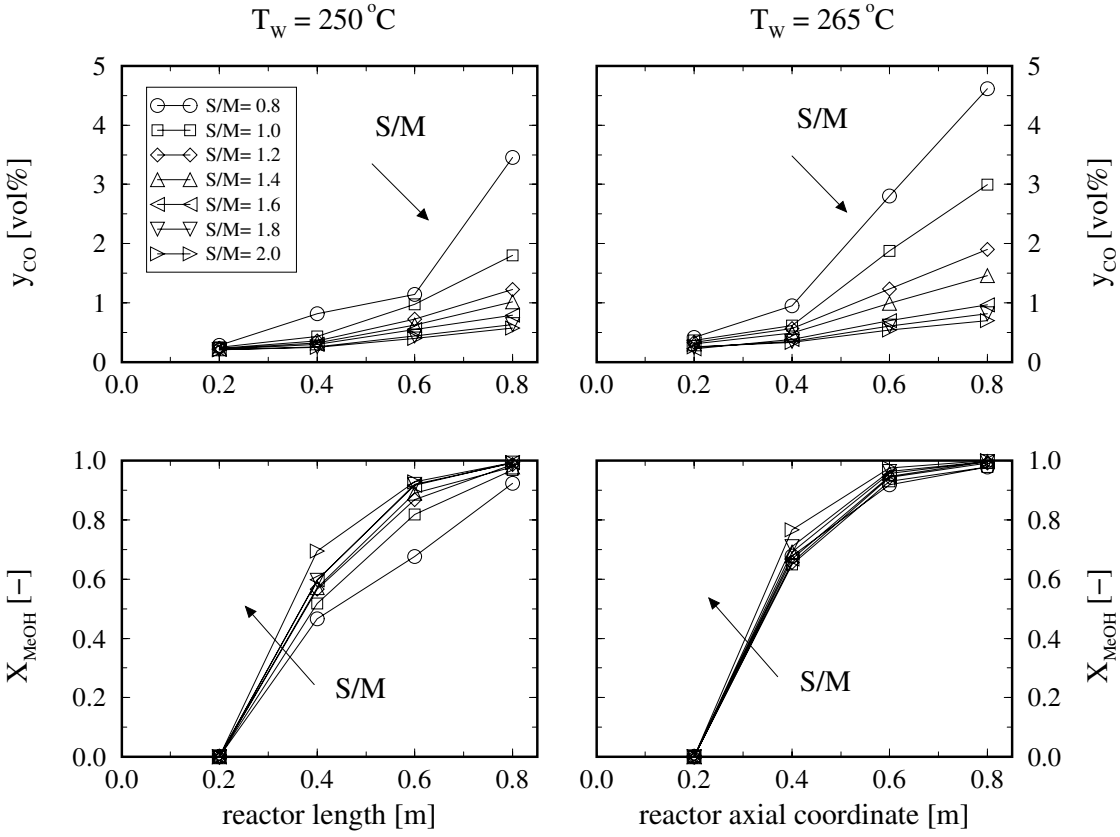

Figure 4.10: Experimental values of CO concentration (y_{CO}) and methanol conversion (X_{MeOH}) for different S/M molar ratios at two wall temperatures (T_w). Notice that the reactor tube from 0 m to 0.2 m is filled with inert material.

values of S/M contribute to elevated CO concentrations. This effect can be explained by the fact that the water excess contributes to shift the chemical equilibrium of the WGS reaction (Eq. 2.23) to the production of hydrogen and carbon dioxide. Figure 4.11 summarizes these results.

Due to the stoichiometry of the steam reforming reaction, the total methanol conversion can only be ensured when operating at S/M ratios above 1.0. It is also expected that over-stoichiometric fed water favors in principle the conversion of methanol according to the equation 2.21 and reduces the reverse WGS reaction (Eq. 2.23). Figure 4.12 reproduces this general behavior: both plotted curves (at T_w = 250 °C and 265 °C) show incomplete methanol consumption at S/M-values below 1.0. For values above 1.0, the methanol conversion tends to the maximum value. In addition, higher wall temperatures yield in combination with higher S/M values, larger methanol conversions.

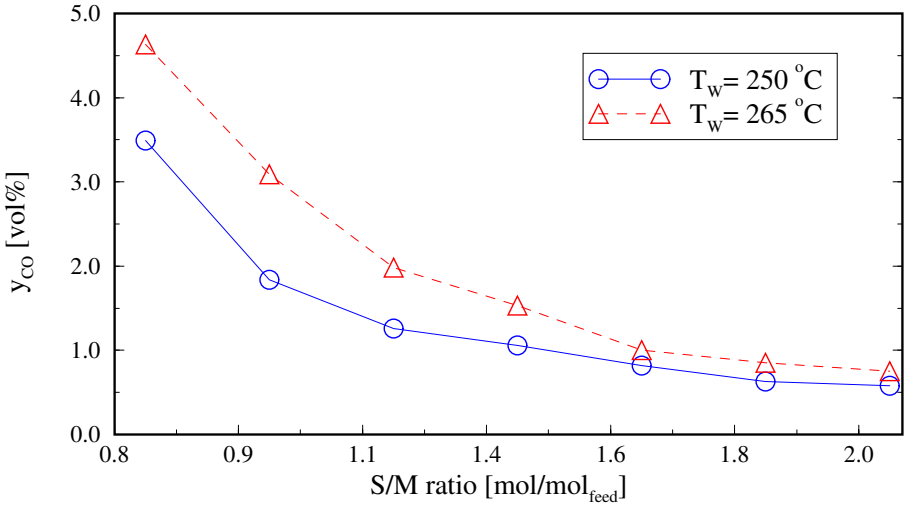

Figure 4.11: Dependence of the CO concentration on the S/M ratio.

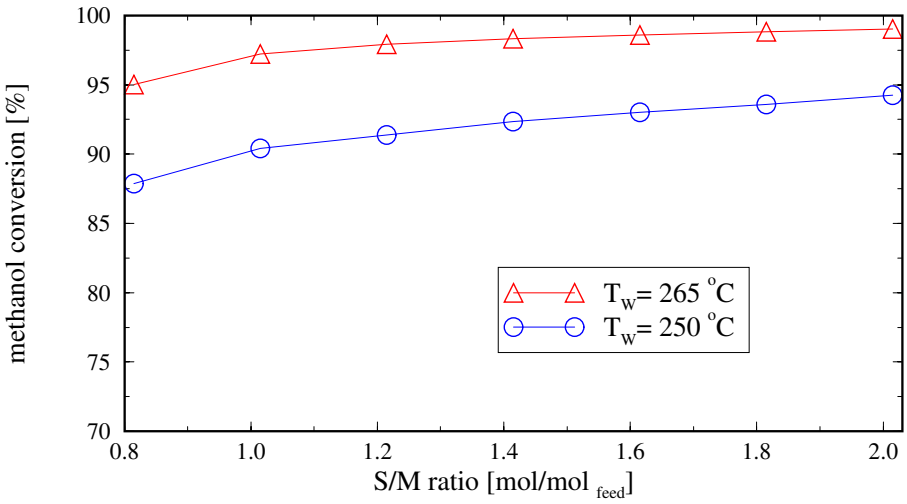

Figure 4.12: Dependence of the methanol conversion on the S/M ratio.

Closing Remark

In conclusion both variables, the methanol conversion and the CO concentration are positively influenced by the increment of the S/M ratio. Nevertheless, excess water in the system affect negatively the overall degree of efficiency, because it introduces elevated costs of energy for evaporating the fed water and for separating the unreacted water from the process outflow in a condenser. S/M values between 1.1 and 1.5 are recommended to attain an enhanced system performance.

4.3 Kinetic Parameter Evaluation

4.3.1 Modeling of the Fixed-bed Reactor for SRM

For comparison between experiment and simulation, and the respective adjustment of the kinetic parameters a simplified reactor model was developed.

It considers mass and energy balances for the kinetic reactor in order to simulate the variation of the most important state variables along the reactor axial coordinate.

4.3.1.1 Model Assumptions

For calculating the reactor behavior, following simplifications were made:

- steady state
- plug flow along the reactor bed (radial temperature and concentration gradients are neglected)
- solid (catalyst) properties are function of the state variables
- reaction rate ($r_{m,i}$) is referred to the catalyst weight
- heat exchange takes place with the constant reactor wall temperature and is modeled by a global heat transfer coefficient.

4.3.1.2 Model Equations

The mass balance for the methanol steam reforming reactions (Eqs. 2.21-2.23) for both key components CH_3OH and CO_2 is stated in weight fractions w_j $\left[\frac{kg_j}{kg_{total}}\right]$, according to:

$$\dot{m}_z \frac{\partial w_j}{\partial z} = M_j(1-\varepsilon^{gas})\,\varrho^{cat} \sum_{i=1}^{3} \nu_{ij}\, r_{m,i} \qquad j = CH_3OH, CO_2 \tag{4.5}$$

The stationary energy balance of the reforming gas mixture is given by:

$$c_{p_{z,T}}\,\dot{m}_z \frac{\partial T}{\partial z} = (1-\varepsilon)\,\varrho^{cat} \sum_{i=1}^{3} r_{m,i}\,(-\Delta H_{R,i}) - U_w\, a^v\,(T - T_w) \tag{4.6}$$

with U_w as the global heat transfer coefficient $\left[\frac{W}{m^2 K}\right]$ and T_w as the adjusted heating temperature. The temperature dependence of the specific heat capacity and the reaction enthalpy are given by:

$$0 = c_{p_{z,T}} - \sum_{j=1}^{J} w_{j_{z,T}}\, c_{p,j}\,(T) \tag{4.7}$$

$$0 = (-\Delta H_{R,i}) - \left[\sum_{j=1}^{J} \nu_j \Delta H_j^0 + \sum_{j=1}^{J} \nu_j \int_{T^0}^{T} c_{p,j}\,(dT)\right] \tag{4.8}$$

Feed conditions for solving the reaction equation system are:

$$w^{+}_{CH_3OH}\Big|_{z=0} = \frac{M_{MeOH}}{M_{MeOH} + M_{H_2O} \cdot \left(\frac{S}{M}\right)} \tag{4.9}$$

$$w^{+}_{CO_2}\Big|_{z=0} = 0 \tag{4.10}$$

$$T^{+}\Big|_{z=0} = T^{+}. \tag{4.11}$$

Typical model parameters for fixed-bed reactors were taken from the literature considering similar reactor geometries and operating conditions [4, 57]. These parameter values are listed in Table 4.6.

parameter	value
U_w	150 $\frac{W}{m^2K}$
ρ^{cat}	1200 $\frac{kg}{m^3}$
ε^{gas}	0.35 [-]

Table 4.6: Typical parameters employed for the mass and energy balance calculations.

4.3.2 Results and Discussion

The kinetic model to be studied was taken from the work of *Peppley et al.* (see section 2.6.3) for SRM employing the commercial catalyst BASF K3-110. Most of the kinetic parameters published by *Peppley* were taken as reported in the literature, with exception of the reaction rate constants. They were adjusted by simulation to own experimental data on the evaluation of the methanol/steam system under isothermal reaction conditions in a fixed-bed tubular reactor (as presented earlier in section 4.2).

The reaction conditions set in the experimental evaluation, used later for the kinetic parameter adjustment are listed in Table 4.7.

First results on the kinetic evaluation showed that the variation of the *reaction rate constants* influences in a more direct way the development of the CO concentration in the dry-gas

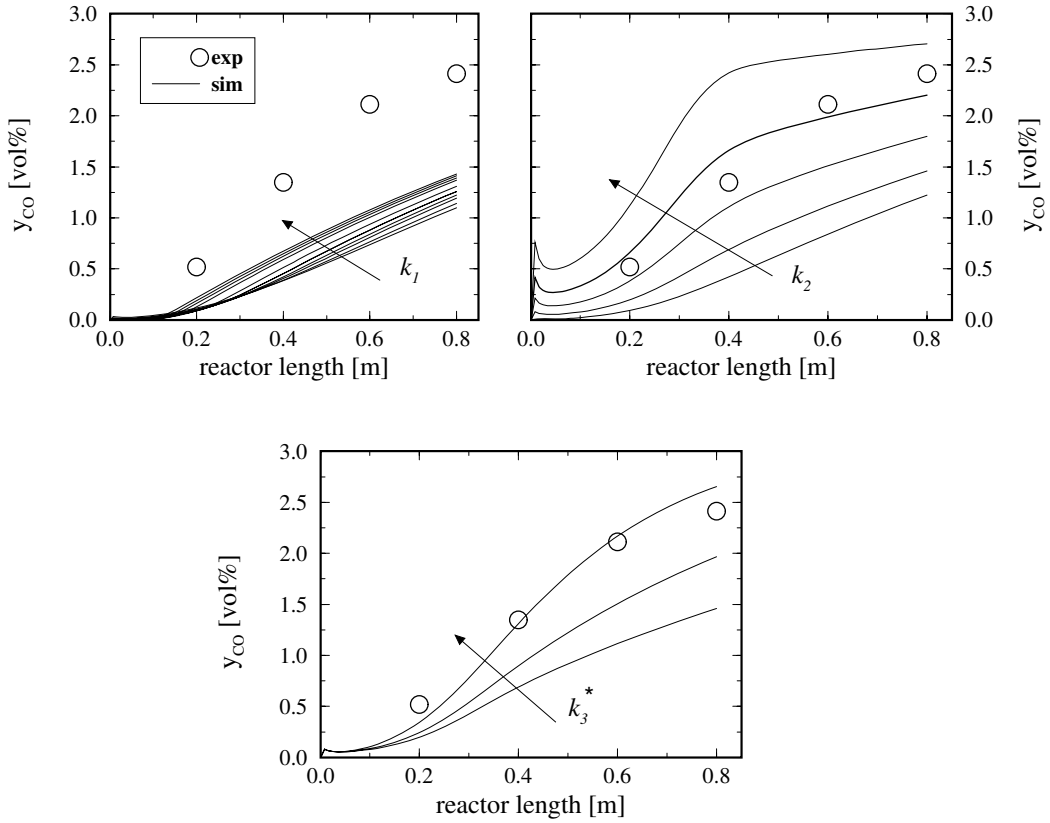

Figure 4.13: Parameter study on the reaction rate constants for all considered reactions: methanol-steam reforming (*upper-left graphic*); methanol decomposition (*upper-right graphic*); water-gas shift reaction (*lower graphic*). Kinetic parameters are listed in Table 4.8.

parameter	**value**
$\dot{m}_{MeOH}$	200 $\frac{g}{h}$
$\dot{m}_{H_2O}$	140 $\frac{g}{h}$
T_w^{iso}	280 °C

Table 4.7: Employed typical parameters for the mass and energy balance calculations.

over the reactor length than the development of the hydrogen/carbon dioxide concentration. In consequence the adjustment process was oriented to fit CO concentration values in the dry-gas. Simultaneously, the fitting between experimental and simulation values of the gas temperature was also procured.

In the Figure 4.13, three different simulation runs are presented for adjusting the kinetic parameters to the experimental data, as example for the operating conditions mentioned above. Adjusted parameters ($k_1,\ k_2,\ k_3^*$) were set to:

parameter	value
k_1 [$\frac{m^2}{s\ mol} \cdot 10^{14}$]	1 / 5 / 7.4$^{(lit)}$ / 10 / 15 / 20$^{(u)}$ / 30 / 50 / 60 / 200 / 400 / 800 / 2000
k_2 [$\frac{m^2}{s\ mol} \cdot 10^{20}$]	3.8$^{(lit)}$ / 38$^{(u)}$ / 100 / 200
k_3^* [$\frac{m^2}{s\ mol} \cdot 10^{14}$]	0.59$^{(lit)}$ / 1.0 / 2.0$^{(u)}$

Table 4.8: Evaluated kinetic parameters for adjustment study ($^{(lit)}$ literature reported value; $^{(u)}$ selected for simulations).

When varying the reaction rate constant for the steam-reforming reaction (k_1, Figure 4.13-upper/left) a poor effect of this variable on the CO formation was observed (see values in Table 4.8). A conservative value for k_1 was assumed (k_1 = $20.0 \cdot 10^{14} \frac{m^2}{s\ mol}$). An increase of the reaction rate constant for methanol decomposition, k_2, showed a first rapid increase of CO, followed by a subsequent drop and then the increase to a plateau value over the reactor length. This would be understandable if methanol decomposition (Eq. 2.22) is the primary reaction while the CO formed is converted to CO_2 with the present water vapor in the subsequent WGS reaction (Eq. 2.23). However this is not reflected by the experimental results.

Obviously the steam reforming reaction (Eq. 2.21) is the primary reaction with the reversible WGS responsible for the gradually increasing CO formation. Therefore k_2 can be fixed to a moderate value of $k_2 = 3.8 \cdot 10^{21} \frac{m^2}{s\ mol}$. The variation of the reaction rate constant for the water-gas shift reaction (k_3^*, Figure 4.13-lower) showed instead a more relevant effect in adjusting the CO concentration. The adjusted value taken for the further simulations was k_3^* = $2.0 \cdot 10^{14} \frac{m^2}{s\ mol}$.

The same good agreement achieved was also encountered when adjusting the kinetic parameters to the experimental results of other temperatures: a graphical comparison of measured and simulated temperatures and gas concentrations is showed in the following drawings (Figures 4.14 to 4.18) at different reactor wall temperatures. For each case, concentration profiles of the wet-gas are presented in the upper-left diagram. The upper-right chart gives the composition of the gas-phase for experimental values and simulation (left scale is related to CO concentration, right scale to hydrogen and CO_2). The lower chart shows a comparison between measured and calculated reforming gas temperature profile.

The fact that the dry gas compositions y_{H_2} and y_{CO_2} are almost constant over the reactor length is another strong argument that for methanol steam reforming, (Eq. 2.21) is the main methanol conversion reaction. It creates H_2 and CO_2 in the constant ratios of 3 to 1 (Figures 4.14 to 4.18) while CO is only formed to a small but steadily increasing extent by reverse WGS (Eq. 2.23) in a consecutive reaction.

Summarizing, the validation of the kinetic model with experimental data was successfully achieved yielding a reasonable quantitative agreement between the experimental data and the model. A complete set of the original and the adjusted rate parameters can be found in Appendix B.2.8.

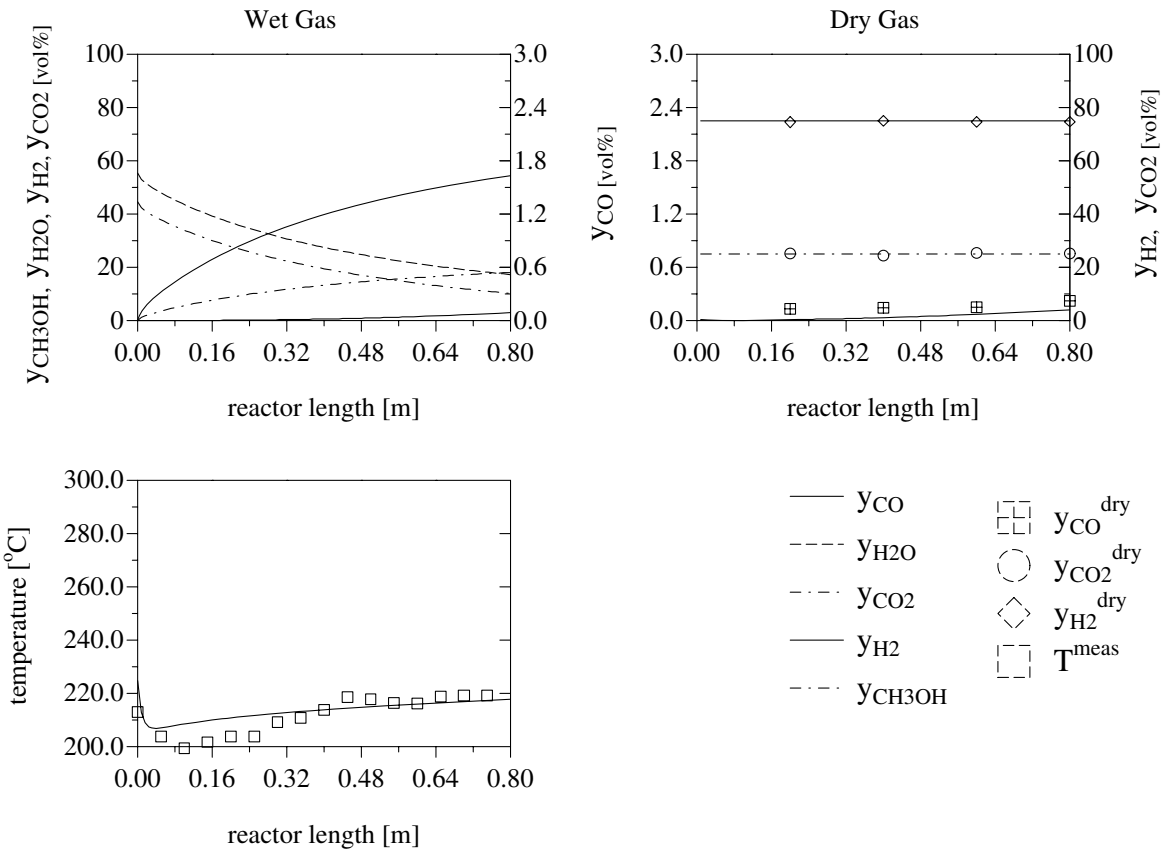

Figure 4.14: Simulations (lines) and experimental measurements (symbols) of temperature and gas concentration along the reactor length for SRM on a fixed-bed reactor. $\dot{m}_z = 0.5\ \frac{kg}{m^2 s}$, $S/M = 1.3$, $\mathbf{T_w} = \mathbf{225}\ ^\circ\mathbf{C}$

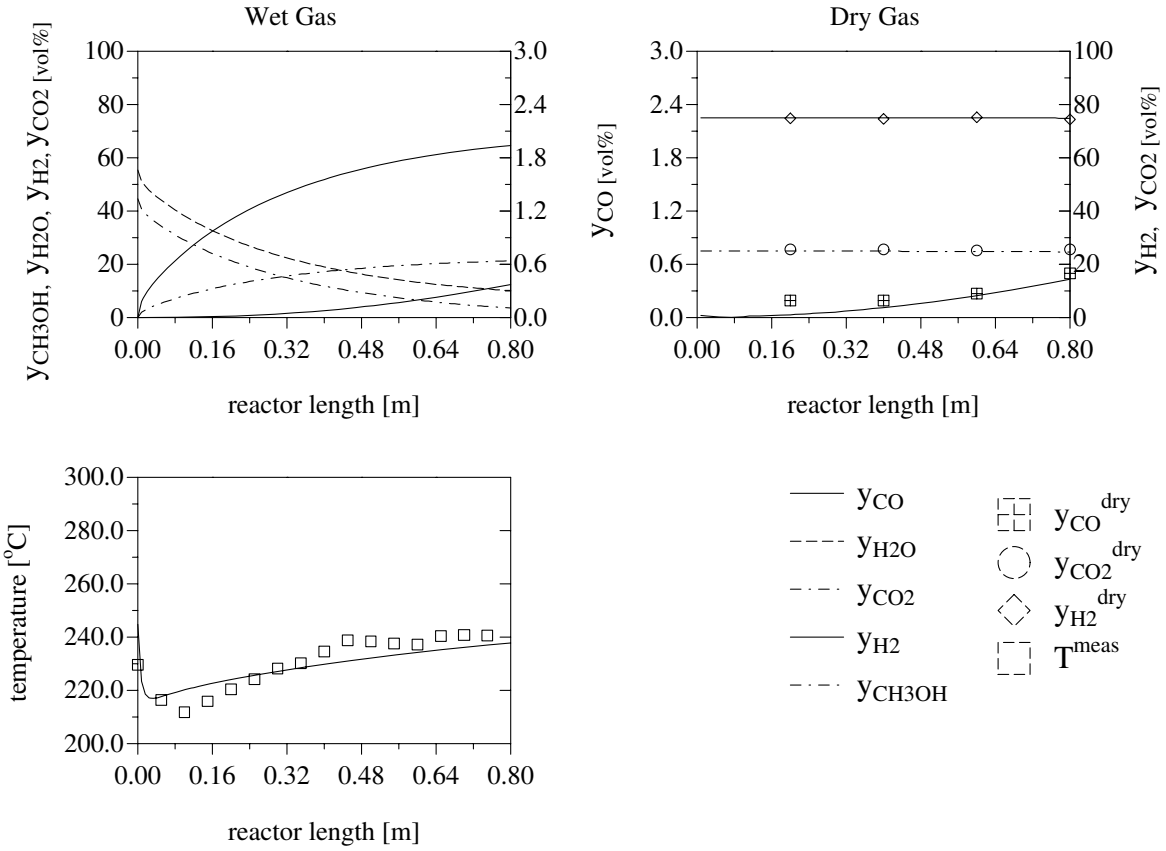

Figure 4.15: Simulations (lines) and experimental measurements (symbols) of temperature and gas concentration along the reactor length for SRM on a fixed-bed reactor. $\dot{m}_z = 0.5\ \frac{kg}{m^2 s}$, $S/M = 1.3$, $\mathbf{T_w} = \mathbf{245}\ ^\circ\mathbf{C}$

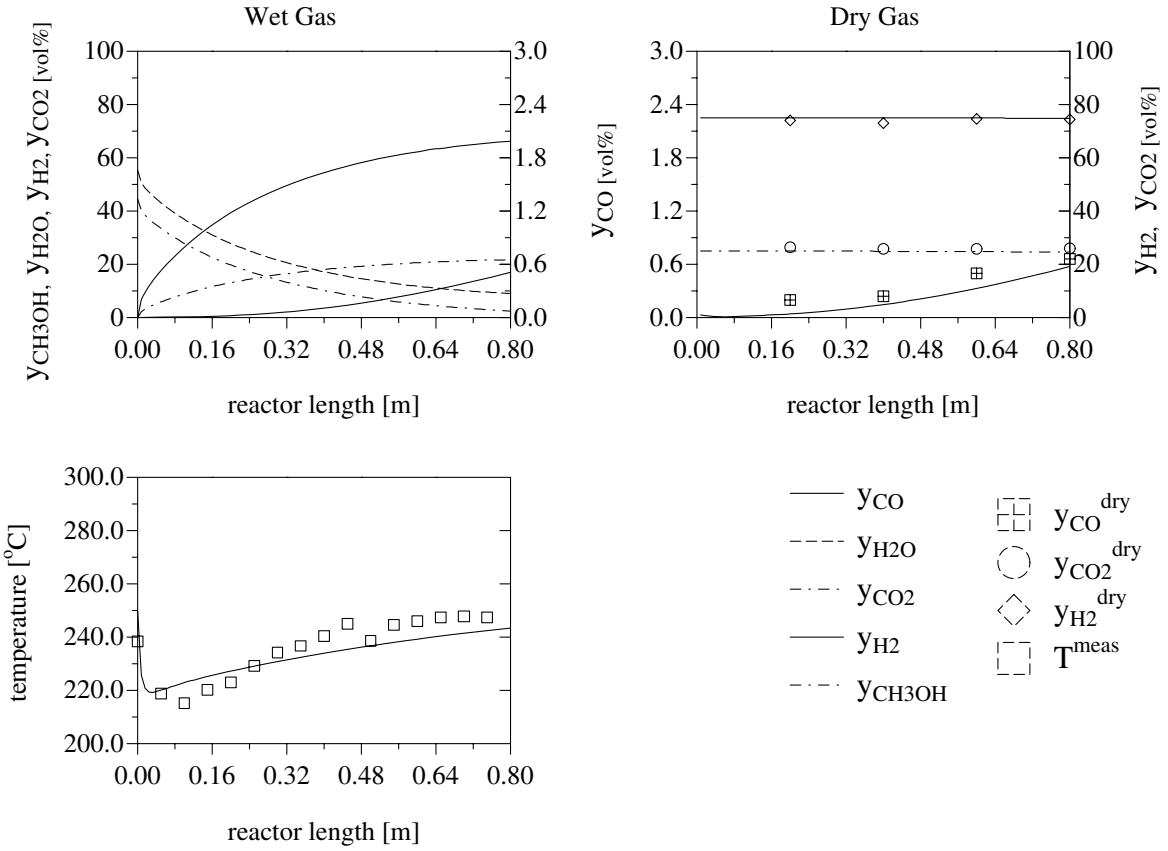

Figure 4.16: Simulations (lines) and experimental measurements (symbols) of temperature and gas concentration along the reactor length for SRM on a fixed-bed reactor. $\dot{m}_z = 0.5\ \frac{kg}{m^2 s}$, $S/M = 1.3$, $\mathbf{T_w} = \mathbf{250}\ ^\circ\mathbf{C}$

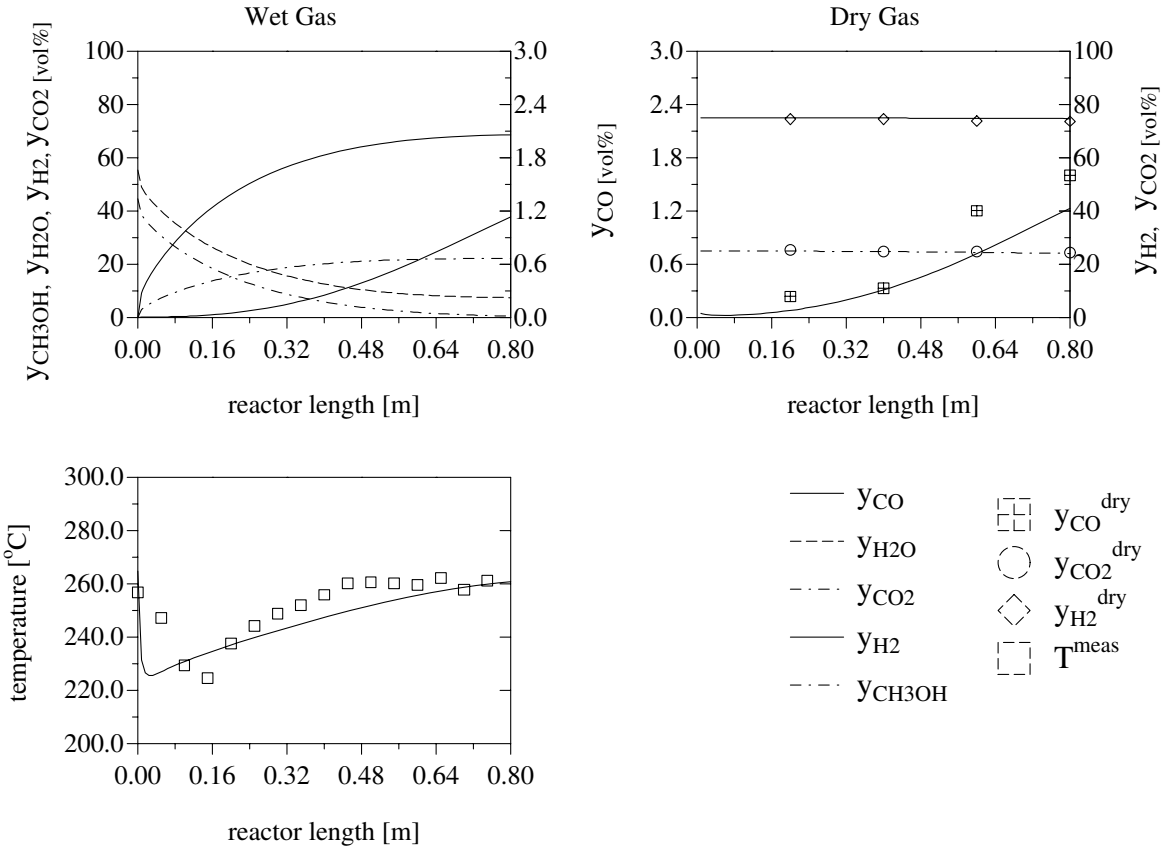

Figure 4.17: Simulations (lines) and experimental measurements (symbols) of temperature and gas concentration along the reactor length for SRM on a fixed-bed reactor. $\dot{m}_z = 0.5\ \frac{kg}{m^2 s}$, $S/M = 1.3$, $\mathbf{T_w} = \mathbf{265}\ ^\circ\mathbf{C}$

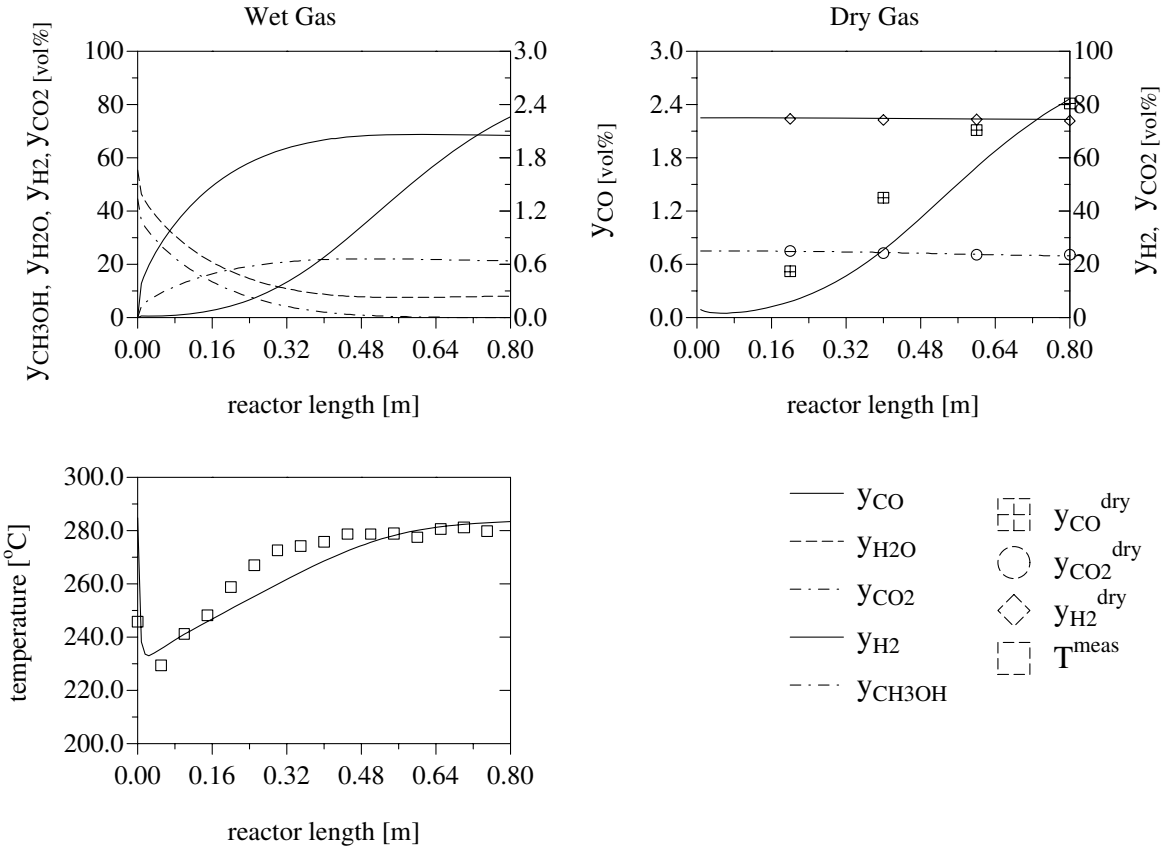

Figure 4.18: Simulations (lines) and experimental measurements (symbols) of temperature and gas concentration along the reactor length for SRM on a fixed-bed reactor. $\dot{m}_z = 0.5\ \frac{kg}{m^2 s}$, $S/M = 1.3$, $\mathbf{T_w} = \mathbf{285}\ ^\circ\mathbf{C}$

Chapter 5

Modeling of Methanol Reforming in a Folded-Sheet Reactor

5.1 Simplified Reaction System for the SRM

Following the discussion in Section 2.6, the reaction system for the steam reforming of methanol can be described by the following overall endothermic reaction network:

(1) Methanol-steam reforming (Eq.2.21):

$$CH_3OH \ + \ H_2O \Longleftrightarrow CO_2 \ + \ 3H_2, \quad \Delta h_R^0 = +49.53 \, \frac{kJ}{mol} \tag{5.1}$$

(2) Methanol decomposition reaction (Eq.2.22):

$$CH_3OH \Longleftrightarrow CO \ + \ 2H_2, \quad \Delta h_R^0 = +90.69 \, \frac{kJ}{mol} \tag{5.2}$$

(3) Water-gas shift reaction (Eq.2.23):

$$CO \ + \ H_2O \Longleftrightarrow CO_2 \ + \ H_2, \quad \Delta h_R^0 = -41.16 \, \frac{kJ}{mol} \tag{5.3}$$

The required heat for the endothermic process stages is supplied through hydrogen combustion, according to:

$$H_2 \ + \ \tfrac{1}{2}O_2 \ \longrightarrow \ H_2O, \qquad \Delta h_R^0 = -241.83 \, \frac{kJ}{mol} \tag{5.4}$$

5.2 Model Assumptions

Compared to the simplified reactor model for the simulation of the kinetic experiments, a more detailed model will now be derived, which takes the specific design features of the folded-sheet reactor into account. To model the axial temperature and concentration profiles of the solid and gas phases, following assumptions and simplifications are made:

- State variables, concentration and temperature, vary only in axial direction: radial profiles are neglected (plug-flow, 1-dimensional model in space).
- Axial mass and heat transport in the gas phase results from both convection and dispersion. Axial heat transport in the solid phase occurs by conduction.
- The reaction rates for the reforming kinetics are described by the *Peppley*-kinetics as given in the previous chapter, Eqs. 2.29, 2.30 and 2.31. For the hydrogen combustion in the combustion channels it is assumed that the reaction at the temperatures considered is infinitely fast and completely mass transfer controlled [58].
- The following 5 specific phases are considered: folded-wall, gas and catalyst (on spacers) at the reforming side, gas and catalyst (on spacers) at the combustion side.
- Heat transfer between the spacers and the separating wall is neglected, due to the small contact area.
- Enthalpy transport by mass transfer between gas and catalyst phase is neglected.
- Material and energy balances of the gas phases are considered quasi-stationary since the changes in the state variables are in relation to the solid phase energy balances very fast.
- Material properties of the solid phases are assumed to be constant.
- Constant pressure along the reactor length is assumed (due to low pressure drop of the corrugated spacers in the narrow channels [59]).
- The reactor case is ideally insulated (adiabatic reactor). Radial heat loses are not permitted. Due to low operating temperatures heat radiation is neglected.
- Gases behave ideally.

5.3 Reactor Model

In this section, a mathematical model for the folded-sheet reactor is presented. The development of this reactor model was initiated by *Frauhammer* and *Becker* [3, 48]. This model will serve to perform detailed simulations and to optimize the overall reactor performance. The reactor model describes the change in time and space of the state variables (temperatures and concentrations) along the main reactor coordinate (1-D, dynamic). This heterogeneous model considers 4 different overall phases: the gas phase (index ***g***), the catalyst phase (***s*** or ***cat***), the folded sheet and the reactor casing. As a simplification the reactor casing and the folded sheet will later form a single phase: the wall phase (index ***w***) with uniform solid properties.

Process streams are denoted as: reforming gas (***ref***), combustion or fuel gas (***fg*** or ***fuel***) and side stream (***side***). The flow coordinate is represented by z and the time by t.

The reactor can be structured in axial direction, so that catalytic and inert zones can be installed. Homogeneous reactions do not take place under the operating conditions considered.

The balance element used to derive the model equations is shown in Figures 5.1 and 5.2.

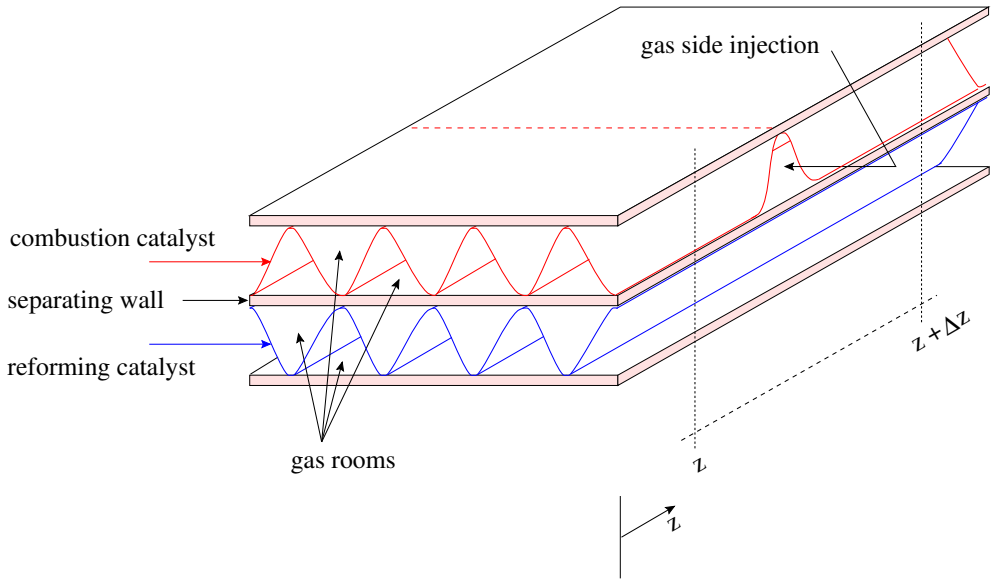

Figure 5.1: General scheme of two parallel reaction channels (reforming and combustion channel), embedded by the folded metal sheet. Notice the axial coordinate z and the side feeds of a typical balance section.

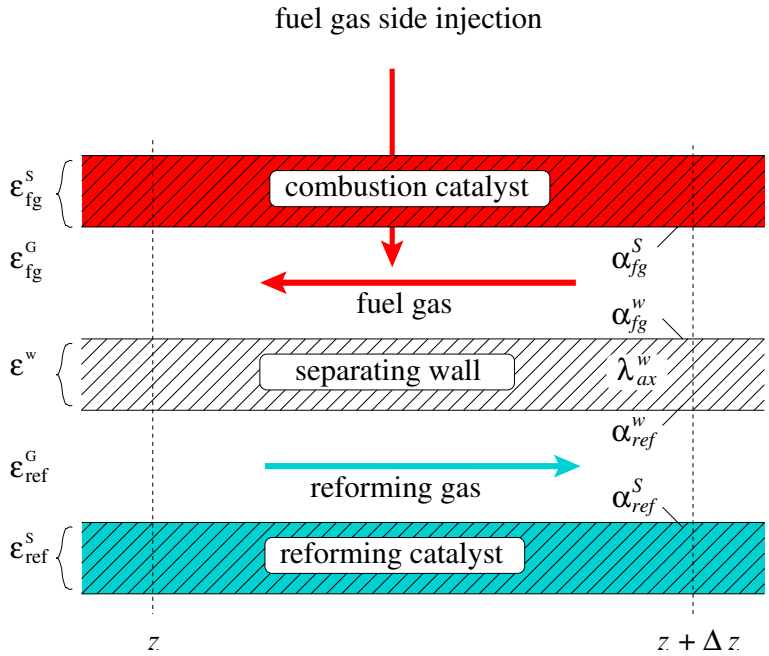

Figure 5.2: Balance element for the multi-phase 1-dimensional model of the countercurrent reactor.

5.4 Model Equations

The reaction system Eqs. 5.1 to 5.3, represented by two linearly independent species balance equations, is modeled including the kinetic models for all participating reactions. The mass and energy fluxes entering and leaving the balance element as well as the mass and energy formation and/or consumption inside the control volume are equated and represented in the general form of a parabolic partial differential equation (PDE), considering convective and dispersive transport mechanisms:

$$\mathbf{B}\frac{\partial \vec{y}}{\partial t} = -\mathbf{C}\frac{\partial \vec{y}}{\partial z} + \frac{\partial}{\partial z}\left(\mathbf{D}\frac{\partial \vec{y}}{\partial z}\right) + \vec{Q} \tag{5.5}$$

Here $\vec{y}$ represents the vector of the simulated state variables, and **B**, **C**, **D** and Q are the accumulation, convection, diffusion and source/sink terms respectively.

Appropriate initial and boundary conditions must be defined. Boundary conditions are of the general *Danckwert's* type:

$$\alpha\,\vec{y}_1 \;+\; \beta\,\frac{\partial \vec{y}}{\partial z}\bigg|_{z=1} \;=\; \gamma, \tag{5.6}$$

where α, β and γ can be functions of time and/or state variables.

The model includes the following state variables:

- Mass fraction of the key components methanol and carbon dioxide on the reforming side ($w_{CH_3OH,ref},\ w_{CO_2,ref}$).
- Mass fraction of hydrogen on the combustion side ($w_{H_2,fg}$).
- Temperature of the separating folded-sheet wall (T_w).
- Temperature of the reforming gas (T^G_{ref}).
- Temperature of the combustion gas (T^G_{fg}).
- Temperature of the reforming catalyst (T^S_{ref}).
- Temperature of the combustion catalyst (T^S_{fg}).

The concentrations of the non-key components of the reaction mixture are calculated from the linear stoichiometric dependencies of reaction equations 5.1 to 5.3. The concentration

of inert components (e.g. N_2 from the air on the combustion side) is calculated by using the closure condition: $\sum_j w_j = 1$.

The specific balance equations and the parameter correlations used have been derived in Appendix A and B. In the following only the final form of the balance equations will be stated.

5.5 Material Balances

5.5.1 Reforming Gas

The reforming gas mass flux $\dot{m}^0_{z,ref}$ is defined as the quotient between the total mass flow[1] and the cross sectional area of the entire reactor A_{tot}.

$$\dot{m}^0_{z,ref} = \frac{\dot{M}_{z,ref}}{A_{tot}} \quad \left[\frac{kg_j}{m^2\ s}\right]. \tag{5.7}$$

For the material balance of the key components (j= CH_3OH, CO_2) quasi-stationarity is assumed:

$$0 = \underbrace{-\dot{m}^0_{z,ref}\frac{\partial w_{j,ref}}{\partial z}}_{convection\ term} + \underbrace{\varepsilon^G_{ref} D^{eff}_{ax,ref}\frac{\partial^2 w_{j,ref}}{\partial z^2}}_{dispersion\ term} + \underbrace{a^v_{ref-S}\, M_j \sum_{i=1}^{I} \nu_{j,i}\, r^{cat}_i}_{reaction\ term} \tag{5.8}$$

The *Danckwert's* boundary conditions are chosen:

$$\begin{aligned} \dot{m}^0_{z,ref}\, w^+_{j,ref} &= \dot{m}^0_{z,ref}\, w_{j,ref}(z=0) - \varepsilon^G_{ref}\, D^{eff}_{ax,ref}\, \left.\frac{\partial w_{j,ref}}{\partial z}\right|_{z=0}, \\ \left.\frac{\partial w_{j,ref}}{\partial z}\right|_{z=L} &= 0. \end{aligned} \tag{5.9}$$

Concentration of the rest of the participant compounds can be calculated by using linear stoichiometric dependencies according to Eqs. 5.1 to 5.3:

$$w_{H_2O,ref}(z) = w^+_{H_2O,ref} - \frac{M_{H_2O}}{M_{CO_2}}\left(w_{CO_2,ref}(z) - w^+_{CO_2,ref}\right), \tag{5.10}$$

$$\begin{aligned} w_{H_2,ref}(z) = w^+_{H_2,ref} &+ \frac{M_{H_2}}{M_{CO_2}}\left(w_{CO_2,ref}(z) - w^+_{CO_2,ref}\right) \\ &-2\frac{M_{H_2}}{M_{MeOH}}\left(w_{MeOH,ref}(z) - w^+_{MeOH,ref}\right), \end{aligned} \tag{5.11}$$

$$\begin{aligned} w_{CO,ref}(z) = w^+_{CO,ref} &- \frac{M_{CO}}{M_{CO_2}}\left(w_{CO_2,ref}(z) - w^+_{CO_2,ref}\right) \\ &- \frac{M_{CO}}{M_{MeOH}}\left(w_{MeOH,ref}(z) - w^+_{MeOH,ref}\right). \end{aligned} \tag{5.12}$$

The concentration of the inert component N_2 is calculated by using a closure balance:

$$\sum_{j=1}^{J} w_{j,ref} = 1. \tag{5.13}$$

[1] It corresponds to the feed conditions since no side streams on the reforming side were considered.

5.5.2 Fuel Gas

Since the fuel gas flows opposite to the z direction, it is negative, leading to total specific mass flux (cross area related):

$$\dot{m}^0_{z,fg} \;=\; -\,\frac{\dot{M}_{z,fg}}{A_{tot}} \quad \left[\frac{kg_j}{m^2\;s}\right], \tag{5.14}$$

with $M_{z,fg}$ as the total mass flow on the fuel-gas side in $\left[\frac{kg}{s}\right]$. In practice, $M_{z,fg}$ is calculated with the volume flow rate and the gas density.

Due to side injections, the mass flux in the combustion channel varies in z-direction. This z-variation is given by:

$$\frac{d\dot{m}^0_{z,fg}}{dz} \;=\; -\sum_{j=1}^{J} \dot{m}^V_{j,side}, \tag{5.15}$$

with

$$\dot{m}^0_{z,fg}\Big|_{z=L} \;=\; -\,\dot{m}^{0,+}_z \;=\; -\,\frac{\dot{V}^+_{fg}\cdot\varrho^{G,+}_{fg}}{A_{tot}}. \tag{5.16}$$

The mass flux coming from the side injection port(s) is related to the volume of the injection section:

$$\dot{m}^V_{j,side} \;=\; \frac{\dot{M}^V_{j,side}}{A_{tot}\;L_{side}} \quad \left[\frac{kg_j}{m^3\;s}\right], \tag{5.17}$$

where L_{side} is the length over which the side stream is linearly distributed. An illustrative scheme of the mass flux on the combustion side is shown in Figure 5.3.

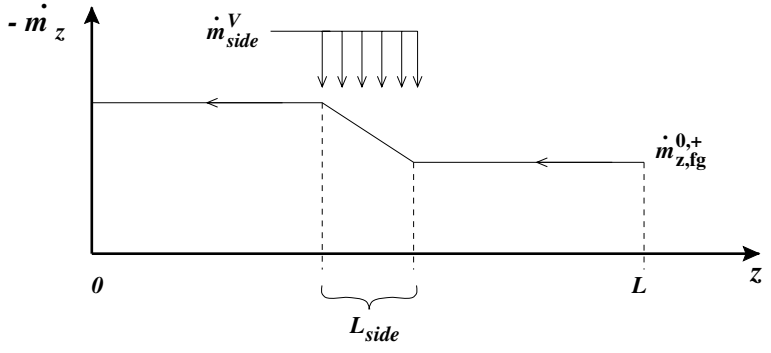

Figure 5.3: Schematic representation of the mass flux change on the combustion gas side considering side injections. Flow direction from right to left.

On the fuel gas side, only the catalytic combustion of hydrogen is considered. The combustion side can be operated at oxygen- or hydrogen-limiting conditions. Adopting a hydrogen-limiting scheme, oxygen as air is dosed in excess, and vice versa. In agreement with this, the steady-state (quasi-stationary) material balance for the key component j (hydrogen OR oxygen) can be written as follows:

$$\begin{aligned} 0 \;=\; & \underbrace{-\dot{m}^0_{z,fg}\frac{\partial w_{j,ref}}{\partial z}}_{convection\ term} \;\; \underbrace{+\,\varepsilon^G_{fg} D^{eff}_{ax,fg}\frac{\partial^2 w_{j,ref}}{\partial z^2}}_{dispersion\ term} \\ & \underbrace{-\,\varepsilon^S_{fg}\, M_j\, a^v_{fg-S}\, \nu_j\, J^{cat}_j}_{mass\ transfer\ term} \\ & \underbrace{+\,\dot{m}^V_{j,side} - w_j \sum_{j=1}^{J} \dot{m}^V_{j,side},}_{side\ injection} \qquad \text{for } j = H_2, O_2. \end{aligned} \tag{5.18}$$

Considering the fuel gas flows counter-currently to the z coordinate, the *Danckwert's* boundary conditions are:

$$\begin{aligned} \left.\frac{\partial w_{j,ref}}{\partial z}\right|_{z=0} &= 0, \\ \dot{m}^0_{z,fg}\, w^+_{j,ref} &= \dot{m}^0_{z,fg}\, w_{j,ref}(z=L) - \varepsilon^G_{fg}\, D^{eff}_{ax,fg} \left.\frac{\partial w_{j,fg}}{\partial z}\right|_{z=L}. \end{aligned} \tag{5.19}$$

The influence of mass transport limitations is considered in the molar flux factor J^{cat}_j by a linear driving force approximation for either hydrogen or oxygen:

$$J^{cat}_j = \frac{\beta_j}{\mathbb{R}\, T^G_{fg}}\,(p^G_j - p^S_j) \;=\; \frac{\beta_j}{\mathbb{R}\, T^G_{fg}}\,(p^G_j \;-\; 0), \qquad \text{for } j = H_2 \textit{ or } O_2. \tag{5.20}$$

The concentration of the second reacting component can be calculated using the following stoichiometric relationship:

$$0 \;=\; w^+_{O_2} - w_{O_2}(z) + \frac{1}{2}\frac{M_{O_2}}{M_{H_2}}\left(w_{H_2}(z) - w^+_{H_2}\right). \tag{5.21}$$

The concentration of the inert component N_2 is calculated from the a closure condition:

$$w_{N_2} = 1 - w_{O_2} - w_{H_2}. \tag{5.22}$$

5.6 Energy Balances

5.6.1 Metallic Sheet

The separating wall (folded metallic sheet) exchanges heat with both reacting gases, the reforming and the fuel gas, as shown in Figure 5.2. The general energy balance for this phase is:

$$\underbrace{\varepsilon^w \varrho_w c_{p,w} \frac{\partial T_w}{\partial t}}_{accumulation} = \underbrace{\varepsilon^w \lambda^w_{ax} \frac{\partial^2 T_w}{\partial z^2}}_{axial\ heat\ conduction} \underbrace{+ \alpha^w_{fg} a^v_{fg} \left(T^G_{fg} - T_w\right)}_{heat\ exchange\ fuel\ gas-wall} \underbrace{+ \alpha^w_{ref} a^v_{ref} \left(T^G_{ref} - T_w\right)}_{heat\ exchange\ wall-ref.\ gas} \underbrace{- \alpha_{iso} a^v_{jack} \left(T_w - T_{amb}\right)}_{heat\ loses}. \tag{5.23}$$

For the following calculations, the heat loses to the surroundings are neglected but could be easily included. Note that no direct exchange term exists between the catalyst (spacer) phase and the metallic sheet due to the small (line- or point-wise) contact area. Instead, all heat transfer between catalyst and the wall is assumed to take place over the respective gas phase.

The separating wall is assumed to be adiabatic at both ends:

$$\left.\frac{\partial T_w}{\partial z}\right|_{z=0} = 0, \quad \left.\frac{\partial T_w}{\partial z}\right|_{z=L} = 0. \tag{5.24}$$

The initial condition is set to the wall initial temperature:

$$T_w(z, t=0) = T^0_w. \tag{5.25}$$

5.6.2 Reforming Gas

The energy balance of the reforming gas is implemented in quasi-stationary form as shown in the following:

$$0 = \underbrace{-\dot{m}^0_{z,ref}\, c^G_{p,ref} \frac{\partial T^G_{ref}}{\partial z}}_{convective\ heat\ transfer} \underbrace{+\varepsilon^G_{ref} \lambda^G_{ref} \frac{\partial^2 T^G_{ref}}{\partial z^2}}_{dispersion} \underbrace{-\alpha^w_{ref} a^v_{ref} \left(T^G_{ref} - T_w\right)}_{heat\ exchange\ wall-ref.\ gas} \underbrace{-\alpha^S_{ref} a^v_{cat} \left(T^G_{ref} - T^S_{ref}\right)}_{heat\ exchange\ ref.\ gas-catalyst}. \tag{5.26}$$

The boundary conditions correspond to the *Danckwert's* type:

$$\begin{aligned} \dot{m}^0_{z,ref}\, c^{G,+}_{p,ref}\, T^{G,+}_{ref} &= \dot{m}^0_{z,ref}\, c^G_{p,ref}\, T^G_{ref}(z=0) - \varepsilon^G_{ref}\lambda^G_{ref}\, \left.\frac{\partial T^G_{ref}}{\partial z}\right|_{z=0}, \\ \left.\frac{\partial T^G_{ref}}{\partial z}\right|_{z=L} &= 0. \end{aligned} \tag{5.27}$$

The initial gas temperature along z is set to the initial temperature of the feed stream:

$$T^G_{ref}(z, t=0) \;=\; T^{G,0}_{ref}. \tag{5.28}$$

5.6.3 Fuel Gas

To formulate the quasi-stationary energy balance for the combustion side, the enthalpy of the side stream has to be considered in the section where gas is injected.

$$\begin{aligned} 0 = \quad & \underbrace{-\dot{m}^0_{z,fg}\, c^G_{p,fg} \frac{\partial T^G_{fg}}{\partial z}}_{convective\ heat\ transport} \quad \underbrace{+ \varepsilon^G_{fg}\lambda^G_{fg} \frac{\partial^2 T^G_{fg}}{\partial z^2}}_{dispersion} \\ & \underbrace{+ \alpha^S_{fg} a^v_{fg-S} \left(T^S_{fg} - T^G_{fg}\right)}_{heat\ exchange\ catalyst-fuel\ gas} \\ & \underbrace{+ \alpha^w_{fg} a^v_{fg-w} \left(T^G_{fg} - T_w\right)}_{heat\ exchange\ fuel\ gas-wall} \\ & \underbrace{+ \sum_{j=1}^{J} max\left(0, \dot{m}^V_{j,side}\right) \Delta\, h^{side}_j \Big|_{T^G}^{T^{side}}}_{side\ injection}. \end{aligned} \tag{5.29}$$

Here the last term in Eq. 5.29 considers the change of the temperature due to enthalpy exchange with the injection stream from the side feed. It is calculated by:

$$\sum_{j=1}^{J} \dot{m}^V_{j,side}(h^+_{j,side} - h^G_{j,fg}) = \sum_{j=1}^{J} \dot{m}_{j,fg} c_{p,j}(T^+ - T^G_{fg}) \tag{5.30}$$

The operator *max* is included for the general completeness of the equation and guarantees that only a change of the temperature can take place by a stream that enters the balance element.

Since the fuel gas flows opposite to the z-coordinate the *Danckwert's* boundary conditions are:

$$\left.\frac{\partial T^G_{fg}}{\partial z}\right|_{z=0} \;=\; 0,$$

$$\dot{m}^0_{z,fg}\, c^{G,+}_{p,fg}\, T^{G,+}_{fg} \;=\; \dot{m}^0_{z,fg}\, c^{G}_{p,fg}\, T^{G}_{fg}(z=L) - \varepsilon^G_{fg}\lambda^G_{fg}\left.\frac{\partial T^G_{fg}}{\partial z}\right|_{z=L}. \tag{5.31}$$

The initial gas temperature is set to the initial entering value:

$$T^G_{fg}(z, t=0) \;=\; T^{G,0}_{fg}. \tag{5.32}$$

5.6.4 Reforming Catalyst

The catalyst temperature, considering only heat exchange with the reforming gas phase, is formulated as follows:

$$\underbrace{\varepsilon^S_{ref}\varrho^S_{ref}c^S_{p,ref}\frac{\partial T^S_{ref}}{\partial t}}_{accumulation} = \underbrace{\varepsilon^S_{ref}\lambda^S_{ref,ax}\frac{\partial^2 T^S_{ref}}{\partial z^2}}_{axial\ heat\ conduction} \underbrace{+\alpha^S_{ref}a^v_{ref,S}\left(T^G_{ref}-T^S_{ref}\right)}_{heat\ exchange\ ref.\ gas-catalyst} \underbrace{+a^v_{ref-S}\sum_{i=1}^{3} r_i\,(-\Delta H_{R,i})}_{reaction\ term}. \tag{5.33}$$

Axial heat flux is set explicitly to zeros at both reactor ends:

$$\left.\frac{\partial T^S_{ref}}{\partial z}\right|_{z=0} \;=\; 0, \quad \left.\frac{\partial T^S_{ref}}{\partial z}\right|_{z=L} \;=\; 0. \tag{5.34}$$

The initial condition is:

$$T^S_{ref}(z, t=0) \;=\; T^{S,0}_{ref}. \tag{5.35}$$

5.6.5 Combustion Catalyst

The solid temperature in the sections where combustion catalyst is placed, is described by the following balance equation:

$$\underbrace{\varepsilon^S_{fg}\varrho^S_{fg}c^S_{p,fg}\frac{\partial T^S_{fg}}{\partial t}}_{accumulation} = \underbrace{\varepsilon^S_{fg}\lambda^S_{fg,ax}\frac{\partial^2 T^S_{fg}}{\partial z^2}}_{axial\ heat\ conduction} \underbrace{-\alpha^S_{fg}a^v_{fg-S}\left(T^S_{fg}-T^G_{fg}\right)}_{heat\ exchange\ catalyst-fuel\ gas} \underbrace{+r_4 a^v_{fg-S}\,(-\Delta H_{R,4})}_{reaction\ term}. \tag{5.36}$$

The catalyst boundaries are set to the following adiabatic conditions:

$$\left.\frac{\partial T^S_{fg}}{\partial z}\right|_{z=0} \;=\; 0, \quad \left.\frac{\partial T^S_{fg}}{\partial z}\right|_{z=L} \;=\; 0. \tag{5.37}$$

The initial solid temperature is set to a start value $T_{fg}^{S,0}$ as follows:

$$T_{fg}^{S}(z, t = 0) \; = \; T_{fg}^{S,0}. \tag{5.38}$$

The rate of heat generation of the hydrogen combustion reaction is also limited by mass transport of hydrogen/oxygen to the catalyst surface. At this place it is assumed that the reaction occurs immediately ($p_j^S = 0$). The following expression prevails:

$$r_4 = J_j^{cat}. \tag{5.39}$$

5.7 Ideal Gas Law

The gases on both the reforming and combustion side are assumed to follow the ideal gas law:

$$\varrho^G \; = \; \frac{p}{\mathbb{R}\, T^G \sum\limits_{j=1}^{J} \frac{w_j}{M_j}}. \tag{5.40}$$

Partial pressures used in the kinetic modeling equations are correlated with weight fractions using the following formula:

$$p_j \; = \; w_j \frac{p}{M_j \sum\limits_{n=1}^{J} \frac{w_n}{M_n}}. \tag{5.41}$$

5.8 Relative Methanol Conversion and CO Selectivity

In order to characterize the reaction behavior, the relative conversion of methanol and the selectivity to CO will be used. It assumes that CO and CO_2 are not fed to the reactor but produced within.

For practical purposes the methanol conversion is referred to the measurable concentrations of CO and CO_2:

$$X_{MeOH} \; = \; \frac{-\Delta \dot{N}_{MeOH}}{\dot{N}_{MeOH}^{+}} \; = \; \frac{\dot{N}_{CO} + \dot{N}_{CO_2}}{\dot{N}_{MeOH}^{+}}. \tag{5.42}$$

The selectivity of the reaction system to the CO production is defined by:

$$S_{CO} \; = \; \frac{\Delta w_{CO}}{\Delta w_{MeOH}} \cdot \frac{M_{MeOH}}{M_{CO}}. \tag{5.43}$$

Both methanol conversion and CO selectivity are the most important design variables used in this work for the optimization of the overall reactor behavior. Maximizing the methanol conversion and minimizing the CO production are the main goals of this design study.

5.9 Numerical Solution Methods

The combined algebraic and parabolic partial differential equation system is solved by using the simulation environment *PDEXPACK* [60], based on *PDEX* [61] algorithms. *PDEX* was developed by *Konrad-Zuse-Zentrum, Berlin* and *ICVT*, and is a fully adaptive code in space and time, which implements a calculation routine to solve equations of the type:

$$\mathbf{B}\frac{\partial \vec{y}}{\partial t} = -\mathbf{C}\frac{\partial \vec{y}}{\partial z} + \frac{\partial}{\partial z}\left(\mathbf{D}\frac{\partial \vec{y}}{\partial z}\right) + \vec{Q}, \tag{5.44}$$

with corresponding initial and boundary conditions.

In *PDEX* the spatial differential operators of the parabolic equations are discretized by using finite differences (*Lagrange*-parabola of 2nd order). For the integration in time of the resulting differential-algebraic system, *PDEX* employs the DA-solver *LIMEX* [62]. The main advantage of *PDEXPACK* consists of an error-oriented spatial regridding and the time step-size control, which allows an accurate resolution of steep gradients and fast-dynamics. *PDEXPACK* also controls the number and location of the necessary grid points. For more details see the respective documentation [63].

Chapter 6

Preliminary Design and Development of the Folded-Sheet Reactor Concept

In the present section, some initial results on the design and development of the **Folded-Sheet Reactor Concept** for SRM are presented. Detailed simulations using the kinetics obtained in Chapter 4 are performed in order to generate first information, which can lead to the design of a final reactor prototype based on the "folded-sheet" concept. The first design simulations will be used for the adjustment of the operating conditions and the optimization of geometrical parameters for a folded-sheet reformer, capable of producing a hydrogen output equivalent to 1 kW thermal energy. The results from the experimental evaluation of the 1-kW$_{th}$ folded-sheet reactor represent the *proof of the principle* for the global concept, and will be taken as starting point for the design and construction of a 10-kW$_{th}$ reactor unit. In the 10-kW prototype not only the reforming stage but also the liquid feed evaporation shall be included. Therefore experiments concerning the pulse-free total evaporation of water in a folded sheet evaporator, heated by a catalytic combustion reaction will also be included in this chapter.

6.1 SRM in the 1-kW Folded-Sheet Reactor

6.1.1 Initial Considerations

- The folded-sheet reactor concept itself allows basically for both operating flow-paths: co-current and counter-current (see Chapter 3). Co-current operation would require high inlet temperatures to ensure a rapid start of the methanol conversion. This would require a large energy to pre-heat the reactant mixture and result in a relatively high gas temperature at the reformer exit. The high outlet temperatures from the reformer would be detrimental for the subsequent WGS section.

  Previous work on the efficiency of such integrated systems shows that for a better energy integration and recovery a counter-current flow path is more efficient when operating at about equal heat capacity flux in the combustion and the reforming channels [3]. A counter-current operation path favors the fact that most of the generated

heat remains in the reactor center and the inlet- and outlet-streams are at low temperatures (”cold in - cold out”). This has the advantage that the hot effluents will be used to heat up the cold feeds and, in addition, a decreasing temperature profile at the exit of the reforming side helps to reduce the formed CO by the water-gas shift reaction (Eq. 5.3) [48].

- In determining the channel geometry of the folded-sheet reactor it was considered that the corrugated spacer structures used at the reforming side as catalyst substrate and at the combustion side as both catalyst substrate and inert structures, are commercially available with a standard wave height of 1 mm. In consequence the minimum channel width that allows the insertion of at least one spacer structure per channel should be 1.2 mm.
- The reformer side will be filled with catalyst coated spacers, and its overall length will be divided in two zones: the first half is filled with reforming-catalyst, while the rest with water-gas shift catalyst coated structures. In between a sample gas port is installed for analysis. Thus a better quantification of the effect of the water-gas shift section on the CO production is possible.
- Different from the experiments in Chapter 4 not the commercially available BASF catalyst K3-110 will be used. Two proprietary catalysts for the reforming and the WGS section supplied by Adam Opel AG will be used instead.
- An axially movable thermocouple will be implemented to measure the gas temperature on the reforming side over the reformer length.

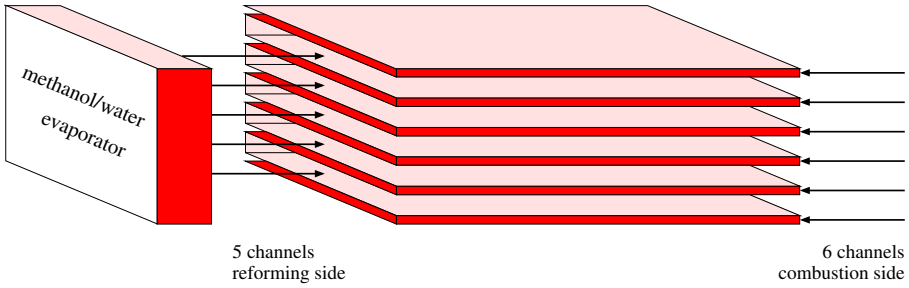

Figure 6.1: Scheme of the channel distribution used for modeling the folded-sheet reactor. The evaporation unit is not included in this study.

6.1.2 Reaction Engineering Simulations

The methanol reformer was simulated employing the model equations developed in Chapter 5. First calculations on the operating conditions for producing a hydrogen-rich reformate with an equivalent thermal power of 1 kW_{th} were carried out. The geometrical parameters were adjusted to an arrangement where five reforming and six combustion channels are in mutual contact over the separating walls[1]. In the following sections only results for one

[1] Further geometrical details are summarized in Appendix C.

single reforming channel and also for one single combustion channel are presented for discussion. The heat exchange areas and the channel cross-sections of these two representative simulation channels (Figures 5.1 and 5.2) are therefore calculated as mean values of the arrangement depicted in Figure 6.1. The methanol/water mixture is supposed to be coming from a separate evaporator unit. A reactor length of 0.6 m was preset.

6.1.2.1 Optimization of the Heat Generation on the Combustion Side

First, simulations on the influence of the location and the distribution of the heat sources on the combustion side and the resulting heat consumption on the reforming side were performed, employing the following general operating conditions[2]:

	parameter	value
reforming side		
	input mass flow rate	300 $\frac{g}{h}$
	S/M ratio	1.30 $\frac{mol}{mol}$
	input gas temperature	150 °C
combustion side		
	input gas temperature	100 °C

Table 6.1: Operating conditions used for simulations of the 1-kW reformer.

Methanol and water vapor are assumed to enter the folded-sheet reformer coming from an evaporator and preheating stage. For the vapor mixture a temperature of 150 °C is assumed. This value lies above the dew temperature of the reactant mixture.

For these first studies, a pre-determined heat amount is assumed to be uniformly produced at the combustion side and is adjusted so that the fed methanol completely reacts ($X_{CH_3OH} > 99.5\ \%$). In the upper half of Figure 6.2 the distribution of the volume-related, produced heat Q_{exo} is depicted over the reformer length, whereas the resulting heat requirement of the reforming reaction is shown in the lower half (Q_{endo}). Starting from a uniformly distributed heat source (dotted curves), the length of the zone over which heat is provided is systematically reduced and its height is adjusted for total methanol conversion. This resizing is continued up to a very narrow heat-producing zone at the reactor entrance (dashed curves). The resulting gas temperature profiles on the reforming side are plotted in the insert (top-right).

The results of this evaluation are shown in Table 6.2, where the reaction zones, the volumetric and the absolute heat flux as well as the general methanol conversion and CO molar fraction are given. In Figure 6.3 the results are plotted along the reactor length.

[2] Rounded values finally result in a hydrogen output equivalent to 1.1 kW_{th}.

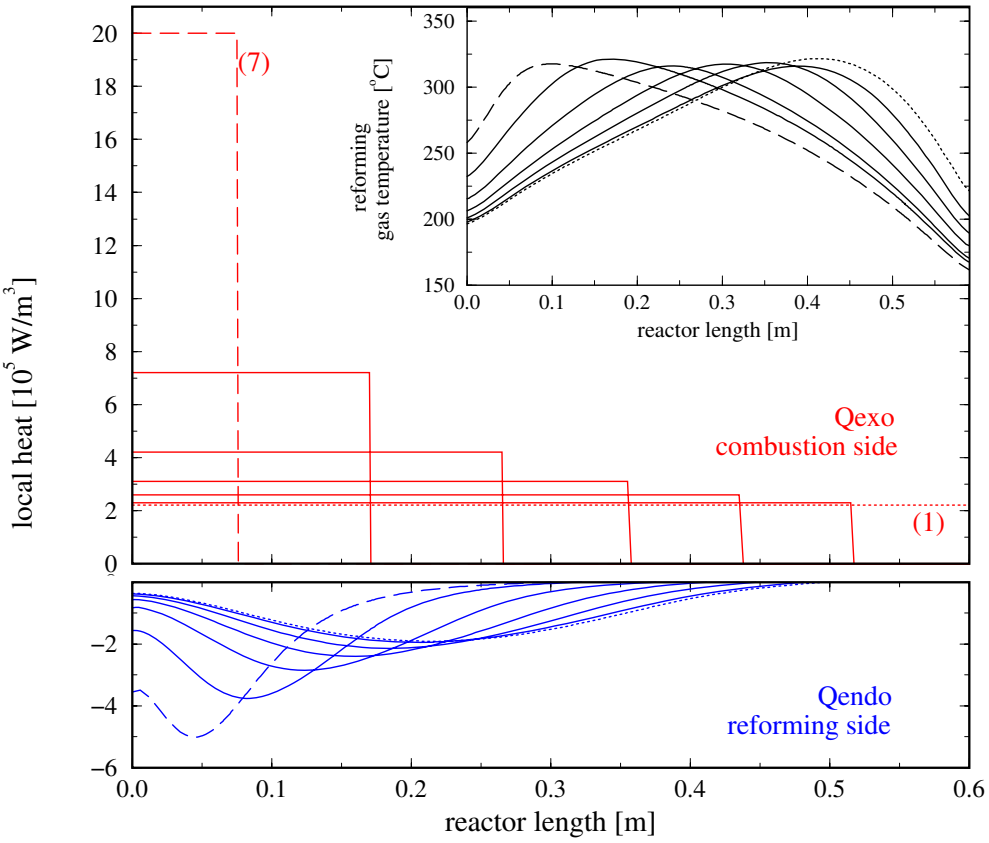

Figure 6.2: Variable heat production on the reforming side (top) and resultant heat requirement on the reforming side (bottom) for a total methanol conversion. Axial gas temperature profile on the reforming side (top-right).

Since most of the heat is used for reaction (along the center of the reactor) and it is not lost through the reactor ends the total amount of heat introduced (the total area under the local heat input) is about constant in the seven cases considered.

It can be noticed that homogeneously distributed heat production over the entire reactor length (dotted curve) leads to a slowly increasing reforming gas temperature profile, which also means a slow-going methanol conversion, utilizing almost all the reforming region. In the middle of the reforming length about 80 % of the fed methanol has been already converted. Simultaneously, CO is formed in the same gradual way.

Once the heat-generating zone is concentrated near the reactor entrance higher methanol conversion values are earlier achieved. For example, in the case where only 1/8 of the reactor length is used (Run 7, dashed lines) almost total conversion is already achieved in the middle of the reactor. Here the CO fraction rises faster, but because of the decreasing temperature profile to the end of the reactor, a substantial amount of CO formed can be converted by means of the water-gas shift reaction.

In other words, maximum methanol conversions can be easily reached by managing the amount of the heat produced on the combustion side. In all cases, methanol conversion reaches total conversion. Nevertheless the associated CO produced during the reforming

run	start	end	local heat		X_{MeOH}	y_{CO}
	[m]	[m]	[W/m^3]	[W]	[-]	[-]
1 (dotted line)	0	0.600	$2.2{\cdot}10^5$	265	0.9980	0.0299
2	0	0.515	$2.3{\cdot}10^5$	238	0.9962	0.0280
3	0	0.435	$2.6{\cdot}10^5$	227	0.9966	0.0275
4	0	0.355	$3.1{\cdot}10^5$	221	0.9959	0.0260
5	0	0.265	$4.2{\cdot}10^5$	224	0.9954	0.0245
6	0	0.170	$7.2{\cdot}10^5$	246	0.9976	0.0244
7 (dashed line)	0	0.075	$20.0{\cdot}10^5$	301	0.9961	0.0227

Table 6.2: Variation of the heat-producing zone and heat released on the combustion side, and the respective resultant values for methanol conversion and CO production on the reforming side.

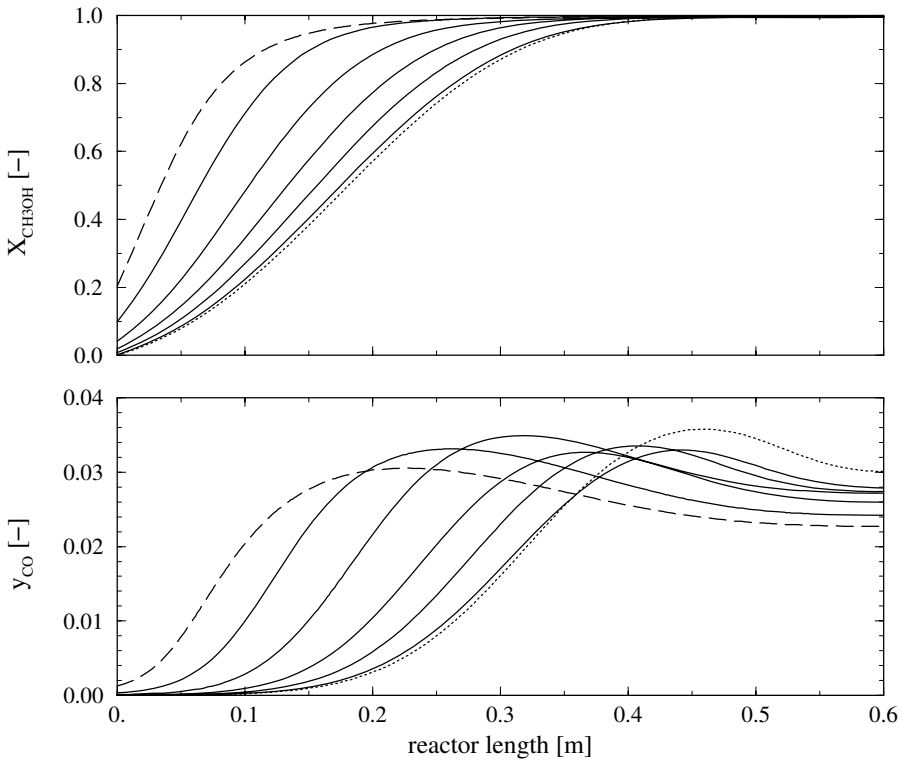

Figure 6.3: Progression of the methanol conversion (top) and CO formation (bottom) over the reactor length for a fix homogeneously distributed heat production on the combustion side.

reaction can be only influenced by the local temperature. CO can be removed by setting lower temperature levels (for example in the second half of the reactor) and letting the

water-gas shift reaction reach its equilibrium level. This requires of course sufficient reactor length.

It is recommended to generate the most of the required heat near the reactor entrance and in the first third of the reactor length so that total methanol conversion is reached along this zone and afterwards the produced CO can be removed by water-gas shift reaction at lower operating temperatures.

A further conclusion from this section is that the assumed reactor length of 0.6 m seems to be sufficient for achieving total methanol conversion under the considered operating conditions. The results obtained in this kinetic study are strictly related to the activity/selectivity presented by the catalyst used. This has to be taken into account in the scaling-up strategy.

6.1.2.2 Optimal Localization of the Combustion Zone

In the following, narrow catalytic zones are placed on the combustion side. The oxidation of hydrogen takes place over these catalytic zones, and a point-like heat peak results from the complete conversion of hydrogen with the oxygen present in the feed air (see Figure 6.4). The positions of the catalyst layers are systematically varied in z-direction. Simulations are performed to evaluate the influence of this point heat source on the methanol conversion and CO selectivity. The operating conditions are summarized in Table 6.3.

	parameter	value
reforming side		
	feed mass flow rate	304.15 $\frac{g}{h}$
	S/M ratio	1.30 $\frac{mol}{mol}$
	feed gas temperature	150 °C
combustion side		
	feed volumetric flow rate	2.5 slm
	feed volumetric fraction of air	1.0 [-]
	feed volumetric fraction of hydrogen	0.0 [-]
	feed gas temperature	100 °C
side injection stream		
	volumetric flow rate	0.70 slm
	volumetric fraction of hydrogen	1.0 [-]
	gas temperature	20 °C

Table 6.3: General operating conditions used for simulations of the 1-kW reformer with one single combustion zone.

The position of one single reaction zone on the combustion side was systematically varied in axial direction for this evaluation. Selected positions for the combustion catalyst slice,

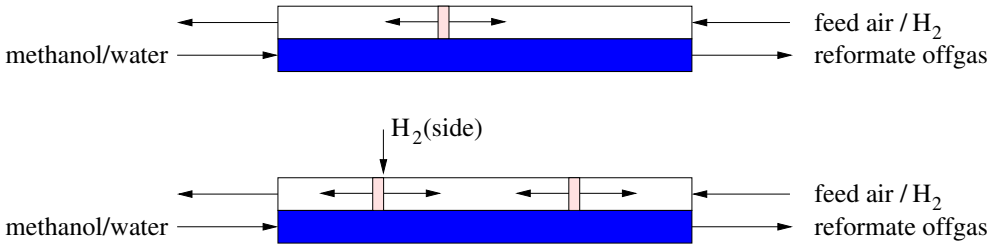

Figure 6.4: Sketch of the positioning of the catalyst layers for the simulation studies. *Top:* one single combustion zone; *bottom:* multiple combustion zones.

as well as experimental results are summarized in Table 6.4. In Figure 6.5 the resulting temperature and methanol conversion profiles are plotted over the reactor axial coordinate.

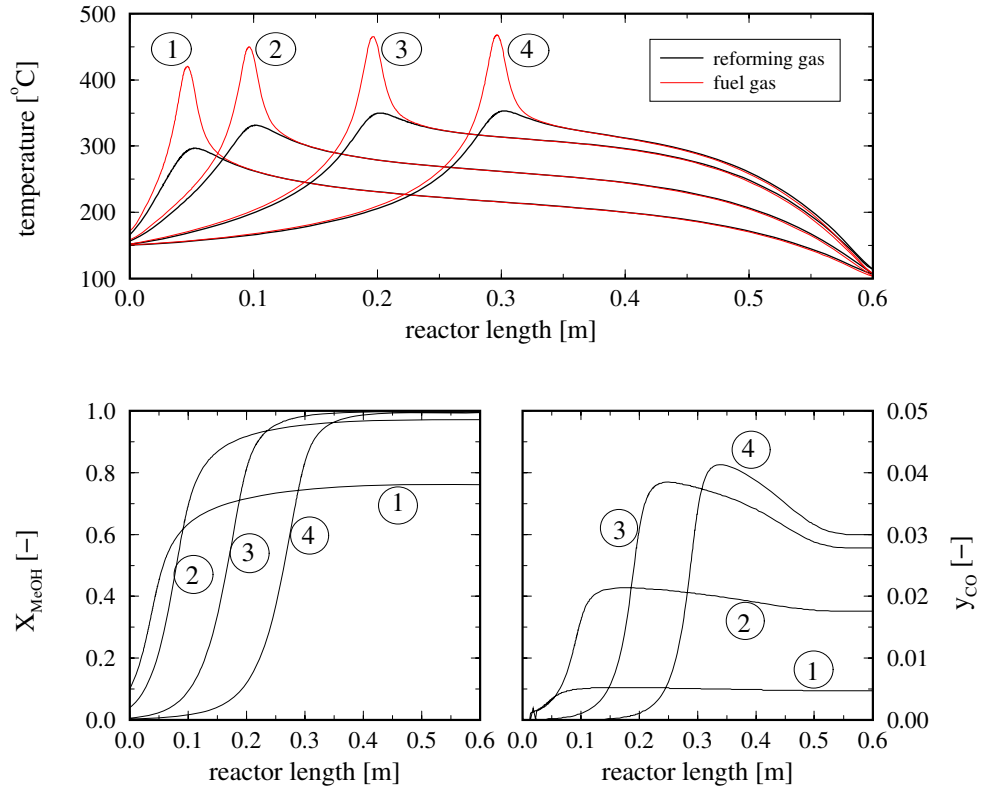

Figure 6.5: Simulation results for SRM supported by a single reaction zone on the combustion side. Reaction parameters in Table 6.3.

As observed in the previous evaluation, the axial position of the hydrogen side feed directly influences the methanol conversion. With a single fuel-gas injection, the temperature profile displays a steep hot spot at the injection point in the combustion channel. A similar smaller hot spot is also observed on the reforming side. A temperature difference between combustion and reforming gas of about 120 °C is observed around the combustion zone. Outside of the combustion zone, the gas temperatures in the reforming and combustion channels rapidly approach each other, demonstrating the excellent heat transfer of the proposed reactor design.

run number	1	2	3	4
$Z_{\ side\ injection}$ [m]	0.05	0.10	0.20	0.30
X_{MeOH} [%]	76.18	97.19	99.81	99.52
y_{CO} [%]	0.47	1.76	2.78	3.00

Table 6.4: Influence of the position of one single combustion zone on the methanol conversion and CO concentration (referred to Figure 6.5).

When placing the combustion zone near the reactor entrance (profile 1 in Figure 6.5) lower methanol conversion is observed. The reasons for this behavior is the short heat exchange length left from the hot spot, where the heat of the combustion gas cannot be sufficiently transferred to the entering reformer feed. Therefore the position of this catalytic zone will be not recommended. On the other hand, methanol conversions above 97 % can be predicted with one single fuel-gas injection when placing the combustion zone at a sufficient distance from the methanol/water mixture entrance (see profile 2-4 in Figure 6.5), and when the average reforming gas temperature nears the 280-300 °C. Reforming gas temperature peaks lying above 300 °C can be directly associated with total methanol conversion, but result also in higher CO concentrations. In addition, CO concentration increases the further to the right the combustion reaction takes place. Therefore, the position of the combustion reaction was not evaluated for $z \geq 0.3\ m$.

	parameter	value
reforming side		
	feed mass flow rate	304.15 $\frac{g}{h}$
	S/M ratio	1.30 $\frac{mol}{mol}$
	feed gas temperature	150 °C
combustion side		
	feed volumetric flow rate	2.5 slm
	feed volumetric fraction of air	0.8772 [-]
	feed volumetric fraction of hydrogen	0.1228 [-]
	feed gas temperature	100 °C
side injection stream		
	volumetric flow rate	0.70 slm
	volumetric fraction of hydrogen	1.0 [-]
	gas temperature	20 °C

Table 6.5: General operating conditions used for simulations of the 1-kW$_{th}$ reformer with multiple combustion zones.

Multiple fuel-gas injections were also evaluated: Here it was assumed that a portion of the hydrogen enters the reactor with the combustion air (in excess) and is completely converted

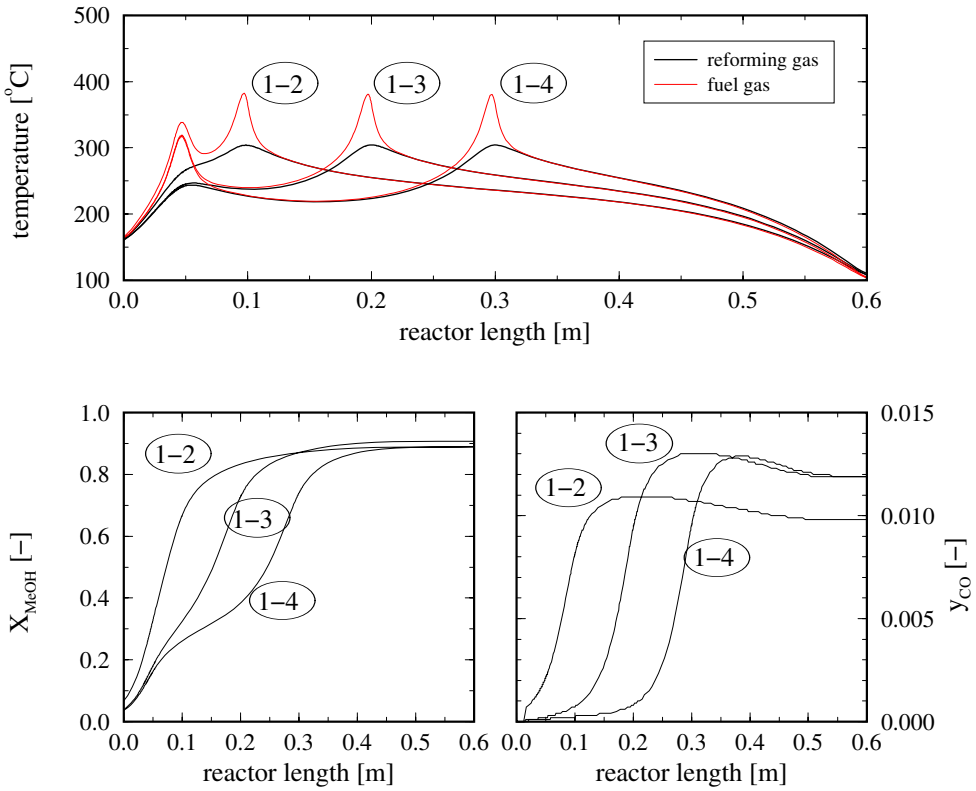

Figure 6.6: Simulation results for SRM supported by a split combustion reaction (variable from right to left: location of first combustion zone; second reaction zone fixed at 0.05 m). Reaction parameters in Table 6.5.

at a first catalytic zone, while the rest of the hydrogen is side-fed directly to a second catalyst layer located at a position further downstream. Reaction parameters are summarized in Table 6.5.

In the first simulations the position of the right combustion zone is varied, whilst the second catalyst layer is fixed at $z = 0.05\ m$. Reaction conditions are set to those evaluated in the preceding section (see Table 6.3). Figure 6.6 shows the simulation results for such a split combustion zone. A generally better effect is observed for the distributed hydrogen combustion. The hot spot temperatures compared to only one reaction zone can be strongly reduced from about 120 °C to 70 °C.

Mean reforming gas temperatures decrease compared to the previous setup with one single combustion zone ($\approx$ 250 °C), leading to lower methanol conversion of only 90 %. As in profile (1) of Figure 6.5 this is a consequence of the reduced energy recovery in the left heat exchange section. The distance between both combustion zones does not influence the methanol conversion significantly, but increases CO exit concentration if the hydrogen side feed is too far to the right. Two close-placed combustion zones at the reformer entrance allow for a faster cooling down of the reforming gas, leading to a deeper CO transformation via water-gas shift reaction. The wider the distance between both combustion zones is set, the higher remains the mean temperature level at the reactor end, and the less the possibility of CO conversion by water-gas shift reaction.

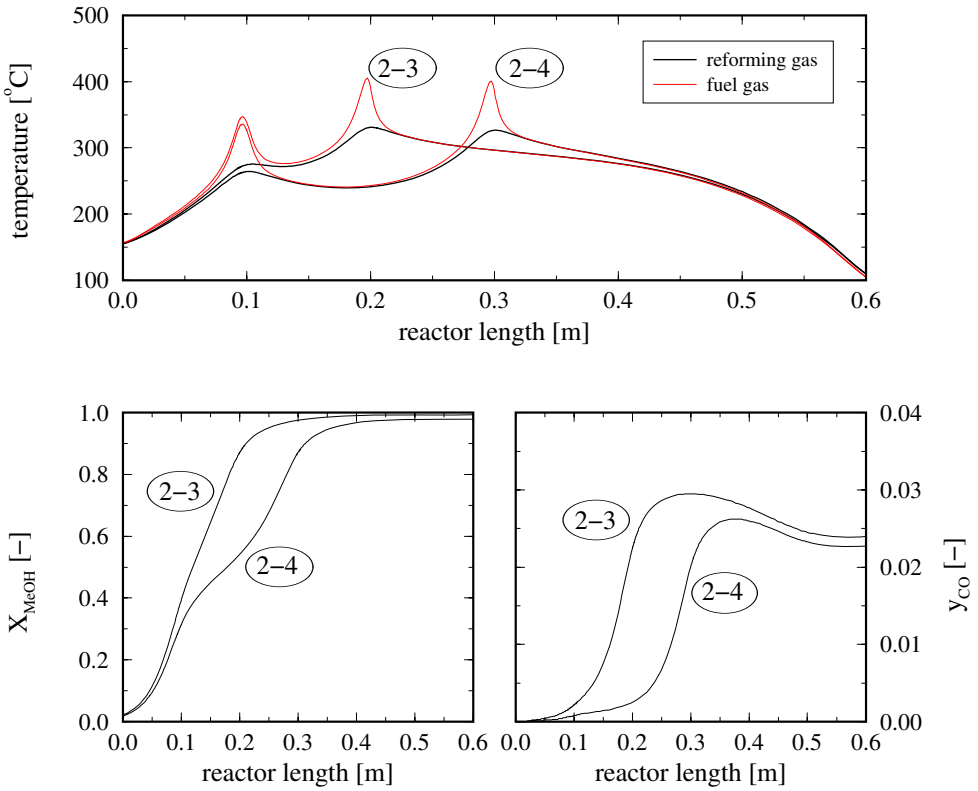

Figure 6.7: Simulation results for SRM supported by a split combustion reaction (variable from right to left: location of first combustion zone; second reaction zone fixed at 0.10 m). Reaction parameters in Table 6.5.

run number	**1-2**	**1-3**	**1-4**	**2-3**	**2-4**	**3-4**
X_{MeOH} [%]	88.95	90.74	88.81	99.33	97.85	99.82
y_{CO} [%]	0.98	1.19	1.19	2.40	2.27	3.04

Table 6.6: Influence of the position of two independent combustion zones on the methanol conversion and CO concentration (referred to Figures 6.6-6.8).

A placement of the combustion zone more to the right improves heat recovery in the left heat exchange section and hence increases the methanol conversion. This can be seen in the simulation results depicted in Figures 6.7 and 6.8, and listed in Table 6.6. But again CO increases if the temperature on the right-hand side is higher. The compromise between maximum methanol conversion and minimum CO concentration in reformate remains critical.

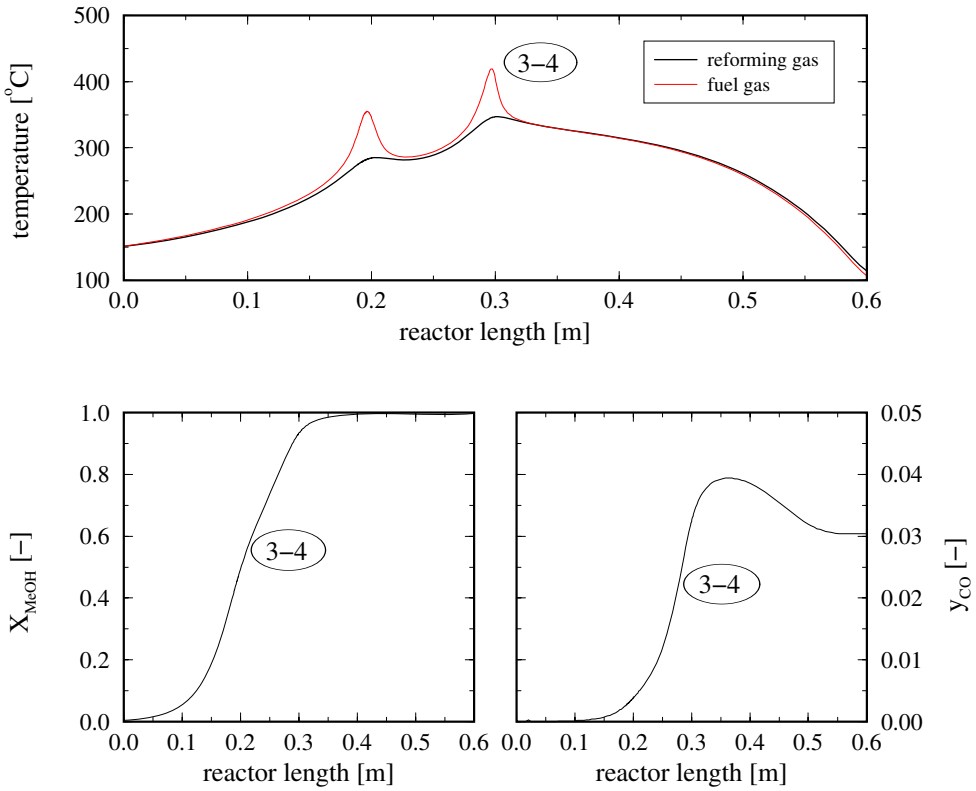

Figure 6.8: Simulation results for SRM supported by a split combustion reaction (variable from right to left: location of first combustion zone; second reaction zone fixed at 0.20 m). Reaction parameters in Table 6.5.

Closing Remark

The simulation studies on the optimal placement of the combustion zone show that a first catalytic combustion section should be installed not to far from the entrance of the methanol/water mixture, so that most of the methanol conversion takes place in the first one-third of the reactor and the rest can be used for the water-gas shift reaction. The second combustion zone should be placed near the reactor center. Based on the simulation results, two reaction zones on the combustion side were chosen for the following studies, placed at $z_1 = 0.1\,m$ and $z_2 = 0.3\,m$.

6.1.2.3 Influence of the Feed Temperatures

Results on the simulations for determining the influence of the feed temperatures are presented in this section. Simulated reaction conditions were taken from the previous studies (see Table 6.5). The feed temperature for the methanol/water mixture was systematically varied from T^{+}_{ref} = 100 to 250 °C. The lower limit was chosen so that it is higher than the boiling point of the higher boiling compound (water). Simulations results are presented in Table 6.7 and in Figure 6.9.

run number	**1**	**2**	**3**	**4**
T^{+}_{ref} [°C]	100	150	200	250
X_{MeOH} [%]	93.01	98.05	99.96	100.00
y_{CO} [%]	1.56	2.31	3.21	4.21

Table 6.7: Influence of the reforming gas feed temperature on the methanol conversion and CO concentration in reformate (referred to Figure 6.9).

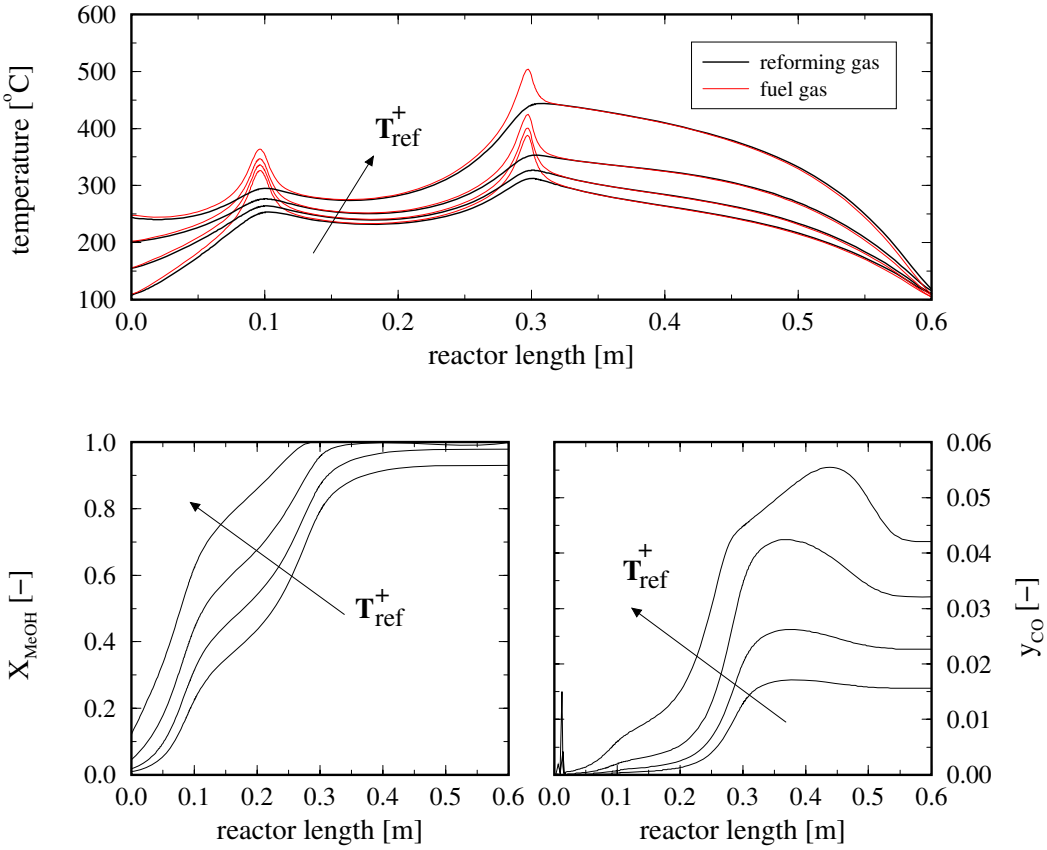

Figure 6.9: Effect of the methanol/water feed temperature on the SRM reaction performance in the folded-sheet reformer.

It can be seen that higher feed temperatures lead to a higher methanol conversion around the reactor entrance. The conversion curves become steeper and total methanol conversion is

achieved faster. In an extreme case, where the methanol/water feed temperature is set higher than 200 °C, methanol can be completely converted before the first one half of the reactor length. Here the second combustion zone is obviously of no use since it only keeps the right-hand side temperature high, which increases CO formation due to reverse water-gas shift.

Since a high preheating temperature requires an extended heat exchanger before the reaction section, a methanol/water feed temperature of 150 °C was chosen as design parameter for next optimization steps.

The variation of the temperature of the feed air on the combustion side shows a less-pronounced effect on the methanol conversion and CO formation. As the fuel cell anode off-gas temperature ranges between 70 and 100 °C and considering that this stream can lose energy before entering the hydrogen processor, the temperature for the feed stream on the combustion side was set to 50 °C for the next simulation studies.

6.1.2.4 Influence of the Heat Capacity Flux Ratio

Different flow rates can be set in the counter-current reformer on both the reforming and combustion side, leading to different heat transfer conditions. The influence of this variable is found to be adequately quantified by expressing the mass flow rate in terms of the heat capacity flux ratio. For this study the heat capacity flux ratio is defined from the mean values as follows:

$$MCP = \frac{(\dot{m}c_p)_{fg}}{(\dot{m}c_p)_{ref}}, \tag{6.1}$$

where $\dot{m}$ denotes the overall mass flow rate of the corresponding process stream in $[\frac{kg}{h}]$ and c_p the thermal heat capacity of the stream in $[\frac{kJ}{kg}]$. As reference temperature for calculations, a mean process temperature of 250 °C for both process streams is chosen.

Reaction conditions are summarized in Table 6.8. *The Heat capacity flux ratio is varied by setting different feed air volumetric flow rates*.

In Table 6.9 the volumetric flow rate of the feed air and the resulting heat capacity flux ratio are given, as well as some general simulation results. In Figure 6.10 axial temperature profiles for the reforming and combustion streams are plotted. Methanol conversion and CO concentration profiles are also displayed.

As can be seen in Figure 6.10 an increase of the heat capacity ratio MCP from low to high values has a substantial influence on the temperature profiles at the left and the right end of the reactor where primarily heat exchange between the hot leaving and the cold entering streams take place.

At low MCP values (low combustion side air flow) the entering air is heated up rapidly to the reforming gas temperature but cannot cool down the reformate sufficiently well, so some of the heat content of the reformate is lost over the right end of the reactor.

At the left side the leaving exhaust is rapidly cooled down by the entering reforming feed,

	parameter	value
reforming side		
	feed mass flow rate	304.15 $\frac{g}{h}$
	S/M ratio	1.30 $\frac{mol}{mol}$
	feed gas temperature	150 °C
combustion side		
	hydrogen feed volumetric flow rate	0.35 slm
	feed gas temperature	50 °C
side injection stream		
	volumetric flow rate	0.35 slm
	volumetric fraction of hydrogen	1.0 [-]
	gas temperature	20 °C

Table 6.8: Operating conditions used for simulations of the influence of the heat capacity flux ratio.

run number	**1**	**2**	**3**	**4**	**5**	**6**
$\dot{V}_{air}$ $[slm]$	0.3	2.5	5.0	10.0	15.0	20.0
MCP [-]	0.05	0.21	0.41	0.83	1.64	1.66
X_{MeOH} [%]	97.22	97.96	98.12	95.04	84.39	64.68
y_{CO} [%]	2.16	2.36	2.48	2.15	1.08	0.30

Table 6.9: Influence of the feed air volumetric flow rate on the methanol conversion and CO concentration in reformate (referred to Figure 6.10).

so no heat is lost at this side.

If MCP approaches 1.0 (MCP = 0.83 in Table 6.9), optimal heat exchange is achieved at the right side with constant slope temperature profiles in the heat exchange section. Constant slope temperature profiles are also obtained at the left side but since the left side heat exchange section is much shorter, no enough heat is recovered here and methanol conversion is somewhat lower than for case 3 with MCP = 0.41. This trend accelerates if MCP increases further (case 5 and 6 in Table 6.9), causing a rapid decrease in methanol conversion.

In addition, the right-side temperature maximum decreases at high MCP values since the right end of the reactor is cooled down so that no all of the fuel feed reacts at the right combustion zone, as can be seen from the shape of the temperature profiles in Figure 6.10.

Based on these results, a volumetric flow rate of combustion air between 2.5 and 5.0 slm ($MCP = 0.41 - 0.83$) is proposed for the design of the 1-kW folded-sheet reformer and for the following simulation studies.

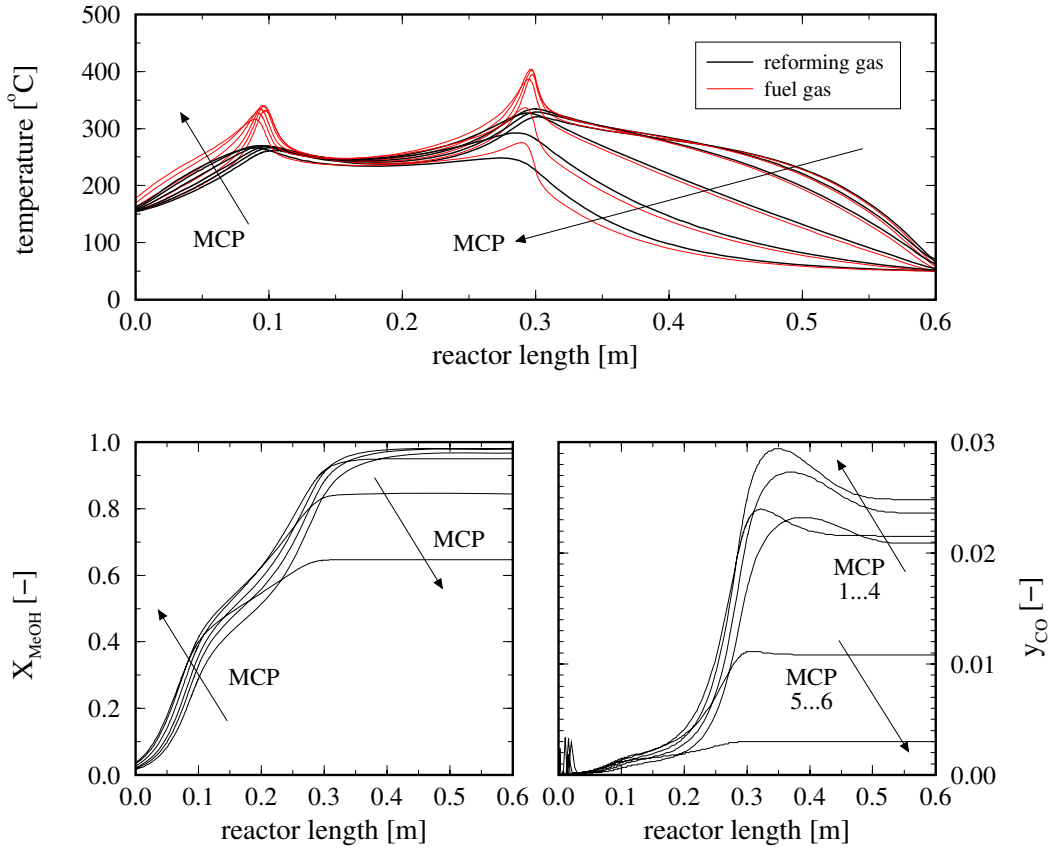

Figure 6.10: Influence of the heat capacity flux ratio (combustion side / reforming side) on the SRM reaction performance. Reaction parameters in Table 6.8.

6.1.3 Experimental Proof of Concept

Based on the design criteria from the previous evaluations, a folded-sheet reactor unit for producing a thermal equivalent amount of hydrogen of 1 kW was successfully constructed and experimentally tested (see Figure F.2 in Appendix F). Results of the experimental evaluation are presented in the following.

6.1.3.1 Description of the Reformer Unit

Main geometrical parameters of the reformer unit are listed in Table 6.10. A general scheme of the 1-kW folded-sheet reactor is given in Figure 6.11.

	parameter	value
reforming channel	number of channels	5
	channel width	4.5 mm
	length of reforming catalyst	250 mm
	length of WGS catalyst	300 mm
combustion channel	number of channels	6
	channel width	1.2 mm
	position 1st reaction zone	100 mm
	position 2nd reaction zone	250 mm
reformer	reactor length	600 mm
	folded-sheet material	avesta [64]
	folded-sheet thickness	0.2 mm
	reactor casing thickness	3 mm

Table 6.10: Main geometrical parameters of the 1-kW reformer.

The core structure of the reformer is the metallic folded-sheet. Inert and catalytically coated spacers are placed inside the channels, as depicted in Figure 6.11. Methanol/water mixture (coming from the evaporation unit) enters the reformer at the bottom and flows vertically upwards. The vapor mixture first meets the steam reforming catalyst[3], where the most of the hydrogen production takes place. The products of this reaction enter a second catalytic section with a water-gas shift catalyst. Reformate leaves the reformer at the reactor top and is burned with air in a catalytic oxidation reactor.

On the combustion side a mixture of fresh-air (in excess) and fuel-gas flows into the reformer at the apparatus top. This mixture first exchanges heat with the outgoing reformate and then reacts at the first catalyst zone. Later, additional fuel gas is side fed to the air stream and reacts at the second catalyst slice.

[3] According to the catalyst provider, the catalytic properties are similar to those of [4].

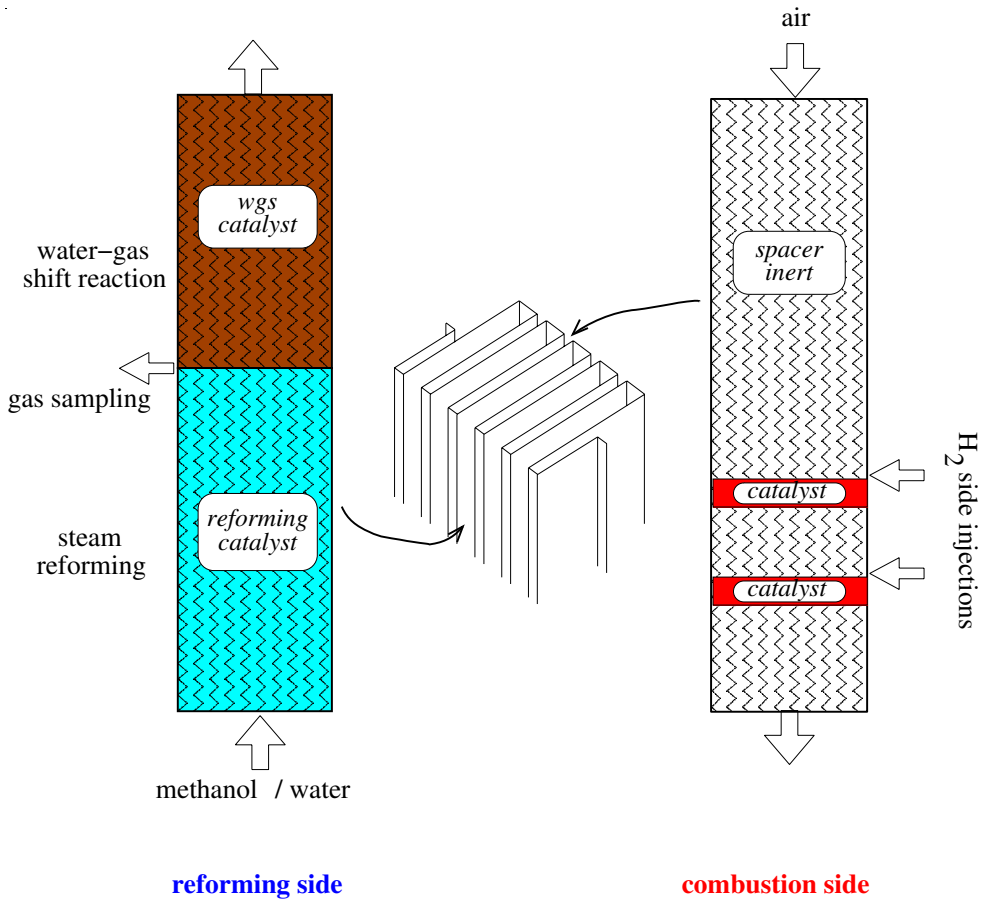

Figure 6.11: Scheme of the catalyst/spacer distribution on the reforming and combustion side for the 1-kW reformer.

6.1.3.2 Description of the Experimental Set-up

As depicted in Figure 6.12 the experimental setup for evaluating the operational performance of the folded-sheet reformer is principally similar to the set-up of Figure 4.1 and consists of feed, reaction, analytic and after-treatment sections. Methanol and water are stored in pressure tanks and are independently fed to the reactor. Each single flow rate is controlled by liquid-flow devices. Methanol and water are evaporated by two electric evaporator units and enter the reformer together. From the off-gas unreacted methanol and water are separated. The main gas stream is first analyzed (determination of the molar gas composition) and finally burned in a catalytic monolith combustor. On the combustion side fresh air enters the reactor counter-currently and reacts catalytically with hydrogen over catalyst slices. Combustion hydrogen is side-fed by means of capillary injection ports. In some cases the amount of hydrogen dosed into the reactor was limited by the maximum capacity of the mass-flow-controllers and could deviate from the optimized parameters of the simulation. Further details on the periphery of the experimental set-up regarding equipment specification and process communication are described in detail in Section 4.1.1.

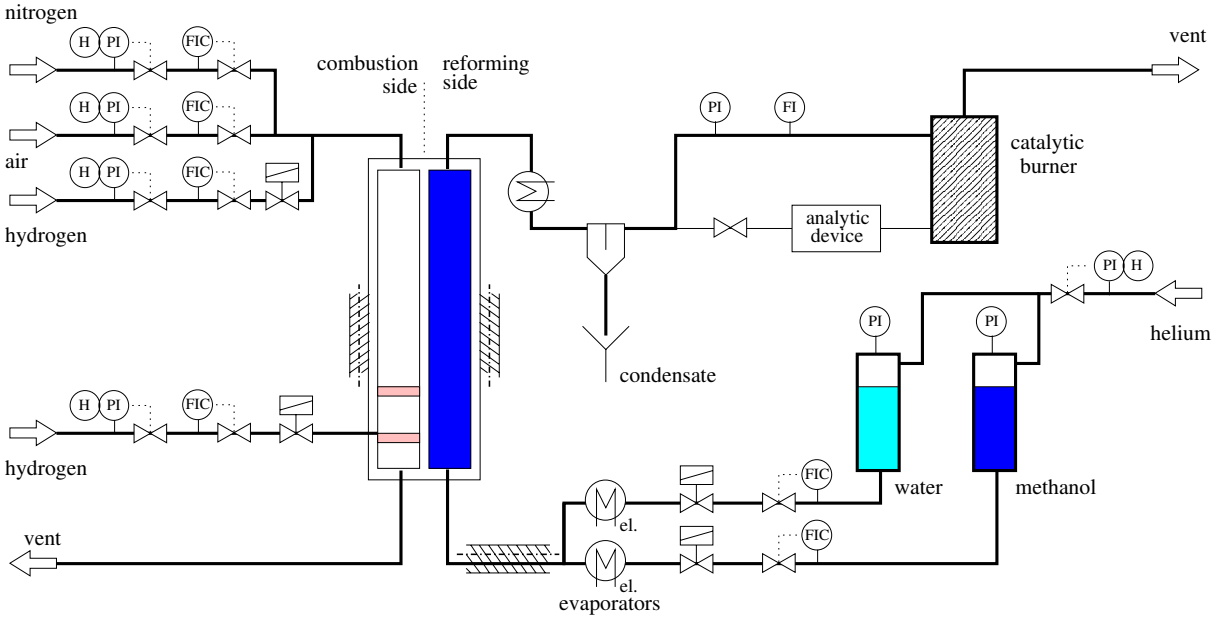

Figure 6.12: Experimental setup for testing the 1-kW folded-sheet reformer.

6.1.3.3 Determination of the Catalyst Activity

Since the reforming and the WGS catalyst coated at the spacers was different from the BASF K3-110 catalyst tested in Chapter 4, an evaluation of the activity and selectivity of the new catalyst was performed first. Initial experiments with the folded sheet reactor were performed using external electrical heating instead of catalytically heat generation on the combustion side.

run	T_w	**reformate gas composition**			**output gas flow**	X_{MeOH}
	[°C]	y_{H_2}	y_{CO_2}	y_{CO}	$[slm]$	[%]
P1	250	0.716	0.265	0.018	3.51	49.2
P2	265	0.718	0.261	0.021	4.45	62.0
P3	290	0.716	0.258	0.026	6.22	87.2

Table 6.11: Experiments conditions for the determination of the catalyst activity (const. electrical heating). Reaction parameters: $\dot{m}_{CH_3OH,ref} = 158.0\ g/h, \dot{m}_{H_2O,ref} = 121\ g/h, \dot{V}^{+}_{N_2,fg} = 1\ slm.$

Here methanol and water vapors were fed to the reactor on the reforming side at $T_w \approx 150$ °C, whereas only nitrogen flowed counter currently on the combustion side. Two independent electrical heating bands were wrapped around the reformer so that nearly isothermal conditions could be obtained. This allowed evaluating the reaction performance and the catalyst activity. With an axially movable thermocouple, the gas temperature profile on the reforming side could be measured. Reaction conditions and experimental results are

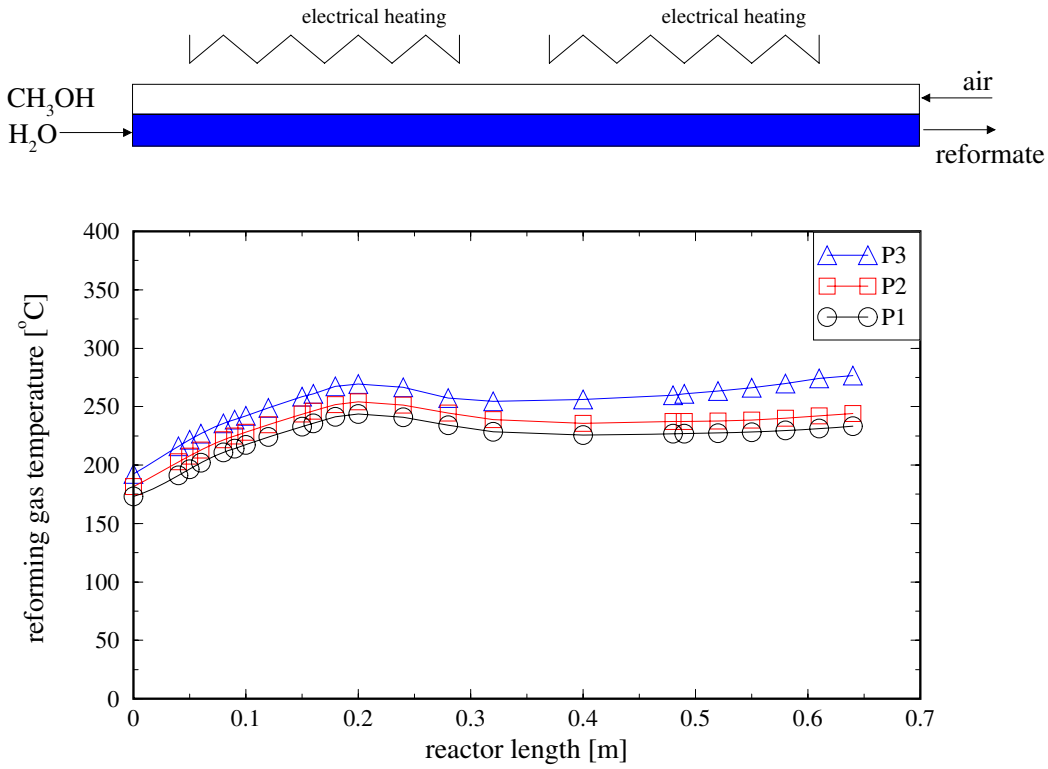

Figure 6.13: Measured reforming gas temperature profiles for steam reforming of methanol in the folded-sheet reactor at different values of electrical heating. Reaction conditions: see Table 6.11.

presented in Figure 6.13 and Table 6.11.

Three operating temperatures (T_w) were evaluated. It can be seen that higher temperatures lead to a higher methanol conversion and an increase of the total output flow rate as a result of the volume-increasing reaction. But also the CO concentration in the reformate tends to increase up to values above 2.5 $vol\%$ without the reaction reaching complete methanol conversion.

This behavior is a clear sign that the employed catalyst is not as active and selective as the BASF catalyst. Higher wall temperatures will be required in order to obtain better methanol conversions; but the CO selectivity would then suffer further.

In the following section, hydrogen is burned on the combustion side for supplying the required energy for the reforming side.

6.1.3.4 Variable Hydrogen Combustion - Fixed Electrical Heating

Similar reaction conditions as evaluated in the section above were adjusted for testing a reaction zone on the combustion side for generating the reaction heat for the reforming stage. The scheme of the experimental setup is depicted in Figure 6.14. On the reforming side a

mixture of methanol/water vapor enters the reactor at $T^{+}_{ref} \approx 150$ °C. On the combustion side fresh air in excess flows through the channels and hydrogen is fed via one side-injection so that the catalytic oxidation reaction takes place at the catalyst slice in the first half of the reactor. Along the second half of the reformer electrical heating keeps a constant wall temperature of about 200 °C. The amount of hydrogen dosed via side-injection is adjusted so that the generated heat can be varied arbitrarily. The experimental results are given in Table 6.12 and Figure 6.14.

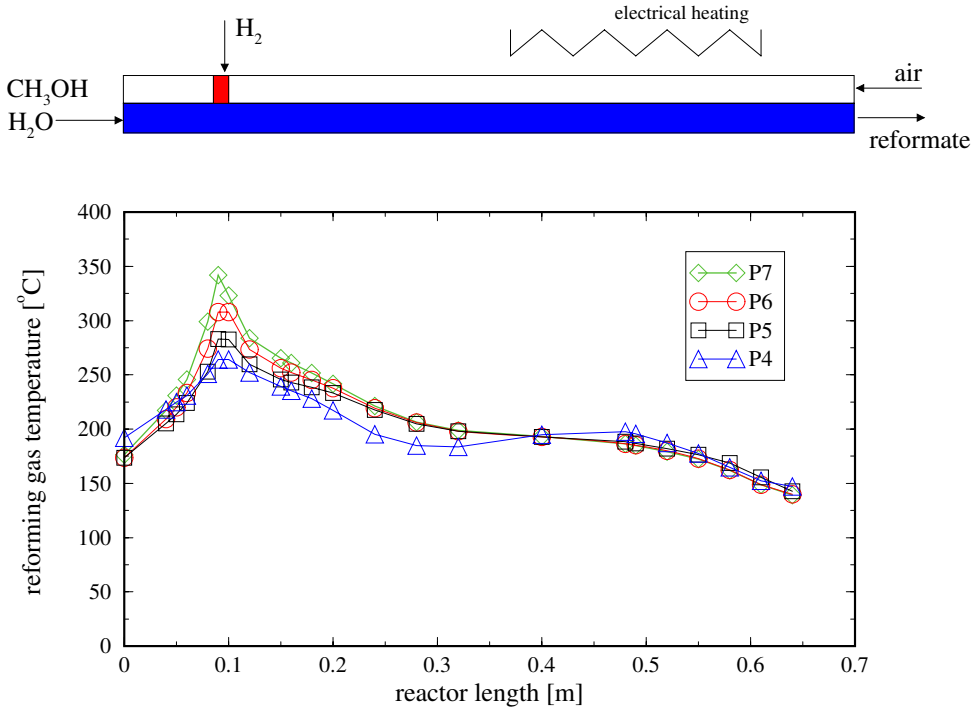

Figure 6.14: Combination of hydrogen oxidation on the combustion side (1 combustion zone) with methanol reforming, supported by constant electrical heating along the second half of the reactor. Measured reforming gas temperature profile on the reforming side. Reaction conditions: see Table 6.12.

It can be seen that the gas temperature profile at the reforming side exhibits a strong hot-spot at the combustion zone. As the hydrogen side feed is systematically increased (runs P4 to P7), the CO content in reformate and the methanol conversion increase as well.

Even with the highest hydrogen feed only 56 % methanol conversion with a CO exit concentration of 3.2 $vol\%$ are obtained. The high CO concentration is obviously a result of the high hot spot temperature and the low catalyst selectivity. The low methanol conversion is a result of the low catalyst activity and the low temperature levels along the second half of the reformer.

Further experimental evaluation of the reformer performance, supported by electrical heating is shown in Appendix D.

run	$\dot{V}^{side}_{H_2,fg}$	reformate gas composition			output gas flow	X_{MeOH}
	$[slm]$	y_{H_2}	y_{CO_2}	y_{CO}	$[slm]$	$[\%]$
P4	0.1	0.727	0.254	0.019	1.72	22.6
P5	0.2	0.725	0.250	0.025	2.85	37.8
P6	0.3	0.725	0.247	0.028	3.55	47.1
P7	0.4	0.723	0.245	0.032	4.22	56.3

Table 6.12: Experimental conditions for test runs according to Figure 6.14. Reaction parameters: $\dot{m}_{CH_3OH,ref} = 158.0\ g/h$, $\dot{m}_{H_2O,ref} = 121\ g/h$, $\dot{V}^{+}_{air,fg} = 7.5\ slm$, T_{w2} = 200 °C.

6.1.3.5 Two Combustion Zones: Combustion of H_2 and C_3H_6

The benefits of two reaction zones on the combustion side to generate the necessary heat for the steam-reforming reaction were studied using the folded-sheet reactor under the configuration depicted in Figure 6.15. Initially, hydrogen was fed at both places, inlet and side injection port. The hydrogen fed together with air reacted immediately in the reactor entrance where normally inert spacers were installed. This behavior suggested that some active catalyst dust may be present in this zone. For testing the reactor concept, experiments with propylene, C_3H_6 as fuel gas, which has a higher ignition temperature were therefore carried out.

Again fresh air in excess enters the reactor with propylene (C_3H_6), counter-currently to the methanol/water mixture. In the first reaction zone propylene reacts with oxygen form the air and in the second hydrogen does. Both fuel-gas flow rates were varied in order to obtain different temperature profiles on the reforming side (runs P14 to P16). Results are presented in Table 6.13 and Figure 6.15.

run	$\dot{V}^{side}_{H_2}$	$\dot{V}^{side}_{C_3H_6}$	reformate gas composition			output gas flow	X_{MeOH}
	$[slm]$	$[slm]$	y_{H_2}	y_{CO_2}	y_{CO}	$[slm]$	$[\%]$
P14	0.28	0.03	0.722	0.227	0.051	4.18	57.3
P15	0.28	0.06	0.721	0.223	0.056	4.45	61.9
P16	0.25	0.07	0.713	0.224	0.063	5.59	79.1

Table 6.13: Experimental results on the evaluation of two combustion zones (H_2 and C_3H_6) on the combustion side. Reaction parameters: $\dot{m}_{CH_3OH,ref} = 158.0\ g/h$, $\dot{m}_{H_2O,ref} = 121\ g/h$, $\dot{V}^{+}_{air,fg} = 7.5\ slm$.

The results show that multiple side feed combustion, simulated in Figure 6.7, can be well realized in the folded-sheet reactor set-up. It leads to a high temperature plateau and hence to

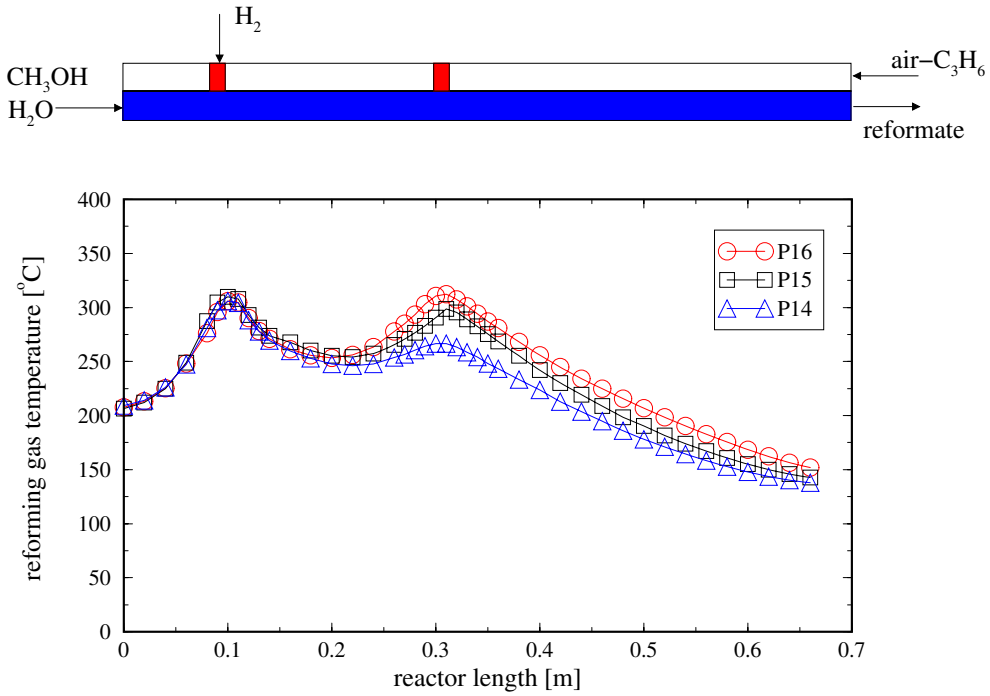

Figure 6.15: Measured reforming gas temperature profile. Variable split reaction zones on the combustion side: hydrogen combustion + propylene combustion. Reaction conditions: see Table 6.13.

elevated methanol conversion. Again the actual conversion and selectivity values are hampered by the poor catalyst performance. It can be noticed in Figure 6.15 that the combustion of hydrogen results in a more spiky temperature peak than that of propylene. This points at the well-known fact that the hydrogen combustion reaction runs very fast compared to most of the hydrocarbon combustion reactions known.

6.1.3.6 Two Hydrogen Combustion Zones

Based upon the previous experiments a new reactor following the same principal design was manufactured. It was equipped with a new batch of reforming and WGS catalysts. The main different features of this reactor can be stated as follows:

- A new batch of reforming and WGS catalysts has been used.
- A sample port between the reforming and the WGS catalyst section has been installed at the reforming side to measure the gas composition after the reforming and after the WGS independently.
- The two combustion zones were moved closer together to obtain subsequently a longer decreasing temperature profile for an effective WGS reaction.

- For simplicity and to avoid undesired reactions outside of the catalyst regions two hydrogen side injection ports were installed. This time hydrogen can be independently dosed exactly in the combustion-catalyst zone.

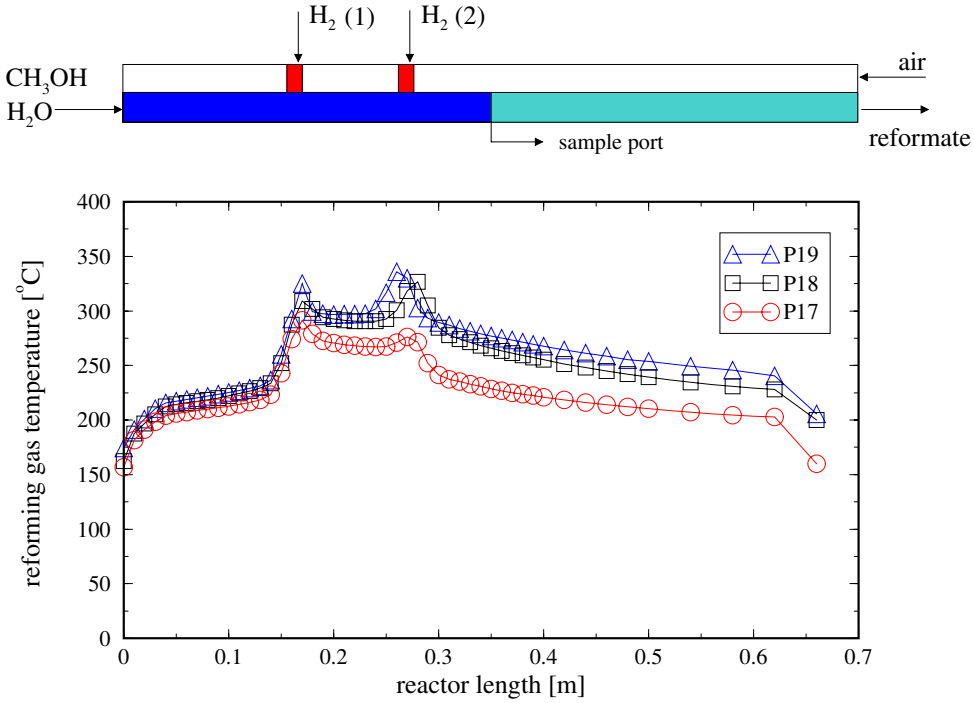

Figure 6.16: Measured reforming gas temperature profile. Variable split hydrogen oxidation on the combustion side. Reaction conditions: see Table 6.14.

A schematic drawing of the experimental setup is shown in upper zone of Figure 6.16.

run	$\dot{V}^{side}_{H_2,(1)}$	$\dot{V}^{side}_{H_2,(2)}$	**reformate gas composition**				**output gas flow**	X_{MeOH}
	$[slm]$	$[slm]$	y_{H_2}	y_{CO_2}	y_{CO}	y^{sample}_{CO}	$[slm]$	$[\%]$
P17	0.30	0.25	0.728	0.246	0.025	0.041	3.20	69.4
P18	0.35	0.30	0.736	0.237	0.026	0.044	3.90	81.9
P19	0.35	0.35	0.727	0.246	0.027	0.058	4.00	86.3

Table 6.14: Experimental results on the evaluation of two independent hydrogen combustion zones on the combustion side. Reaction parameters: $\dot{m}_{CH_3OH,ref} = 158.0\ g/h, \dot{m}_{H_2O,ref} = 121\ g/h, \dot{V}^{+}_{air,fg} = 7.5\ slm.$

Three different reaction conditions were used for evaluating the new catalyst. Operating conditions and experimental results on the reformate (gas) composition and methanol conversion are given in Table 6.14. Resulting temperature profiles of the reforming gas are plotted in Figure 6.16.

Again it can be recognized that the higher the heat input the better the methanol conversion. At temperature levels between 300 and 330 °C the methanol conversion reaches values around 86 % while the CO concentration in reformate remains as low as 2.6 $vol\%$. As seen from the sample port composition (y_{CO}^{side}) the strongly reduced mole fraction is a consequence of CO reduction in the WGS section. The WGS stage can reduce the produced CO by about 50 %, resulting in an acceptable CO-selectivity for the overall process.

6.1.3.7 Experiment vs. Simulation

Results of the experimental evaluation were compared with simulations stated previously. Figure 6.17 show graphically this comparison by means of temperature profiles of the reforming gas.

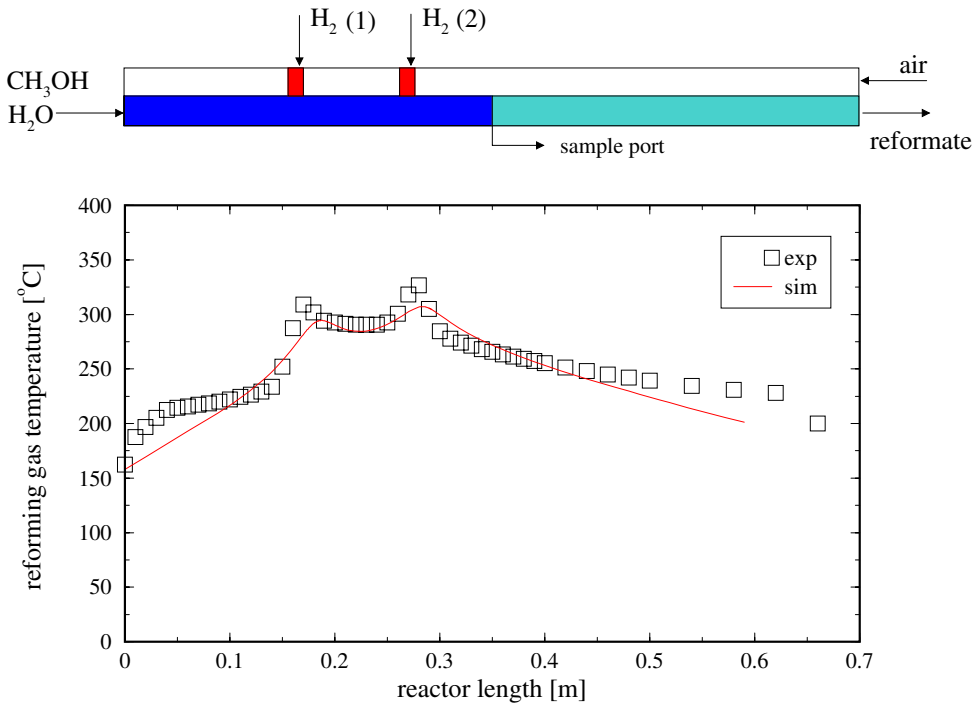

Figure 6.17: Comparison between experimental results with respective simulation. Reaction parameters of run P18 (see Table 6.14).

In general experiments are well reproduced by simulation. This means that the kinetic model developed for the fixed-bed reactor can be transferred to the folded sheet reformer and the catalyst employed in the folded-sheet reformer behaves similar to BASF K3-110.

A general good agreement between experiment and simulation results is observed (see Figure 6.17). Nevertheless the reforming gas temperature profile of the experiment run has a more flat slope than in the simulations at the reactor left end. This suggest that in the experimental reformer the hot combustion gas exit stream warms up the methanol/water feed more rapid than predicted by the model.

Closing Remark

The general applicability of the folded-sheet reactor concept for hydrogen production via steam-reforming of methanol was successfully demonstrated at laboratory scale. The performance of the reforming reaction can be easily controlled by adjusting the heat release on the combustion side, i.e. by controlling the fuel-gas feed. Hydrogen as well as propylene was employed as fuel gas, confirming the versatility and capability of the concept to work with different fuels.

6.2 Evaporation Studies

In this section the design and evaluation of a compact catalytically heated evaporator unit is presented and discussed. The evaporation unit for a methanol/water mixture was developed and tested with the aim to later be integrated into the folded-sheet SRM reactor.

Two folded-sheet evaporator units were the basis for the study: a small unit for visualization purposes and proof of principle, and a larger one for evaluating evaporation under real operating conditions.

6.2.1 Description of the Evaporation Unit

In both cases, the core structure of the evaporator is represented again by a metallic sheet of thickness 0.2 mm, folded in accordion form, resulting in 4 liquid/steam and 5 combustion chambers (see Figure 6.18 and Figure F.3 in Appendix F). On the combustion side the catalytic oxidation of hydrogen with oxygen (from the air) takes place to generate the heat necessary for the evaporation and superheating of the methanol/water mixture. The goal for the evaporation unit is a pulse-free total evaporation of the methanol/water mixture, leading to a constant vapor composition and flow rate for a broad spectrum of possible throughputs. To achieve this goal, experience from small scale electrically heated total evaporators developed at ICVT has been adopted [51]. This experience states that total evaporation should be performed in well-heated parallel micro-channels of <1 mm diameter and sufficient length. Such micro-channels have been processed from both sides into evaporation plates which completely fill the evaporation channels (Figure 6.18).

Metal wires coiled in spiral form are placed in each small diameter micro-channel to minimize ejection of liquid droplets.

To achieve a total evaporation and sufficient superheating of the vapor, the energy input is distributed over two combustion zones, one for the evaporation and one for the super heating (Figure 6.18, right). The evaporation can be controlled through the hydrogen side feed. For visual inspection of the success of evaporation the casing of the first version of the folded-sheet evaporator was equipped with a glass plate on one side (see Figure E.2 in Appendix E).

The second evaporator, conceived for evaporating larger amounts of liquid, has the same configuration as the “glass-plate” evaporator, but this time the number of evaporation channels was increased up to 21, and the number of combustion chambers to 22. The folded-foil thickness is 0.5 mm and the metallic casing with a cross section (base) of 80 mm x 40 mm is 2 mm thick. In Figure E.3 (Appendix E) the design drawing of this unit is shown.

6.2.2 Description of the Experimental Setup

A flowchart of the experimental setup for evaporation is given in Figure 6.19. In this set-up both the “glass-plate” for visualization and the up-scaled evaporator have been tested. Air

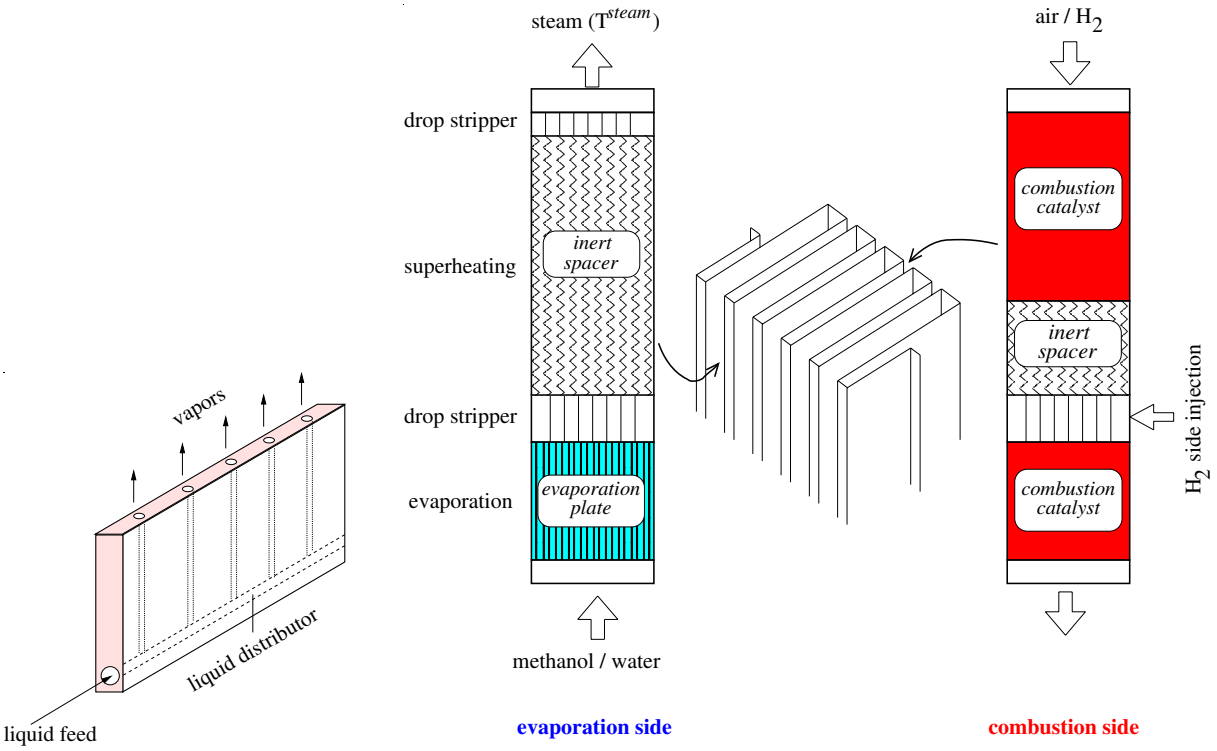

Figure 6.18: Details on the folded-sheet evaporator. *Left:* Sketch of an evaporation plate; *right:* Structuring of the evaporation and combustion channel in the counter-current folded-sheet evaporator.

and hydrogen are fed to the evaporator from the top at the combustion side by means of mass-flow controllers, as well. Additional hydrogen to the second reaction zone is added via side-feed. Methanol and water are stored in an open tank in prefixed proportions. From the tank bottom the mixture is fed to the evaporator by means of a piston pump. The superheated mixture from the evaporator is diluted with air and conducted (tempered at ca. 60-80 °C) to the analytical section. This consists of an anemometer sensor in parallel to a capacitive humidity sensor. With the anemometer sensor the flow velocity is measured, with the humidity sensor the composition of the mixture (% of water in the stream) is determined.

6.2.3 Description of the Data Acquisition Method

The capacitive humidity sensor of the company Ahlborn [65] consists of a dielectric which is able to adsorb humidity between two electrodes. The operational principle is based on the fact that water and/or water vapor has a higher dielectric constant than dry air ($\epsilon_{H_2O} = 81$; $\epsilon_{air} = 1.0$). An uptake of humidity thus causes (exactly the same as with a condenser) a change of the dielectric constants and thus a change of the capacity. A proportional voltage signal is transmitted by RS-232 to the laboratory PC.

The anemometer sensor of the company Dantec [66] is used to measure the constancy of the mass flow of steam produced. A certain disadvantage of the probe is its susceptibility to

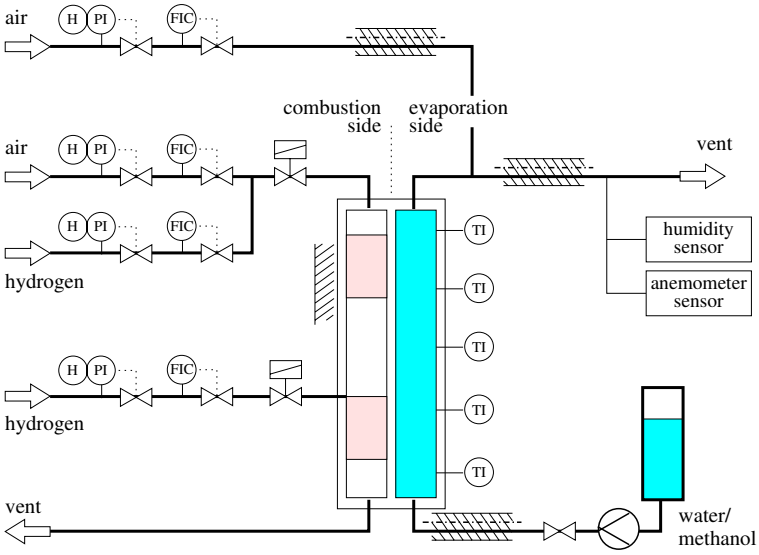

Figure 6.19: Flowchart of the experimental setup employed for evaporation studies.

re-condensation of the steam due to the very thin measuring gage. Drop condensation at the probe wire leads to falsified volt signals.

6.2.4 Experimental Evaluation

6.2.4.1 Preliminary Studies

Several preliminary experiments were carried out with the glass-plate evaporator using the setup and the unit configuration shown in Figures 6.18 and 6.19.

Previous work [67] has shown that it is not easy to carry out total evaporation experiments without pulsations in the outstream. The causes for such instabilities could be elucidated.

If the heat input into the evaporator plates is too strong, water tends to evaporate before entering the evaporation channels. This causes a geyser-like instability where the steam formed is blown out and replaced by cold water. After this water is sufficiently heated up and evaporates, the cycle starts again.

If the heat input through hydrogen combustion is too low, insufficient evaporation with a spray of tiny and re-condensing water droplets is formed.

Because of the heat losses from the evaporator unit to the surroundings the heat generated from the catalytic oxidation of hydrogen has to exceed the theoretical requirement by at least 20-30 %. When activating only one combustion zone along the evaporation section (near the liquid feed), recondensation problems were observed because the incoming cold air cools the outgoing steam.

Once the second combustion zone above the evaporation section is activated, the steam mixture flows out of the evaporator in superheated form. This second combustion zone helps

to compensate for the heat loses of the evaporator unit and avoids the cooling down effect of the cold-air inflow. Additionally, this superheating zone favors the heating of the steam up to the operating temperature of the next process step, i.e. the catalytic steam reforming reaction.

Since the evaporation studies have been performed with the aim of integrating the evaporator section into the steam reformer, only counter-current operation of liquid/steam vs. burner gas is reported.

6.2.4.2 Minimum Combustion Heat Requirement for Evaporation

To evaporate $\dot{V}^{+}_{H_2O}$ 100 $\frac{g}{h}$ of water, starting from the liquid at room temperature (25 °C) the needed energy can be calculated as follows ($p = 1\ bar$):

$$\begin{aligned}
\Delta\dot{Q}_{evap} &= \dot{m}_{H_2O}\left[\bar{c}_{p,liq}\left(\Delta T\right) + \Delta H_{evap}\right] && (6.2)\\
&= 100\ \frac{g_{H_2O}}{h}\left[4.17\ \frac{J}{g_{H_2O}K}\left(373.15\ K - 298.15\ K\right) + 2257.30\ \frac{J}{g_{H_2O}}\right] && (6.3)\\
&= 8.69\ W + 62.70\ W && (6.4)\\
&= 71.39\ W && (6.5)
\end{aligned}$$

This amount of energy must be supplied by the catalytic oxidation of hydrogen on the combustion side. Then, the required hydrogen throughput ($\dot{n}_{H_2}$) theoretically needed to generate this heat is given by:

$$\begin{aligned}
\dot{n}_{H_2} &= \frac{\Delta\dot{Q}_{evap}}{\Delta h_{R,H_2O}} && (6.6)\\
&= \frac{71.39\ W}{241.83\ \frac{kJ}{mol}} && (6.7)\\
&= 1.06\ \frac{mol}{h} \approx 0.40\ slm && (6.8)
\end{aligned}$$

In practice, more than twice as much hydrogen was needed to compensate the heat loses. Table 6.15. contains a compilation of experimental results.

6.2.4.3 Evaporation Results

Based upon the preliminary studies in the glass plate evaporator, the second evaporator (see Figure E.3 in Appendix E) was designed and tested. Tests included diluted hydrogen as combustion side feed gas and air addition as well as air as feed gas and hydrogen addition.

$\dot{V}^{+}_{H_2O}$ $\left[\frac{ml}{min}\right]$	$\dot{V}^{+}_{air}$ $[slm]$	$\dot{V}^{+}_{H_2}$ $[slm]$	$\dot{V}^{side}_{H_2}$ $[slm]$	T^{steam} $[^{\circ}\mathbf{C}]$	**observations**
100	16	0.5	0.60	100	evaporation not possible
100	16	0.5	0.70	100	higher pulsations
100	16	0.5	0.75	100	liquid level ascends
100	16	0.5	0.80	100	low pulsations
85	16	0.5	0.60	140	pulsation decreases, T^{steam} increases
75	16	0.5	0.60	170	higher T^{steam}

Table 6.15: Variation of water feed and side-fed hydrogen and its influence on the evaporation behavior.

With respect to the subsequent integration of the evaporation section into the SRM unit, only the latter option will be discussed in the following.

Although both the evaporation side and the combustion side channels had been equipped with movable thermocouples, the measured temperature profiles turned out to be strongly influenced by heat losses and random wall contact and will not be discussed in the following.

Since the most important information concerns the uniformity of evaporation, the water content in air as measured by the humidity sensor (Figure 6.19) will be discussed. Evaporation instabilities can be caused both if the heat input compared to the water feed is too low (Table 6.15) or if the heat input is too high so that the geyser-type instabilities are induced. The first type of instabilities can be reduced by increasing the heat input or decreasing the water feed (Figure 6.20 vs. 6.21). For the geyser-type instability the heat input to the evaporation zone has to be decreased or the water flow increased.

After a proper adjustment of liquid and fuel feed a very stable evaporation behavior could be realized, in both short (Figures 6.21 and 6.22) and long term experiments (Figure 6.23). No significant pulsations are experienced and the stability of the process with steam temperature (T^{steam}) between 165 - 175 °C was proven.

In Figure 6.24 comparison of experimental results between the evaporation of 75 g/h of pure water and a water/methanol mixture are presented. In this case a diluted hydrogen stream was fed into which air was side-fed. It can be recognized that pulsations slightly increase when evaporating the liquid mixture. Nevertheless evaporation process shows no relevant differences when employing pure liquids or mixtures for evaporation. Only occasionally, steeply flow signal peaks were observed. These peaks show a determined periodicity, which can be attributed to failures in the liquid dosing pump.

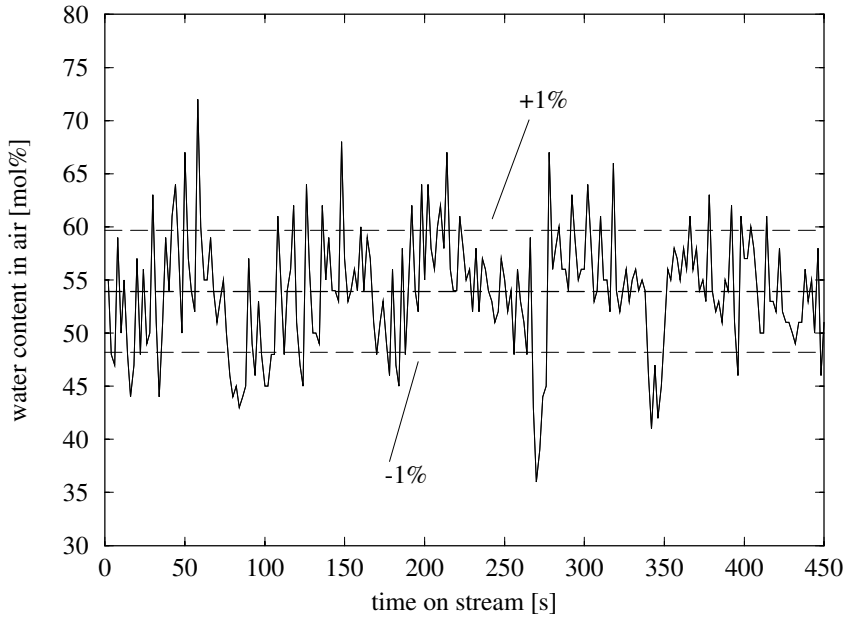

Figure 6.20: Pulsation diagram for experimental continuous evaporation of water: $\dot{V}^{+}_{H_2O} = 75\,ml/h$, $\dot{V}^{+}_{air} = 20\,slm$, $\dot{V}^{+}_{H_2} = 0.5\,slm$, $\dot{V}^{side}_{H_2} = 0.4\,slm$.

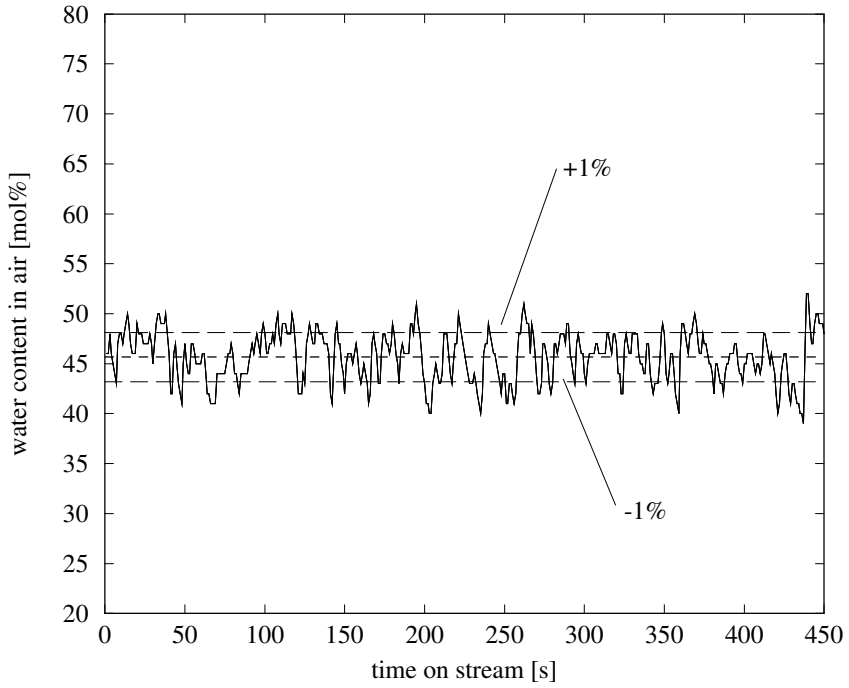

Figure 6.21: Pulsation diagram for experimental continuous evaporation of water: $\dot{V}^{+}_{H_2O} = 70\,ml/h$, $\dot{V}^{+}_{air} = 20\,slm$, $\dot{V}^{+}_{H_2} = 0.5\,slm$, $\dot{V}^{side}_{H_2} = 0.4\,slm$.

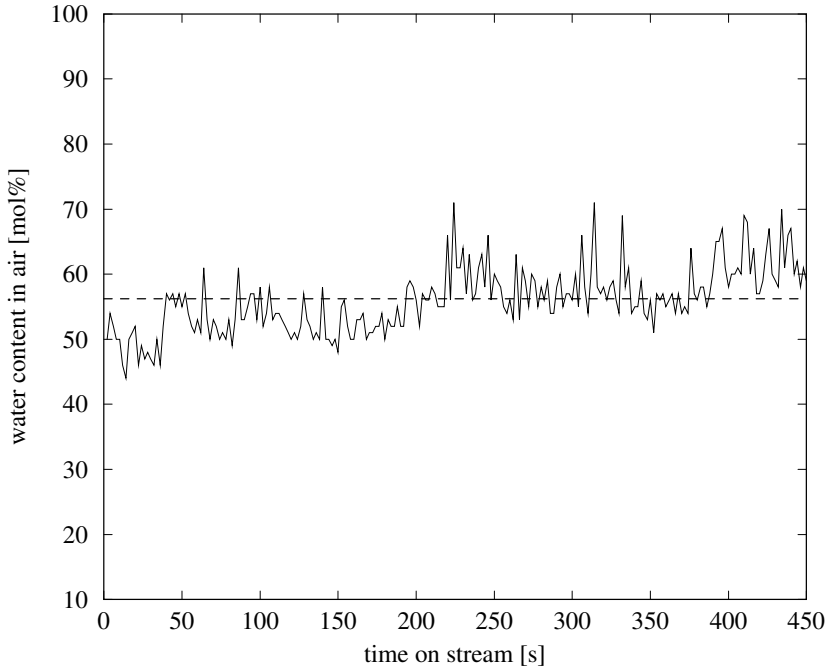

Figure 6.22: Pulsation diagram for experimental continuous evaporation of water: $\dot{V}^{+}_{H_2O} = 85\,ml/h$, $\dot{V}^{+}_{air} = 20\,slm$, $\dot{V}^{+}_{H_2} = 0.5\,slm$, $\dot{V}^{side}_{H_2} = 0.6\,slm$.

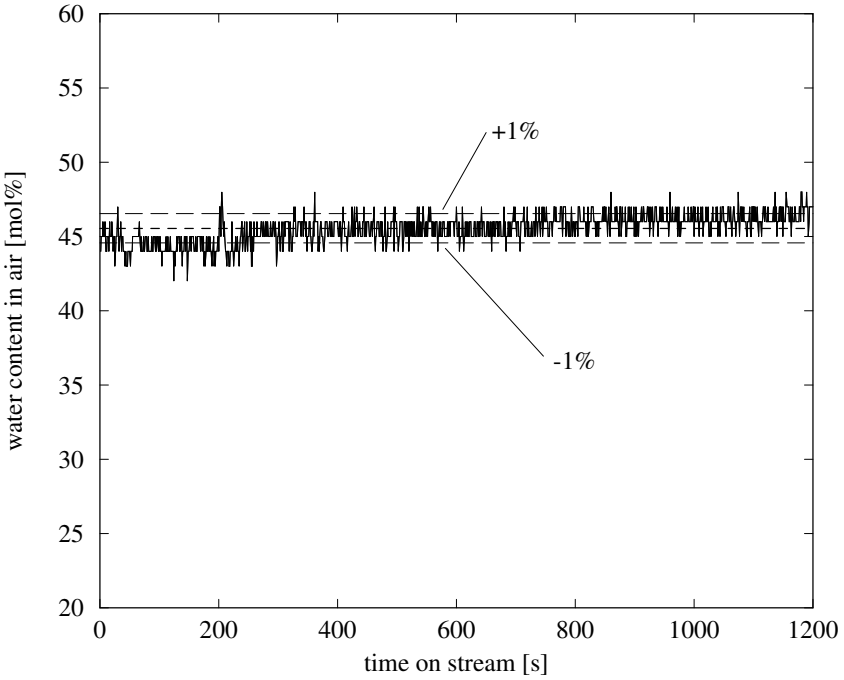

Figure 6.23: Pulsation diagram for experimental steady-state evaporation of water (long-time production): $\dot{V}^{+}_{H_2O} = 75\ ml/h$, $\dot{V}^{+}_{air} = 20\ slm$, $\dot{V}^{+}_{H_2} = 0.5\ slm$, $\dot{V}^{side}_{H_2} = 0.6\ slm$.

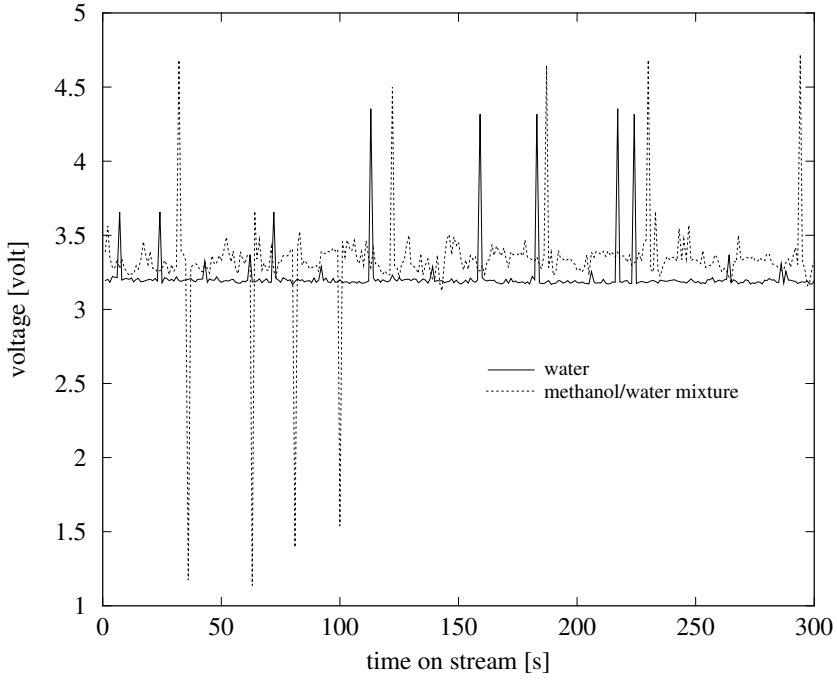

Figure 6.24: Pulsation diagram for experimental evaporation of water/methanol mixture: $\dot{m}^{+} = 75\ g/h$ ($w_{CH_3OH} = 0.42$, $w_{H_2O} = 0.58$), $\dot{V}^{+}_{air} = 2\ slm$, $\dot{V}^{+}_{H_2} = 0.9\ slm$, $\dot{V}^{side}_{air} = 6\ slm$ (oxygen controlling). The occasional spikes are due to pump malfunction.

6.2.4.4 Evaporator Cold-Start and Shut-Down Behavior

In this section experiments for evaporator cold-start and shut-down are reported.

Initially the evaporator has been started from a “warm” state. The unit was preheated with help of the combustion reaction on the combustion side up to temperatures above 100 °C. When the water-pump in switched on, the entering water evaporated before entering the micro-channels of the evaporator plates. It takes about 5 min and a sequence of vapor pulsations before the entrance section is sufficiently cooled down so that no pre-evaporation takes place and evaporation is confined to the micro-channels (Figure 6.25).

Inversely, if the liquid pump is switched off and the heating by hydrogen combustion is continued, the evaporation zone move into the liquid entrance section where a pulsating evaporation takes place until water is completely evaporated (Figure 6.26).

These results show that for evaporator start-up and shut-down a controlled adjustment of heat and liquid input has to be realized. Too high preheating temperatures of the evaporator must be avoided so that pre-evaporation in the feed line does not take place. This can be realized by installing appropriate control/monitoring systems in the feed. Otherwise a decoupling of the evaporator to the following system components during the shut-down phase would avoid further problems in the system.

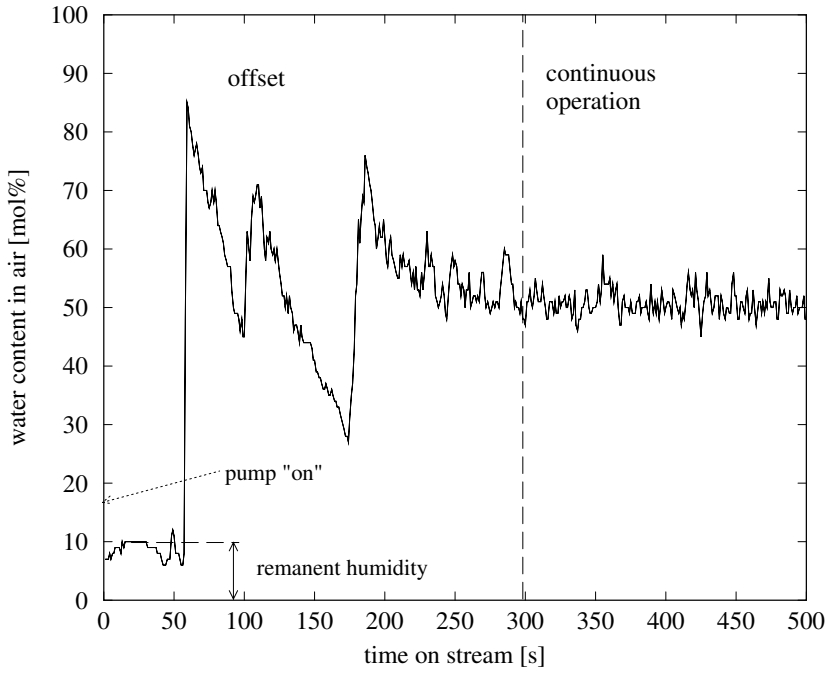

Figure 6.25: Pulsation diagram for switching on the evaporation unit. Operating parameters: $\dot{V}^{+}_{H_2O} = 75\ ml/h$, $\dot{V}^{+}_{air} = 12\ slm$, $\dot{V}^{+}_{H_2} = 0.5\ slm$, $\dot{V}^{side}_{H_2} = 0.4\ slm$.

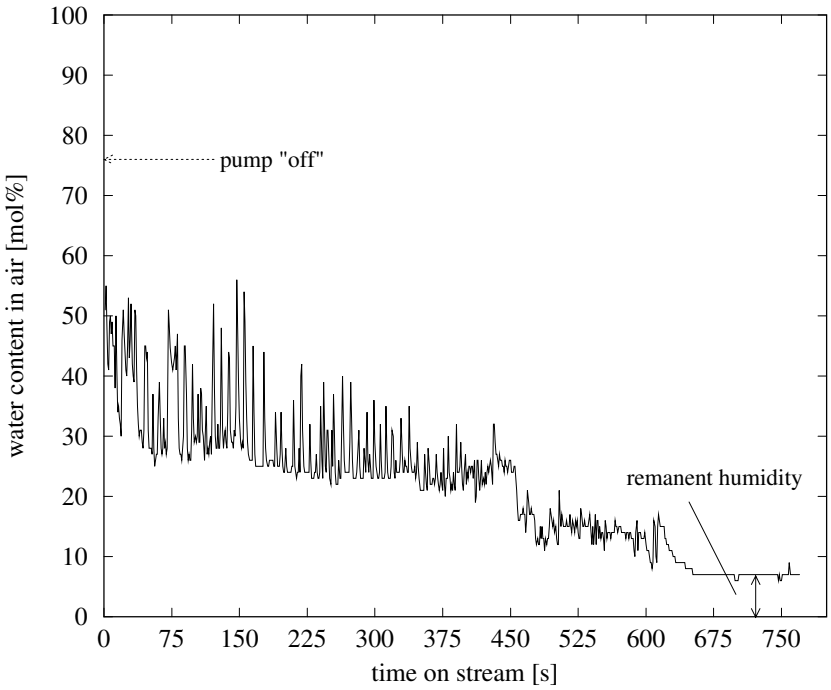

Figure 6.26: Pulsation diagram for shutting down on the evaporation unit. Operating parameters: $\dot{V}_{air}^{+} = 12\ slm$, $\dot{V}_{H_2}^{+} = 0.5\ slm$, $\dot{V}_{H_2}^{side} = 0.4\ slm$.

Closing Remark

Results on the evaluations on the folded-sheet concept, this time functioning as catalytically heated evaporator for the liquid feed, indicate that the evaporation process can well be performed in such a configuration. Problems regarding output pulsation were only recognized either when exceeding a critical liquid load in the feed or when the liquid feed system (pump) does not work properly. In general, liquid evaporation showed a very stable behavior in long-time experiments. When starting-up and shutting-down the evaporator unit, it becomes necessary to finely adjust the heat input. Unstable behavior in this short time is expected: initially, pre-evaporation is observed before the liquid enters the pre-heated evaporator; and inversely, when liquid-pump is shut down, the heat front migrates to the liquid entrance causing pulsations in the output.

Chapter 7

THE 10-KW SRM REACTOR

7.1 Up-Scaling Strategies

The scale-up of the 10-kW SRM reactor is based upon characteristic data of the 1-kW$_{th}$ reformer successfully evaluated in Chapter 6.

The most relevant dimensions of the 1-kW folded-sheet reformer design are shown in (Fig. 7.1) and listed in Table 7.1:

parameter	**value**
number of reforming channels	5
reforming channel width	4.5 mm (4.4 mm measured)
reforming channel depth	40 mm (39 mm measured)
number of combustion channels	6
combustion channel width	1.2 mm
combustion channel depth	40 mm (36.5 mm measured)
reforming channel cross section	858.0 mm^2
combustion channel cross section	262.8 mm^2
total cross section	1120.8 mm^2

Table 7.1: Geometric parameters of the 1-kW$_{th}$ folded-sheet reformer unit.

In Table 7.2 typical operating conditions for the 1-kW$_{th}$ reactor are summarized. They are close to the standard operating condition of 158 g/l methanol and 121 g/l water feed, tested in Chapter 6. A methanol conversion of 100 $\%$ and a CO selectivity of zero would be required to produce the depicted 14.9 $mol\ H_2/h$ with a lower heating value of $LHV\ = 1$ kW.

For scale-up it will be assumed that the reforming side mass flux $\dot{m}_{z,ref}$ should be the same in the 1-kW and the 10-kW reformer. This means that the total cross section area of all

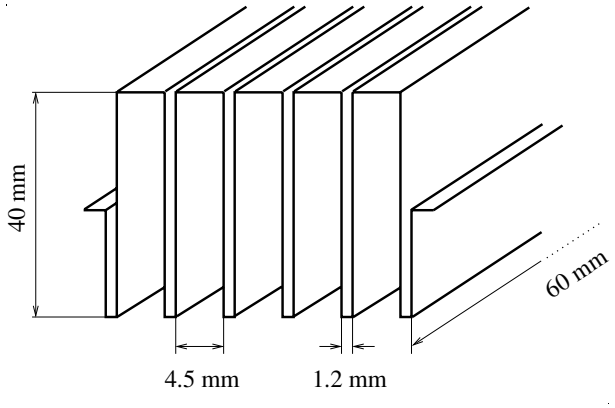

Figure 7.1: Main dimensions of the 1-kW reformer.

parameter	**value**
methanol flow rate	158.8 $\frac{g}{h}$
water flow rate	116.1 $\frac{g}{h}$
total flow rate reforming side	274.9 $\frac{g}{h}$
S/M ratio	1.3 $\frac{mol}{mol}$
produced H_2 amount	14.9 $\frac{mol}{h}$ *(5.56 slm)*

Table 7.2: Reaction parameters for the production of 1 kW_{th} theoretical equivalent of hydrogen at total methanol conversion.

reforming channels has to be enlarged by a factor of 10, as the total feed mass flow. The reforming-side cross-section area is given by:

$$A_{ref}^{1kW} = 5\ channels \cdot 39\ mm \cdot 4.4\ mm = 858\ mm^2 \tag{7.1}$$

and the specific mass flow rate of the feed stream, related to the reforming side cross-sectional area, results to:

$$\dot{m}_{z,ref}^{0} = \frac{274.9\ \frac{g}{h}}{858\ mm^2} = 0.32040\ \frac{g}{h\ mm^2}. \tag{7.2}$$

This results in an increase of the reforming side cross sectional area to:

$$A_{ref}^{10kW} = 8580\ mm^2. \tag{7.3}$$

In addition it was assumed that the width of the reformer channels should stay fixed at 4.5 mm. The combustion channels however should be enlarged from 1 mm to a width of 3 mm. This allows to place 2 aluminium sheets of 1 mm thickness into each combustion channel. Due to their excellent heat conductivity and low weight the aluminium sheets

should help to distribute the heat of combustion more uniformly over the wall surface and reduce hot spots.

Concerning the channel depth it was assumed that the final reactor should have an about squarely cross section so that the channel depth $X2$ and the sum of all channel widths have to be about equal. Then the following conditions must be simultaneously fulfilled:

$$A_{ref}^{10kW} = 8580\ mm^2 = n_{ref} \cdot 4.5\ mm \cdot X_2 \tag{7.4}$$

$$X_1 = \underbrace{n_{ref}\ 4.5\ mm}_{reforming\ channels} + \underbrace{(n_{ref}+1)\ 3\ mm}_{combustion\ channels} + \underbrace{(2n_{ref}+2)\ \tfrac{3}{10}\ mm}_{folded\ sheet} \tag{7.5}$$

$$X_1 = X_2 = X, \tag{7.6}$$

with n_{ref} as the number of reforming gas channels. Solving for n_{ref} equals:

$$n_{ref} = 15.12 \cong 15 \tag{7.7}$$

Substituting this value in equation 7.5 a side dimension for a reactor squarely cross section of $X = 126\ mm$ is obtained. In order to cover manufacturing uncertainties as well as possible differences in the catalyst activity, the number of reforming channels will be increased to $n_{ref} = 16$ and a reforming channel depth of $X = 133\ mm$ has been chosen. Respectively, the number of combustion gas channels results in 17 ($n_{ref} + 1$). the final dimensions are summarized in Table 7.3.

parameter	**value**
number of reforming channels	16
reforming channel width	4.5 mm
reforming channel depth	133 mm
number of combustion channels	17
combustion channel width	3 mm
reforming channel cross section	8580 mm^2

Table 7.3: Resulting geometric parameters of the up-scaled 10-kW$_{th}$ folded-sheet reformer unit.

The results of the evaluation of the 1-kW reformer (Chapter 6) show that for the considered reforming side mass flux a reactor length of about 400 mm should suffice for total methanol conversion (depending on the catalyst activity).

7.2 Reaction Engineering Simulations

In order to gain a better understanding about the reactor behavior at scaled-up conditions and to define further design specifics, detailed simulations were performed using the reformer model developed in Chapter 5. Here an arrangement of 16 parallel reforming gas channels, each of them bounded by two combustion gas channels resulting in an array similar to that depicted in Figure 6.1, was considered. For discussion, simulations for two representative channels, one reforming and one combustion channel, are presented. It is assumed that methanol and water are entering the reformer evaporated (only the reformer process is modeled). Both optimal steady state operation as well as the dynamical reformer start-up behavior is evaluated and discussed.

7.2.1 Determination of the 10-kW Operating Conditions

In order to find appropriate reaction conditions for the 10-kW folded-sheet reformer, following criteria were stated: total methanol conversion must be reached, CO production should remain as low as possible and local steep temperature peaks should be avoided along the reactor length.

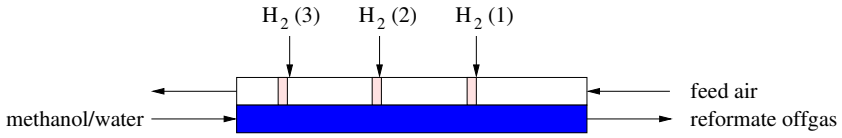

Figure 7.2: Graphic representation of the main process streams in the 10-kW reformer.

On the reforming side, methanol and water enter the reformer pre-evaporated. On the combustion side solely air (in excess) enters the reactor, counter-currently to the reforming gas. Combustion hydrogen is side-fed to the main air stream and reacts over specifically placed catalyst slices (catalytically coated spacers). In order to achieve a lower mean temperature level in the reactor (to avoid temperature hot spots) three reaction zones are suggested along the combustion side. Reaction zones are placed equidistant to each other. An overall flow scheme of the reactor is depicted in Figure 7.2.

From the previous simulation studies on the 1-kW reformer the placing of the first combustion zone (3) near the reactor entrance (referred to the reforming gas flow direction) turned out to be important. Here, most of methanol conversion must take place. Another reason for placing this reaction zone near the water/methanol feed is to avoid the cooling of the entering superheated reactant mixture. Further two combustion zones (2 and 1) should serve to reach total methanol conversion at moderate operating temperatures and to control the CO formation.

For the simulation study, the flow rate of methanol/water feed is kept constant, as well as the feed air flow rate. Hydrogen is fed to the combustion side via side gas injectors at three different positions, into the combustion catalyst zones. The amount of hydrogen to be side-fed is systematically varied aiming at a maximum methanol conversion. General initial

	parameter	value
reforming side		
	feed mass flow rate	2857 $\frac{g}{h}$
	S/M ratio	1.30 $\frac{mol}{mol}$
	feed gas temperature	150 °C
combustion side		
	vol. flow rate of feed air	100.0 slm
	feed gas temperature	20 °C
side injection		
	volumetric fraction of hydrogen	1.0 [-]
	gas temperature	20 °C

Table 7.4: General operating conditions used for simulations of the 10-kW$_{th}$ reformer.

run	$\dot{V}_{H_2}(3)$ **[slm]**	$\dot{V}_{H_2}(2)$ **[slm]**	$\dot{V}_{H_2}(1)$ **[slm]**	X_{MeOH} [%]	y_{CO} [%]
A	2.5	2.1	2.1	99.20	3.10
B	2.0	2.9	2.0	99.79	3.85
C	3.5	2.0	1.8	99.99	4.15

Table 7.5: Data for the evaluation of optimum operating conditions for the 10-kW folded-sheet reformer.

conditions and simulation results are given in Tables 7.4 and 7.5.

As can be seen in Figure 7.3, high temperature levels at the first combustion zone (3) lead to achieve higher conversions of methanol along the entire reactor length. If total methanol conversion is achieved already in the middle of the reactor (profiles B, C) the third (rightmost) combustion zone is of no advantage since it only increases CO by reverse water-gas shift. Better operating conditions are achieved when moderate temperatures are kept along the entire reformer, i.e. most of methanol is converted at the reactor entrance at moderate CO formation and the temperatures are kept as low as possible along the second half of the reformer (profile A).

For the next simulation studies and as a reference for the subsequent experimental evaluation, operating conditions according to the simulation run A will be taken into account.

7.2.2 Dynamic Simulations on the Cold Reactor Warm-Up

Due to the high heat capacity of the metallic structure, large start-up times are expected for the 10 kW-reformer. In order to quantify this effect, dynamic simulations on the cold start-up

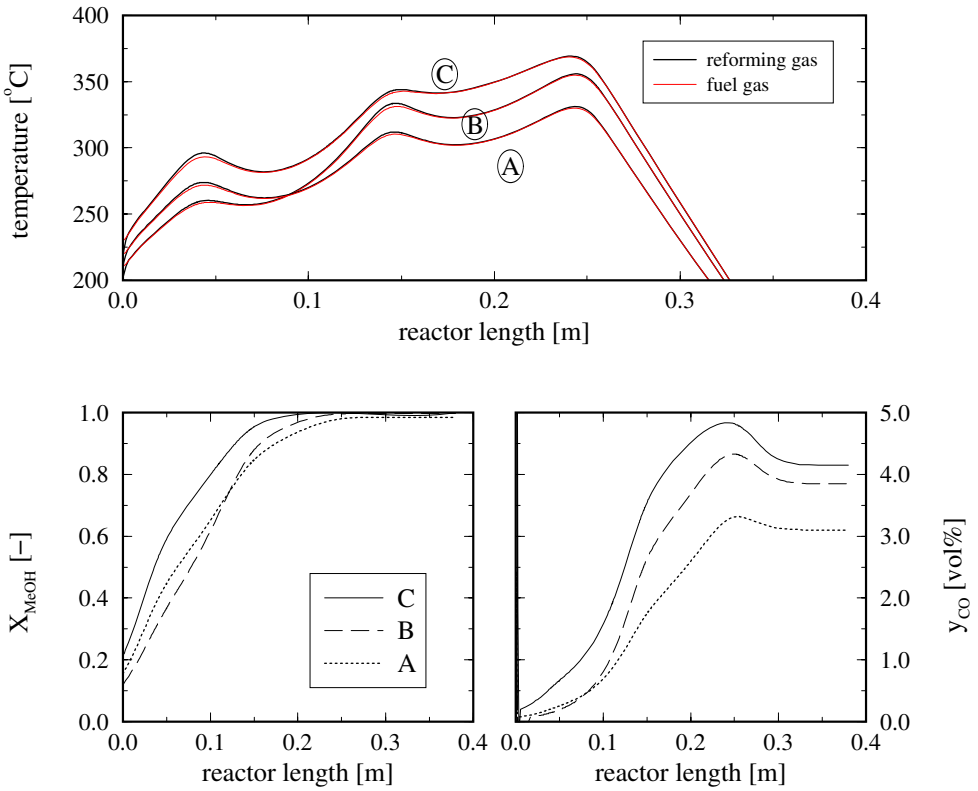

Figure 7.3: Temperature and concentration profiles on the reforming (left) and combustion side (right). Simulation results on methanol conversion and CO concentration/selectivity. Reaction parameters in Tables 7.4 and 7.5.

of the folded-sheet reformer were performed. For the start-up two steps will be considered in the following. Step one is a warm-up to the necessary minimum reforming temperature. In step two the start-up of the reforming reaction in the preheated reactor will be considered.

In step one the cold reactor is warmed-up by only activating the hydrogen combustion on the combustion side whereas only nitrogen flows on the reforming side. This pre-heating phase can also be used for reforming catalyst pre-conditioning. For this purpose, once the reactor reaches an operating temperature of about 150-200 °C, feed nitrogen is mixed with hydrogen.

On the combustion side, settings for a subsequent 10-kW reforming reaction operation are assumed. This setting directly determines the duration of the heating-up process.

Operating conditions used for simulation are listed in Table 7.6. For compensating the cooling effect of the cold air feed, strong hydrogen combustion is assumed at position $\mathrm{H}(1)$ (see reference in Figure 7.2).

In Figure 7.4 the temperature profiles of reforming and combustion gas are shown for different times elapsed. It can be noticed that the reactor reaches about 50 % of the expected temperature increase after approx. 10 minutes. A steady-state profile is reached after about 26 minutes.

	parameter	value
reforming side feed		
	nitrogen mass flow rate	150 $\frac{g}{h}$
	feed gas temperature	20 °C
combustion side		
	volumetric flow rate of feed air	100.0 slm
	feed gas temperature	20 °C
side feed		
	feed gas temperature	20 °C
	hydrogen mass flow rate at (1)	2.1 slm
	hydrogen mass flow rate at (2)	2.1 slm
	hydrogen mass flow rate at (3)	2.5 slm

Table 7.6: Parameters used for dynamic simulations of the 10-kW$_{th}$ reformer at cold-start conditions. Notation is according to Figure 7.2.

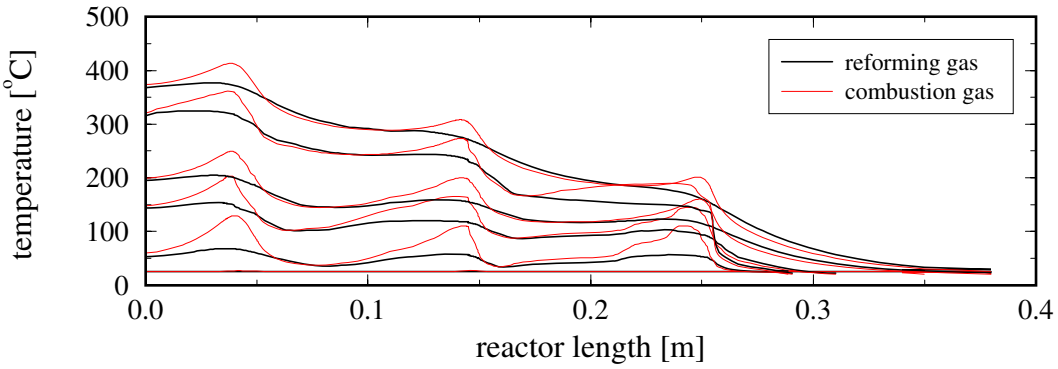

Figure 7.4: Dynamic temperature profiles of reforming and combustion-side gas during reactor warm-up. Curves respectively correspond to following operating times: 0 s, 109 s, 393 s, 589 s, 1136 s and 1511 s.

These results reveal that the 10-kW reformer requires a long time for start-up. If such a hydrogen processor is to be implemented in a fuel cell powered vehicle for supplying the process gas, lower starting times are required. Although lower starting-up times could be achieved by increasing the combustion, this decision would endanger the mechanical stability of the reformer unit, leading to strong thermal stresses and possibly causing ruptures in some reactor junctions. A possible solution would be to use autothermal reforming during start-up, i.e. to add air to the reforming side as soon as a respective ignition temperature has been reached, but such studies are not within the scope of this work.

7.2.3 Dynamic Simulations on the Start-up of Reforming

Once the reformer is pre-heated by means of the hydrogen combustion reaction on the combustion side, methanol and water are fed to the reactor for starting the steam reforming reaction. Since the start-up of the evaporation section is not included in the simulations, the reforming feed is assumed to enter the reaction section as vapor of 150 °C. Reaction settings of combustion side gas streams are kept constant during this transition. Reaction parameters of reforming side feed are presented in Table 7.7.

	parameter	**value**
reforming side		
	feed mass flow rate	2857 $\frac{g}{h}$
	feed gas temperature	150 °C
	molar fraction of methanol	0.439 [-]
	molar fraction of water	0.561 [-]

Table 7.7: Parameters used for dynamic simulations of the 10-kW$_{th}$ reformer at SRM initiation conditions. Combustion side operating conditions are listed in Table 7.6.

Results depicted in Figure 7.5 show that once the reformer is preheated, and methanol and water are fed to the reactor, the SRM reaction starts almost immediately. Even in the very first seconds of this start-up step, hydrogen is produced in large amounts. The reaction runs slowly to steady-state conditions. After about 2 minutes 70 $\%$ methanol conversion is achieved. For times $>$ 20 minutes methanol conversion above 90 $\%$ can be guaranteed. CO concentrations around 2-3 $vol\ \%$ are predicted.

The results show that the reforming reaction can be started over a sufficiently preheated and preconditioned catalyst rapidly, obtaining high methanol conversions and moderate CO-concentrations, within short times. The main remaining problem is the duration of the warm-up step (Section 7.2.2).

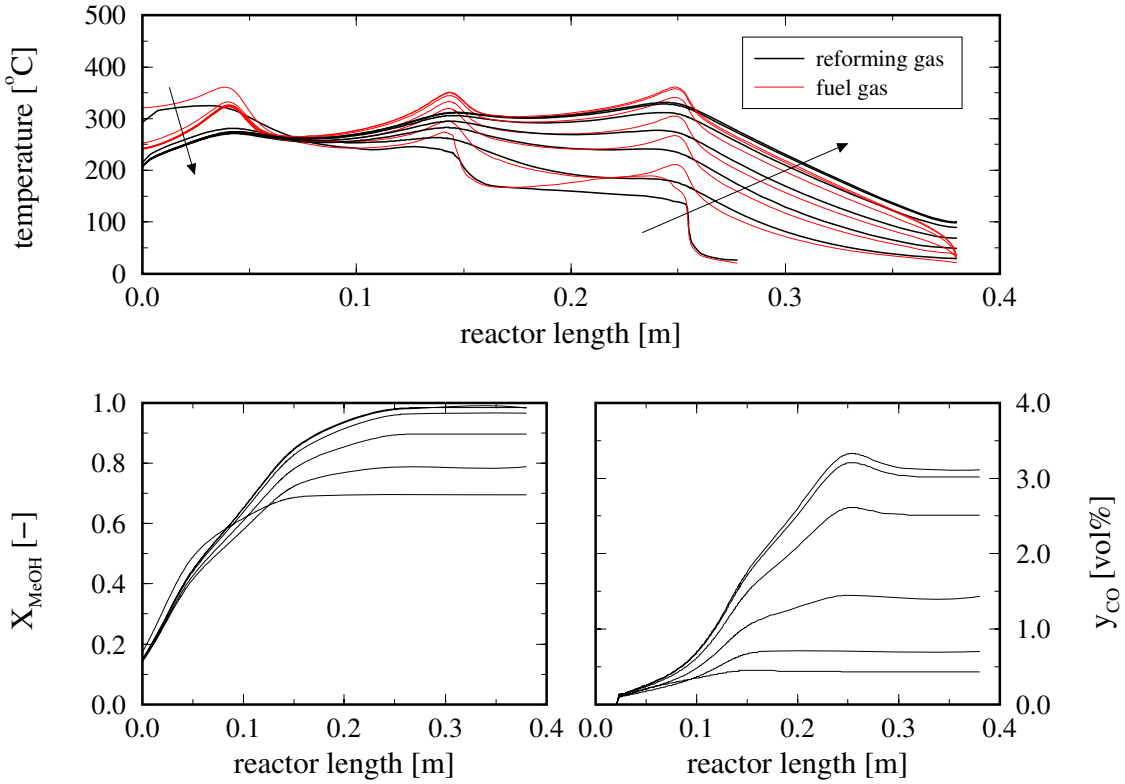

Figure 7.5: Start-up behavior of the preheated folded-sheet reformer under full load (10 kW_{th}). Depicted profiles correspond to following elapsed times: 155 s, 638 s, 1220 s, 2550 s, 5040 s and 10070 s after warm-up.

7.3 Reactor Configuration and Distribution of Feed

7.3.1 Operating Principle

The 10-kW reformer consists of 16 reformer channels and 17 adjacent combustion channels separated by the metallic folded sheet (see Figure 7.6). Each reforming and each combustion channel is structured identically, so describing one reforming and one combustion channel characterizes the whole device.

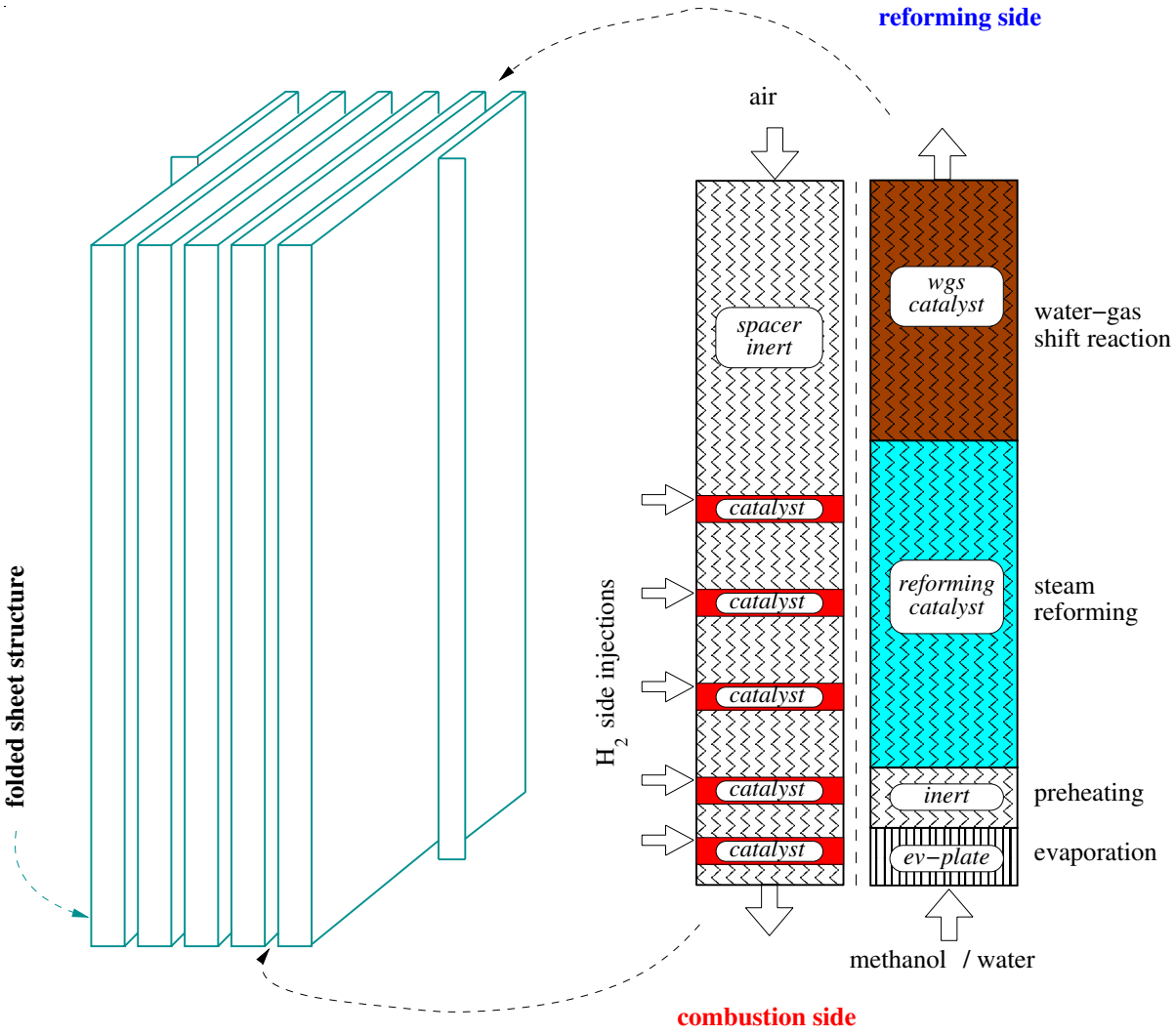

Figure 7.6: The 10-kW folded-sheet reactor. *Left:* Scheme of the folded-sheet and the resulting reactor chambers; *right:* Axial structuring of the combustion and reforming side.

Methanol and water previously mixed are fed at room temperature into the reformer channels at the reactor bottom.

This mixture is evenly distributed over the depth of each of the 16 parallel reforming channels by means of liquid distributors (drilled metal-bars, Figure 6.18-*left*) and then the mixture enters the micro-channels of the evaporation plates (see Figure 7.6, *ev-plate*), in which the mixture is evaporated.

After leaving the evaporation plates the methanol-water steam passes through inert spacers, in which the mixture is superheated up to the reforming temperature. The spacers generate additionally turbulences so that uniform heat transfer takes place and condensed drops are re-evaporated.

Subsequently the superheated mixture enters the catalytic steam reforming zone where the reforming reaction takes place at the spacers coated with steam-reforming catalyst.

Reaction gases (unreacted methanol and water, as well as the product gases) leave the reforming zone and enter the water-gas shift reaction zone. Here again spacers coated with water-gas shift catalyst fill the channels and help to catalytically reduce the CO content in the reformate whilst producing additional hydrogen (see Eq. 2.23).

The purified reformate leaves the reformer at the top to be further purified for use in, e.g., fuel cells.

On the combustion side air in excess flows counter-currently through the channels. Along the water-gas shift section, the airflow has the only function of cool down the hot reforming side stream. Hence the combustion side channels contain inert spacers in this zone.

At the height of the steam-reforming zone three sections filled with catalytically coated spacers, serve as substrate for the catalytic oxidation of the side feed hydrogen with the oxygen from the main air stream and supplies the heat for the SRM reaction.

The combustion side gas then proceeds to the preheating zone into a fourth catalytic zone where hydrogen (side-fed) reacts with the oxygen to generate the heat required for superheating the reactant mixture.

A last hydrogen oxidation takes place at the catalyst coated spacers of the evaporation section to provide the necessary evaporation heat.

The exhaust gas leaves the reactor at the bottom after having exchanged its heat with the methanol-water mixture.

7.3.2 Optimization of the Combustion Side Feed

For proper operation of the reactor it is necessary to distribute both the reforming feed and the combustion air uniformly into each of the parallel channels and over the depth of each channel.

For the reforming side the liquid feed distribution has been achieved by drilled metal bars in each pocket, similar to the evaporation plate shown in Figure 6.18.

For the optimization of the combustion side air distribution and the hydrogen side feed,

separate experiments were performed. They are described in the next section (7.3.3).

For the proper air feed distribution over the depth of each combustion channel an experimental set-up, as shown in Figure 7.7, was built. The device emulates a single combustion channel of 130 mm depth and a sufficient length, and allows studying the flow distribution by visualization techniques.

A static mixer is installed at the gas entrance to create a determined pressure drop and therefore achieve a better feed gas distribution in the channel depth. The static mixer consists of a corrugated wire-mesh made of stainless-steel (material code 1.4404) with a wire diameter of 0.63 mm and mesh aperture of 50 μm (see Figure 7.8). For the 10-kW reformer, mesh line paths of the static mixer were not aligned to the flow direction, on the contrary, they were set inclined to offer bigger flow resistance and enhance the mixing effect.

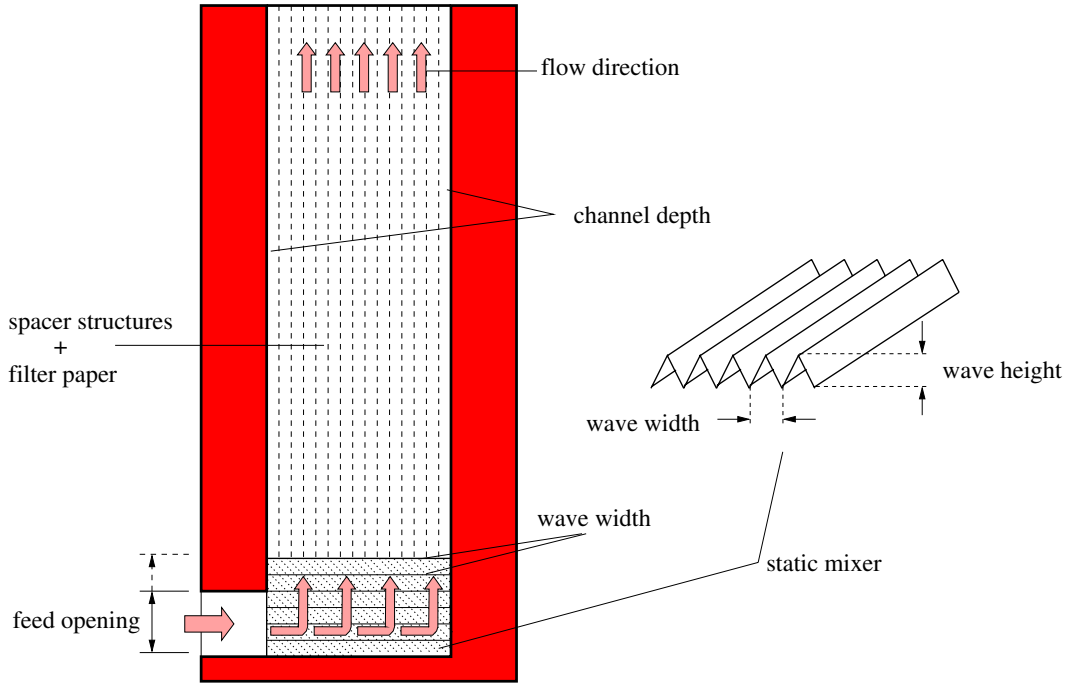

Figure 7.7: Test stand for visualization experiments. *Left:* Sketch of the device configuration; *right:* Wave-like metallic structure as static mixer for a uniformly distributed feed gas.

To optimize the flow distribution, both the wave height and width of the spacer (Figure 7.8) as well as the opening of the feed entrance (Figure 7.7) were varied for this evaluation. The feed openings tested were 15 mm and 25 mm.

7.3.2.1 Visualization Principle

Based on the method developed by *Kottke* and *Blenke* [68, 69] for the measurement of convective mass transfer coefficients, it is possible to obtain images of the flow distribution in a reaction channel. The channel walls are covered with a white filter paper which is soaked with a chloride solution of manganese II.

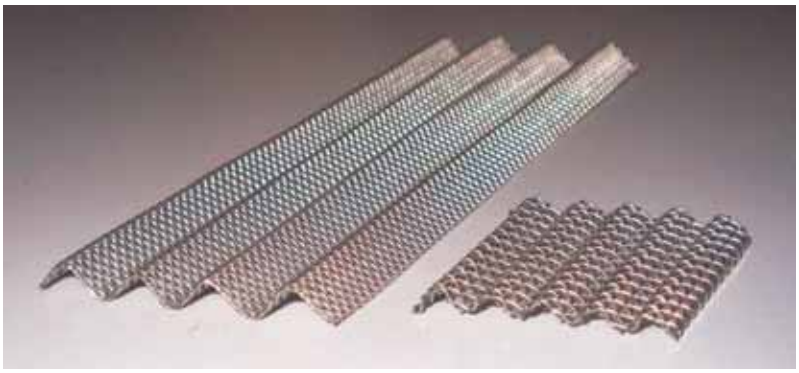

Figure 7.8: Metallic static mixer for the 1-kW (*right*) and 10-kW (*left*) folded-sheet reformer.

Into the air feed-stream, a pulse of ammonia as reaction component is added. Ammonia is absorbed at the filter paper in the aqueous phase where the following mass-transfer controlled reactions take place:

$$NH_3 + H_2O \quad \Longleftrightarrow \quad NH_4^+ + OH^- \tag{7.8}$$

$$2NH_4OH + MnCl_2 \quad \longrightarrow \quad 2NH_4Cl + Mn(OH)_2 \tag{7.9}$$

$$Mn(OH)_2 \quad \overset{O_2,\ H_2O_2}{\longrightarrow} \quad MnO_2 \tag{7.10}$$

The final product (manganese dioxide) is brown colored, chemically stable and remains locally fixed in the filter paper. The brown coloration is therefore a measurement of the reaction velocity and marks the flow pass and the intensity of mass or heat transfer.

7.3.2.2 Results and Discussion

In Figures 7.9 and 7.10 some experimental results on the distribution of the air flow on the combustion side are shown. The wall of the test device was coated with filter paper previously impregnated with a solution of $MnCl_2$. An air feed-stream of 70 slm was introduced and distributed by the static mixer made of Figure 7.8 (wave length = 7 mm, and wave height = 3 mm). The height of the feed entrance was varied. It can be seen that in Figure 7.9-right the short wave length of the static mixer causes a relatively high pressure drop into the depth of the channel, so that the fluid tends to turn rapidly to the left, leading to a non-uniform distribution of the fluid. When employing a narrow feed entrance (Fig. 7.9-left) this negative effect is even more pronounced.

In Figure 7.10 an increased channel height of 5 mm and a new static mixer (wave length = 12 mm, and wave height = 5 mm) was employed. It can be seen that the flow distribution along the channel depth is now much more uniform since the flow of the gas now proceeds up to the channel end (depth). A wider feed entrance (Fig. 7.10-right) leads to more homogeneous flow distribution since the feed entrance jet of a narrow feed opening induces some recirculation (see Fig. 7.10-left, circled zone).

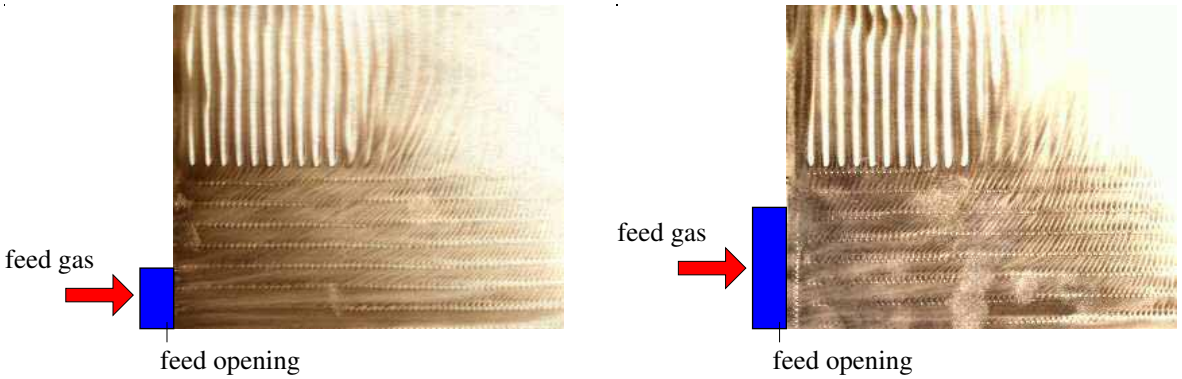

Figure 7.9: Visualization for a feed gas flux of 70 slm on the combustion side. Static mixer with a wave length of 7 mm and wave height of 3 mm. *Left:* Feed opening width = 15 cm. *Right:* Feed opening width = 25 cm.

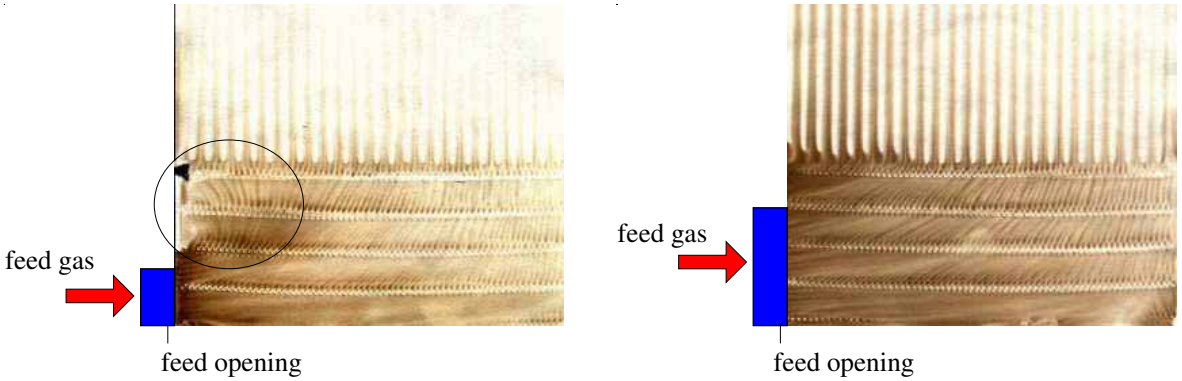

Figure 7.10: Visualization for a feed gas flux of 70 slm on the combustion side. Static mixer with a wave length of 12 mm and wave height of 5 mm. *Left:* Feed opening width = 15 cm. *Right:* Feed opening width = 25 cm.

7.3.3 Optimization of the Fuel Gas Feed

At the side feed locations hydrogen is added to the main air stream. Again it is essential that this hydrogen side-feed is equally distributed over the whole depth of each combustion channel so that it can mix uniformly into the air flow before entering the catalyst section.

This distribution was performed by horizontal capillary tubes entering each channel of the combustion side. The design is similar to the gas distributor shown in Figure E.6. Four holes in the capillary tubes of different dimensions have been tested by feeding the required hydrogen flow and observing the resulting flame distribution after the hydrogen was ignited. Figures 7.11 to 7.13 show the resulting flame images for the conditions specified in the legends.

First experiments were made with capillary tubes with side bores of different drilling diameters. It can be noted that the larger pressure drop of smaller bore diameters (Figures 7.11-*a*) results in a more uniform flame image.

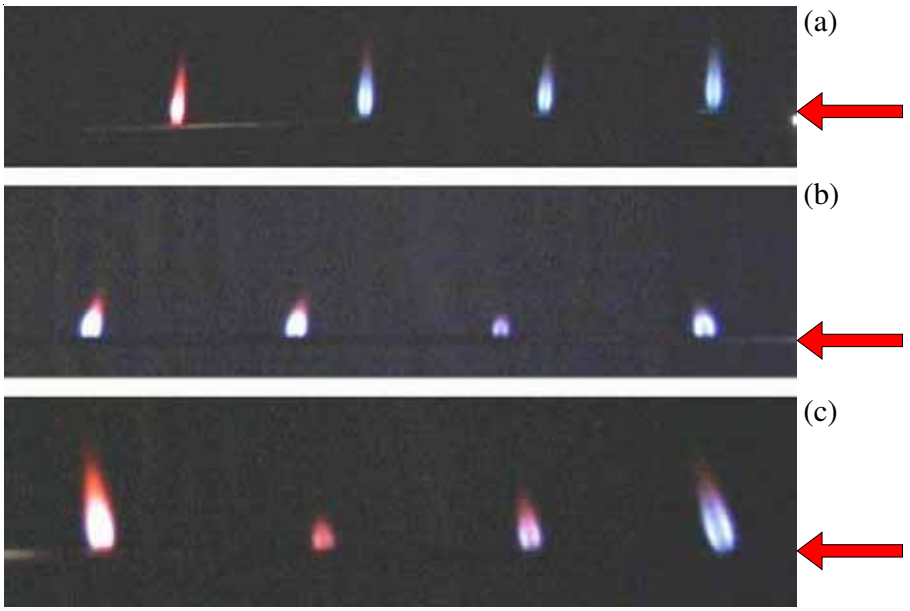

Figure 7.11: Visualization experiments with capillary tubes with side bores of different diameter. Capillary tube diameter: inner = 1.1 mm, outer = 1.4 mm. Hydrogen-feed flow rate = 0.5 slm. Bore diameter: *(a)* 0.1 mm, *(b)* 0.15 mm, *(c)* 0.2 mm (flow direction from right to left).

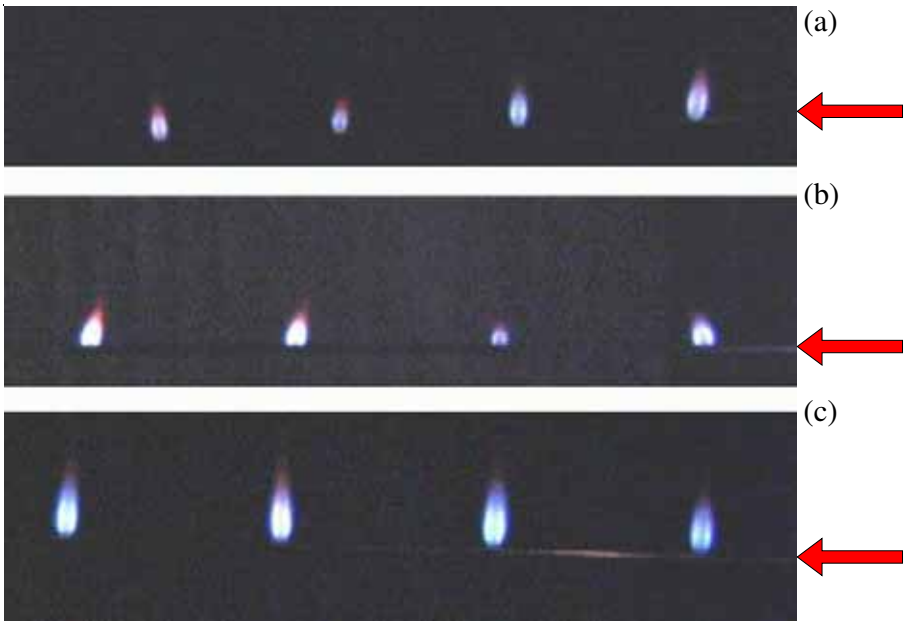

Figure 7.12: Visualization experiments with capillary tubes with different capillary wall thickness. Bore diameter = 0.15 mm. Hydrogen-feed flow rate = 0.5 slm. Capillary wall thickness ratio (inner/outer diameter in mm): *(a)* 1.0/1.5, *(b)* 1.0/1.4, *(c)* 1.3/1.5 (flow direction from right to left).

Further tests with capillary tubes with different wall thickness and (almost) constant outer diameter were also performed (Figure 7.12). Here the capillaries with the largest inner diameter (lowest lateral pressure drop) gave the most uniform performance.

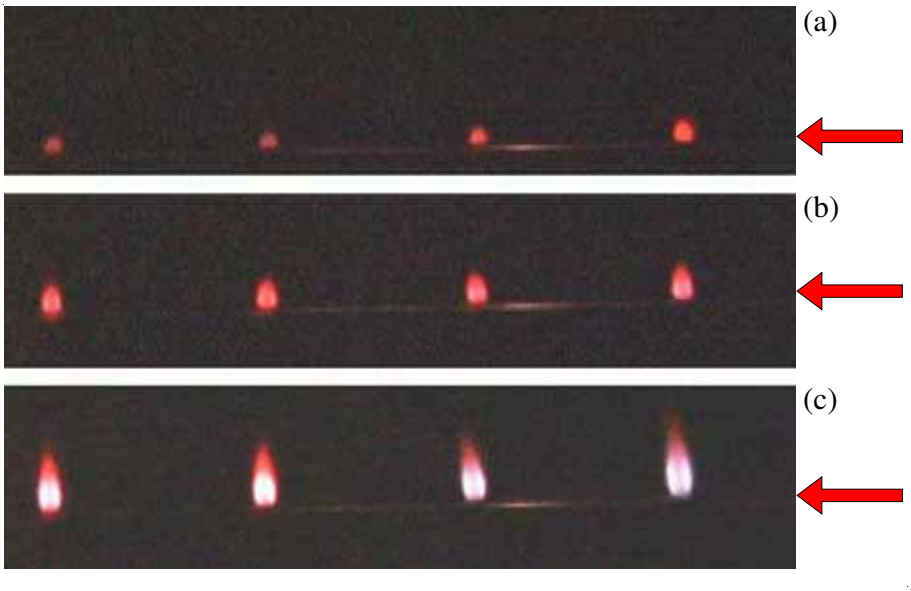

Figure 7.13: Visualization experiments driving different hydrogen flow rates. Capillary tube diameter: inner = 1.3 mm, outer = 1.5 mm. Bore diameter = 0.2 mm. Hydrogen flow rate: *(a)* 0.1 slm, *(b)* 0.2 slm, *(c)* 0.5 slm (flow direction from right to left).

Finally, the effect of variable flow rates of hydrogen through the capillary tubes was evaluated. As shown in Table C.7 (Appendix C), a capillary tube has to be operated with one of three values of flow rate: 100, 200 and 500 sccm depending of the combustion zone where the fuel gas is supplied. The optimum configuration of Figure 7.12-*c* was tested in Figure 7.13 for different gas flows. As can be seen in Figure 7.13 an equally uniform flame image results for all relevant gas flows tested.

7.4 Reformer Construction and Experimental Testing

The up-scaled prototype resulted in an array of 16 reforming and 17 combustion chambers with a channel depth of 130 mm. It was successfully constructed and experimentally evaluated. The experimental setup used for the evaluation of the 10-kW reformer is depicted in Figure 7.14 and Figure F.5 in Appendix F.

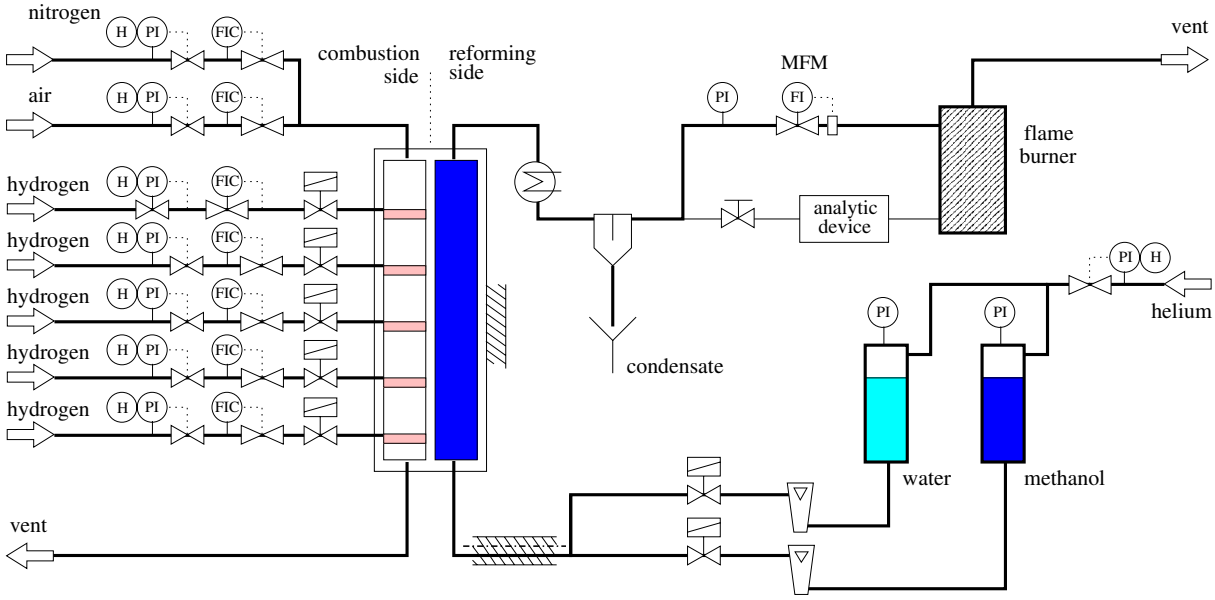

Figure 7.14: Experimental setup for testing the 10-kW folded-sheet reformer.

Here it can be recognized that liquid methanol and water are independently fed from two separate helium-pressurized tanks by separated liquid mass flow meters (and later because of higher load demand: liquid rotameters), which were previously tested and calibrated for each liquid. Both feeds are mixed and enter the reformer at the bottom side into the evaporation zone. The mixture is evaporated and further heated up to reaction temperature. After this the mixture passes through the reforming/WGS section. The reformate is conducted through a intensive-condenser, afterwards gas and condensate are separated in a splitter. The reformate gas is conducted through a pressure control element to the after burning unit (flame burner, see Figure F.7 in Appendix F). Exhaust gases are released to the vent system. By opening a bypass valve, a fraction of the reformate can be taken off for analysis.

On the other side, fresh air is counter currently fed at the top of the reformer and combustion gas (hydrogen) is side fed through the side injectors to the respective reaction zones. Produced steam from the hydrogen/oxygen combustion is also released via vent system.

The whole laboratory and plant/device configuration follows the same disposition and principles described in Chapter 4, Section 4.1.1.

7.4.1 Monitoring of the Reaction Behavior

Due to the complexity of the construction of the folded-sheet reformer it was not possible to incorporate temperature measurement inside the apparatus. For this reason outside placed thermocouples helped (indirectly) monitoring the internal temperature progress. Thermocouple locations are shown in Figure 7.15.

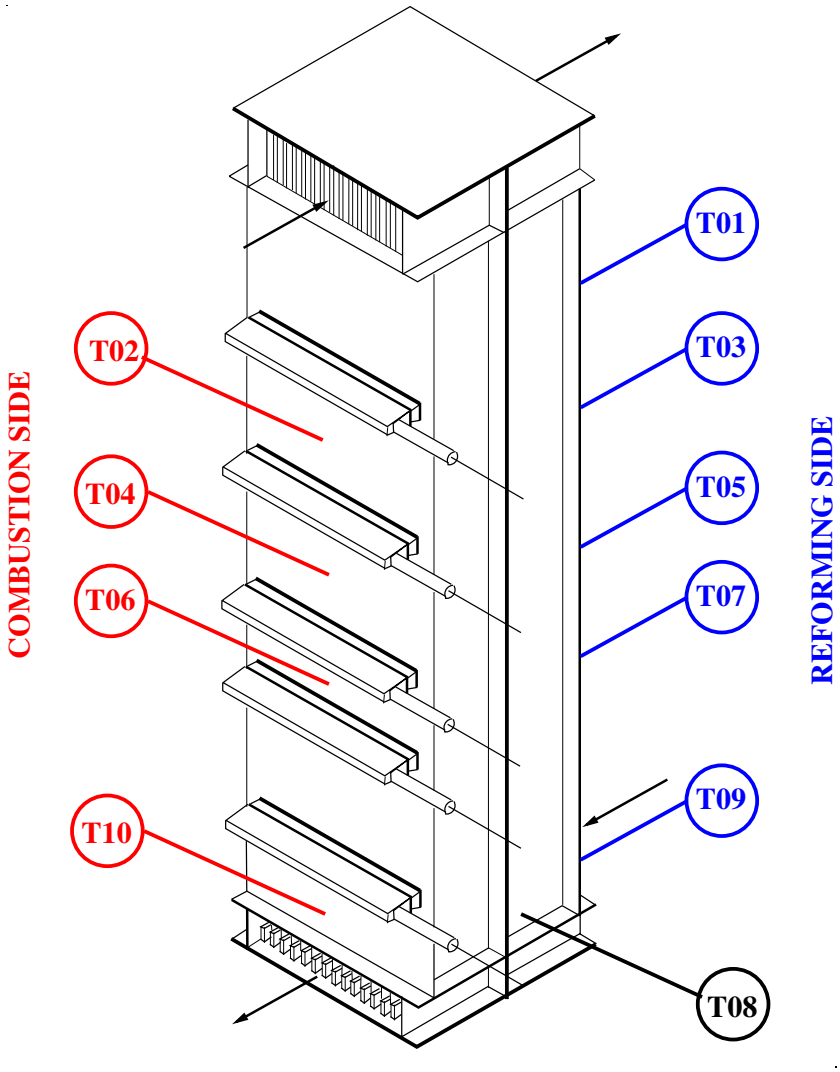

Figure 7.15: Temperature measuring positions along the outer reactor wall. Temperature measurements are taken as a reference for the inlet reactor temperature.

Because too high reaction temperatures can derive in catalyst damages and wrong reaction performance, the external reactor wall temperature was monitored so that it does not surpass a pre-established limit value of 275 °C.

As an example, a steady-state temperature profile is depicted in Figure 7.16. Here the reformer is operating to produce a hydrogen flow equivalent to 1.5 kW of thermally power in a fully developed operating state (details on the reforming reaction behavior are discussed

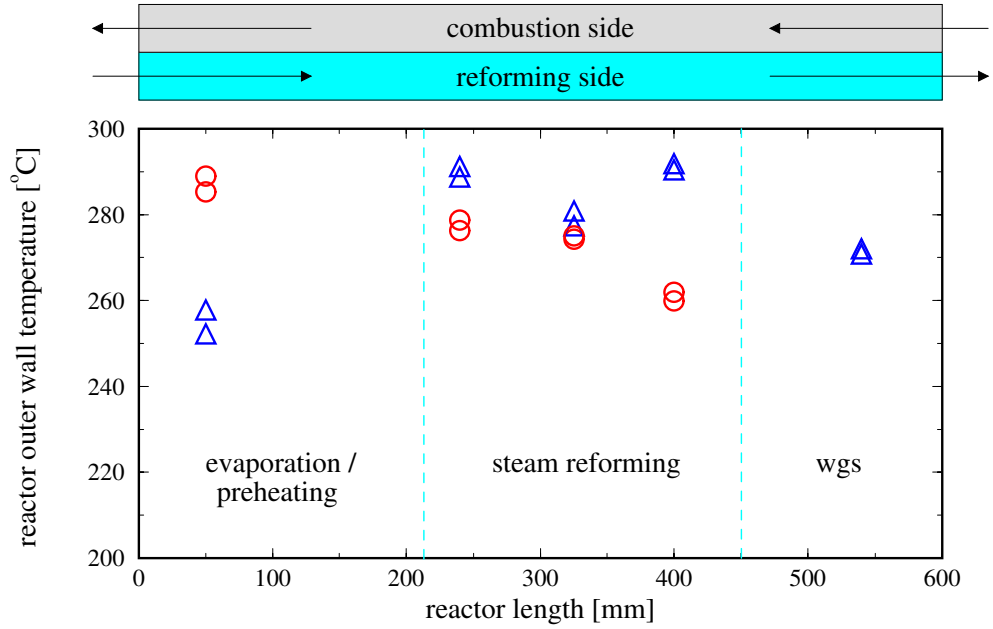

Figure 7.16: Axial temperature profile of the reformer outer wall: (△)-symbols represent the temperature measured along the reforming side wall; (○)-symbols the wall temperature on the combustion side. Temperature measurement positions are according to Figure 7.15. Operating parameters are listed in Table 7.8.

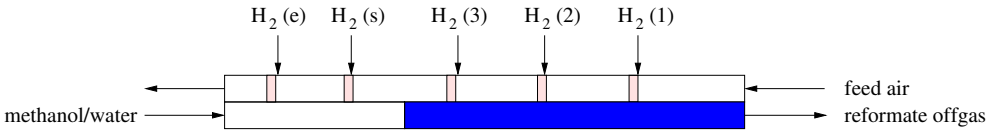

Figure 7.17: Graphic representation of the main process streams of the 10-kW reformer working with integrated evaporation and superheating sections.

in the following sections). Reaction parameters are shown in Table 7.8. The triangle-form measurement points describe the evolution of the temperature on the reforming side, the circle-shaped that on the combustion side wall. It is interesting to remark that the wall temperature rises slowly on the reforming side, beginning with the evaporation zone where a large amount of heat is needed to evaporate the reactant mixture at nearly constant temperature, followed by the overheating/reforming sections where the maximum temperature is reached in a plateau-like profile, and ending with a slight cool down towards the (right) end of the reactor, which is suitable for the water-gas shift reaction. On the other side, cold fresh air enters counter-currently into the combustion side (from right to left) and exchange heat with the outgoing reformate stream. At the left side the combustion mixture leaves the reactor at its maximum temperature to provide the heat for the liquid evaporation.

	parameter	value
reforming side		
	mass flow rate MeOH	242.6 $\frac{g}{h}$
	S/M ratio	1.30 $\frac{mol}{mol}$
combustion side		
	vol. flow rate of feed air	230 slm
	feed gas temperature	20 °C
side feed		
	feed gas temperature	20 °C
	H_2 flow rate at: (1)	0.38 slm
	(2)	0.38 slm
	(3)	0.38 slm
	(s)	0.72 slm
	(e)	1.72 slm
output	vol. gas flow rate	9.6 slm
	y_{H_2}	0.733 [-]
	y_{CO_2}	0.2583 [-]
	y_{CO}	0.01636 [-]
	X_{MeOH}	92.41 %

Table 7.8: Reaction parameters for experiments on the 10-kW reformer operating at nominal 1.5 kW_{th} output conditions (Figure 7.16). Stream labeling according to Figure 7.17.

7.4.2 Experiments on the Reformer Start-up

Previous simulations showed that the starting-up time represents one of the most relevant factors in the dynamic behavior of the folded-sheet reformer unit. Due to the large heat capacity of the reformer, higher heat amounts are required for warming it up to operating temperature. If the heating rate is set too high, then the reactor material could suffer thermal stress, which could favor mechanical failure of the reactor casing and/or the internal metallic structures. On the other side, if the heating rate is set to low, the reactor warming-up step would take much more time as permitted. For the present experimental evaluation, heat generation at the combustion side was conservatively adjusted for the 10-kW (SRM) design specification.

7.4.2.1 Reactor Heat-Up

The initial heating-up offers the possibility of pre-conditioning the reforming catalyst by feeding a nitrogen/hydrogen mixture, as suggested by *Düsterwald et al.* [10]. Only nitrogen

is fed at the reforming side while the reactor is heated from ambient temperature up to about 150-200 °C. When the outer reactor temperature reached this temperature, a mixture of nitrogen/hydrogen is fed to the reformer to reduce the reforming catalyst (pre-conditioning). While the temperature in the reformer continues rising, the hydrogen-to-nitrogen ratio is progressively increased until only hydrogen is fed to the reactor.

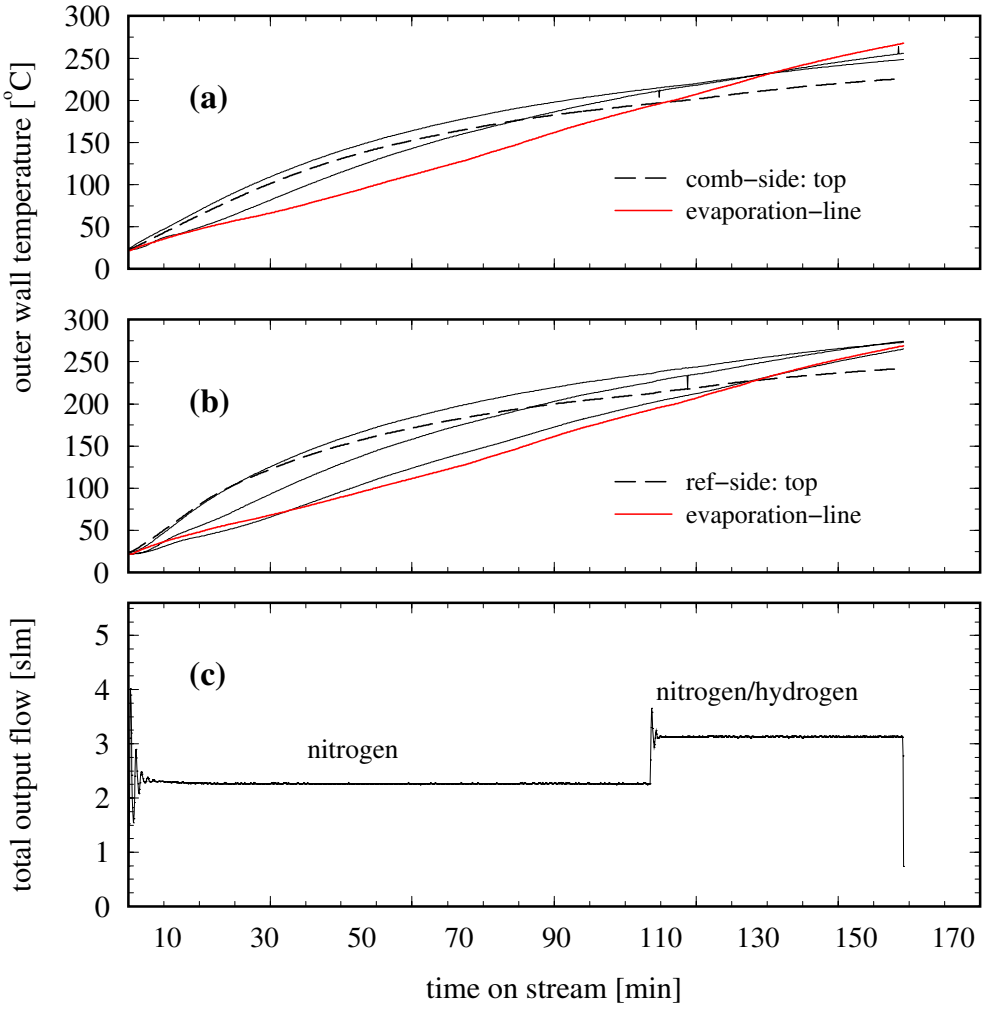

Figure 7.18: Dynamic behavior on the 10-kW reformer warm-up under the feed conditions specified in Table 7.9. **(a)** Figure gives the temperature profile of the combustion side reactor casing measured at positions defined in Figure 7.15. **(b)** Idem but on the reforming side. **(c)** Figure shows the mass flow rate at the reforming gas exit at two operating conditions: only nitrogen feed during the pre-heating phase and nitrogen/hydrogen feed during catalyst pre-conditioning.

In Figure 7.18 two graphs show the transient development of the reactor casing temperatures at start-up conditions and the output mass flow of the reforming side. Reactor casing temperatures measured at 10 different positions (see Figure 7.15) show a relatively slow increasing in time.

	parameter	value
reforming side		
	N_2 flow rate (t = 0...110 min)	2.5 slm
	N_2/H_2 flow rate (t = 110...170 min)	3.2 slm
combustion side		
	vol. flow rate of feed air	230 slm
	feed gas temperature	20 °C
side feed		
	feed gas temperature	20 °C
	H_2 flow rate at: (1)	0.90 slm
	(2)	0.90 slm
	(3)	0.70 slm
	(s)	0.75 slm
	(e)	1.0 slm

Table 7.9: Operating conditions for warm-up the 10-kW reformer and preconditioning the reforming catalyst (Figure 7.18). Stream labeling according to Figure 7.17.

It can be seen that the folded-sheet reformer needs about 100 minutes to reach a suitable operating temperature for starting the reforming reaction. This time results from setting conservative reaction conditions at the combustion side. Long cold-starting times must be avoided when attempting to incorporate such a hydrogen processor in a mobile fuel-cell system. For automotive applications rapid cold-start conditions are a prerequisite. Cold start time could be reduced by applying more severe reaction conditions on the combustion side. Such a test was not scheduled in the context of this work in order to avoid possible damages of the reactor which would impede further experimental evaluations.

7.4.2.2 Start of Reforming Reaction

Once the reactor is preheated to operating temperature and the catalyst is adequately preconditioned, methanol/water mixture is fed to the reformer. The reformer was tested under two operating conditions, see Table 7.10: (1) with a feed load for a nominal hydrogen production equivalent to 1.5 kW and (2) with an increased feed load for 2.5 kW. Conditions on the combustion side for the first reforming load were taken from the preconditioning stage (Section 7.4.2.1). For the reforming condition 2 the reaction parameters on the combustion side were not adjusted in order to evaluate the response of the reformer.

In the experiments the combustion side air feed flow rate was adjusted to a comparatively high value in order to reduce the reformate temperature towards its exit, expecting lower CO selectivities (see Section 6.1.2.4). The transient reformer wall temperatures as well as the total reformate output flow rate are plotted in Figure 7.19. In this figure the wall temperature

	parameter	value
reforming side		
	total flow rate (t = 0...40 min)	412.36 $\frac{g}{h}$ (1.5 kW)
	(t = 40...72 min)	687.26 $\frac{g}{h}$ (2.5 kW)
	S/M ratio	1.30 $\frac{mol}{mol}$

Table 7.10: Reaction parameters for experiments on the 10-kW reformer operating at two feed loading conditions (Figure 7.19). Operating conditions on the combustion side are taken from the preconditioning stage (Section 7.4.2.1, Table 7.9). Stream labeling according to Figure 7.17.

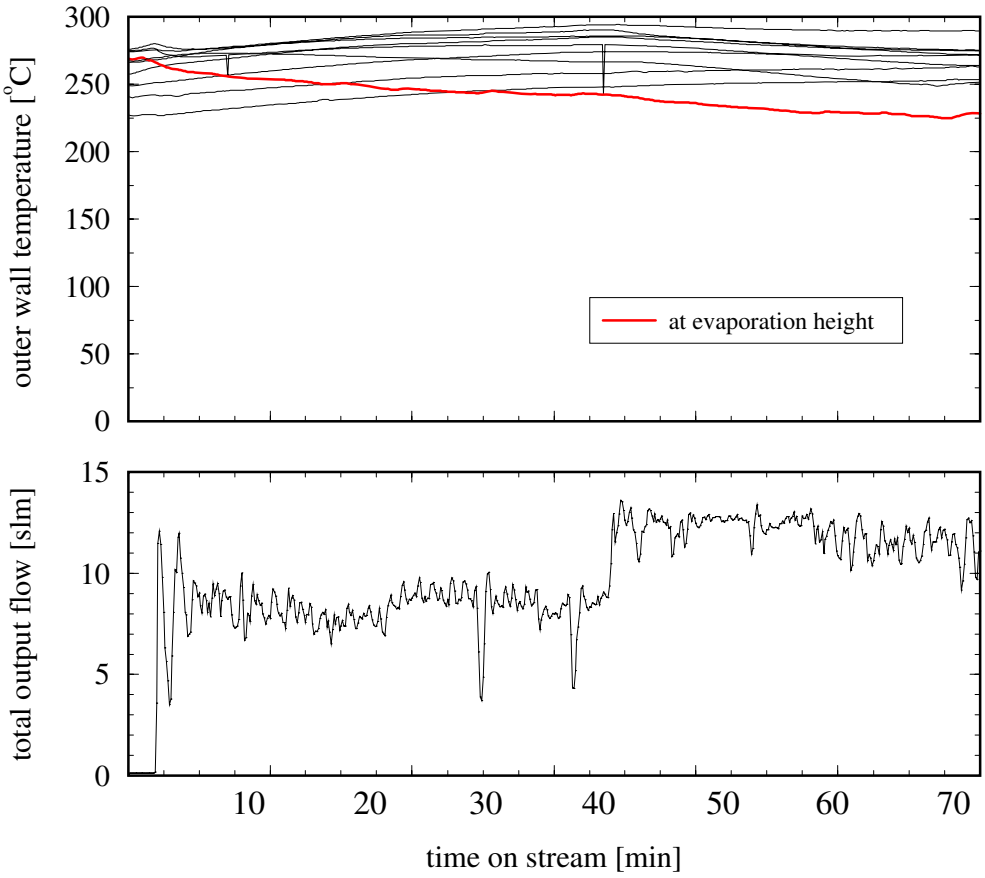

Figure 7.19: *Top:* Dynamic behavior during onset of reaction after reactor warm-up. Temperature profiles of the outer reformer wall measured at different positions (see reference points in Figure 7.15). *Bottom:* reformate flow rate. Operating conditions are given in Table 7.10.

corresponding to the evaporation section is drawn as a thick line. It can be noticed that the reforming reaction starts with a short dead time of 2 min after the liquid feed has been turned on. Some oscillations are observed initially and could be caused by instabilities in the evaporation section (see results in Section 6.2.4.1). After a short time the output flow

becomes stable. At this time, the reformer wall temperature remains slightly increasing with exception of the temperature corresponding to the evaporation section. Here the temperature starts to decrease steadily, indicating that the combustion gas (hydrogen) side feed at the evaporation section was too low to cover the high energy consumption of evaporation.

After about 40 minutes of operation liquid feed was increased for a hydrogen production equivalent to 2.5 kW, without properly adjusting the heat production on the combustion side (only hydrogen fed at the position $H_{(e)}$ was slightly increased). Now, not only the wall temperature of the evaporation section but all the reactor temperatures start to decrease slowly. The change of load provokes again an immediately change in the output stream, which stabilizes in a very short time. After a few minutes of overall operation some pulsations and declination in the output flow rate are observed in the output stream, revealing instabilities in the feed evaporation as a consequence of an insufficient heat supplying.

theoretical thermal power output	**reformate molar composition (dry gas)**			X_{MeOH}
$[kW]$	y_{H_2}	y_{CO_2}	y_{CO}	$[\%]$
1.5	0.7260	0.2481	0.0259	79.21
2.5	0.7310	0.2399	0.0291	67.38

Table 7.11: Experimental evaluation of the folded-sheet reformer at dynamic conditions. Reference data to Figure 7.19.

Quantitative results of this experiments are shown in Table 7.11. No total conversion was reached in the experiments. In addition the CO concentration in reformate was relatively high. The probable reasons for this behavior are: (a) the feed air flow rate was set too high, leading to lower operating temperatures inside the reformer. The low operating temperatures in the second half of the reformer length did not allow for total methanol conversion. Nevertheless possible temperature peaks in the first reforming zone could have caused high CO concentrations. Alternatively the high CO concentrations are again a result of too low catalyst activity and selectivity; (b) the no-adjustment of the operating conditions on the combustion side for the increased reforming load resulted in an instable evaporation.

7.4.3 Load Changes During Reformer Operation

After the reformer has been tested for low reforming load, further evaluations at increased load were carried out. This time, experiments for long-time operation were performed not only at a constant feed load but also with increasing/decreasing ramps in the mass flow rate of methanol/water feed. Because these elevated feed mass flow rates exceed the capacity of the liquid mass flow controllers employed in the previous experiments, rotameters with a capacity of 3 l/h methanol and water were installed.

Again, the process is started with the catalyst pre-conditioning phase (whilst the reformer is preheated) and, when the operating temperature is reached, methanol/water feed is

turned on. On the combustion side, hydrogen side feed was carefully adjusted for sufficient methanol conversions on the reforming side. As a limit for hydrogen side feed the overall wall temperature must not exceed the predefined level of 275 °C. First, operating conditions for a hydrogen output equivalent to 5 kW_{th} were adjusted. In successive steps the methanol/water feed flow rate was increased for 6, 7, and 10 kW. Operating conditions are summarized in table 7.12.

run	**liquid input**		S/M	**feed air**	H_2 **flow rate at**				
	methanol	**water**		**vol. flow rate**	(e)	(s)	(1)	(2)	(3)
	$[l/h]$	$[l/h]$	$\left[\frac{mol}{mol}\right]$	$[slm]$	$[slm]$	$[slm]$	$[slm]$	$[slm]$	$[slm]$
1	1.0	0.6	1.35	50	3.39	1.41	0.75	0.75	0.75
2	1.2	0.7	1.31	50	4.06	1.69	0.90	0.90	0.90
3	1.6	0.95	1.33	50	5.42	2.26	1.20	1.20	1.20
4	2.1	1.2	1.28	50	6.77	2.82	1.50	1.50	1.50

Table 7.12: Operating conditions for experiments with the 10-kW reformer operating under changes of feed load (Figure 7.20). Stream labeling according to Figure 7.17.

Product-gas flow rates measured for the different feed flow rates are plotted as a function of time in Figure 7.20. Results of the long-time operation behavior of the 10-kW reformer are depicted in Table 7.13. In the region (1) of the Figure it can be seen that the output flow rate increases abruptly from the pre-conditioning state up to the 5 kW operation in a very stable way. After a short initial oscillation, the output stream quickly reaches steady state, which remains constant over more than 1 hour of operating time. Poor methanol conversion was observed, probably because the hydrogen side feed on the combustion side were chosen too low.

run	**thermal power output**	**reformate molar composition (dry gas)**			X_{MeOH}
		y_{H_2}	y_{CO_2}	y_{CO}	$[\%]$
(1)	5	0.731	0.340	0.016	70
(2)	6	0.732	0.296	0.040	85
(3)	7	0.733	0.309	0.041	84
(4)	10	0.721	0.310	0.043	90

Table 7.13: Results of experimental evaluation of the 10-kW_{th} folded-sheet reformer for different loads at operating conditions listed in Table 7.12. Reference data to Figure 7.20.

Subsequently, higher liquid feeds where applied while simultaneously adjusting the hydrogen flow rates at the side-feeds for higher methanol conversions. Runs (2), (3) and (4)

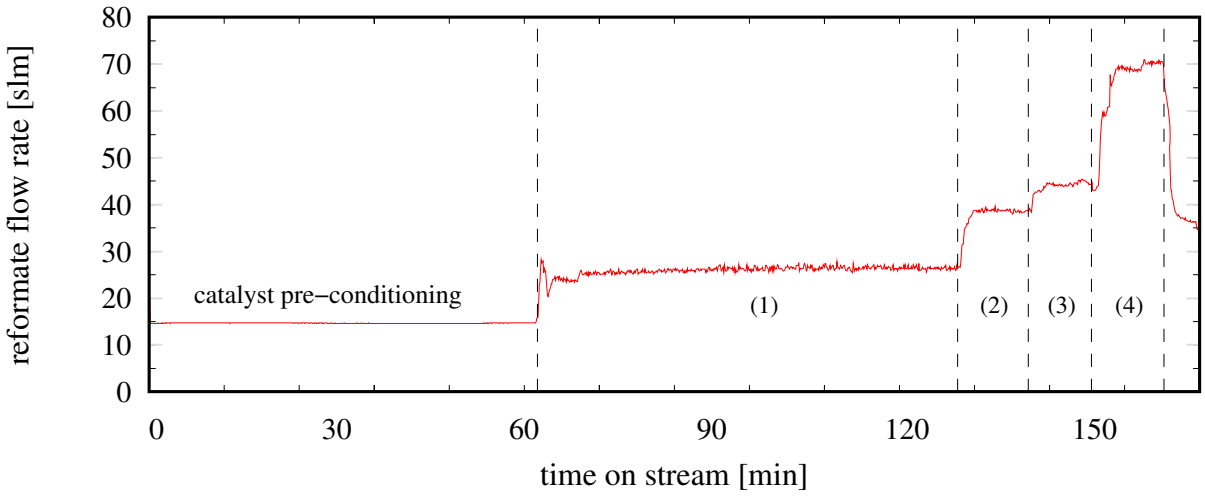

Figure 7.20: Long-time experimental behavior of the 10-kW reformer at different reforming loads, with successive adjustment of heat generated on the combustion side. Associated data in Table 7.13. Theoretical hydrogen output is depicted above the respective graphic area.

represent the transient to and the steady-state operation to the reformer operating for 6, 7 and 10 kW_{th} respectively. It can be observed that the output reformate flow follows the step load changes immediately, even at larger load changes (from 7 to 10 kW). As in the previous start-up experiments this is a direct consequence of the high heat capacity of the reformer which result only in slow changes of the reforming temperature. By adjusting the hydrogen side feed, higher methanol conversions were obtained at these increased load conditions. As expected higher methanol conversions again lead to higher CO outlet concentrations. Total methanol conversion (100 %) was not achieved within the temperature limits tested. The elevated CO concentrations can be attributed to a reforming catalyst with either a low activity, so that a higher temperature is necessary to achieve maximum methanol conversion, or a poor CO selectivity. Adequate catalyst activity and selectivity will be crucial for a further improvement of performance.

Closing Remark

The folded-sheet reformer prototype demonstrated a rapid output response to changes in the feed load. This dynamical behavior becomes important when attempting to develop a hydrogen-producing device for fuel cell applications for the automotive sector.

In summary, the operating temperature in the reformer unit can be easily influenced and adjusted by the combustion side feed, demonstrating that the overall heat transfer is no longer the limiting step. The successful integration and validation of liquid feed evaporation and vapor overheating is an additional important benefit of the experimental evaluation. The resulting integrated reactor design can be usable in a large range of applications.

Appendixes

In the following complementary information to this work is presented. First the general derivation of the mass and energy balance equations used for modelling the folded-sheet reactor is given. Afterwards important information on the reaction and transport parameters and properties, as well as the modeling of the geometry of the folded-sheet reactor concept are given. A simplified balance of the reaction system (idealized) is stated, which was the basis for the first reaction evaluation and understanding. An additional experimental evaluation of the first protype of the 1-kW folded-sheet reactor is presented as complement to the evaluation described in the previous chapters. Finally technical drawings and photographs of the diverse reformer development steps are shown as documentation of the entire work.

Appendix A

General Derivation of the Balance Equations

For the derivation of the overall balance equations an infinitesimal volume element as in Fig. A.1 is considered. The mass and energy fluxes entering in, and outgoing from this balance element as well as the mass and energy formation and/or consumption inside the control volume are equated and represented in the general form of a parabolic partial differential equation.

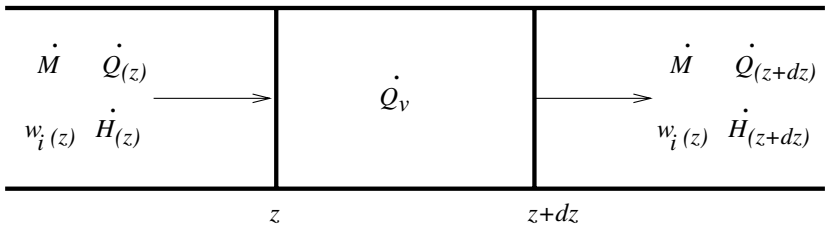

Figure A.1: Balance element for the derivation of the mass and energy balance equations.

A.1 Mass Balance

The mass flux of the specie *i* in gaseous state consists of a convective and a dispersive term:

$$\dot{M}_i^{conv} = \rho(z)\ v(z)\ A\ w_i \tag{A.1}$$

$$\dot{M}_i^{diff} = -D_{ax}^{eff} A \frac{\partial w_i}{\partial z}. \tag{A.2}$$

Herein represent $\rho(z)$ the density and $v(z)$ the gas flux velocity at the position z, while w_i denotes the mass fraction of the component i. The coefficient D_{ax}^{eff} takes into consideration the dispersion effect.

When balancing all the convective and diffusive in and out flows, the change in the mass of the component i in the infinitesimally volume section is as follows:

$$\frac{\partial m_i}{\partial t} = \dot{M}_i^{conv}(z) - \dot{M}_i^{conv}(z+dz) + \dot{M}_i^{diff}(z) - \dot{M}_i^{diff}(z+dz) + d\dot{Q}. \tag{A.3}$$

The source term $d\dot{Q}$ considers the change of the mass of i due to chemical reaction. Developing the terms of outgoing mass flux according to the Taylor Series and truncating at the linear term leads to:

$$\dot{M}(z+dz) = \dot{M}(z) + \frac{\partial \dot{M}}{\partial z}\bigg|_z dz. \tag{A.4}$$

Substituting eqn. A.4 in eqn. A.3, the following expression is obtained:

$$\frac{\partial m_i}{\partial t} = -\frac{\partial \dot{M}_i^{conv}}{\partial z}\bigg|_z dz - \frac{\partial \dot{M}_i^{diff}}{\partial z}\bigg|_z dz + d\dot{Q}. \tag{A.5}$$

By introducing the definitions of both the convective and the diffusive mass fluxes results in:

$$\begin{aligned} w_i \frac{\partial\left(\rho(z) dz A\right)}{\partial t} + \rho(z) dz A \frac{\partial w_i}{\partial t} &= -\left(w_i \frac{\partial\left(\rho(z) v(z) A\right)}{\partial z} + \rho(z) v(z) A \frac{\partial w_i}{\partial z} \right)\bigg|_z dz \\ &\quad + \frac{\partial}{\partial z}\left(D_{ax}^{eff} A \frac{\partial w_i}{\partial z} \right)\bigg|_z dz + d\dot{Q}. \end{aligned} \tag{A.6}$$

When applying a global mass balance for the sum of all component masses the dispersion and source terms drop out because the overall mass flux remains constant. This leads to the continuity equation, which is represented by:

$$\frac{\partial\left(\rho(z) dz A\right)}{\partial t} = -\frac{\partial\left(\rho(z) v(z) A\right)}{\partial z}\bigg|_z dz. \tag{A.7}$$

The final mass balance equation employed in the modeling of the reaction system is obtained by substituting the expression A.7 into the equation A.6, followed by the division by Adz, the substitution of the specific mass flux $\dot{m}_z = \rho(z)v(z)$, and the inclusion of the definition of the volume-related source-term $\dot{Q}_V = \frac{d\dot{Q}}{Adz}$:

$$\boxed{\rho(z)\frac{\partial w_i}{\partial t} = -\dot{m}_z \frac{\partial w_i}{\partial z} + \frac{\partial}{\partial z}\left(D_{ax}^{eff} \frac{\partial w_i}{\partial z} \right) + \dot{Q}_V.} \tag{A.8}$$

If we consider the continuity equation to be in (quasi) steady state, the specific mass flux ($\dot{m}_z$) remains constant and independent of the state variables along the control volume. In Chapter 4 (Section 4.3) only the steady state mass balances will be used since, compared to the wall energy balances, the fluid balances are in quasi-steady state.

A.2 Energy Balance

The change of the internal energy U in a control volume as depicted in Figure A.1 is the result of the changes caused by the incoming and outgoing fluid streams (internal energy and performed expansion work for each process stream) and the heat transport by conduction. If changes in the kinetic and potential energy are neglected a general energy balance can then be stated as follows:

$$Adz\frac{\partial(u\rho)}{\partial t} = \dot{H}(z) - \dot{H}(z+dz) + \dot{Q}(z) - \dot{Q}(z+dz), \tag{A.9}$$

Developing the enthalpy flux and heat conduction terms until the linear elements of a Taylor Series gives:

$$\dot{H}(z+dz) = \dot{H}(z) + \frac{\partial \dot{H}}{\partial z}\bigg|_z dz \tag{A.10}$$

$$\dot{Q}(z+dz) = \dot{Q}(z) + \frac{\partial \dot{Q}}{\partial z}\bigg|_z dz. \tag{A.11}$$

Introducing these terms in equation A.9 results:

$$Adz\frac{\partial(u\rho)}{\partial t} = -\frac{\partial \dot{H}}{\partial z}\bigg|_z dz - \frac{\partial \dot{Q}}{\partial z}\bigg|_z dz. \tag{A.12}$$

With the definition equation for the axial thermal conduction

$$\dot{Q} = -\lambda_{ax} A\frac{\partial T}{\partial z} \tag{A.13}$$

and introducing the specific enthalpy h,

$$\dot{H} = \dot{m}h = \rho v A h \tag{A.14}$$

the following relationship results

$$\frac{(\partial \rho u)}{\partial t} = -\frac{\partial(\rho v h)}{\partial z} + \frac{\partial}{\partial z}\left(\lambda_{ax}\frac{\partial T}{\partial z}\right). \tag{A.15}$$

The internal energy can be eliminated by $h = u + pv^v = u + \frac{p}{\rho}$, leading to:

$$\frac{\partial(\rho h - p)}{\partial t} = -\frac{\partial(\rho v h)}{\partial z} + \frac{\partial}{\partial z}\left(\lambda_{ax}\frac{\partial T}{\partial z}\right). \tag{A.16}$$

If the pressure is considered constant, the differentiation leads to:

$$\rho\frac{\partial h}{\partial t} + h\frac{\partial \rho}{\partial t} = -\rho v\frac{\partial h}{\partial z} - h\frac{(\rho v)}{\partial z} + \frac{\partial}{\partial z}\left(\lambda_{ax}\frac{\partial T}{\partial z}\right). \tag{A.17}$$

Introducing the continuity equation developed in the previous section (eqn. A.7), the following simplification is obtained:

$$\rho\frac{\partial h}{\partial t} + \rho v\frac{\partial h}{\partial z} = \frac{\partial}{\partial z}\left(\lambda_{ax}\frac{\partial T}{\partial z}\right). \tag{A.18}$$

By employing the appropriate definition of the substantial derivation in time ($\frac{D}{Dt} = \frac{\partial}{\partial t} + v\frac{\partial}{\partial z}$) results:

$$\rho\frac{Dh}{Dt} = \frac{\partial}{\partial z}\left(\lambda_{ax}\frac{\partial T}{\partial z}\right). \tag{A.19}$$

Because the enthalpy of the participating component i depends on the temperature and the mass fraction of i, the total derivative of h can be developed as follows:

$$Dh = \frac{\partial h}{\partial T}\Big|_{w_i} DT + \sum_i \frac{\partial h}{\partial w_i}\Big|_{T,p,w_{k\neq i}} Dw_i. \tag{A.20}$$

At constant internal (reactor) pressure the enthalpy varies only with the temperature and the composition of the fluid stream. Under consideration of the definition of the specific heat capacity:

$$\frac{\partial h}{\partial T}\Big|_{p,w_i} = c_p \tag{A.21}$$

and by introducing the partial mass related enthalpy of component i

$$\frac{\partial h}{\partial w_i}\Big|_{T,P,w_{k\neq j}} = h_i \tag{A.22}$$

the following equation results

$$\rho c_p\frac{DT}{Dt} + \rho\sum_i h_i\frac{Dw_i}{Dt} = \frac{\partial}{\partial z}\left(\lambda_{ax}\frac{\partial T}{\partial z}\right). \tag{A.23}$$

The time derivation of the concentration can be eliminated by introducing the mass balance equation (eqn. A.8), leading to:

$$\rho\frac{Dw_i}{Dt} = \rho\frac{\partial w_i}{\partial t} + \rho v\frac{\partial w_i}{\partial z} = \frac{\partial}{\partial z}\left(D_{ax}\frac{\partial w_i}{\partial z}\right) + \sum_j \left(\nu_{ji} M_i r_j \frac{m_{cat}}{V}\right). \tag{A.24}$$

Here the source term $\dot{Q}_V$ was substituted by the term that describes the changes in the concentration due to the chemical reactions j. After regrouping the summands and solving the substantial derivatives results:

$$\rho c_p\frac{\partial T}{\partial t} + \rho v c_p\frac{\partial T}{\partial z} + \sum_i \left[\frac{\partial}{\partial z}\left(D_{ax}\frac{\partial w_i}{\partial z}\right) + \sum_j \left(\nu_{ij} M_i r_j \frac{m_{cat}}{V}\right)\right] = \frac{\partial}{\partial z}\left(\lambda_{ax}\frac{\partial T}{\partial z}\right) \tag{A.25}$$

By including the definition of the reaction enthalpy

$$\Delta H_{r,j} = \sum_i \nu_{ij} h_i M_i \tag{A.26}$$

the desired energy balance equation is obtained

$$\boxed{\rho c_p\frac{\partial T}{\partial t} = -\rho v c_p\frac{\partial T}{\partial z} + \frac{\partial}{\partial z}\left(\lambda_{ax}\frac{\partial T}{\partial z}\right) - \sum_i h_i\frac{\partial}{\partial z}\left(D_{ax}\frac{\partial w_i}{\partial z}\right) + \frac{m_{cat}}{V}\sum_j r_j\left(-\Delta H_{r,j}\right)} \tag{A.27}$$

The term that describes the energy transport due to diffusion is neglected for the calculations performed in this work.

Appendix B

Reaction Parameters and Geometry of the Folded-Sheet Reactor

For establishing the mass and energy balances for methanol steam-reforming in the folded-sheet reactor, the following reaction system properties and reactor dimensioning were considered.

B.1 Reactor Geometry

The balance equations developed in Chapter 5 represent only the mass and energy transfer relationships for both combustion and reforming channels. In these equations, the geometrical parameters are varied in order to optimize the reactor performance. The parametrical model employed for describing the folded-sheet reactor geometry is based on variable widths and heights as depicted in Figure B.1.

In this figure a schematic cut of the reactor cross section is given. The combustion and reforming channel of height h_{ref} and h_{fg} respectively, the channel width (b_s),the folded-sheet (separating wall) of thickness s, the corrugated spacers and the reactor casing of thickness s_c can be identified. In the simplest case, both reforming and combustion channels have only one spacer and their heights are:

$$h_{ref} = h_{fg} = h_{ch}. \tag{B.1}$$

In general, the channel high on the reforming side depends on the number of spacer structures inserted in. Taking as base the standard channel height, then:

$$h_{ref} = n_{sp/ch}\, h_{ch}. \tag{B.2}$$

The geometrical model is used for the determination of the phase fractions in a volume element (ε) and the specific transfer area between neighboring phases (a^v). The definition of the phase fractions and specific transfer areas is illustrated in Figure B.2.

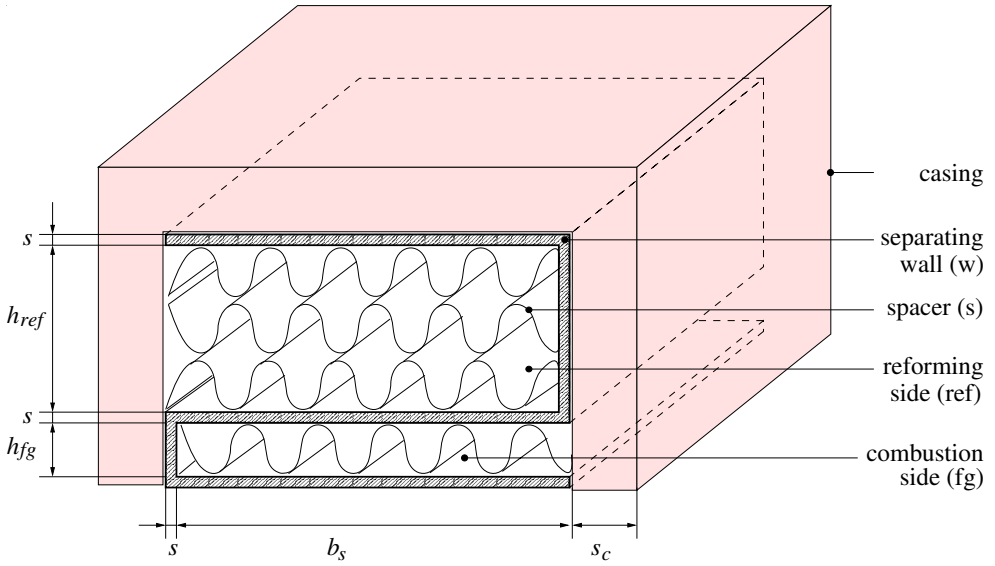

Figure B.1: Reference sketch on the geometrical parameters of two neighbored channels for modeling the folded-sheet reactor.

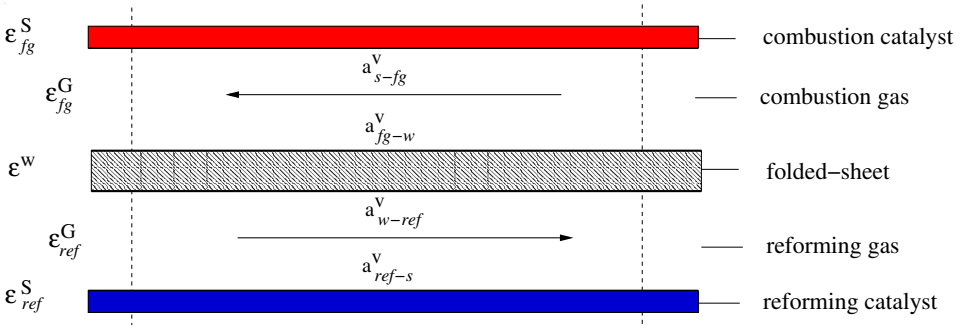

Figure B.2: Phase fractions and specific transfer areas in a balance element.

B.1.1 Spacer Geometry and Reactor Total Volume

Before proposing the general correlations for the phase fractions and specific areas, two important variables have first to be declared: the transfer area and the cross section of a spacer structure, as well as the reactor total volume.

As the spacer structure does not present a regular, easy to measure (particularly when filled in the channels) geometry, a general approximation based on the dimensions depicted in Figure B.3 has to be stated. Here a sine-like shape is proposed for the frontal section of a spacer metal-sheet.

A first simplification consists in the similarity of the spacer cross section with a triangle of base λ (wave length) und height a (amplitude). So the total length (perimeter) of all subsequent triangles b^o_{sp} is given by:

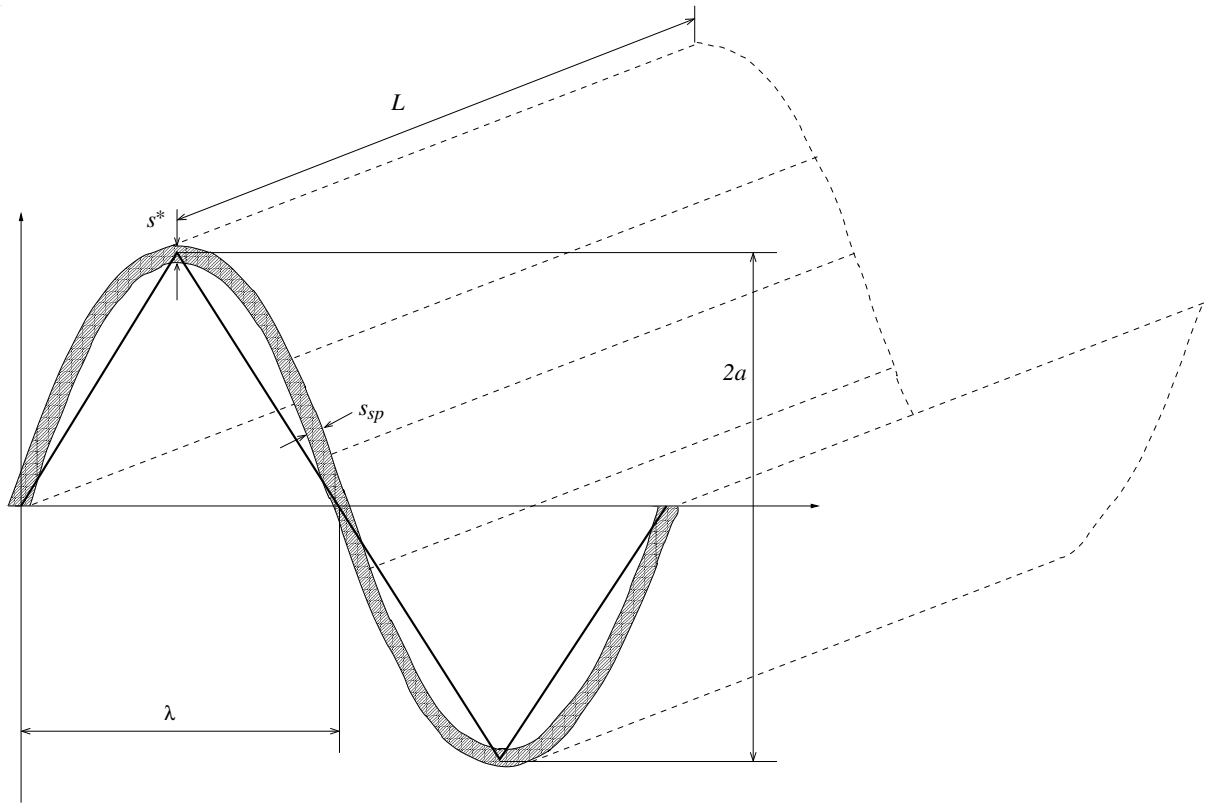

Figure B.3: Simplified geometrical model of the spacer structure.

$$b_{sp}^{o} = n_a \, 4 \sqrt{a^2 + \frac{\lambda^2}{4}}, \tag{B.3}$$

where n_a is the number of waves of amplitude $2a$ present per total channel width (Fig. B.3).

Now, the simplified mathematical model for the mass transfer area of the spacer (including an additional factor of 2 because both sides are in flow contact) is, with L as the reactor length:

$$\boxed{A_{sp} = b_{sp}^{o} \, L = 2 \left(n_a \, 4 \sqrt{a^2 + \frac{\lambda^2}{4}} \right) \, L} \tag{B.4}$$

For the spacer cross section the same proposed triangle is used to define the form of the frontal shape. The thickness of the metal foil is s_{sp} and its thickness in the curvature (as defined in Figure B.4) is s^*. *A first proposal* for the cross section area of the spacer is defined by:

$$A^o_{sp} = s_{sp}\, b^o_{sp} = s_{sp}\, \left(n_a\, 4\, \sqrt{a^2 + \frac{\lambda^2}{4}} \right). \tag{B.5}$$

An additional thought considers that a section of an extended triangle (similar to that stated above) has an area $A^{section}_{sp}$ as shown in Figure B.4.

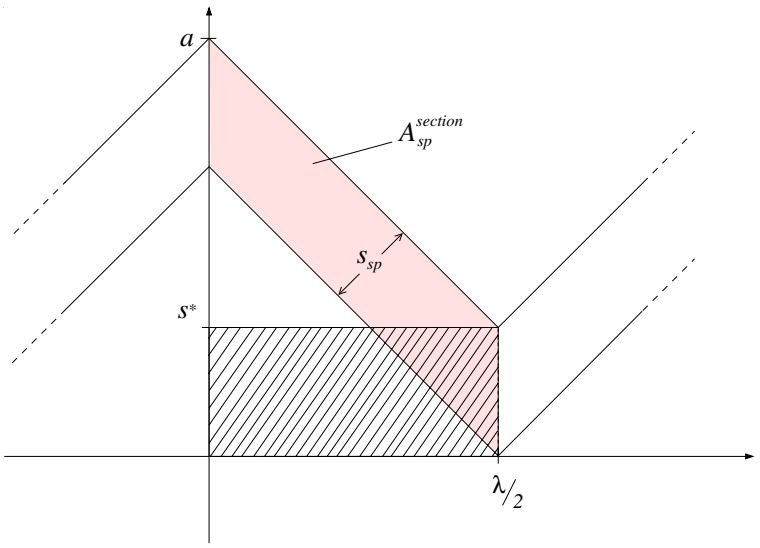

Figure B.4: Second simplified geometrical model of the spacer structure.

It is easy to mathematically demonstrate that for the spacer section proposed:

$$A^{section}_{sp} = \frac{\lambda}{2} \cdot s^*. \tag{B.6}$$

From the triangle formed by s_{sp} and s^* follows:

$$s^* = \sqrt{2}\, s_{sp}. \tag{B.7}$$

If the statement before is true then one can also extend this formula for the overall channel width, which is occupied for one spacer structure as follows:

$$A^o_{sp} = b_s \cdot s^* = b_s \cdot \sqrt{2} \cdot s_{sp}. \tag{B.8}$$

For the simulations, the calculation of the cross section area of one spacer structure the first formulation (equation B.5) is used.

On the other hand, the total volume of the reactor per unit of length ($V^L_{tot} = V_{tot}/L$) is given by the following formula, considering that each reforming channel is embedded in

two combustion channels (single volume unit) and the whole is covered by a four-sided reactor insulation:

$$V_{tot}^{L} = (b_s + 2s_c + s)\left[n_{ref}h_{ref} + (n_{ref}+1)\,h_{fg} + 2\,(n_{ref}+1)\,s + 2s_c\right] \tag{B.9}$$

where n_{ref} is the number of reforming gas and $(n_{ref}+1)$ the number of combustion gas channels.

B.1.2 Phase Volumetric Fraction

Generally, the volumetric fraction of the phase ph is calculated in this work by the general correlation $\varepsilon^{ph} = \left[\frac{volume\ of\ phase\ ph}{total\ reactor\ volume}\right]$.

The formulas for the calculation of the phase fraction of respectively wall, reforming gas, combustion gas, reforming catalyst and combustion catalyst are developed in the following, assuming that the number of spacers are only varied in the reforming channel:

Reactor Wall

$$\varepsilon^{W} = \frac{s\ \left[2\left(n_{ref}+1\right)\left(b_s+s\right)+n_{ref}h_{ref}+\left(n_{ref}+1\right)h_{fg}\right]}{V_{tot}^{L}} \tag{B.10}$$

$$+ \frac{s_c\ \left[2s_c+s+b_s+2\left(n_{ref}+1\right)s+n_{ref}h_{ref}+\left(n_{ref}+1\right)h_{fg}\right]}{V_{tot}^{L}} \tag{B.11}$$

Reforming Catalyst

$$\varepsilon_{ref}^{S} = \frac{n_{ref}\ n_{\frac{sp}{ch}}\ 4\ n_a\ s_{sp}\ \sqrt{a^2+\frac{\lambda^2}{4}}}{V_{tot}^{L}} \tag{B.12}$$

Combustion Catalyst

$$\varepsilon_{fg}^{S} = \frac{\left(n_{ref}+1\right)\ 4\ n_a\ s_{sp}\ \sqrt{a^2+\frac{\lambda^2}{4}}}{V_{tot}^{L}}. \tag{B.13}$$

Reforming Gas

$$\varepsilon_{ref}^{G} = \frac{n_{ref}\ h_{ref}\ b_s}{V_{tot}^{L}} - \varepsilon_{ref}^{S} \tag{B.14}$$

Combustion Gas

$$\varepsilon_{fg}^{G} = \frac{\left(n_{ref}+1\right)\ h_{fg}\ b_s}{V_{tot}^{L}} - \varepsilon_{fg}^{S} \tag{B.15}$$

parameter	value
s	0.5 mm
s_c	3 mm
b_s	40 mm
h_{ref}	1.2 $\cdot$ $n_{\frac{sp}{ch}}$
h_{fg}	1.2 mm
n_{ref} (reference)	20 / $n_{\frac{sp}{ch}}$

Table B.1: Parameters on reactor geometry.

parameter	value
$2a$	1.2 mm
λ	1.2 mm
n_a	17 [-]
s_{sp}	0.1 mm

Table B.2: Parameters on spacer geometry.

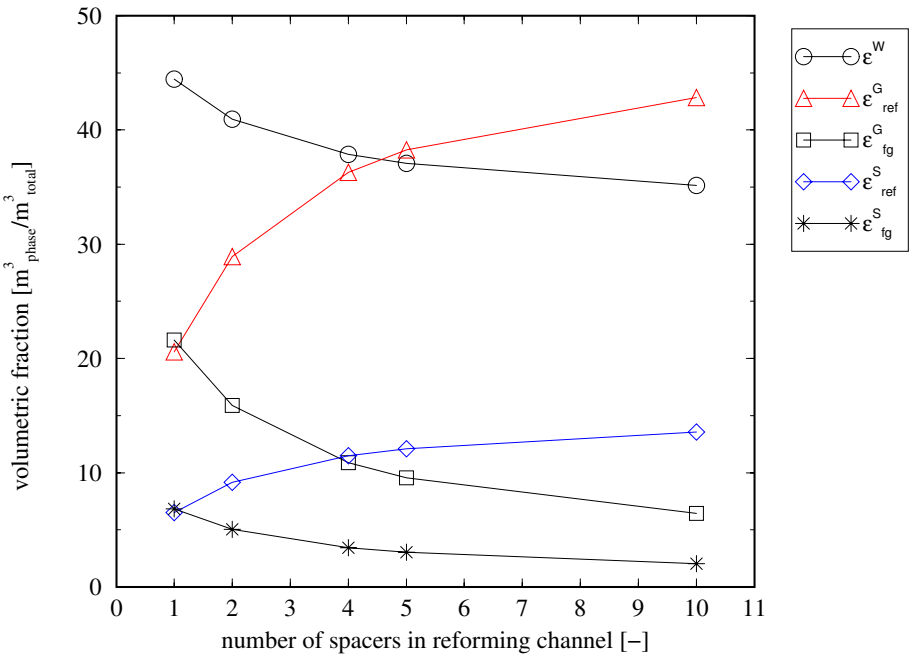

Figure B.5: Variation of the volumetric fractions of the involved phases with respect to the number of spacers in the reforming channel. Calculation parameters in Tables B.1-B.2.

B.1.3 Specific Transfer Area

For the calculation of the specific area for transfer between 2 phases, a general correlation of the form $a^v = \left[\frac{transfer\ surface}{total\ reactor\ volume}\right]$. Then, the models proposed for each involved phase are:

Transfer Area Wall-Reforming Gas

$$a^v_{ref,W} = \frac{2\, n_{ref}\, (b_s + s + h_{ref})}{V^L_{tot}} \tag{B.16}$$

Transfer Area Wall-Combustion Gas

$$a^v_{fg,W} = \frac{2\ (n_{ref} + 1)\, (b_s + s + h_{fg})}{V^L_{tot}} \tag{B.17}$$

Transfer Area Reforming Gas-Catalyst

$$a^v_{ref,S} = \frac{2\ \left(4\, n_{sp/ch}\, n_{ref}\, n_a\, \sqrt{a^2 + \frac{\lambda^2}{4}}\right)}{V^L_{tot}} \tag{B.18}$$

Transfer Area Combustion Gas-Catalyst

$$a^v_{fg,S} = \frac{2\ \left[4\ (n_{ref} + 1)\ n_a\, \sqrt{a^2 + \frac{\lambda^2}{4}}\right]}{V^L_{tot}} \tag{B.19}$$

Transfer Area Casing-Surroundings

$$a^v_{jack} = \frac{2\ [(b_s + 2s_c + s) + n_{ref} h_{ref} + (n_{ref} + 1)\, h_{fg}]}{V^L_{tot}} \tag{B.20}$$

$$+ \frac{2\ [2\, (n_{ref} + 1)\, s + 2s_c]}{V^L_{tot}} \tag{B.21}$$

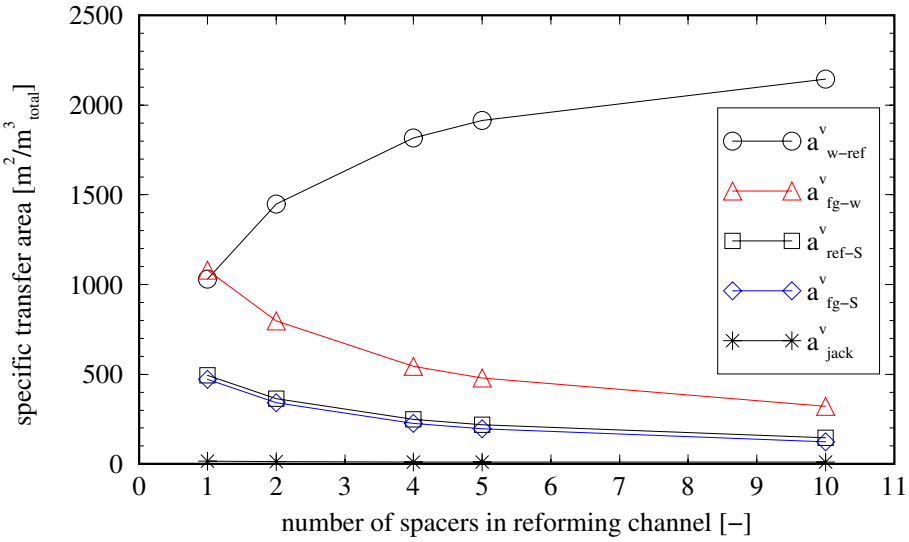

Figure B.6: Graphical illustration of the variation of the specific transfer area with the number of spacers per channel. Calculation parameters in Tables B.1-B.2

B.2 Transport Parameters and Material Properties

B.2.1 Specific Heat Capacity

For the calculation of the heat capacity of (real) gases pressure influence is neglected. $c^*_{p,j} = f(T) \neq f(p)$. Hence, c_p can be mathematically determined in a good extent by a polynomial function of T as follows:

$$C^*_{p,j}(T^G) = \alpha^*_j + \beta^*_j T + \gamma^*_j T^2 \qquad \left[\frac{J}{molK}\right], \tag{B.22}$$

where α^*_j, β^*_j and γ^*_j are the compound-specific coefficients, see literature source [70]. A short list with the compound parameters is given in Table B.3. The calculated molar heat capacity must be converted to mass-related units, so the molar weight (M_j) is used:

$$c^*_{p,j} = \frac{C^*_{p,j}}{M_j} \qquad \left[\frac{kJ}{kgK}\right]. \tag{B.23}$$

The specific heat capacity of the entire gas stream at both reforming and combustion side was calculated by weighting the heat capacity of the pure gaseous components involved (eqn. B.23) with the respective gas weight fractions [57]:

$$\overline{c}^G_p(z,t) = \sum_{j=1}^{J} w_j(z,t)\; c^*_{p,j}(T^G). \tag{B.24}$$

For the heat capacity of the solid phase (reactor casing, folded-sheet and spacers) stainless steel is assumed. A standard value of

$$c_{p,w} = c^S_p = 0.5\;\frac{kJ}{kg\;K} \tag{B.25}$$

is taken.

For changes in the specific heat capacity of the species considered over temperature see Figure B.7. It can be noticed that the heat capacity of hydrogen (○) is remarkable higher as those of the rest of the participants. Almost all species show a relatively constant heat capacity over the temperature range. Only methanol (□) tends to slightly increase at higher temperatures.

B.2.2 Solid Density

Similar to the heat capacity and the thermal conductivity, for the solid phase a constant value of density is assumed. Properties for standard stainless steel are considered [57].

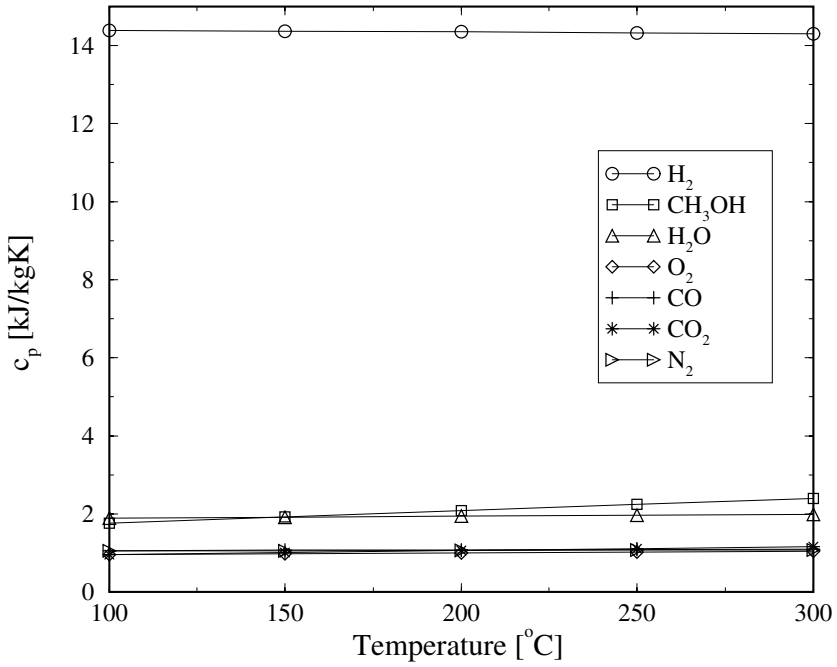

Figure B.7: Variation of c_p with the temperature for all involved species.

$$\varrho^S = 7880 \, \frac{kg}{m^3}. \tag{B.26}$$

B.2.3 Effective Axial Dispersion

Since no reliable formula for axial dispersion in the corrugated spacer structures of Figure 3.8 is available and since the influence of axial dispersion at the flow velocities considered is known to be small, a pragmatic approach has been applied.

The axial dispersion coefficient was adjusted to such a high value that numerical instabilities during simulation of the hydrogen combustion are sufficiently dampened. Such instabilities arise due to the rapid combustion reaction which leads to negative concentrations unless the simulation grid is extremely fine.

In consequence the effective axial dispersion coefficient was set to:

$$D_{ax,ref}^{eff} = 3.0 \cdot 10^{-3} \, \frac{m^2}{s}. \tag{B.27}$$

B.2.4 Effective Axial Thermal Conductivity

It is well known that the thermal conductivity at the gas phase is negligible as compared to that of the solid phase. It is therefore again set to a value which helps to stabilize the

numerical simulation results.

The value assumed is:

$$\lambda_{ax}^{G} \approx 1 \frac{W}{mK}. \tag{B.28}$$

The thermal conductivity of the solid phase (reactor casing, folded-sheet and spacers) is assumed to be constant, and the following reference value for stainless steel [57] is employed for the calculations:

$$\lambda_{ax}^{S}(T = 293K) = 21 \, \frac{W}{mK}. \tag{B.29}$$

B.2.5 Convective Heat and Mass Transfer Coefficients

In general, the heat transfer is described by the *Nusselt* correlation, defined by the equation:

$$Nu = \frac{\alpha \, d_{h,sp}}{\lambda^{G}(T^{G})} \tag{B.30}$$

Heat Transfer Fluid-Reactor Wall (Folded-Sheet)

Assuming laminar flow through parallel plates, the resulting wall Nusselt number is [71]:

$$Nu = 7.55, \tag{B.31}$$

and the hydraulic diameter (as a function of the channel height):

$$d_{h,sp} = 2h_{ch}. \tag{B.32}$$

The thermal conductivity variations of the single components with respect to the temperature are assumed to follow Sutherland's laws for gases [72]. Sutherland's parameters are listed in Table B.3. Hereby, the thermal conductivity rises with the gas temperature (T^{G}) as follows:

$$\lambda_j(T^{G}) = \lambda_0 \cdot \frac{T_0 + T_{Su}}{T^{G} + T_{Su}} \cdot \left(\frac{T^{G}}{T_0} \right)^{\frac{3}{2}}. \tag{B.33}$$

For the gas mixture the thermal conductivity is calculated by employing the following weighting formula [73]:

$$\lambda^{G}(T^{G}) = \frac{\sum_j \lambda_j y_j \sqrt{M_j}}{\sum_j y_j \sqrt{M_j}}. \tag{B.34}$$

Substituting the thermal conductivity of the gas mixture, the convective heat transfer coefficient fluid-wall on the combustion and reforming channel ($\alpha^w_{ref},\ \alpha^w_{fg}$) can be determined. In the simulation tool, α^w_{ch} is calculated explicitly, depending on the state variables. Since the influence of the spacers on the flow field has been neglected in the above derivation, it can only be considered a conservative (minimum heat transfer) approximation.

Heat Transfer Fluid-Spacer

No mathematical correlation exists for the calculation of the convective heat transfer coefficient from spacer structure to the gas phase. Assuming that the spacer structures enhance the heat transfer between these phases, due to their elevated heat transfer (and contact) area, a large value for the heat transfer coefficient is preset:

$$\alpha^S_{ref} = \alpha^S_{fg} = 200\ \frac{W}{m^2 K}. \tag{B.35}$$

Mass Transfer Fluid-Spacer

Due to typical limitations by mass transfer of the hydrogen combustion reaction (combustion side), the mass transfer coefficient from gas phase to solid phase (catalyst) can be introduced, using analogy to the heat transfer coefficient:

$$Nu = Sh = \frac{\beta\ d_{h,sp}}{D_{ax}} \tag{B.36}$$

For the calculations, a typical value for this mass transfer coefficient is assumed:

$$\beta_{O_2} = \beta_{H_2} = 0.2\ \frac{m}{s} \tag{B.37}$$

On the reforming side, the same value is fixed as a constant $\beta_{ref} = 0.2\ \frac{m}{s}$.

B.2.6 Calculation of the Chemical Equilibrium Constant

The chemical equilibrium constants (K_i^{eq} and K^*) employed in the modeling of the kinetic of the reaction system (Section 2.6.3) were calculated as in [70]. This estimation bases on the definition of the temperature-dependence of the equilibrium constant:

$$K(T) = exp\left(-\frac{\Delta g^0_R(T)}{\mathbb{R}T}\right). \tag{B.38}$$

The changes in Gibbs free energy are stated for an operating temperature T:

$$\Delta g^0_r(T) = \Delta h^*_R(p^0, T) - T\Delta s^*_R(T). \tag{B.39}$$

Here the reaction enthalpy and standard entropy are calculated as follows:

$$\Delta h_R(p^0,T) = \sum_j \nu_j h_j^*(p^0,T) = \sum_j \nu_j \left(\Delta h_j^0(p^0,T^0) + \int_{T^0}^{T} c_{p,j}^*(p^0,T)dT \right) \quad \text{(B.40)}$$

$$\Delta s_R(T) = \sum_j \nu_j s_j^*(T) = \sum_j \nu_j \left(s_j^0(p^0,T^0) + \int_{T^0}^{T} \frac{c_{p,j}^*(p^0,T)}{T} dT \right). \quad \text{(B.41)}$$

In both cases the correction of the reaction enthalpy and standard entropy due to pressures $p \neq p^0$ is neglected. A list of the most important parameters employed for the calculation of diverse material and compound properties is given in Table B.3.

B.2.7 Pool on Chemical Data

		CH_3OH	H_2O	H_2	O_2	CO	CO_2	N_2
Molecular weight								
M_j	$\left[\frac{kg}{kmol}\right]$	32.00	18.00	2.00	32.00	28.00	44.00	28.00
Heat capacity [70]								
α_j^*	$\left[\frac{J}{molK}\right]$	18.40	30.38	29.09	25.74	26.88	26.02	27.31
$\beta_j^* \cdot 10^3$	$\left[\frac{J}{molK^2}\right]$	101.64	9.62	-0.84	12.99	6.97	43.53	5.23
$\gamma_j^* \cdot 10^6$	$\left[\frac{J}{molK^3}\right]$	28.70	1.18	2.01	-3.86	-0.82	-14.84	-0.0042
Enthalpy of formation and standard entropy (at 298.15 K and 1.013 bar) [70]								
Δh_j^0	$\left[\frac{kJ}{mol}\right]$	-201.20	-241.80	0.00	0.00	-110.50	-393.50	0.00
Δs_j^0	$\left[\frac{J}{molK}\right]$	237.70	188.72	130.60	205.00	197.91	213.64	191.50
Thermal conductivity (*Sutherland*) [72]								
$\lambda_j(T_0)$	$\left[\frac{W}{mK}\right]$	0.023	0.023	0.163	0.025	0.023	0.015	0.024
T_0	$[K]$	300.00	300.00	300.00	300.00	300.00	300.00	300.00
T_{Su}	$[K]$	177.00	177.00	166.00	222.00	177.00	222.00	166.00

Table B.3: Compound specific parameters used for the calculations.

B.2.8 *Peppley's* Kinetic Data

	Peppley		in this work
	k_i^∞ $(\frac{m^2}{s\ mol})$	E_i $(\frac{kJ}{mol})$	k_i^∞ $(\frac{m^2}{s\ mol})$
k_1 $(\frac{m^2}{s\ mol})$	7.4E+14	102.8	20.0E+14
k_2 $(\frac{m^2}{s\ mol})$	3.8E+20	170.0	38.0E+20
k_3^* $(\frac{m^2}{s\ mol})$	5.9E+13	87.6	2.0E+13

Table B.4: Parameters for Calculating the Rate Constants according to [5] (*Arrhenius Expression* $k_i = k_i^\infty e^{-\frac{E_i}{\mathbb{R}T}}$) and values of the frequency factor k^∞ determinated in Chapter 4.

	ΔS_i $(\frac{J}{mol\ K})$	ΔH_i $(\frac{kJ}{mol})$
$K^*_{CH_3O^{(1)}}$ $(bar^{-0.5})$	-41.8	-20.0
$K^*_{OH^{(1)}}$ $(bar^{-0.5})$	-44.5	-20.0
$K_{H^{(1a)}}$ $(bar^{-0.5})$	-100.8	-50.0
$K^*_{HCOO_2^{(1)}}$ $(bar^{-1.5})$	179.2	100.0
$K^*_{CH_3O^{(2)}}$ $(bar^{-0.5})$	30.0	-20.0
$K^*_{OH^{(2)}}$ $(bar^{-0.5})$	30.0	-20.0
$K_{H^{(2a)}}$ $(bar^{-0.5})$	-46.2	-50.0

Table B.5: Parameters for Calculating the Absorption Constants for Intermediate Species according to [5] (*van't Hoff Expression* $K_i^* = e^{\frac{\Delta S_i^*}{\mathbb{R}} - \frac{\Delta H_i^*}{\mathbb{R}T}}$).

Appendix C

Overall Balances for the (idealized) 10-kW Reformer

C.1 Overall balances of the 10-kW reformer under the conditions specified in Table C.1.

Assumptions	
thermal power generation	10 kW
S/M-ratio	1.3 [-]
methanol conversion	100 $\%$
CO_2/CO molar ratio (selectivity)	12
combustion side air-feed	100 slm
feed temperature	25 °C
reforming temperature	285 °C

Table C.1: Initial assumptions for the theoretical calculation of mass and energy balances for SRM. Graphical reference in Figure C.1 (page 169).

Reactor Inflow	
required methanol	50.93 mol/h
required water	66.21 mol/h
$y^+_{CH_3OH}$	0.435
$y^+_{H_2O}$	0.565
$w^+_{CH_3OH}$	0.578
$w^+_{H_2O}$	0.422

Table C.2: Reforming side inflow stream for conditions listed in Table C.1.

ξ_1	47.01
ξ_2	3.92

Table C.3: Calculated extent of the involved independent reactions (methanol reforming and decomposition) for conditions listed in Table C.1.

Reactor Outflow	
unreacted methanol	0.00 mol/h
unreacted water	19.20 mol/h
produced hydrogen	55.61 slm
	148.46 mol/h
produced CO	3.92 mol/h
produced CO_2	47.01 mol/h
Dry Gas Composition	
y_{H_2}	0.745
y_{CO}	0.020
y_{CO_2}	0.235
Wet Gas Composition	
y_{CH_3OH}	0.000
y_{H_2O}	0.088
y_{H_2}	0.668
y_{CO_2}	0.215
y_{CO}	0.018

Table C.4: Reforming side outflow stream for conditions listed in Table C.1.

Properties	
$\Delta h^0_{CH_3OH}$	49.50 $\frac{kJ}{mol}$
$\Delta h^0_{H_2O}$	241.83 $\frac{kJ}{mol}$
$\Delta h_{v,CH_3OH}$	1100.00 $\frac{kJ}{kg}$
$\Delta h_{v,H_2O}$	2257.30 $\frac{kJ}{kg}$
$\Delta h^+_{v,ref}$	1588.80 $\frac{kJ}{kg}$
c_{p,CH_3OH}	2.68 $\frac{kJ}{kgK}$
c_{p,H_2O}	4.17 $\frac{kJ}{kgK}$
$c^+_{p,ref}$	3.30 $\frac{kJ}{kgK}$

Table C.5: Reaction heat, heat of vaporization and heat capacity of the reforming side feed for conditions listed in Table C.1.

Process Heat		
$\Delta\dot{Q}_{evap}$	4482.68 $\frac{kJ}{h}$	(0.47 %)
	1.25 kW	
$\Delta\dot{Q}_{overh}$	1867.39 $\frac{kJ}{h}$	(0.20 %)
	0.52 kW	
$\Delta\dot{Q}_{ref}$	3148.50 $\frac{kJ}{h}$	(0.33 %)
	0.87 kW	
$\Delta\dot{Q}_{total}$	9498.57 $\frac{kJ}{h}$	
	2.64 kW	

Table C.6: Calculated required heat for evaporation, overheating and reaction on the reforming side for conditions listed in Table C.1.

Combustion Hydrogen			
$\dot{N}_{H_2,evap}$	18.54 $\frac{mol}{h}$	$\rightarrow$ 6.92 slm	$\rightarrow$ 407.31 $sccm$ per injector
$\dot{N}_{H_2,overh}$	7.74 $\frac{mol}{h}$	$\rightarrow$ 2.88 slm	$\rightarrow$ 169.68 $sccm$ per injector
$\dot{N}_{H_2,ref}$	13.02 $\frac{mol}{h}$	$\rightarrow$ 4.86 slm	$\rightarrow$ 95.36 $sccm$ per injector
$\dot{N}_{H_2,total}$	26.26 $\frac{mol}{h}$	$\rightarrow$ 9.81 slm	

Table C.7: Necessary combustion of hydrogen for covering the heat requirements for conditions listed in Table C.6.

C.2 Mass and heat flow diagram

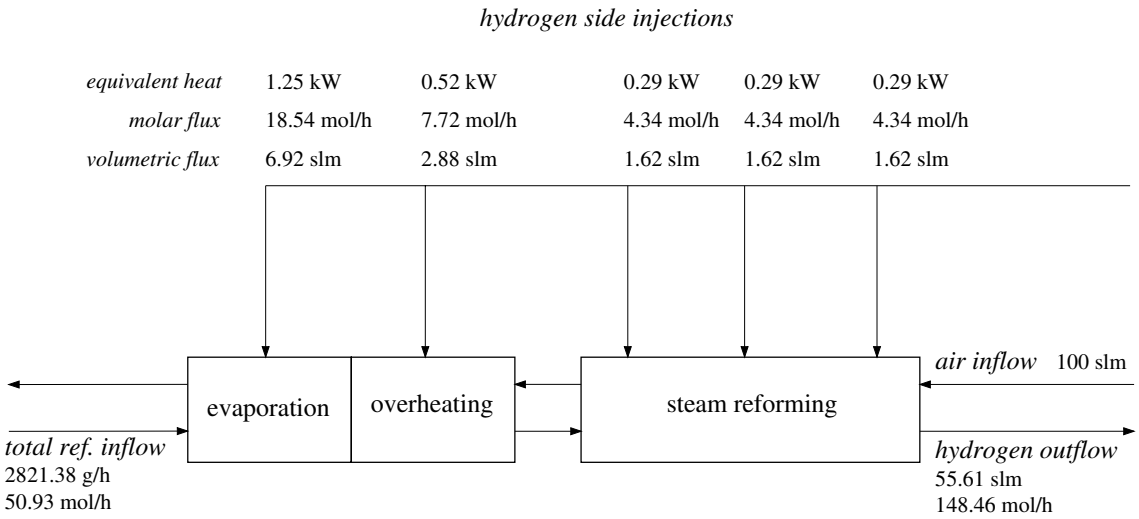

Figure C.1: Graphical overview of the stream definitions for the 10-kW SRM. Conditions are listed in Table C.1.

Appendix D

Complementary Experimental Evaluation of the 1-kW Folded-Sheet Reformer

D.1 Fixed Hydrogen Combustion - Variable Electrical Heating

Based on the experimental setup described in section 6.1.3.2, additional experiments on the heat input for the reforming reaction will be reported. Here the hydrogen flow rate in the side-feed ports is kept constant while the set-up temperature of the electrical heating band along the second half of the reformer is varied. The scheme of the experimental configuration is shown in Figure D.1. Methanol/water mixture enters the reformer at T$\approx$ 200 °C. In general, the hot-spot observed in the experiments of section 6.1.3 is present here again. Maximum reforming gas temperature around the combustion zone averages 340 °C. Heating band temperature is varied in order to evaluate the reaction performance under these operating conditions (profiles P8-P13). Further reaction conditions and experimental results on the methanol conversion and reformate gas composition are given in Table D.1.

At lower heating-band temperatures (run P8) a poor methanol conversion of 32 $\%$ is observed. At this temperature level carbon monoxide is produced in elevated amounts (3.7 vol $\%$). When increasing the setup temperature of the heating band, methanol conversion improves up to 86 $\%$ (see profile P12). The CO concentration still remains high (3.6 vol $\%$). Starting from this "warmed-reactor" state the heating band temperature is set to 150 °C (see profile P13). While the methanol conversion remains acceptably high the CO concentration slightly goes back to 3.4 vol $\%$.

This observed behavior reveals that influencing the form of the temperature profile is an appropriate way to optimize the reactor performance. The temperature level reached in the first half of the reactor defines to a great extent the conversion of methanol. On the other hand, CO, once generated in the first reactor section, cannot be easily reduced by WGS. The temperature profile in the second half of the reactor has to be gradually decreased to about 150 °C, to provide optimal conditions for the reverse water-shift reaction.

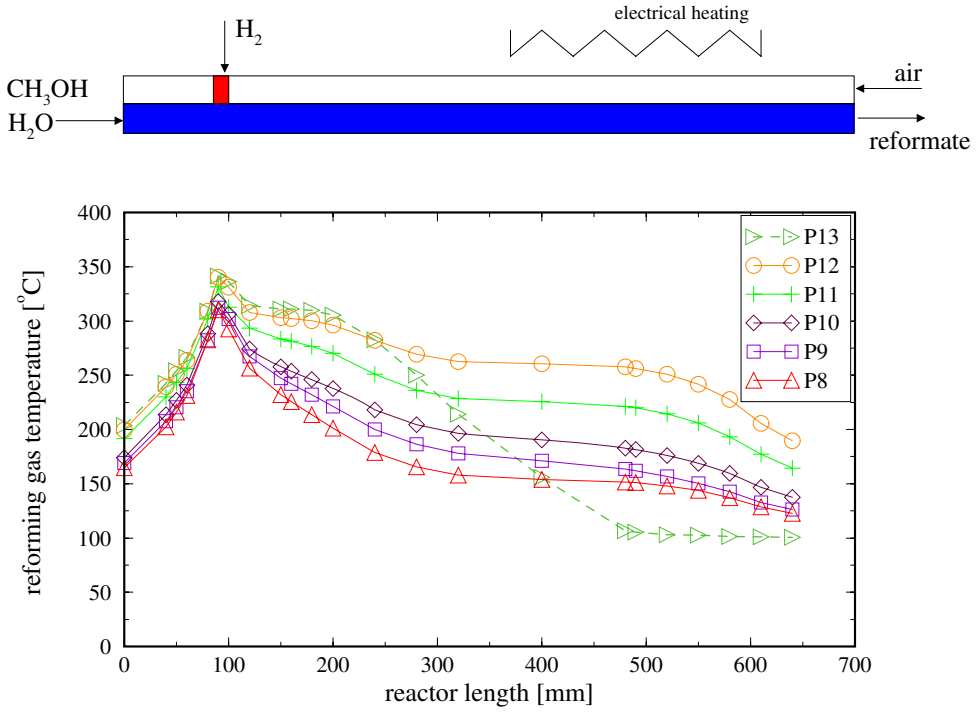

Figure D.1: Measured reforming gas temperature profile. Constant hydrogen flow rate on the combustion side and variable set-up temperature of the electrical heating. Reaction conditions: see Table D.1.

run	$\dot{V}_{H_2}^{side}$	**T**^{set}	**reformate gas composition**			**output gas flow**	X_{MeOH}
	$[slm]$	[°C]	y_{H_2}	y_{CO_2}	y_{CO}	$[slm]$	$[\%]$
P8	0.3	160	0.723	0.240	0.037	2.34	32.0
P9	0.3	180	0.722	0.237	0.037	2.76	37.4
P10	0.3	200	0.723	0.235	0.037	3.22	43.5
P11	0.3	240	0.722	0.235	0.036	4.97	66.9
P12	0.3	280	0.722	0.235	0.036	6.41	86.2
P13	0.3	150	0.719	0.229	0.034	6.16	84.0

Table D.1: Single hydrogen combustion zone coupled with variable electrical heating: product quality and reaction performance. Reaction parameters: $\dot{m}_{CH_3OH,ref} = 158.0\ g/h$, $\dot{m}_{H_2O,ref} = 121\ g/h$, $\dot{V}^{+}_{air,fg} = 7.5\ slm$.

Appendix E

Technical Drawings

In the present section construction drawings for all developed prototypes are presented. These technical drawings show not only main measures of the apparatus but also in some cases, related construction steps.

The drawing sequence covers all experimental devices used from the first experiments with the plug-flow tubular reactor, through intermediate steps regarding the construction of the first folded evaporator with glass-plate-cover (for visualization) the larger-scale folded-sheet evaporator over the first reformer unit for 1-kW output power up to the 10-kW folded sheet reformer prototype.

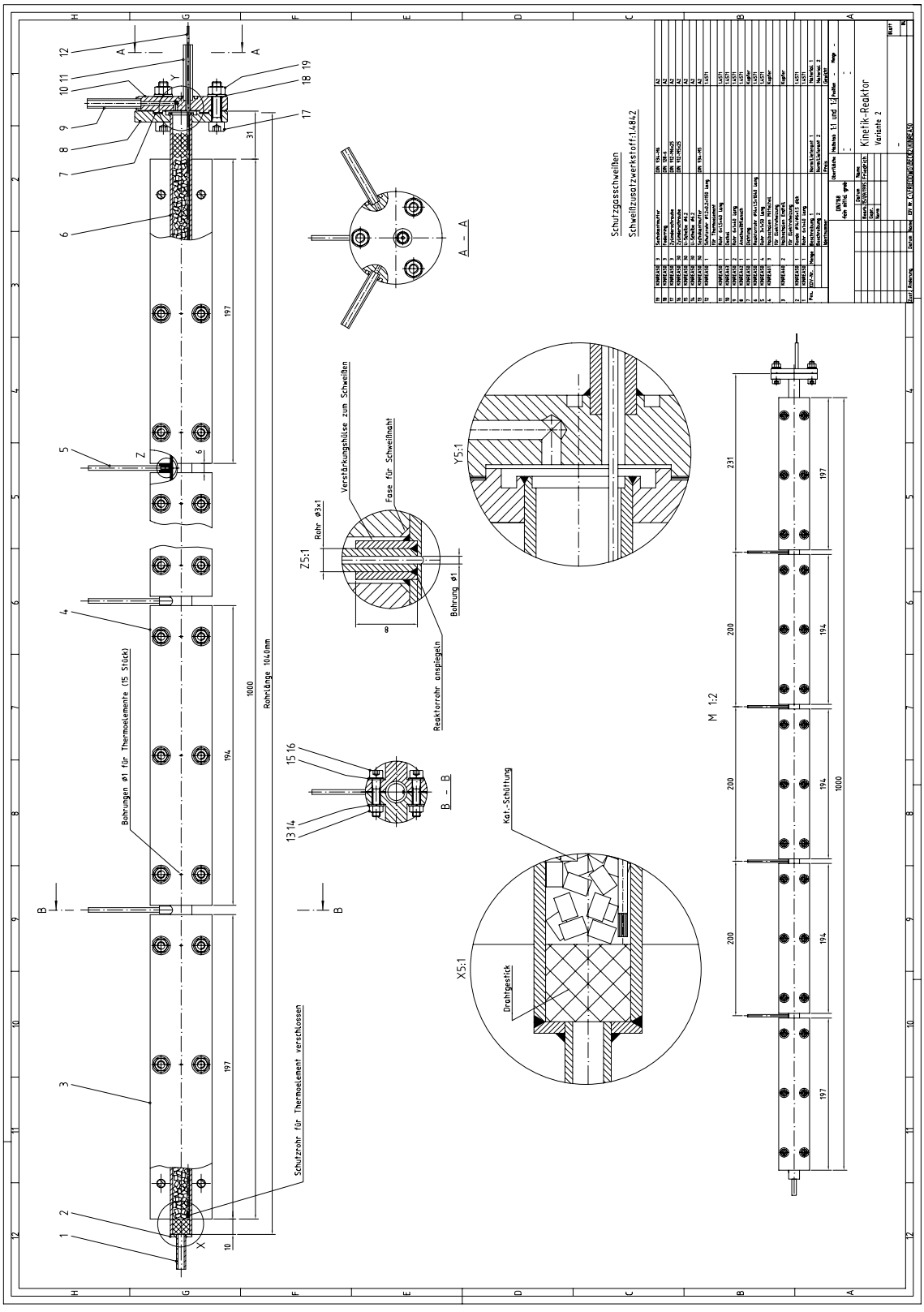

Figure E.1: Construction drawing of the catalytic fixed-bed (tubular) reactor. **Description** (from left to right): longitudinal structuring of the reactor including casing shells, connectors and catalyst location; detailed drawings of some specific cuts (see reference points); general overview of the reactor including axial dimensioning and positioning of the sample ports.

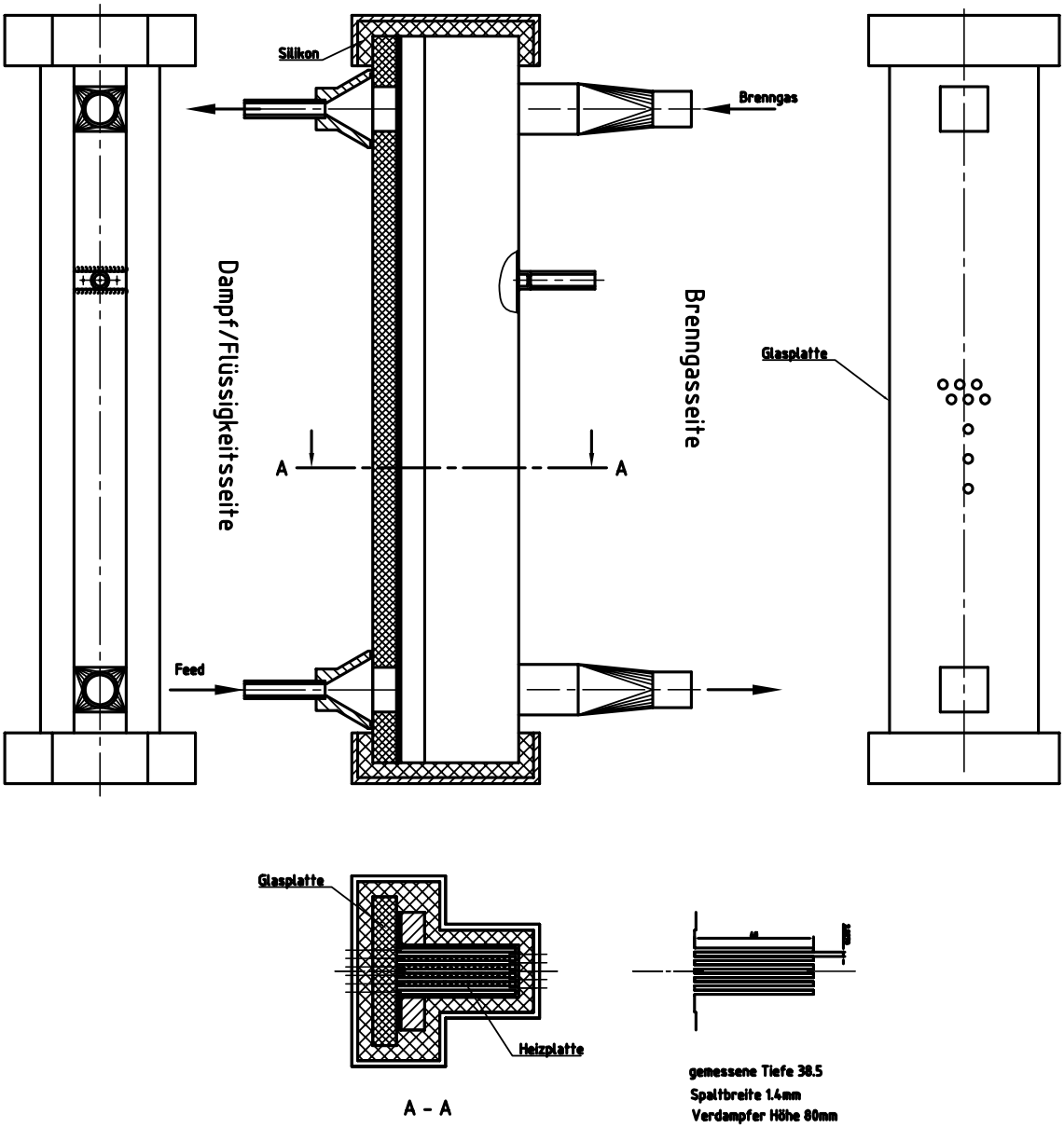

Figure E.2: Design drawings and details on the catalytic countercurrent folded-sheet "*Glass-Plate*" evaporator. **Upper drawings** *(from left to right):* rear, side, and front view of the evaporator unit. Note that the figure corresponding to the back view of the evaporator unit shows the connectors of feed and off-gas on the combustion side. The front view of the evaporator shows the glass plate and its respective connectors. The combustion gas side feed port can be better recognized from the side view (intermediate connector). **Lower drawings:** top view of the evaporator unit, and top view of the folded-sheet core structure.

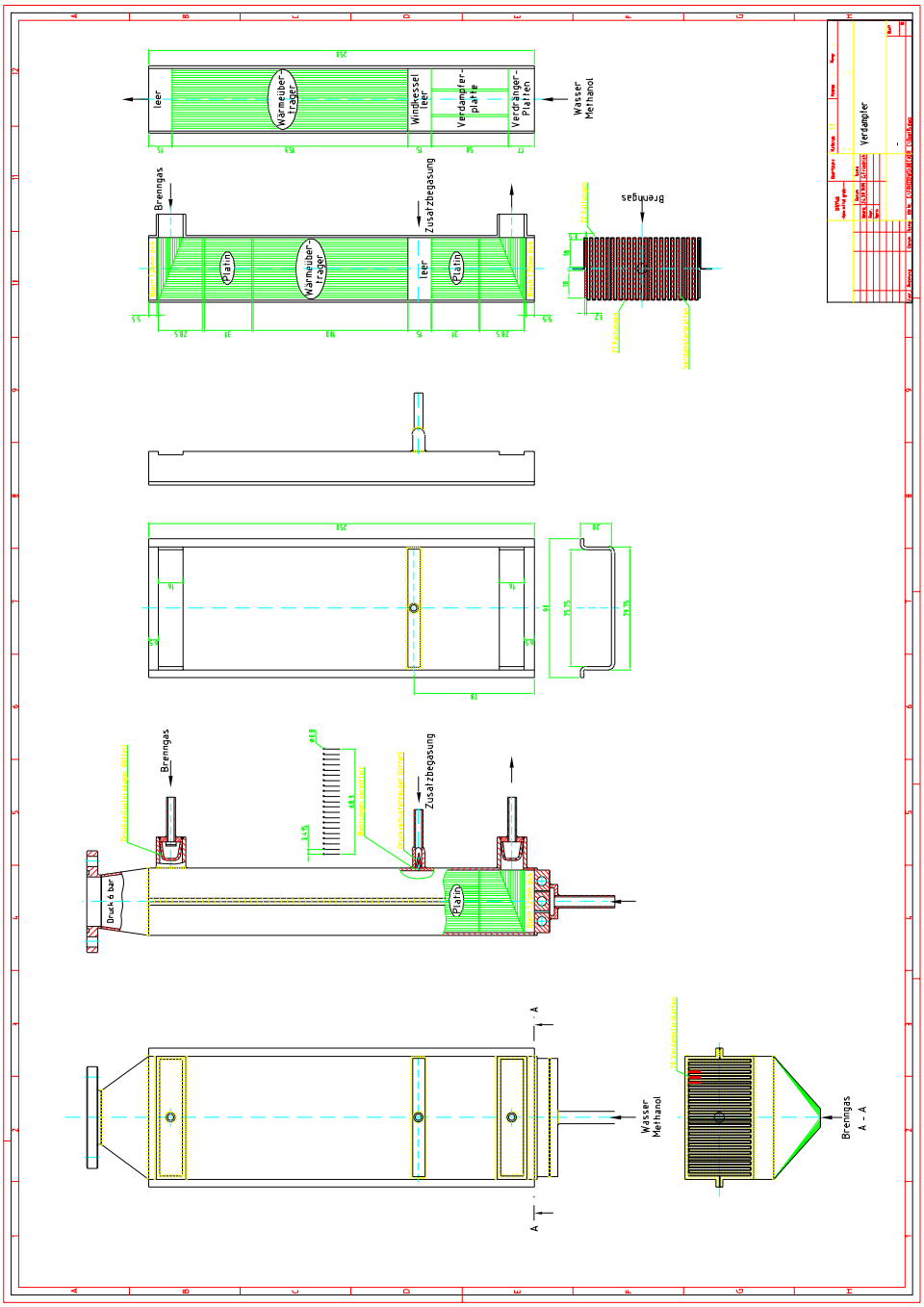

Figure E.3: Catalytic Countercurrent Folded-Sheet Evaporator. **Description** *(from left to right):* rear (combustion side) and side view of the evaporator; apparatus casing shells; and axial catalyst/spacer distribution.

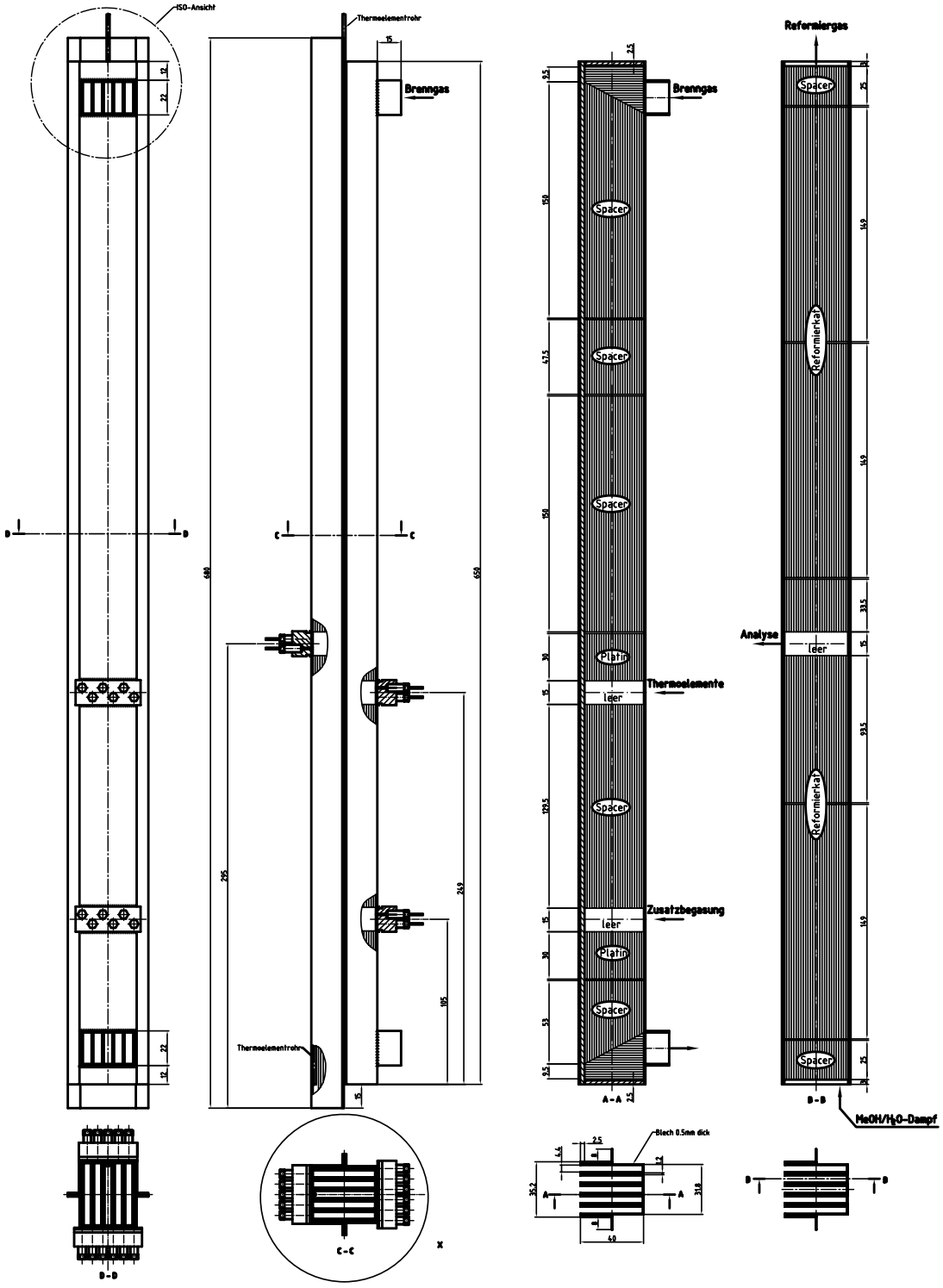

Figure E.4: 1-kW Counter-current reformer (1st version). Note that the reformer has two side feeds on the combustion side in addition to the feed/exit ports at each end of the reactor. The feed/exit to the reforming channels is axially through the bottom/top. **Description** *(from left to right):* front view of the combustion side with 2 fuel gas injection ports; side view (left reforming side, right combustion side); axial structuring combustion side; and axial structuring reforming side.

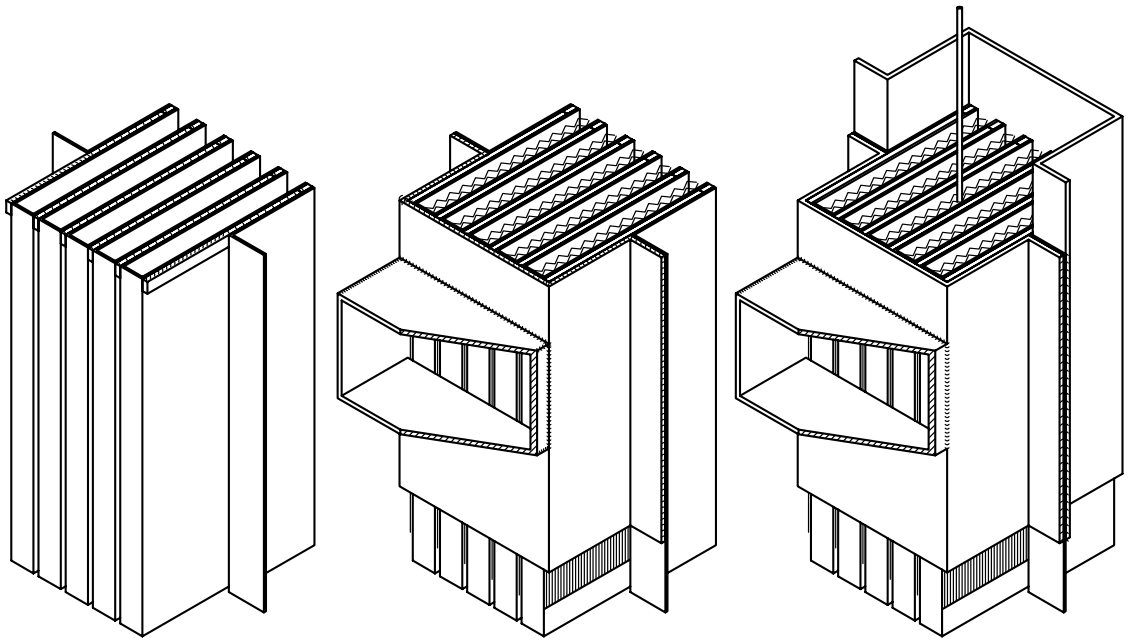

Figure E.5: 1-kW Counter-current reformer (1st version). Design details of the core folded sheet structure and reactor casing with the drawing concept of the feed/exit port on the combustion side. Notice the sealing of the top openings of all combustion gas channels, which allows feed the reforming side from the top. In the center of the middle reforming channel a thermocouple capillary tube for measuring of the axial temperature in the channel can be recognized.

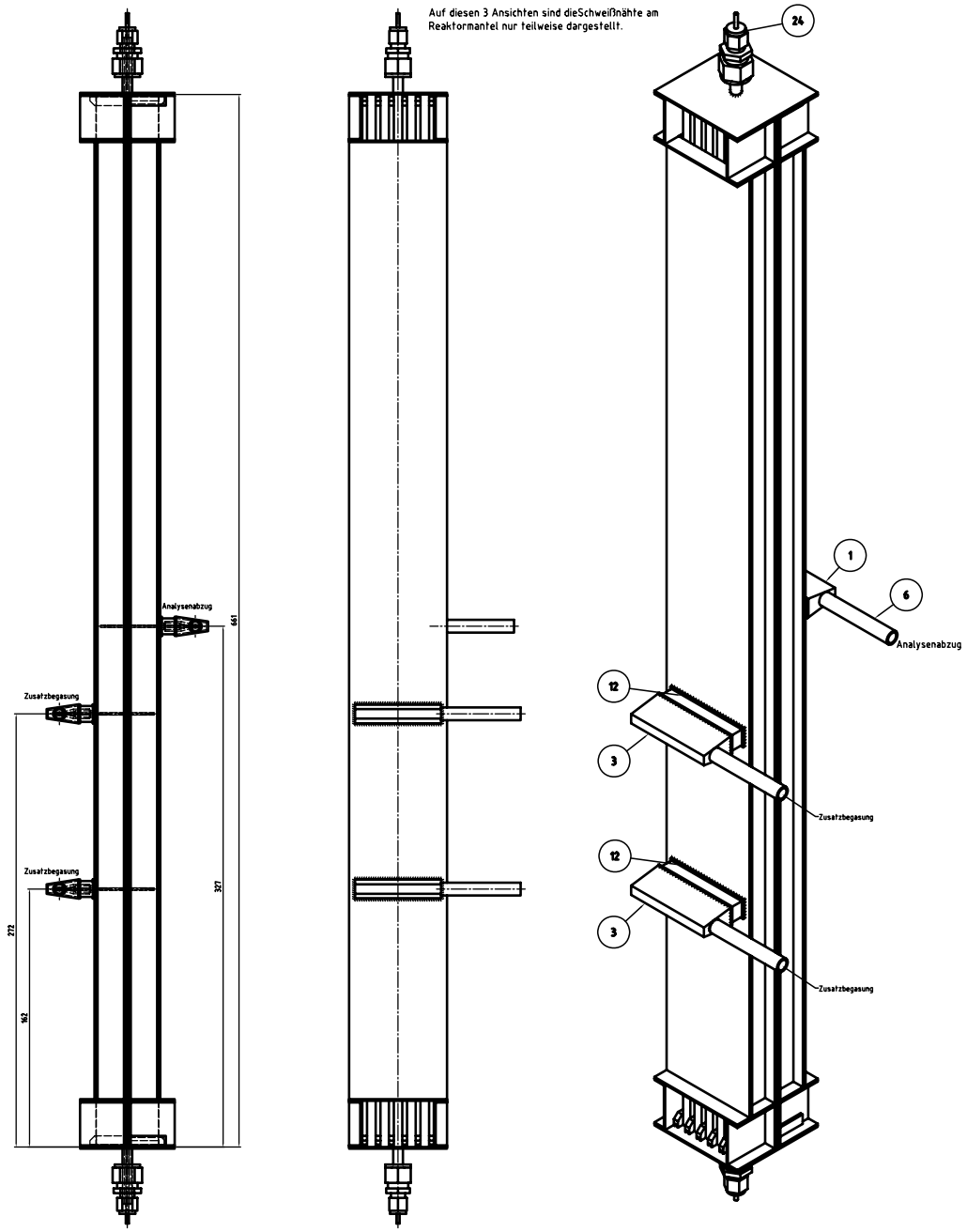

Figure E.6: 1-kW Counter-current reformer (2nd version). **Description** *(from left to right):* side and front (combustion side) view of the reformer; and isometric projection of the whole apparatus. Now both the reforming and the combustion side are basically symmetric with feed/exit ports from the sides. The combustion side has two additional side ports for hydrogen feed and the reforming side one additional side port for gas analysis.

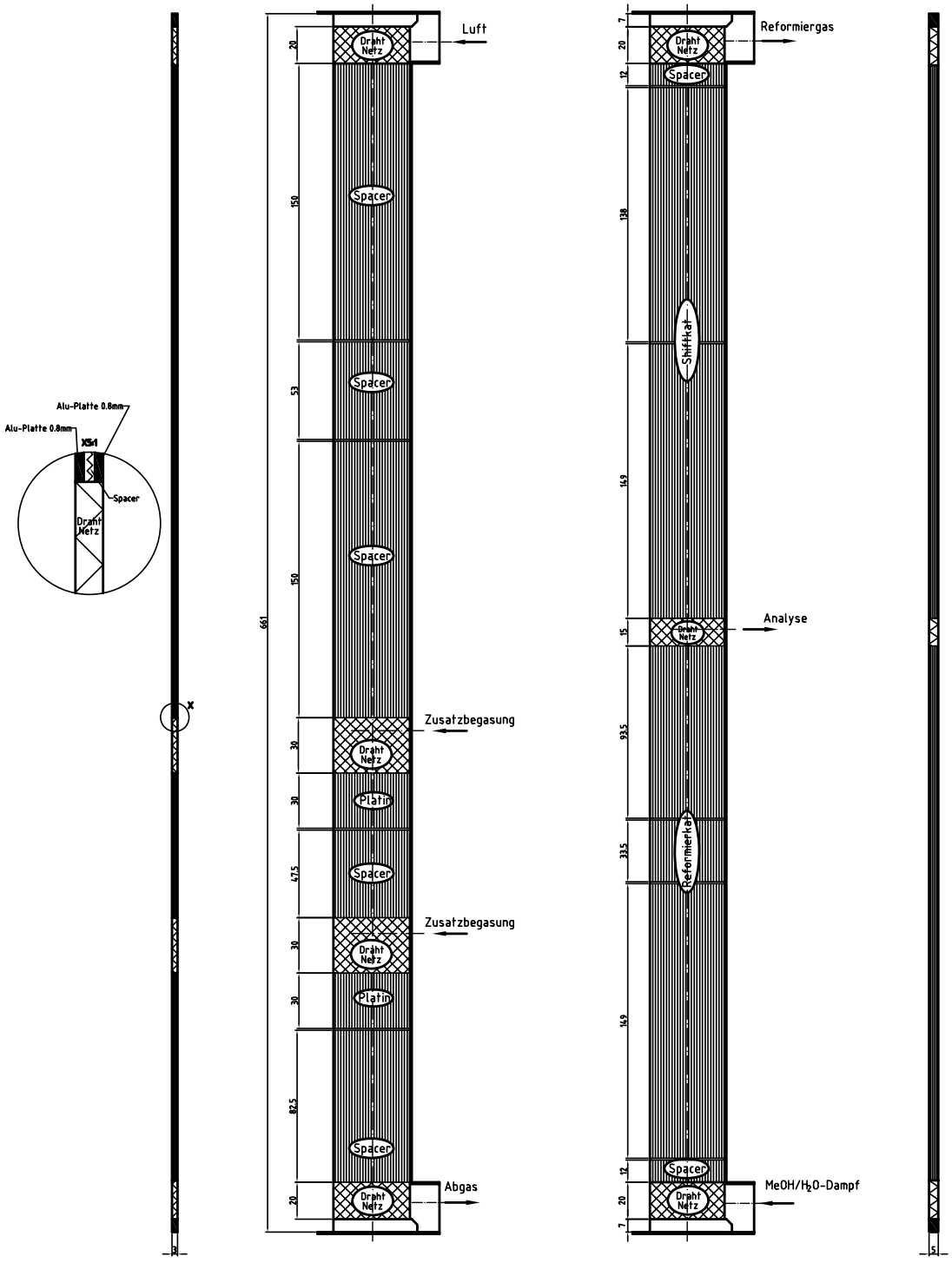

Figure E.7: Catalyst/spacer structuring of the 1-kW reformer, 2nd version. **Left***:* combustion side. Flow from top to bottom. Inert spacers with exception of two catalytic zones (”Platin”); **Right:** reforming side. Flow from bottom to top. Completely filled with reforming catalyst. There is an inert zone in the middle of the reactor, from where gas sample can be taken for analysis.

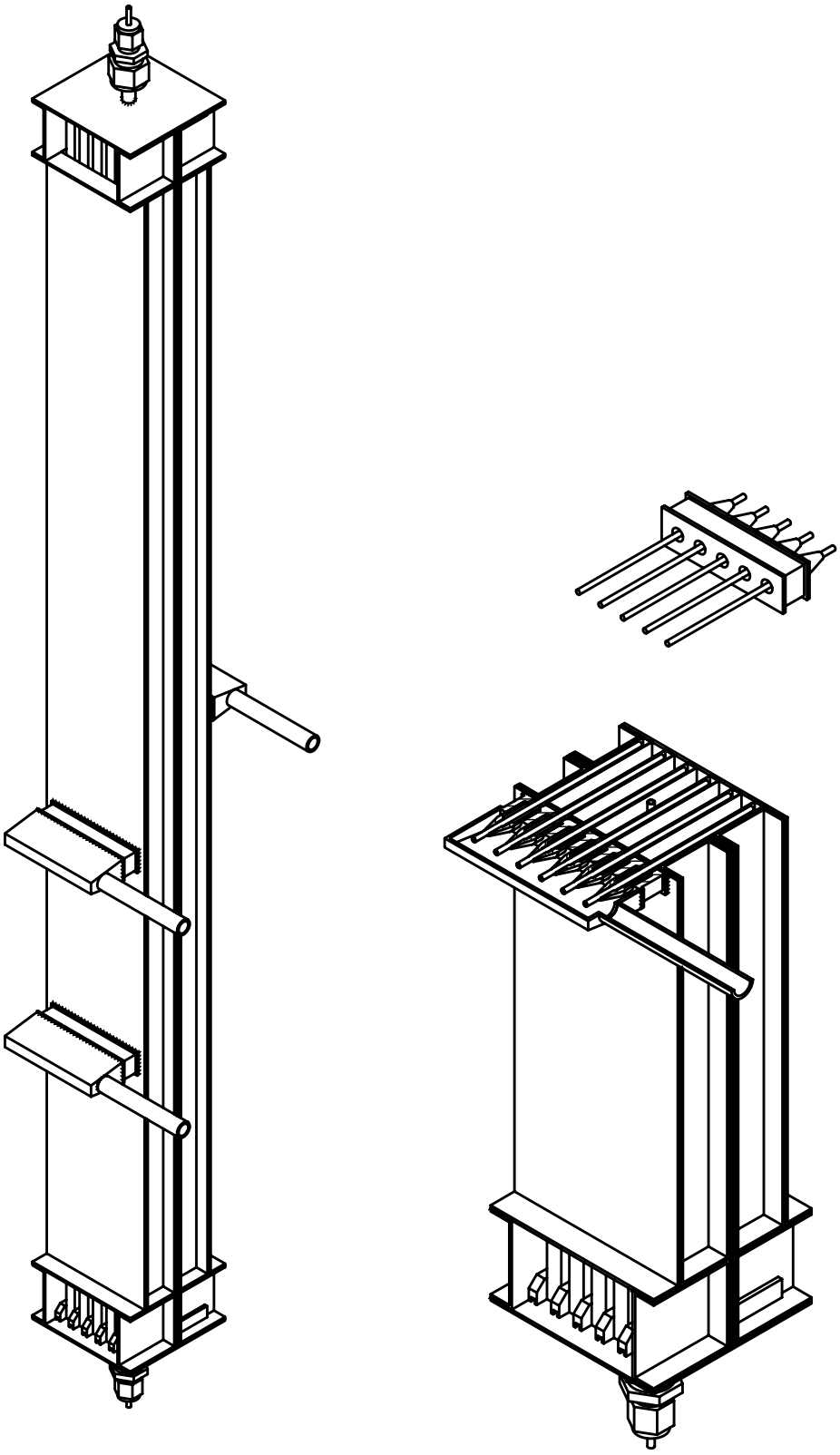

Figure E.8: 1-kW Reformer, 2nd version. Details on the gas side feed injectors. Capillary tubes are individually conducted into each combustion channel and hydrogen is uniformly distributed. Each capillary injector has 3 small radial bores for a better gas distribution over the channel depth.

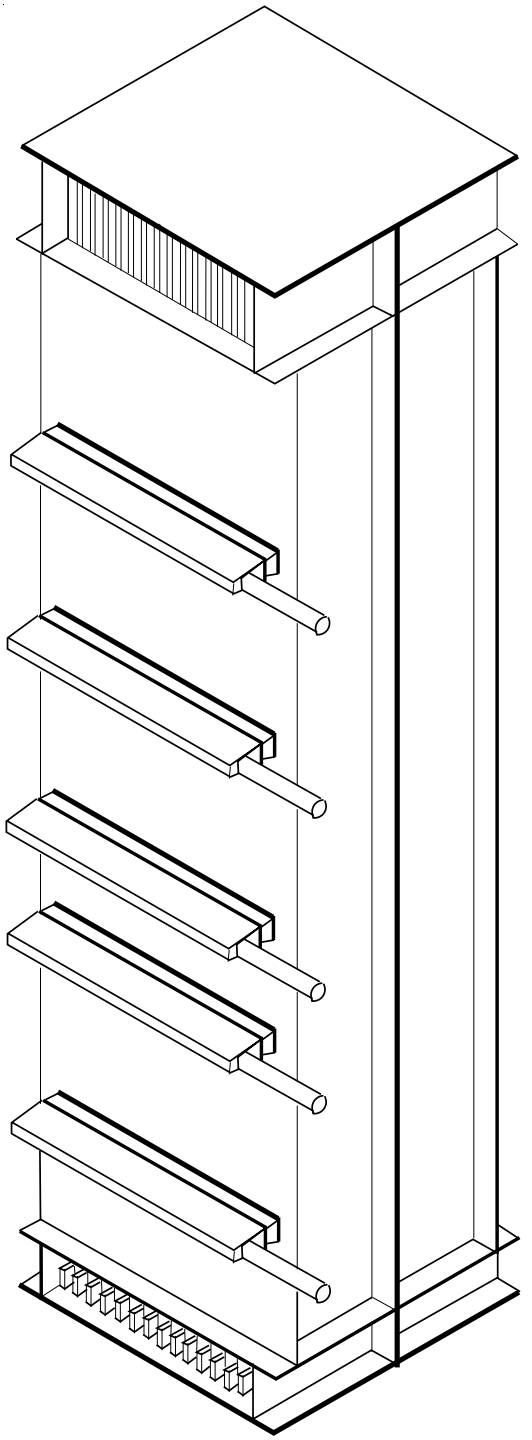

Figure E.9: Isometric projection of the 10-kW folded sheet reactor prototype with integrated feed evaporation and superheating. Only the combustion side (left side) is provided with five hydrogen side feed ports for a distributed heat generation along the reactor axial coordinate. Details on the reactor dimensioning are presented in Section 7.1.

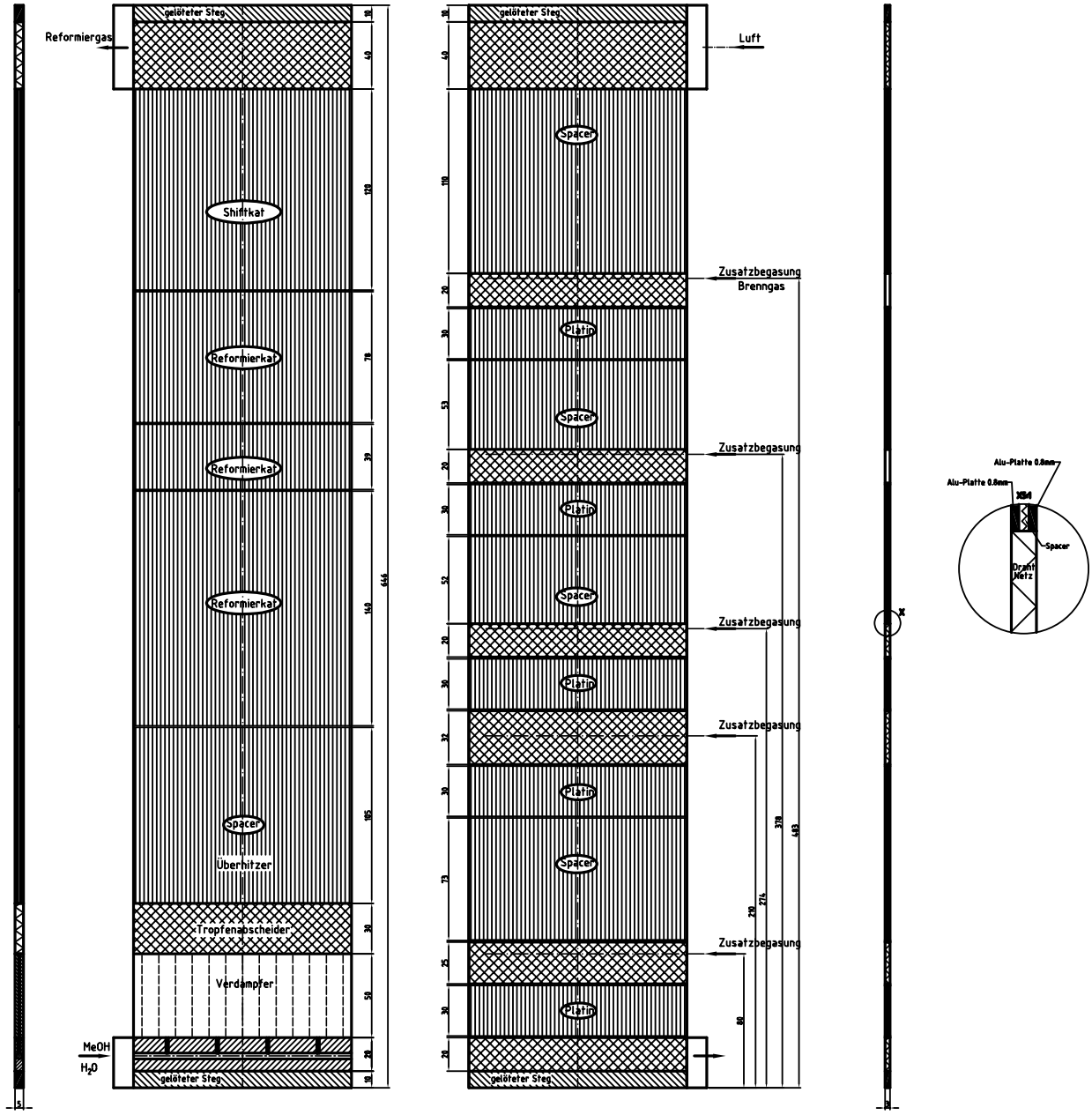

Figure E.10: Details on the spacer/catalyst distribution of one representative pair of channels along the reactor axial coordinate. **Left***:* reforming side; **Right:** combustion side. Notice the presence of different catalyst zones (”Reformierkat”; ”Shiftkat”) along the reforming side and the respective distribution of the catalytic zones (”Platin”) in the combustion channel for a targeted heat generation.

Appendix F

Photographs

In the following, some photographs illustrate the development of the folded-sheet reactor concept. The reactor conception, assambly and final construction, as well as the montage in the experimental setup are described in a graphical form as a part of the development process.

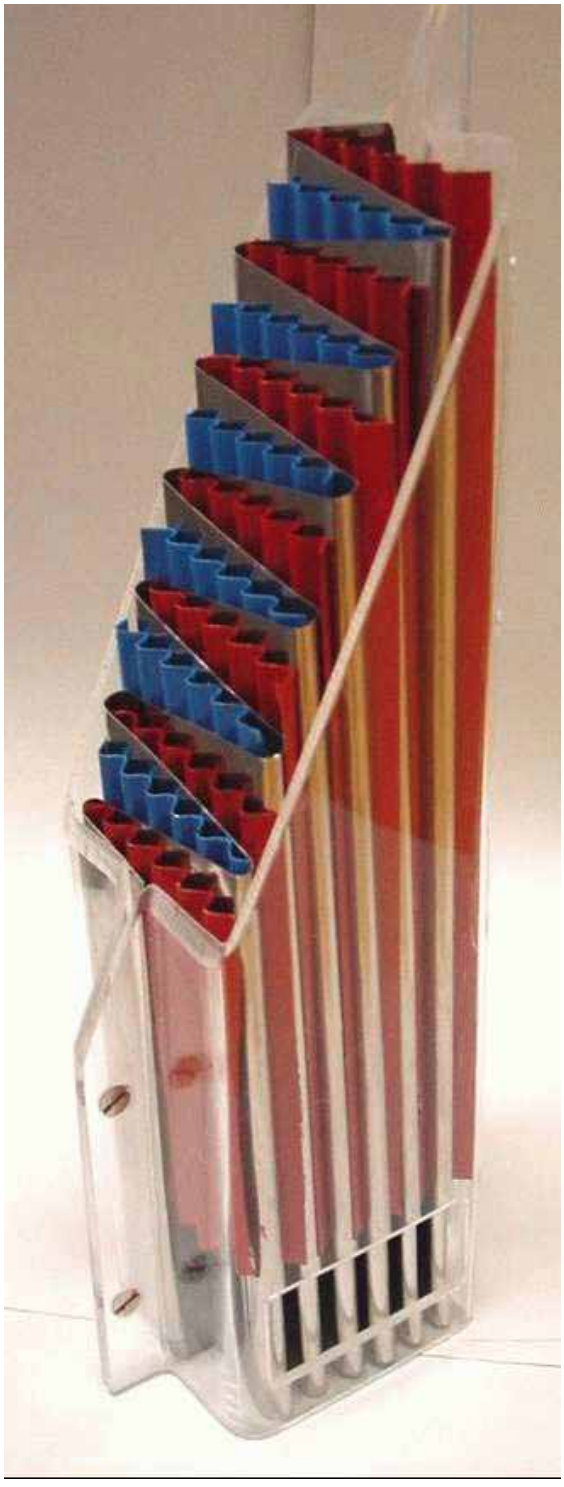

Figure F.1: Scaled model illustrating the folded-sheet reactor principle.

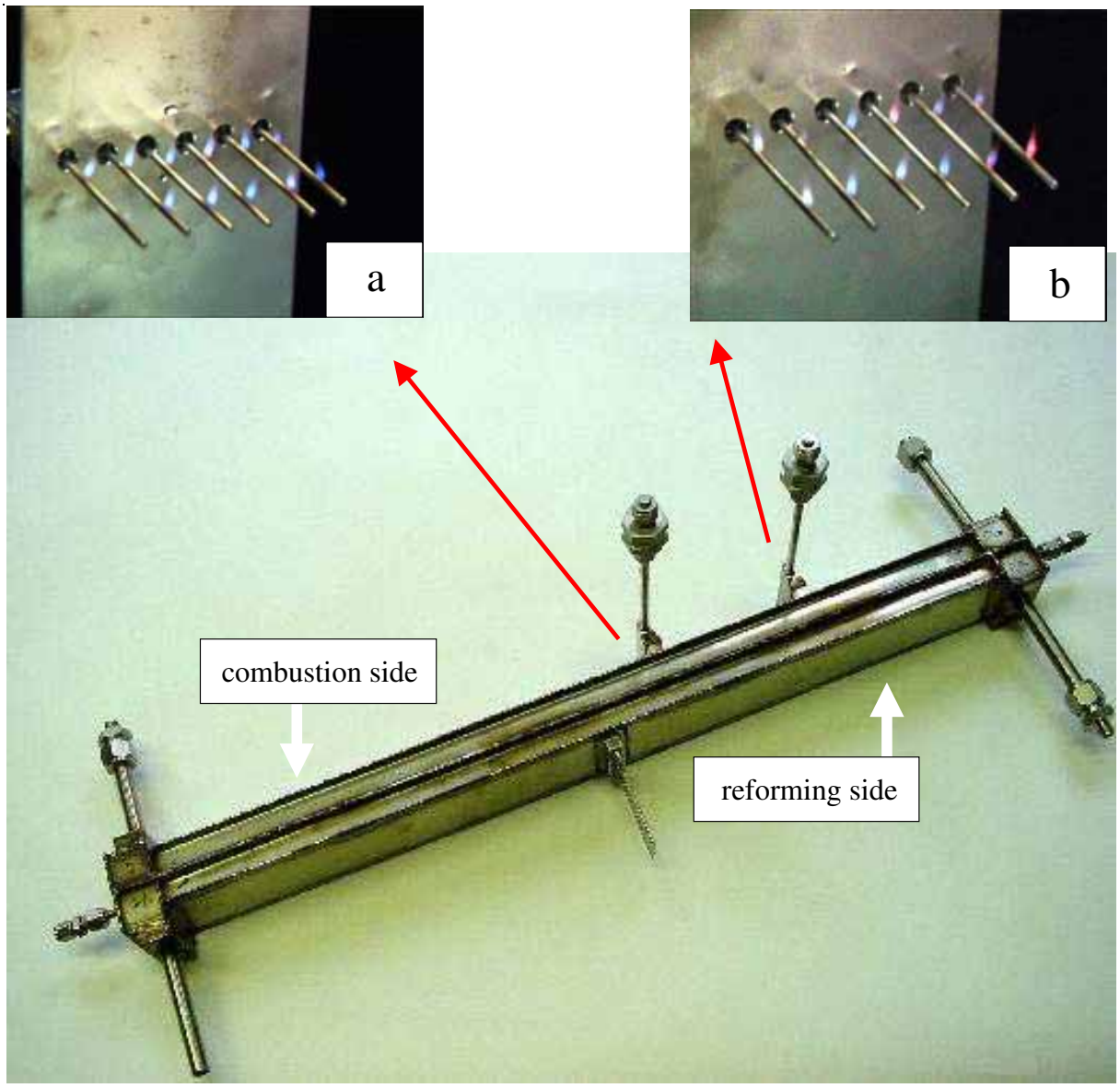

Figure F.2: 1-kW folded-sheet hydrogen processor with two fuel-gas side injection systems (version 2): Two snapshot photos of the gas distributors **(a** and **b)** show flame visualization experiments to determine the uniformity of the gas outlet through each single capillary tube.

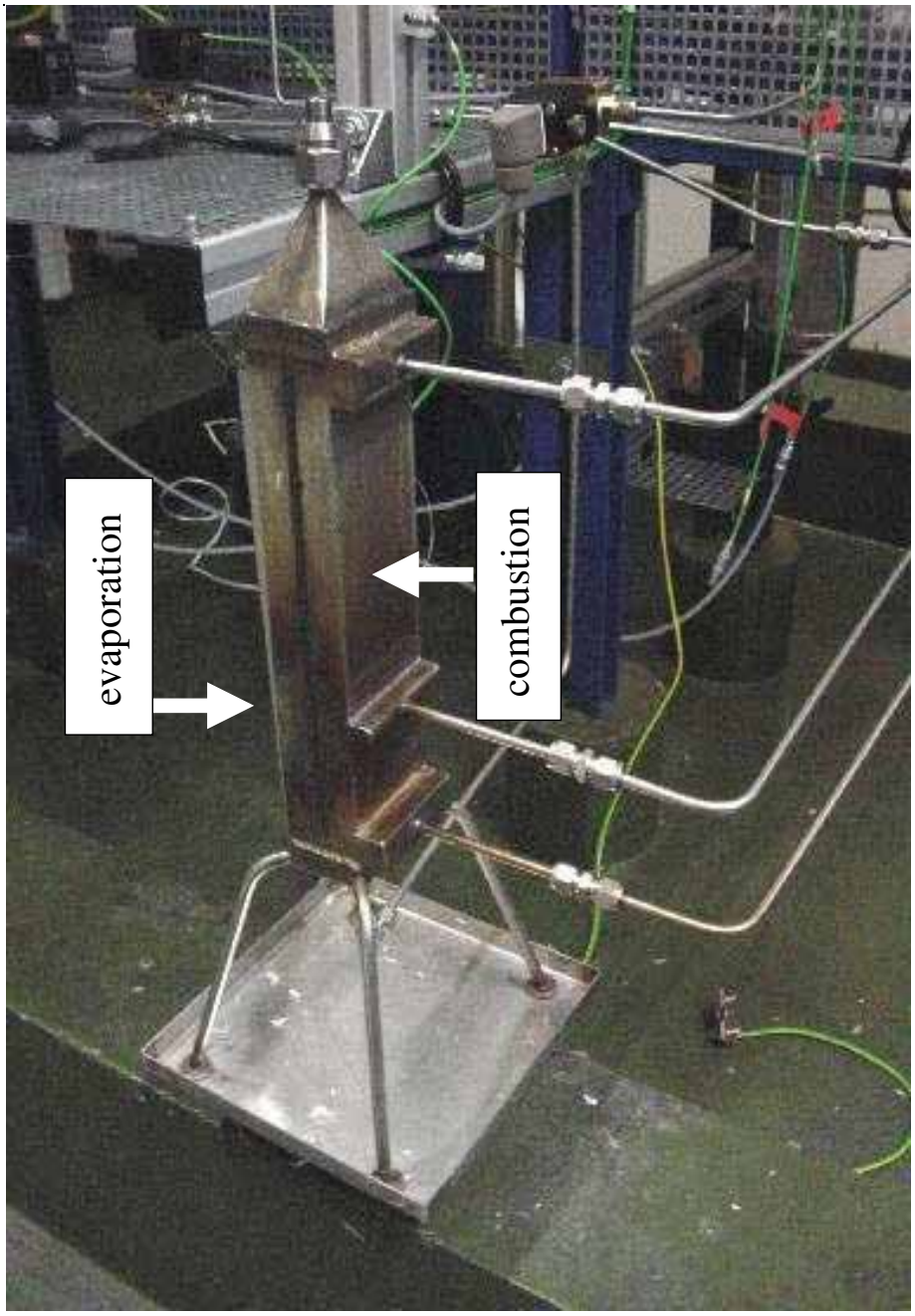

Figure F.3: Counter-current catalytic evaporator for the methanol/water mixture.

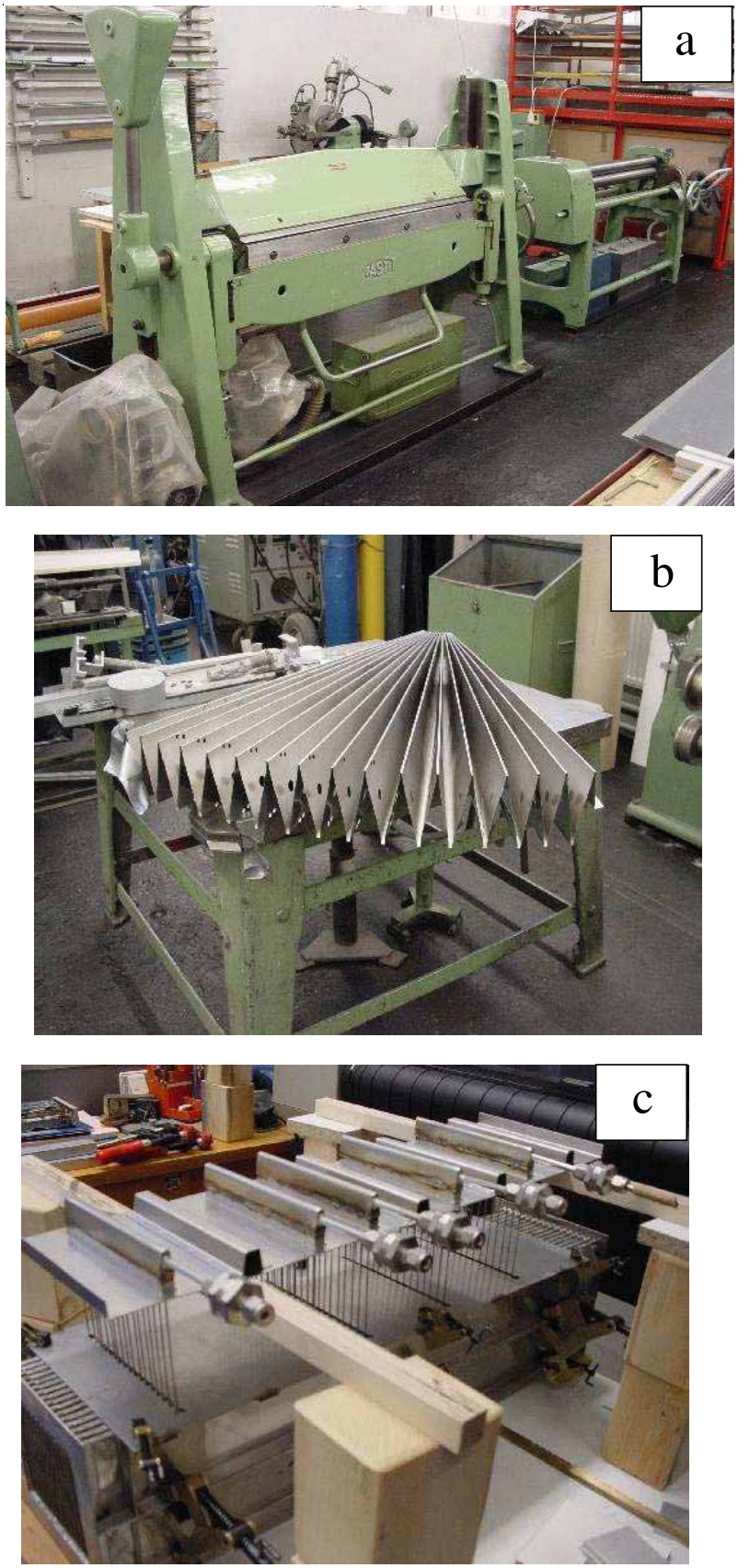

Figure F.4: **(a)** Bending machine. **(b)** Folded-sheet core structure. **(c)** Inserting the casing wall with multiple side injection ports.

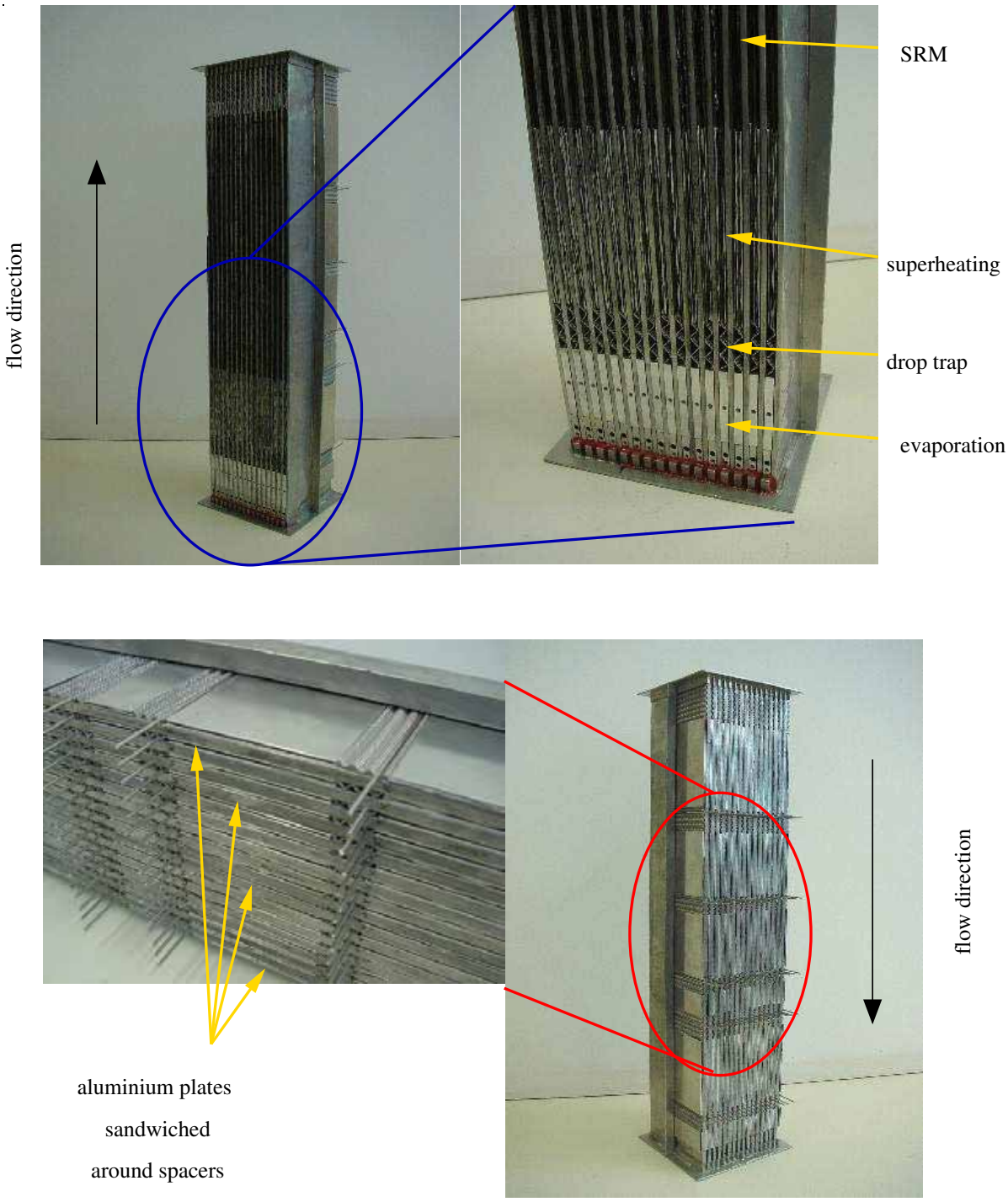

Figure F.5: Top-Left: Reforming side structuring; flow direction from the bottom upwards. **Top-Right:** details on the structuring on the reforming side. **Bottom-Right:** Combustion side of folded-sheet reactor with inserted catalyst/spacer structures, without casing; flow direction from top downwards. **Bottom-Left:** details on the combustion side - fuel injection zone: note the aluminium plates at each side of the spacer structures providing improved heat distribution through conduction.

Figure F.6: Photo of the 10-kW Folded-Sheet Reformer for SRM. Notice that the 5 side-feed injection ports are provided with particle filters, avoiding the intrusion of solid particles to the gas distributor.

Figure F.7: Top: 10-kW Folded-Sheet Reformer installed in the experimental set-up. **Bottom:** Off-gas flame burner.

Figure F.8: Experimental Set-up.

Bibliography

[1] Internet reference. http://www.daimlerchrysler.com/, consulted in 2005.

[2] A. Karim, J. Bravo and A. Datye. *Nonisothermality in packed bed reactors for steam reforming of methanol*. Appl. Cat. A, **1**, 101–109, 2005.

[3] J. Frauhammer. Ein neues Hochtemperaturreaktorkonzept zur Kopplung von endothermen und exothermen Reaktionen am Beispiel der Methan-Dampf-Reformierung. PhD Thesis, Institute for Chemical Process Engineering, University of Stuttgart, 2003.

[4] BASF AG. Technical Leaflet: BASF-Catalyst K3-110/K3-110/1, January 1996.

[5] B. A. Peppley, J. C. Amphlett, L. M. Kearns and R. F. Mann. *Methanol-steam reforming on $Cu/ZnO/Al_2O_3$ catalysts. Part 2: A comprehensive kinetic model*. Appl. Cat. A, **1**, 31–49, 1999.

[6] A. Shigeru. Patent Abstract of Japan: *Spiral type heat exchanger* (JP 10253272 A), 1998.

[7] A. Shigeru and Y. Shiger. Patent Abstract of Japan: *Method of operating spiral type heat exchanger and its device* (JP 7004874 A2), 1995.

[8] S. Thomas and M. Zalbowitz. *Fuel Cells - Green Power*. Technical Report, U.S. Department of Energy, Los Alamos National Laboratory, Los Alamos, New Mexico, 1999. Office of Advanced Automotive Technologies, Office of Transportation Technologies.

[9] V. Agarwal, S. Patel and K. K. Pant. *H_2 production by steam reforming of methanol over Cu/ZnO/Al_2O_3 catalysts: transient deactivation kinetics modeling*. Appl. Cat. A, **279**, 155–164, 2005.

[10] H. G. Düsterwald, B. Höhlein, H. Kraut, J. Meusinger, R. Peters and U. Stimming. *Methanol Steam Reforming in a Catalytic Fixed-Bed Reactor*. Chem. Eng. Technol., **20**, 617–623, 1997.

[11] B. Gerl. *Innovative Automobilantriebe: Konzepte auf der Basis von Brennstoffzellen, Traktionsbatterien und alternativen Kraftstoffen*. Technical Report ISBN 3-478-93275-0, Landsberg/ Lech : Moderne Industrie, 2002.

[12] Internet reference. http://www.idatech.com/, consulted in 2003.

[13] Internet reference: The Energy Conservation Center Japan. http://www.eccj.or.jp/, consulted in 2006.

[14] M. Kreutzer et al. *Hydrodynamics and Mass Transfer in Three-Phase Monolith Reactors*. Technical Report, Delf University of Technology, Department of Chemical Engineering, Section Industrial Calalysis, 2000. http://www.dct.tudelft.nl/monoliet/.

[15] Internet reference. http://www.johnson-matthey.com/, consulted in 2002.

[16] Internet reference. http://www.inspi.ufl.edu/, consulted in 2005.

[17] Internet reference. http://www.ngk.co.jp/, consulted in 2005.

[18] P. Reuse, A. Renken, K. Haas-Santo, O. Gorke and K. Schubert. *Hydrogen production for fuel cell application in an autothermal micro-channel reactor*. Chemical Engineering Journal, **11**, 133, 2004.

[19] Internet reference. http://www.ihi.co.jp/, consulted in 2005.

[20] Internet reference. http://www.advanticatech.com/, consulted in 2005.

[21] A. L. Dicks, S. L. Jones, R. Judd, K. Pointon and A. Gough. *Assessment of advanced catalyst performance and fabrication options for a compact steam reformer*. Technical Report ETSU Report F/02/00180/Rep, Harwell, UK, 2001.

[22] A. L. Dicks, R. Judd and P. Goulding. *Compact Reactor*, UK Patent, 2001.

[23] A. L. Dicks, R. W. Judd, K. D. Pointon, A. Siddle, S. L. Jones, P. S. Goulding and R. W. Judd. *Compact Shift Reactor*. World Patent (PCT) WO 03035544, 2003.

[24] X. Zhang et al. *Production of hydrogen for fuel cells by steam reforming of methanol on $Cu/ZrO_2/Al_2O_3$ catalysts*. Fuel Processing Technology, **83**, 183–192, 2003.

[25] M. Zanfir and A. Gavriilidis. *Modeling of a catalytic plate reactor for dehydrogenation-combustion coupling*. Chemical Engineering Science, **56**, 2671–2863, 2001.

[26] M. Zanfir and A. Gavriilidis. *Catalytic combustion assisted methane steam reforming in a catalytic plate reactor*. Chemical Engineering Science, **58**, 3947–3960, 2003.

[27] Internet reference. http://www.pnl.gov/microcats/apps/transport/, consulted in 2005.

[28] G. A. Whyatt, L. R. Pederson, C. F. Fischer and J. M. Davis. *FY 2005 Progress Report; Forecourt Fuel Processing: Micro-Channel Steam Reforming of Natural Gas for Distributed Hydrogen Production*. Technical Report, Pacific Northwest National Laboratory, 2005.

[29] R. J. Brandi, O. M. Alfano and A. E. Cassano. *Modeling of radiation absorption in a flat plate photocatalytic reactor*. Chemical Engineering Science, **51**, 3169–3174, 1996.

[30] Z. Zhang, W. A. Anderson and M. Moo-Young. *Modeling of corrugated plate photocatalytic reactors and experimental verification*. Chemical Engineering Science, **58**, 911–914, 2003.

[31] F. Babarada, M. D. Profirescu and C. Duane. *Parallel Plate Plasma Etching for MEMS Processing - Reactor Modeling*. In *Computational Publications*, S. 526–529, Cambridge, MA, 2003.

[32] A. Siddle, K. D. Pointon, R. W. Judd and S. L. Jones. *Fuel processing for fuel cells - A status review and assessment of prospects*. Technical Report ETSU F/03/00252/REP URN 031644, Advantica Ltd., 2003.

[33] M. Wilson, J. Valero and S. Gottesfeld. *Low platinum loading electrodes for polymer electrolyte fuel cell fabricated using thermoplastic ionomers*. Electrochimica Acta, **40**, 355–363, 1995.

[34] T. R. Ralph, G. A. Hards, J. E. Keating, S. A. Campbell, D. P. Wilkinson, M. Davis, J. St-Piere and M. C. Johnson. *Low cost electrodes for proton exchange membrane fuel cell - Performance in single cells and Ballard stacks* -. J. Electrochem. Soc.., **144**, 3845–3857, 1997.

[35] R. Kötz, M.Bärtschi, F. Büchi, R. Gallay and Ph. Dietrich. *HY.POWER - A Fuel Cell Car Boosted with Supercapacitors*. Technical Report, Paul Scherrer Institut, Switzerland, 2002. http://ecl.web.psi.ch.

[36] IEEE Transmission and Distribution Conference (Ed.). Fuel Parameter and Quality Constraints for Fuel Cell Distributed Generators. Wichita State University, 2003.

[37] R. R. Woods, J. Cruzens and J. Mauzey. *Fuel-flexible, fuel processor subsystem development - An update*. In *Fuel Cell Reforming Conference*, S. 92–106, South Coast Air Quality Management District, Dianmond Bar, Califormia, 1999.

[38] P. Häussinger, R. Lohmüller and A. M. Watson. *Ullmann's encyclopedia of industrial chemistry*, Chapter Hydrogen, S. 297, 442, 319, 376–377. VCH Verlagsgesellschaft mbH Weinheim, 1989.

[39] J. R. Lattner and M. P. Harold. *Comparison of methanol-based fuel processors for PEM fuel cell systems*. App. Cat. B: Env., **56**, 149–169, 2005.

[40] S. Ahmed and M. Krumpelt. *Hydrogen from hydrocarbon fuels for fuel cells*. Int. J. Hydrogen Energy, **26**, 291–301, 2001.

[41] L. Brown. *A comparative study of fuels for on-board hydrogen production for fuel-cell-powered automobiles*. In. J. Hydrogen Energy, **26**, 381 397, 2001.

[42] P. Hübner. *Reformierung von Kohlenwasserstoffen zur Wasserstofferzeugung für Brennstoffzellen*. Technical Report, Fraunhofer-Institut für Solare Energiesysteme ISE, 2003. http://www.h2-ise.de.

[43] A. K. Avci, Z. I. Önsan and D. L. Trimm. *On-board fuel conversion for hydrogen fuel cells: comparison of different fuels by computer simulations*. Appl. Cat., **216**, 243–256, 2001.

[44] W. Yanhui and W. Diyong. *The experimental research for production of hydrogen from n-octane through partially oxidizing and steam reforming method.* Int. J. Hydrogen Energy, **26**, 795–800, 2001.

[45] J. C. Amphlett, K. A. Creber, J. M. Davis, R. F. Mann, B. A. Peppley and D. M. Stokes. *Hydrogen Production by Steam Reforming of Methanol for Polymer Electrolyte Fuel Cells*. In. J. Hydrogen Energy, **19**, 131–137, 1994.

[46] E. Supp. *Ullmann's encyclopedia of industrial chemistry*, Chapter 5.1 Carbon, Gas Production from Carbon and Hydrocarbons, S. 422. VCH Verlagsgesellschaft mbH Weinheim, 1997.

[47] A. Morillo. *Aufbau und Inbetriebnahme einer Versuchsanlage für die Methanol-Dampfreformierung zur Wasserstofferzeugung*. Master's thesis, Institute for Chemical Engineering, University of Stuttgart, 2000.

[48] C. Becker. Katalytische Wandreaktorkonzepte für MSA-Synthese und Methanol-Dampfreformierung. PhD Thesis, Institute for Chemical Process Engineering, University of Stuttgart, 2002.

[49] N. E. Amadeo and M. A. Laborde. *Hydrogen production from the low-temperature water-gas shift reaction: kinetics and simulation of the industrial reactor*. Int. J. Hydrogen Energy, **20**, 949–956, 1995.

[50] B. A. Peppley, J. C. Amphlett, L. M. Kearns and R. F. Mann. *Methanol-steam reforming on $Cu/ZnO/Al_2O_3$. Part 1: the reaction network.* Appl. Cat. A, **1**, 21–29, 1999.

[51] G. Friedrich, G. Kolios and G. Eigenberger. German Patent: *Direktverdampfer für kleine Flüssigkeitsströme* (DE 197 23 68 B4), 1998.

[52] Internet reference. http://www.keithley.com/, consulted in 2003.

[53] Internet reference. http://www.hpac.com/, consulted in 2001.

[54] HORST GmbH. Technical Leaflet: HT60 Bedienungshandbuch, 1992.

[55] S. P. Asprey, B. W. Wojciechowski and B. P. Peppley. *Kinetic studies using temperature-scanning: the steam-reforming of methanol*. Appl. Cat. A, **1**, 51–70, 1999.

[56] G. A. Colsman. Verfahrenstechnische Optimierung der Brenngaserzeugung für Brennstoffzellen in Kraftfahrzeugen. PhD Thesis, Technische Hochschule Aachen, 1995.

[57] Verein Deutscher Ingenieure (Ed.). VDI–Wärmeatlas. VDI–Verlag, 1991.

[58] G. Kolios. Zur autothermen Führung der Styrolsynthese mit periodischem Wechsel der Strömungsrichtung. PhD Thesis, Institute for Chemical Process Engineering, University of Stuttgart, 1997.

[59] G. Gaiser. Strömungs- und Transportvorgänge in gewellten Strukturen. PhD Thesis, Institute for Chemical Process Engineering, University of Stuttgart, 1990.

[60] U. Nowak, J. Frauhammer and U. Nieken. *A fully adaptive algorithm for parabolic partial differential equations in one space dimension*. Comp. Chem. Eng., **20**, 547–561, 1996.

[61] U. Nowak. *Adaptive Linienmethoden für parabolische Systeme in einer Raumdimension*. Technical Report TR93-14, Konrad-Zuse-Zentrum für Informationstechnik, Berlin, 1993.

[62] P. Deuflhard, E. Hairer and J. Zugk. *One-step and extrapolation methods for differential-algebraic systems*. Numer. Math., **51**, 501–516, 1987.

[63] J. Frauhammer. *Numerische Lösung von eindimensionalen parabolischen Systemen mit adaptiven Gittern*. User's guide, Institute for Chemical Process Engineering, University of Stuttgart, 1992.

[64] Avesta Polarit Stainless Tube AB. Technical Leaflet: Material Code: AST 253 MA, 2000.

[65] ALMEMO. *Betriebsanleitung; Kapazitive Feuchtefühler FH A646*. Technical Report Psychrometer FN A846, FP A836, AHLBORN Mess- und Regelungstechnik, 1999.

[66] Dantec. Technical Leaflet, 2000.

[67] G. Hofmann. *Entwicklung und Inbetriebnahme eines neuartigen Gegenstromverdampfers zur Verdampfung von Methanol/Wassergemischen*. Master's thesis, Institute for Chemical Process Engineering, University of Stuttgart, 2000.

[68] V. Kottke, H. Blenke and K. D. Schmidt. *Eine remissions-fotometrische Meßmethode zur Bestimmung örtlicher Stoffübertragungskoeffizienten bei Zwangskonvektion in Luft*. Wärme und Stoffübertragung, **10**, 9–21, 1977.

[69] V. Kottke and H. Blenke. *Meßmethoden konvektiver Stoffübertragung*. Chem. Ind. Tech., **50**, 81–90, 1978.

[70] G. Eigenberger. *Chemische Reaktionstechnik I (Chemical Reaction Engineering I)*. Lecture script, Institute for Chemical Process Engineering, University of Stuttgart, 2001.

[71] R. K. Shah and A. L. London. Laminar Flow Forced Convection in Ducts. Academic Press, 1978.

[72] F. M. White. Viscous Fluid Flow. McGraw-Hill New York, 2 edition, 1991. 28 pp.

[73] R. C. Reid, J. M. Prausnitz and T. K. Sherwood. The Properties of Gases and Liquids. McGraw-Hill Book Company, 1977.

CURRICULUM VITAE

Personal Data		Arístides Morillo born on November 1974 in Valencia, Venezuela
Education	Sep/86 - Jul/91	**Baccalaureate in Science** Instituto Educacional Juan XXIII. Valencia, Venezuela Grade: High School Diploma
	Oct/91 - Oct/97	**Chemical Engineering** Universidad de Carabobo. Valencia, Venezuela Specialization: Chemical and Petrochemical Processes **Undergraduate Thesis** at PDVSA-Intevep (Internship) Research and Technological Support Centre of Petróleos de Venezuela, Venezuela Grade: Chemical Engineer
Professional Experience	Nov/97 - Sep/98	**Research Engineer in Reservoir Simulation** PDVSA-Intevep Research and Technological Support Centre of Petróleos de Venezuela, Venezuela
	Apr/99 - Mar/04	**Ph.D. Studies** financially supported by Fundayacucho Institute for Chemical Process Engineering of the University of Stuttgart, Germany
	Apr/04 - Jan/05	**Research Engineer in Exploration and Production** PDVSA-Intevep Research and Technological Support Centre of Petróleos de Venezuela, Venezuela
	Feb/05 - Jan/06	**Postdoc-Researcher in Process Development** Institute for Chemical Process Engineering of the University of Stuttgart, Germany
	Feb/06 -	**Research Engineer** BASF AG, GCT/S - Safety Engineering Ludwigshafen, Germany

Ludwigshafen am Rhein,
January, 2008